Real-space detection and manipulation of topological edge modes with ultracold atoms

Christoph Braun

München 2024

Real-space detection and manipulation of topological edge modes with ultracold atoms

Dissertation an der Fakultät für Physik
Ludwig-Maximilians-Universität München

vorgelegt von

Christoph Braun

aus Freudenstadt

München, den 4. Januar 2024

Zusammenfassung

In dieser Arbeit wird über die Beobachtung chiraler Randmoden mit Hilfe von ultrakalten Atomen in einem optischen Honigwabengitter, in dem das Tunneln moduliert wird, berichtet. Durch periodische Modulation des Hamiltonians, auch bekannt als Floquet-Engineering, realisieren wir drei Floquet topologische Phasen, darunter eine anomale Floquet-Phase, in der die Chern-Zahl verschwindet, aber dennoch topologische Randmoden existieren.

Das Vorhandensein von Randzuständen in topologischen Materialien ist über die Korrespondenz zwischen Volumen und Rand direkt mit den topologischen Invarianten des Volumens verbunden. In periodisch angetriebenen Systemen ist dieses Grundprinzip jedoch modifiziert und die Kenntnis über konventionelle topologische Invarianten ist nicht ausreichend, um das Vorhandensein von topologischen Randmoden vorherzusagen. Eine vollständige topologische Charakterisierung der drei Floquet topologischen Phasen mittels Windungszahlen wird durch die Messung der Lückenschließungen der Quasi-Energielücken und der Änderung der Berry-Krümmung an den Phasenübergängen ermöglicht. Wir verfolgen die Größe der Quasi-Energielücken in dem modulierten System mit Hilfe von Stückelberg-Interferometrie. Die Berry-Krümmung wird Quasiimpuls-aufgelöst gemessen, indem die im Impulsraum lokalisierte Atomwolke durch die Brillouin-Zone beschleunigt und die durch die Berry-Krümmung hervorgerufene anomale Auslenkung aufgezeichnet wird.

Topologisch geschützte Randmoden spielen eine entscheidende Rolle bei der Untersuchung von topologischen Phasen der Materie. Die Randmoden sind robust gegenüber schwachen Störungen wie Unordnung und können einen dissipationsfreien Transport ermöglichen. Dies steht im Gegensatz zu dem Verhalten in gewöhnlichen Isolatoren und kann wertvolle Erkenntnisse darüber liefern, unter welchen Bedingungen topologische Phasen entstehen oder verschwinden. Wir demonstrieren ein experimentelles Protokoll zur Realisierung chiraler Randmoden in optischen Gittern, indem wir eine topologische Schnittstelle mit Hilfe einer Potentialstufe erzeugen, die mit einem programmierbaren optischen Potential erzeugt wird. Wir zeigen, wie man effizient Teilchen in diesen Randmoden in den drei verschiedenen topologischen Floquet-Regimen präparieren kann. Indem wir die Höhe der Potentialstufe kontrollieren, zeigen wir, wie die Randmoden an der topologischen Schnittstelle entstehen. Wir beobachten, wie die Eigenschaften der Potentialstufe die Randmode in den drei Regimen beeinflussen, und wir zeigen, wie die Breite der Potentialstufe die Randmode im Haldane-Regime beeinflusst.

Die Beobachtung von Randmoden erweitert den Werkzeugkasten für kalte Atome erheblich, um topologische Eigenschaften in verschiedenen Phasen der Materie mit ultrakalten Atomen zu untersuchen, insbesondere in langsam getriebenen Systemen und bei Vorhandensein von Unordnung im Gitter, wo andere Techniken nicht anwendbar sind.

Abstract

This thesis reports on the observation of chiral edge modes using ultracold atoms in a tunneling modulated optical honeycomb lattice. By periodically modulating the Hamiltonian, also known as Floquet engineering, we realize three Floquet topological regimes, among which an anomalous Floquet phase, where the Chern number vanishes, yet topological edge modes persist.

The presence of edge states in topological materials is directly connected to the topological invariants of the bulk via the bulk-boundary correspondence. In periodically-driven systems, however, this fundamental principle is modified and knowledge about conventional bulk topological invariants is insufficient to predict the existence of topological edge modes. A full topological characterization of the three Floquet topological regimes using winding numbers is performed by measuring the gap closings of the quasienergy gaps and the change of Berry curvature at the phase transitions. We track the size of the quasienergy gaps in the modulated system by employing Stückelberg interferometry. The Berry curvature is measured in a quasimomentum resolved fashion by accelerating the atomic cloud, which is localized in momentum space, through the Brillouin zone and recording the anomalous displacement induced by the Berry curvature.

Topologically protected edge modes play a crucial role in the study of topological phases of matter. The edge modes are robust to weak perturbations such as disorder and can allow for dissipationless transport, which contrasts with the behavior in ordinary insulators and can provide valuable insights under which conditions topological phases emerge or disappear. We demonstrate an experimental protocol for realizing chiral edge modes in optical lattices, by creating a topological interface using a potential step that is generated with a programmable optical potential. We show how to efficiently prepare particles in these edge modes in the three distinct Floquet topological regimes. Controlling the height of the potential step we reveal how edge modes emerge at the topological interface. We observe how the properties of the edge influence the edge mode in the three regimes and show how the edge width influences the edge mode in the Haldane regime.

The observation and manipulation of edge modes greatly expands the cold atom toolbox to probe topological features of different phases of matter with ultracold atoms, in particular in slowly-driven systems and in the presence of disorder, where other techniques are not applicable.

Contents

CHAPTER 1

Introduction

The ability to probe the behavior of a quantum mechanical system close to its ground state has been greatly improved with the preparation of Bose Einstein condensates (BEC) [1–3] and degenerate Fermi gases [4]. With the unique control and access to novel observables inaccessible to solid state system, ultracold atoms provide a unique platform to investigate a wide range of phenomena [5, 6].

Being able to independently control the interaction among the particles [7], their geometry [8] or dimensionality allows experiments in very different regimes [9]. In three dimensions we find e.g. Bose Einstein condensation of atoms [10] and molecules made up of fermionic atoms [11–14] in the BEC-BCS crossover [15]. In two dimensions with a continuous symmetry true long-range order is absent at any finite temperature [16, 17] and atoms only condense to quasi-condensates due to the unbinding of vortex–antivortex pairs [18–20]. In one dimensional systems, which can be realized utilizing a two dimensional optical lattice [21], the properties of bosonic particles exhibit properties of fermionic particles in the so-called Tonks-Giradeau-Gas [22–26]. Tuning individual parameters of these cold atomic samples enables probing of the phase transition from a thermal gas to a BEC, or the formation of a quantum droplet [27–30] or supersolid [31–35].

Not only the ability to prepare quantum systems in a vast landscape of experimental parameters but also the observation of the resulting phases is dramatically changed by the microscopic manipulation techniques that have been developed in recent years in cold atom platforms. Quantum gas microscopes enable the observation of individual snapshots of the microscopic many-body wave functions [36–38]. Preparing engineered initial states allows for direct observation of quasiparticles [39, 40] and their time evolution [40, 41], and such preparations can be facilitated by new techniques where atoms are sorted into defect-free arrays [42, 43]. Finally dynamically tuning parameters of the Hamiltonian across phase transitions and observing the underlying dynamics enables a new approach to investigate quantum critical phenomena [44, 45].

In contrast to thermodynamic phase transitions, where thermal fluctuations are driving the phase transitions, some of the mentioned above represent a quantum phase transitions, where quantum fluctuations due to the Heisenberg uncertainty principle [46] drive the phase transition [47].

In contrast to the notion of a phase as illustrated above, which are distinguished by the presence or absence of a symmetry or equivalently described by a local order parameter [47, 48], such as continuous translational symmetry in a liquid compared to a discrete translational symmetry in a solid, we can also identify topological phases of matter, which go beyond the usual classification of phases of matter based on symmetry breaking and cannot be characterized by a local order parameter. The arguably most prominent example is the integer quantum Hall effect [49–51]. When a current I_x runs through a sample with an applied transversal magnetic field B_z, a transverse voltage V_y builds up. For sufficiently strong magnetic fields at low enough temperatures, and if the sample can be described as a two-dimensional electron gas, we find plateaus of the transverse conductivity [52]

$$G_{xy} \equiv \frac{I_x}{V_y} = n\frac{e^2}{h}, \tag{1.1}$$

with $n \in \mathbb{N}$. These plateaus are extremely stable and solely depend on the fundamental constants of the electron charge e and Planck's constant h, furthermore they are insensitive to the geometry of the sample and the microscopic parameters of the system [53]. Since the redefinition of the SI-units in 2019, e^2/h is a fixed quantity [54]. The precise quantization of the transverse conductivity is directly related to the topological invariants of the system, i.e., even though n may differ for various bands the system does not undergo a phase transition where the symmetries of the system change. The transverse conductivity is intimately linked to the existence of chiral edge modes of the sample via the bulk-boundary correspondence [55].

Topology in mathematics is concerned with the properties of a geometric object that are preserved under continuous deformations [56]. An example for such a topological invariant would be the genus g of a closed surface, which quantifies the number of holes in the surface. The genus does not change as long as the number of holes is unchanged, i.e., a bottle and a sphere are equivalent with $g = 0$, while a mug can be continuously deformed to a torus, which both exhibit $g = 1$. The genus can be connected to the integrated curvature over the surface, highlighting that the genus is not a local but a global quantity of the surface.

In a similar fashion we can define a curvature of a gapped, non-degenerate band in the Brillouin zone, the Berry Curvature, which when integrated also results in an integer invariant, the Chern number. The invariant n in the integer quantum Hall effect, is simply the sum of the Chern numbers of all occupied bands. Two bands with the same Chern number can only be continuously transformed, i.e., without closing of the energy gap, between one another if they exhibit the same value of the topological invariant, i.e., belong to the same topological class [57, 58]. More generally Hamiltonians can be classified by their symmetry class and dimensionality. According to the Altland-Zirnbauer classification [59, 60] the Hamiltonians can be categorized conditional on whether they exhibit time-reversal, chiral and particle-hole symmetry. A system exhibiting the integer quantum Hall effect in the presence of a magnetic field breaks time reversal symmetry, similarly does the seminal Haldane model even though it does not require a net magnetic field [61]. According to the

Altland-Zirnbauer classification the system is described by a $\mathbb{Z}$ invariant in the absence of chiral and particle-hole symmetry. This $\mathbb{Z}$ invariant is the Chern number for a single band.

Coupling the spin and orbit degree of freedom results in a system additionally conserving time reversal symmetry [62, 63]: the quantum spin Hall insulator, which was experimentally observed soon after the theoretical proposal [64, 65]. Here the topological classification of the topological insulator is described by a $\mathbb{Z}_2$ invariant. While the integer and quantum spin Hall effect can be explained in a single particle picture, the fractional quantum Hall effect [66–68] requires interacting particles. The resulting quasi particles obey fractional statistics [69, 70], exhibit long-range entanglement [71, 72] and can exhibit non-Abelian states [71, 73]. Common to all topologically non-trivial systems is the existence of gapless boundary states predicted via the bulk-boundary correspondence [57, 60].

The topological invariants are robust to small perturbations, because the invariant cannot change unless a gap in the spectrum is closing. Therefore also the gapless boundary states are not affected by these perturbations. Considering again the integer quantum Hall effect, the transverse conductivity can be explained by one dimensional metallic states located in close vicinity to the edge of the system [55, 74–78]. These edge modes are chiral i.e., they only transport current in one direction and do not scatter e.g. due to disorder in the lattice [57, 79]. The detection of topological chiral edge modes presents direct evidence of the topological nature of the underlying system.

The implementation with ultracold atoms requires further efforts in order to implement a topological band structure because a magnetic field does not break time reversal symmetry for charge neutral particles, such as ultracold atoms in an optical lattice. To mimic the coupling of a charged particle on a lattice to a magnetic field, the coupling to its vector potential is implemented via a complex tunneling element [80]. Applying an oscillating force to a particle in a lattice strongly affects its tunneling rate [81, 82]. Shaking, i.e., periodically applying a force to the lattice, in a two-dimensional honeycomb lattice enables the realization of complex tunneling and the implementation of the Haldane model [83, 84], in a similar fashion this enabled the direct observation of edge modes in a lattice of photonic waveguides [85]. Other modulation schemes such as laser assisted tunneling or a direct modulation of the tunnel coupling also implement interesting band strutures [80, 86–88], such as the Hofstadter Hamiltonian [89]. Common to all the schemes which rely on a periodic modulation is breaking of time translational invariance, which results in a periodic quasienergy restricted to, in analogy to the momentum in a lattice, the Floquet Brillouin zone with a width proportional to the modulation frequency. If the energy scales of the system become comparable to the modulation frequency an anomalous Floquet phase can emerge, where a different topological description is necessary compared to static systems [86, 87]. The concept of classifying driven systems by their symmetries and dimensionality can be extended to the stationary states of the driven system by considering the evolution operator of the system [90]. Periodic modulation, also referred to as Floquet engineering, offers a wide parameter range to explore [88, 91], which implements the equivalence of static systems in the high frequency limit [88, 92, 93] and genuine out of equilibrium systems for low driving frequencies [86, 87]. Such an out of equilibrium phase which does not have a static counterpart is the aforementioned anomalous Floquet phase. It is characterized

by a Chern number of zero, i.e., the conventional bulk-boundary correspondence would predict no edge modes, however the system still exhibits edge modes. The topological classification can then be performed by identifying a new set of invariants - the winding numbers [87]. The full characterization of a N band system then requires the knowledge of N winding numbers or alternatively the knowledge of $N - 1$ Chern numbers and one winding number or any other combination.

A striking difference compared to e.g. the Haldane model is the behavior in the presence of disorder, where the anomalous Floquet phase is expected to host chiral edge modes even when all bulk states are fully localized, the anomalous Floquet Anderson insulator [94–96]. In the presence of disorder probing the bulk topological features of the band structure experimentally is challenging, however the observation of the edge mode of the system can serve as a clear signature whether the system is topological or not. This can serve as a sensitive probe to identify topological phase transitions induced by disorder or interactions.

Topologically protected edge modes play a crucial role in the study of topological phases of matter as they provide hallmark evidence of the quantized transport. By creating more than one edge in a fractional quantum Hall system, edge modes can collide [97] or interfere [98, 99] and provide evidence of the anyonic exchange statistic of the underlying quasiparticles. Understanding how the edge potential modifies the spatial structure of modes on the edge in quantum Hall system still poses interesting questions [100–104]. In the presence of smooth confining potentials interactions may induce quantum phase transitions on the edge, while leaving the bulk unperturbed, resulting in additional structure on the edge [103]. Directly observing how electrons, or atoms in optical lattices, move along the edge might give insights to the microscopic behavior of these systems. While cold atom experiments are taking significant steps towards realizing fractional quantum Hall physics [105, 106], faithful preparation of the initial state will be challenging in larger systems [107]. Implementations of their non-interacting counterpart provide access to the bulk topological invariants [108–111], but have so far not been probed on the edge.

The observation of edge modes in systems simulating the effects of the integer quantum Hall effect, such as a lattice of twisted waveguides [85, 112–114], electronic circuits [115] or the internal levels of an atom [116–118] is facilitated by the naturally sharp boundaries of these systems. In cold atom systems the edges are typically smooth, hindering the preparation of a sharp boundary. Despite many proposals for two-dimensional systems [119–122] observation of edge modes in real space with cold atoms so far remained elusive.

This thesis

Here we present the observation of chiral edge modes in a two-dimensional real-space Floquet system by generating a topological interface in the lattice. The work presented in this thesis builds on and extends the toolbox used to probe ultracold atoms in topological band structures. By periodically modulating the tunneling in the optical honeycomb lattice [86] we implement a Floquet topological system that can realize the Haldane model and the anomalous Floquet phase, thus realizing a system close to the quantum Hall system and a

topological phase in the out of equilibrium setting without static counterpart. By probing the energy gap using Stückelberg interferometry we directly identify the phase transition between the two regimes, which also highlights the robustness of the topological phases over a wide parameter range. Tracking the evolution of the Berry curvature at the phase transition allows for reconstruction of the topological invariants of the system presenting a full characterization of the topological invariants [111].

In a second experiment [123] we build on the knowledge of the phase diagram and implement a topological interface in the lattice by applying a potential step. We present the observation of chiral edge modes in a two-dimensional real-space Floquet system at a topological interface. Precisely controlling the spatial extent, position and phase profile of the initial wave function using an optical tweezer we probe the existence and properties of the chiral edge modes. Being able to probe the bulk and edge of the system we can verify the bulk-boundary correspondence and observe edge modes in the non-trivial phases, but observe non in the static lattice. We identify the presence of edge modes also in the anomalous Floquet phase confirming the previous topological characterization. The tunability of the edge potential allows us for the first time to investigate the emergence of edge modes as we establish a topological interface by varying the height of the potential. Tuning the width of the potential we observe a slowing of the edge mode.

Outline

This thesis is divided into six chapter as follows.

Chapter 2 introduces the concept of geometrical phases and establishes the connection between the topological invariants and the existence of edge modes. The Haldane model is discussed to gain some intuition for the physics in the honeycomb lattice. It proceeds by reviewing the concept of Floquet engineering and illustrates the tunneling modulated honeycomb lattice. Anomalous Floquet phases are discussed comparing different driving protocols.

The experimental setup is briefly introduced in Chapter 3. The cooling scheme is introduced and the optical potentials are discussed in greater detail. Implementing high resolution optical potentials requires careful alignment of the large NA optics which is discussed along with a method to characterize the achieved resolution.

The full characterization of the topological invariants in the tunnel-modulated honeycomb lattice is presented in Chapter 4. We introduce the experimentally implemented driving protocol and highlight the measurement of the quasi energy gaps. By measuring Hall deflections we track the evolution of the Berry curvature at the phase transitions. Combining the closing of the quasienergy gap and the change of the Berry curvature, we derive winding numbers in the three topological phases presenting a full topological characterization of the invariants.

Chapter 5 presents the observation and manipulation of edge modes in a two-dimensional real-space Floquet topological system. Illustrating the initial state preparation, we confirm the coherent evolution in the lattice by tracking the evolution of a initially localized wave packet in the static lattice. We then present the observation of edge modes in the anomalous Floquet regime, and compare its evolution to the static system. We show how to prepare

edge modes in the Haldane regime and probe the phase profile ot these states. Quantifying the velocity of the edge mode we study the emergence of edge modes as we increase the height of the potential step. Changing the width of the step potential we observe a slowing down of the edge mode as expected from theory.

The main findings are summarized in Chapter 6 and it provides a brief outlook on future directions.

Publications

The central results presented in this thesis have been published or appeared as preprints in the following references:

- K. Wintersperger, **C. Braun**, F. N. Ünal, A. Eckardt, M. D. Liberto, N. Goldman, I. Bloch, and M. Aidelsburger, *Realization of an Anomalous Floquet Topological System with Ultracold Atoms*, Nature Physics **16**, 1058 (2020)

- **C. Braun**, R. Saint-Jalm, A. Hesse, J. Arceri, I. Bloch, and M. Aidelsburger, *Real-Space Detection and Manipulation of Topological Edge Modes with Ultracold Atoms*, 2023, arXiv:2304.01980, preprint

Topological phases and the tunneling modulated honeycomb lattice

The behavior of non-interacting electrons in solids is commonly described by a band structure [124, 125]. The eigenstates associated with these energy bands can be classified according to their topological structure [55]. We will first introduce the concept of geometric phases which can arise in cyclic adiabatic processes in Section 2.1. Section 2.2 will review the paradigmatic Haldane model and discuss its topological properties. Section 2.3 will illustrate the implications of a periodically driven Hamiltonian, then Section 2.4 will discuss how the previously introduced concepts can be utilized to generate topologically non-trivial bands with charge neutral particles by modulating the Hamiltonian periodically. The resulting anomalous Floquet phase is introduced in Section 2.5 and the new necessary invariants to characterize its topology will be discussed in Section 2.5.2.

2.1 Geometric Phases

A prominent example for a geometric phase arising in a classical system is the Foucault pendulum. We consider a pendulum located somewhere on the surface of the earth, which is rotating around its axis of rotation, therefore the path the pendulum follows is a circle. A fixed pendulum oscillates in a plane, upon moving the pendulum on the surface of the earth this plane will move. For example, transport at constant latitude θ will introduce a rotation of the plane of the pendulum by $2\pi\cos(\theta)$. For a general path the angle of rotation will be given by the solid angle enclosed by the path [126]. The angle of rotation is independent of the speed at which the pendulum is traveling, as long as it is not too fast, and solely depends on the geometry of the path, which justifies its name. In a similar fashion we can find geometric phases emerging in quantum system for adiabatic transport - the Berry phase.

2.1.1 Cyclic adiabatic evolution

In the following we will illustrate the effect of cyclic adiabatic evolution and the possibility of an emerging *topological* phase factor [127, 128]. We will consider the evolution of a quantum state $|\psi(t)\rangle$ under the influence of a time-varying Hamiltonian $\hat{H}(t) = \hat{H}(\mathbf{P}(t))$, where $\mathbf{P}(t)$

is representing the time-varying parameters of the Hamiltonian. $\mathbf{P}(t)$ is a point in the parameter space with a certain dimension of the Hamiltonian. The instantaneous eigenstates $|n, \mathbf{P}\rangle$ and eigenenergies $E_n(\mathbf{P})$ will be related to the Hamiltonian at setting $\mathbf{P}$ according to

$$\hat{H}(\mathbf{P}) |n, \mathbf{P}\rangle = E_n(\mathbf{P}) |n, \mathbf{P}\rangle \tag{2.1}$$
$$\langle m, \mathbf{P}|n, \mathbf{P}\rangle = \delta_{m,n},$$

where $\delta_{m,n}$ is the Kronecker-Delta. The change of the parameters $\mathbf{P}(t)$ will be periodic along a closed path $\mathbf{C}$ with a period T, i.e.,

$$\mathbf{C} : \mathbf{P}(0) \rightarrow \mathbf{P}(t) \rightarrow \mathbf{P}(T) = \mathbf{P}(0). \tag{2.2}$$

Starting from an eigenstate of the Hamiltonian, we assume that the parameters $\mathbf{P}$ are evolving such that the evolution is adiabatic, i.e., there is no admixture of other states during the evolution, this condition can be expressed as

$$\langle m, \mathbf{P}(t)| \left[\frac{\mathrm{d}}{\mathrm{d}t} \hat{H}(t) \right] |n, \mathbf{P}(t)\rangle \ll \frac{|E_n(\mathbf{P}(t)) - E_m(\mathbf{P}(t))|^2}{\hbar}, \text{ for all } m \neq n, \tag{2.3}$$

where $E_i(\mathbf{P}(t))$ corresponds to the eigenenergy of state $|i, \mathbf{P}(t)\rangle$, which means that the change of energy related to the left side of Equation 2.3, is significantly smaller than the relevant angular frequency associated to energy gaps of the Hamiltonian, especially the gaps in energy with respect to the state under consideration $|n, \mathbf{P}\rangle$.

During a cyclic evolution of a static, i.e., time-independent Hamiltonian, the state $|\psi(t)\rangle$ with energy E_ψ will only pick up a *dynamical phase factor* according to the energy of the state

$$|\psi(T)\rangle = \mathrm{e}^{-\frac{i}{\hbar} E_\psi T} |\psi(0)\rangle. \tag{2.4}$$

For a more general, time-dependent Hamiltonian, the evolution will follow the Schrödinger equation

$$i\hbar \frac{\mathrm{d}}{\mathrm{d}t} |\psi(t)\rangle = \hat{H}(\mathbf{P}(t)) |\psi(t)\rangle, \tag{2.5}$$

we can express the state vector in the basis $\{|n, \mathbf{P}\rangle\}$ with time-dependent coefficients $c_n(t)$

$$|\psi(t)\rangle = \sum_j c_j(t) |j, \mathbf{P}(t)\rangle, \tag{2.6}$$

and after plugging it into the Schrödinger equation find for the coefficients

$$\frac{\mathrm{d}}{\mathrm{d}t} c_n(t) = -c_n(t) \left(\frac{i}{\hbar} E_n(t) + \langle n, \mathbf{P}(t)| \frac{\mathrm{d}}{\mathrm{d}t} |n, \mathbf{P}(t)\rangle \right). \tag{2.7}$$

We can now integrate Equation 2.7 and find for the coefficients

$$c_n(t) = \mathrm{e}^{-\frac{i}{\hbar} \int_0^t E_n(t')\mathrm{d}t'} \, \mathrm{e}^{i \int_0^t i \langle n, \mathbf{P}(t')| \frac{\mathrm{d}}{\mathrm{d}t'} |n, \mathbf{P}(t')\rangle \mathrm{d}t'} + c_n(0), \tag{2.8}$$

where we again recover the dynamical phase, but also find an additional phase factor due to the evolution of the eigenvectors, with $c_n(0)$ representing the initial phase. We can rewrite the second term such that it is time-independent, and only depends on the path of $\mathbf{P}$ in parameter space [128]

$$
\begin{aligned}
\gamma_n(t) &= \int_0^t i \langle n, \mathbf{P}(t')| \frac{\mathrm{d}}{\mathrm{d}t'} |n, \mathbf{P}(t)\rangle \, \mathrm{d}t' \\
&= \sum_j \int_{P_j(0)}^{P_j(t)} i \langle n, \mathbf{P}(t)| \frac{\partial}{\partial P_j} |n, \mathbf{P}(t)\rangle \, \mathrm{d}P_j \\
&= \int_{\mathbf{P}(0)}^{\mathbf{P}(t)} \mathcal{A}^{\mathbf{n}}(\mathbf{P}) \mathrm{d}\mathbf{P}.
\end{aligned}
\tag{2.9}
$$

$$
\mathcal{A}^{\mathbf{n}}(\mathbf{P}) = i \langle n, \mathbf{P}(t)| \nabla_{\mathbf{P}} |n, \mathbf{P}(t)\rangle
\tag{2.10}
$$

is referred to as *Berry connection* or *Berry potential*. Note that $\langle n, \mathbf{P}(t)| \nabla_{\mathbf{P}} |n, \mathbf{P}(t)\rangle$ is purely imaginary, as

$$
2\Re(\langle n, \mathbf{P}(t)| \nabla_{\mathbf{P}} |n, \mathbf{P}(t)\rangle) = \langle n, \mathbf{P}(t)| (\nabla_{\mathbf{P}} |n, \mathbf{P}(t)\rangle) + (\nabla_{\mathbf{P}} \langle n, \mathbf{P}(t)|) |n, \mathbf{P}(t)\rangle
\tag{2.11}
$$

$$
= \nabla_{\mathbf{P}} \langle n, \mathbf{P}(t)|n, \mathbf{P}(t)\rangle = 0.
\tag{2.12}
$$

The cyclic evolution of the state vector $|\psi(t)\rangle$ along the parameter trajectory $\mathbf{C}$, assuming it initially was in an eigenstate $|n, \mathbf{P}(t)\rangle$, therefore results in two phase factors

$$
|\psi(t)\rangle = \mathrm{e}^{-\frac{i}{\hbar} \int_0^t E_n(t')\mathrm{d}t'} \mathrm{e}^{i\gamma_n(t)} |n, \mathbf{P}(t)\rangle,
\tag{2.13}
$$

where $\gamma_n(t)$ solely arises from the eigenvectors $|n, \mathbf{P}(t)\rangle$ of $\hat{H}(\mathbf{P}(t))$. For an open path we can always find a gauge transformation in order to remove $\gamma_n(t)$, since the eigenvectors are only defined up to an arbitrary phase. If however the path is closed, one cannot remove $\gamma_n(T)$ by a gauge transformation because the start and endpoint correspond to the same point, this phase is called *Berry phase* [127]. Note that the Berry phase is gauge invariant, while the Berry connection is not. Therefore the Berry phase may lead to a physically relevant observable, e.g. the Aharonov-Bohm phase [129, 130], while the Berry connection is gauge-dependent and can therefore not be observed [127, 131]. The Aharonov-Bohm phase is picked up by encircling a magnetic flux with charged particles, even though the magnetic field is not present in the trajectory of the charged particles, which can be shown e.g. in an interferometer [132].

From Equation 2.10, we can derive an anti-symmetric second-rank tensor, the *Berry Curvature*

$$
\mathbf{\Omega}^n(\mathbf{P}) = \nabla_{\mathbf{P}} \times \mathcal{A}^{\mathbf{n}}(\mathbf{P}).
\tag{2.14}
$$

In contrast to the Berry connection the Berry Curvature is gauge independent and can thus be observed experimentally. Using Stokes' theorem we can convert the Berry phase integral over the loop $\mathbf{C}$ to a surface integral over the surface S enclosed by $\mathbf{C}$

$$\gamma_n(\mathbf{C}) = \oint_{\mathbf{C}} \mathcal{A}^{\mathbf{n}} = \int_S \mathbf{\Omega}_n(\mathbf{P}). \tag{2.15}$$

Note that only phases mod 2π are observable. An alternative way of expressing $\Omega_n(\mathbf{P})$, which also is well defined, if $|n, \mathbf{P}\rangle$ is not smoothly single-valued, reads

$$\mathbf{\Omega}^n(\mathbf{P}) = i \sum_{n \neq m} \frac{\langle n, \mathbf{P}| \nabla_{\mathbf{P}} \hat{H}(\mathbf{P}) |m, \mathbf{P}\rangle \times \langle m, \mathbf{P}| \nabla_{\mathbf{P}} \hat{H}(\mathbf{P}) |n, \mathbf{P}\rangle}{(E_m(\mathbf{P}) - E_n(\mathbf{P}))^2}. \tag{2.16}$$

Equation 2.16 shows that the Berry curvature can exhibit singularities whenever the eigenenergies become degenerate. These points can host topological phase transitions, where the properties of the underlying system can change abruptly.

2.1.2 Geometric Phases in Periodic potentials

For most solid state materials a periodic potential is the starting point for a microscopic theory. A periodic potential $V(\mathbf{r}) = V(\mathbf{r} + \mathbf{R})$, where $\mathbf{R}$ is any point on the Bravais lattice, according to Bloch's theorem requires the solution to have the same periodicity [124, 133]. For the stationary Schrödinger equation describing a single particle at quasimomentum $\mathbf{k}$ in energy band n

$$\hat{H}(\mathbf{r})\psi_{\mathbf{k}}^n(\mathbf{r}) = \left(\frac{\hat{\mathbf{p}}^2}{2m} + V(\mathbf{r}) \right) \psi_{\mathbf{k}}^n(\mathbf{r}) = E_{\mathbf{k}}^n \psi_{\mathbf{k}}^n(\mathbf{r}) \tag{2.17}$$

the resulting eigenstates are the so called Bloch-waves which are made up of a plane wave $e^{i\mathbf{k}\cdot\mathbf{r}}$ and a cell periodic function $u_{\mathbf{k}}^n(\mathbf{r}) = u_{\mathbf{k}}^n(\mathbf{r}+\mathbf{R})$ with the same symmetry as the potential:

$$\psi_{\mathbf{k}}^n(\mathbf{r}) = e^{i\mathbf{k}\cdot\mathbf{r}} u_{\mathbf{k}}^n(\mathbf{r}). \tag{2.18}$$

Upon combining Equation 2.18 and Equation 2.17 we find an explicit dependence of the cell periodic functions, $u_{\mathbf{k}}^n(\mathbf{r})$ on the respective quasimomentum $\mathbf{k}$,

$$\left(\frac{(\hat{\mathbf{p}} + \hbar\mathbf{k})^2}{2m} + V(\mathbf{r}) \right) u_{\mathbf{k}}^n(\mathbf{r}) = E_{\mathbf{k}}^n u_{\mathbf{k}}^n(\mathbf{r}). \tag{2.19}$$

As the quasimomentum dependence is inherent to the problem of particles in a periodic potential, various Berry phase effects can occur when $\mathbf{k}$ is changed in crystals [131]. We can therefore rephrase the Berry connection (Equation 2.10) and Berry curvature (Equation 2.14 on the lattice as a function of quasimomentum, where the abstract parameter $\mathbf{P}$ is now the quasimomentum $\mathbf{k}$

$$\mathcal{A}^n(\mathbf{k}) = \langle u_{\mathbf{k}}^n| \, i\nabla \, |u_{\mathbf{k}}^n\rangle \tag{2.20}$$

$$\mathbf{\Omega}^n(\mathbf{k}) = \nabla_{\mathbf{k}} \times \mathcal{A}^n(\mathbf{k}) = \langle \nabla_{\mathbf{k}} u_{\mathbf{k}}^n| \times |\nabla_{\mathbf{k}} u_{\mathbf{k}}^n\rangle. \tag{2.21}$$

Note that the quasimomentum can always be transferred back to the first Brillouin zone by adding a linear combination of reciprocal lattice vectors. The Brillouin zone has the topology of a circle in one dimension, a torus in two dimensions and that of an n-dimensional torus in n-dimensions, i.e., the quasimomentum is periodic.

2.1.3 The bulk-boundary correspondence

The Berry curvature has real physical consequences; it is instructive to consider the current resulting from an external constant electric field **E** [55, 128]. This way we can connect the Berry curvature and the transverse conductivity, i.e., the Hall resistance. Assuming an the electric field is homogeneous and pointing in the x-direciton, we find the expectation value of the velocity in y-direction to be

$$\bar{v}_y = \frac{1}{\hbar}\frac{\partial E_n}{\partial k_y} - i\frac{eE_x}{\hbar}\left(\langle\partial_{k_x}u^n_{\mathbf{k}}|\partial_{k_y}u^n_{\mathbf{k}}\rangle - \langle\partial_{k_y}u^n_{\mathbf{k}}|\partial_{k_x}u^n_{\mathbf{k}}\rangle\right), \tag{2.22}$$

where e is the elementary charge and E_x the electric field strength. This result is obtained by considering the linear response to the electric field using the Kubo formula, for a more detailed derivation see e.g. [134]. The system performs Bloch oscillations under the influence of the weak electric field and gives rise to a Hall current perpendicular to the electric field. For a filled band the velocity due to the Bloch oscillations vanishes and only the second part remains, the Hall conductivity σ_H, which is the ratio of the current density and electric field E_x is then given by

$$\sigma_H = \frac{e^2}{h}i\int_{BZ}\frac{\mathrm{d}k_x\mathrm{d}k_y}{2\pi}\left(\langle\partial_{k_x}u^n_{\mathbf{k}}|\partial_{k_y}u^n_{\mathbf{k}}\rangle - \langle\partial_{k_y}u^n_{\mathbf{k}}|\partial_{k_x}u^n_{\mathbf{k}}\rangle\right) \tag{2.23}$$

$$= \frac{e^2}{h}\frac{i}{2\pi}\int_{BZ}\mathrm{d}\mathbf{k}\,\mathbf{\Omega}^n(\mathbf{k}), \tag{2.24}$$

where the electron density per reciprocal space is $\frac{\mathrm{d}k_x\mathrm{d}k_y}{(2\pi)^2}$. The right part of the equation resembles the Berry curvature integrated over the Brillouin zone, it is necessarily an integer and therefore highlights that the transverse Hall conductivity is quantized in terms of the so-called *Chern number*

$$\mathcal{C}^n = \frac{i}{2\pi}\int_{BZ}\mathrm{d}\mathbf{k}\,\Omega^n(\mathbf{k}) \in \mathbb{Z}, \tag{2.25}$$

where Ω^n corresponds to the component of $\mathbf{\Omega}^n$ perpendicular to the plane of $\mathbf{k}$. The Chern number is a property of the energy bands of the Hamiltonian and it is robust to continuous perturbations as long as no energy gaps are closing. This gives rise to remarkably stable transverse conductivity if the Fermi energy lies within a spectral gap of the Hamiltonian. The integer quantum Hall effect resembles a system with non-zero Chern number and was first experimentally discovered by von Klitzing in 1980 [49]. The transverse conductivity is restricted to integer multiples of e^2/h, the exact multiple is determined by the sum of the Chern numbers over all occupied bands below the Fermi energy. The connection between the precise quantization and the topological order of the bulk bands was first

derived by Thouless, Kohmoto, Nightingale and den Nijs and is commonly referred to as *TKNN*-invariant [55]. Shortly before, Halperin realized that on the edge of a sample, in which the integer quantum Hall effect can be observed, extended states localized at the edge of the sample can carry a current, whereas the bulk dispersion of the sample exhibits a gap and is therefore insulating [75]. The existence of these conducting edge modes was then unambiguously related to the bulk topological invariant by Hatsugai [76, 77]. This established the *bulk-boundary-correspondence*. For a topologically non-trivial bulk band there must exist an edge mode bridging the gap to the next band.

2.2　The Haldane Model

The Haldane model is one of the paradigmatic models featuring topologically trivial and non-trivial states [61]. In the presence of magnetic fields two-dimensional electron gases exhibit Landau levels and exhibit quantized transverse resistance values depending on the Fermi energy, which is known as the integer quantum Hall effect [49, 128, 135]. The quantized transverse conductivity emerges from the topological properties of the bands, i.e., the Berry curvature and its integrand over the Brillouin zone: the Chern number [128]. In contrast to the integer quantum Hall effect, where a magnetic field is crucial, the Haldane model does not require a net magnetic flux through the plaquette, which is the smallest closed loop on the lattice.

2.2.1　Geometry of the Haldane model

The Haldane model relies on a real nearest neighbor tunneling in combination with a complex next-nearest neighbor tunneling on a honeycomb lattice, i.e., whenever a particle tunnels along this bond its wave function picks up a complex phase ϕ. This complex phase results from the coupling of a charged particle to a vector potential $\mathbf{A}$, which gives rise to a magnetic field $\mathbf{B} = \nabla \times \mathbf{A}$. In a microscopic picture this coupling can be expressed via the Peierl's phase ϕ that we attached to the tunneling [136], it is equivalent to the Aharonov Bohm phase the particle picks up on a closed path encircling a magnetic flux [129, 130].

The flux pattern of the Haldane model is depicted in Figure 2.1, it respects the symmetry of the honeycomb lattice and threads the unit cell with positive and negative magnetic flux $\pm\Phi$, which corresponds to the surface integral of the normal component of the magnetic field passing through the respective surface. The honeycomb lattice is no Bravais lattice but a combination of two triangular lattices, i.e., there are two kinds of lattice sites: A- and B-sites. One choice of lattice vectors, where a is the distance between an A- and B-site, is

$$\mathbf{a}_1 = \frac{a}{2} \begin{pmatrix} 3 \\ \sqrt{3} \end{pmatrix} \qquad\qquad \mathbf{a}_2 = \frac{a}{2} \begin{pmatrix} 3 \\ -\sqrt{3} \end{pmatrix}. \qquad (2.26)$$
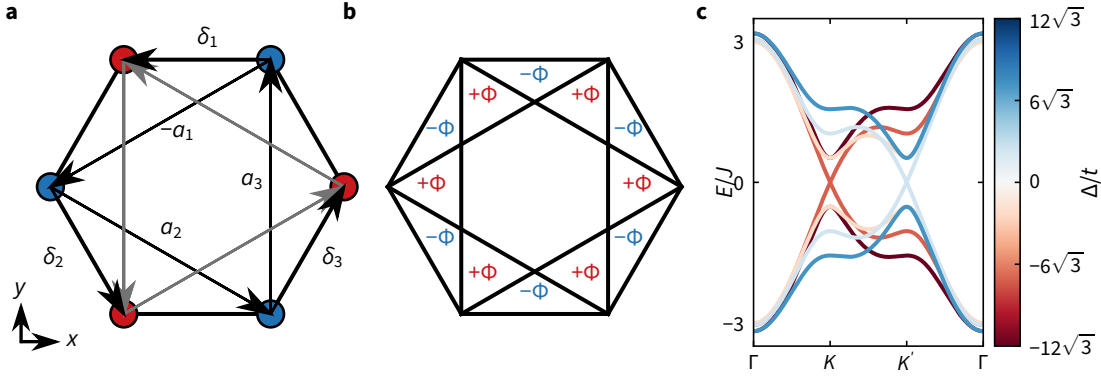
Figure 2.1 | Tunneling directions, flux pattern and resulting dispersion for the Haldane Model. a, Plaquette of the honeycomb lattice with *A*- (red) and *B*-sites (blue). The directions relevant for nearest and next-nearest neighbor tunneling are also depicted. The arrows connecting the same sublattice indicate the directions for which the tunneling process is related to a positive phase. **b**, Flux pattern in the unit cell. The unit cell is cut into 13 segments, out of which the central one is not pierced by a magnetic flux. The remaining segments are alternatingly pierced by positive and negative flux $\pm\Phi$. There is no net flux piercing the unit cell. **c**, Dispersion relation for changing sublattice offset Δ. The dispersion shows the two gap closings at *K* for negative Δ and *K'* for positive Δ. The color of the dispersion corresponds to Δ indicated with the colorbar. The complex tunneling here is $t/J = 0.1$ with a phase $\varphi = \pi/2$.

The lattice vectors span a rhomboid unit cell containing one *A*- and one *B*-site. The corresponding unit cell in reciprocal space is spanned by the two reciprocal lattice vectors

$$\mathbf{K}_1 = \frac{k_L}{2}\begin{pmatrix}\sqrt{3}\\3\end{pmatrix} \qquad \mathbf{K}_2 = \frac{k_L}{2}\begin{pmatrix}\sqrt{3}\\-3\end{pmatrix} \qquad k_L = \frac{4\pi}{3\sqrt{3}a}. \qquad (2.27)$$

The reciprocal lattice is also hexagonal, but rotated by 90° compared to the real-space lattice, cf. Figure 2.1a and Figure 2.2a. In the Haldane model the nearest neighbor tunneling along $\boldsymbol{\delta}_j$, $j \in \{1,2,3\}$ is real with amplitude J, the next-nearest neighbor tunneling J' can have a complex phase ϕ and can be written as

$$J' = t\mathrm{e}^{i\phi}, \qquad (2.28)$$

with $t = |J'|$. The tunneling directions are illustrated in Figure 2.1a and are, in addition to the lattice vectors (Equation 2.26), given by

$$\mathbf{a}_3 = \mathbf{a}_1 - \mathbf{a}_2 \qquad \boldsymbol{\delta}_1 = a\begin{pmatrix}-1\\0\end{pmatrix} \qquad \boldsymbol{\delta}_2 = \frac{a}{2}\begin{pmatrix}1\\-\sqrt{3}\end{pmatrix} \qquad \boldsymbol{\delta}_3 = \frac{a}{2}\begin{pmatrix}1\\\sqrt{3}\end{pmatrix} \qquad (2.29)$$

The next-nearest neighbor tunneling occurs with positive phase $+\phi$, with $\phi \in [0, 2\pi)$, when connecting *A*- to *A*-sites and negative phase $-\phi$ when connecting *B*-sites with the same vector $\mathbf{a}_j$, this is illustrated by the direction of the arrows in Figure 2.1 which always represent a positive phase. The flux pattern is chosen such that a particle tunneling in a loop along the edge of a plaquette acquires no phase, whereas a particle tunneling along the

directions $-\mathbf{a}_1 \rightarrow \mathbf{a}_2 \rightarrow \mathbf{a}_3$, again forming a loop, picks up a phase of $2\pi \times 3\Phi/\Phi_0$, the reverse direction would pick up a phase of $-2\pi \times 3\Phi/\Phi_0$, where $\Phi_0 = |h/e|$ is the flux quantum. In addition to the tunneling on the lattice a potential offset between A- and B-sites can be present, which is denoted by Δ. Depending on the magnitude of inversion symmetry breaking due to Δ and broken time-reversal symmetry due to the complex tunneling J' the system can either be in a topologically trivial state or in an integer quantum Hall state with non-trivial topology. Inversion symmetry is present if changing $\mathbf{r} \rightarrow -\mathbf{r}$ leaves the system unchanged, which is no longer the case for $\Delta \neq 0$.

2.2.2 Tight binding description

We start from a microscopic description of the Haldane model in real-space by summing the tunneling over all A-sites $\mathbf{r}_A$, and translate the position by $-\boldsymbol{\delta}_1$ to also cover B-sites, the Hamiltonian then reads

$$\hat{H} = \sum_{\mathbf{r}_A} \left[J \sum_{j=1}^{3} (\hat{a}_{\mathbf{r}_A}^\dagger \hat{a}_{\mathbf{r}_A+\delta_j} + h.c.) + \frac{\Delta}{2} (\hat{a}_{\mathbf{r}_A}^\dagger \hat{a}_{\mathbf{r}_A} - \hat{a}_{\mathbf{r}_A-\boldsymbol{\delta}_1}^\dagger \hat{a}_{\mathbf{r}_A-\boldsymbol{\delta}_1}) \right.$$
$$\left. \sum_{j=1}^{3} (J' \hat{a}_{\mathbf{r}_A}^\dagger \hat{a}_{\mathbf{r}_A+\mathbf{a}_j} + h.c.) + \sum_{j=1}^{3} (J' \hat{a}_{\mathbf{r}_A-\boldsymbol{\delta}_1}^\dagger \hat{a}_{\mathbf{r}_A-\boldsymbol{\delta}_1-\mathbf{a}_j} + h.c.) \right] \qquad (2.30)$$

The operator $\hat{a}_{\mathbf{r}}$ annihilates a particle at position $\mathbf{r}$, while $\hat{a}_{\mathbf{r}}^\dagger$ creates one. Note that the $\mathbf{a}_j \in \{-\mathbf{a}_1, \mathbf{a}_2, \mathbf{a}_3\}$ in order to have the proper orientation of the complex tunneling. We Fourier transform the Hamiltonian to momentum space $\mathbf{k}$ to determine the dispersion relation of the Haldane model. The creation and annihilation operators are given by

$$\hat{a}_{\mathbf{r}_A}^\dagger = \frac{1}{\sqrt{N}} \sum_{\mathbf{r}} e^{-i\mathbf{k}\cdot\mathbf{r}_A} \hat{a}_{\mathbf{k}}^\dagger \qquad\qquad \hat{a}_{\mathbf{r}_A+\boldsymbol{\delta}_j}^\dagger = \frac{1}{\sqrt{N}} \sum_{\mathbf{r}_A} e^{-i\mathbf{k}\cdot(\mathbf{r}_A+\boldsymbol{\delta}_j)} \hat{b}_{\mathbf{k}}^\dagger, \qquad (2.31)$$

where N counts the number of unit cells. We find

$$\hat{H} = \sum_{\mathbf{k}} \sum_{j=1}^{3} J(\hat{a}_{\mathbf{k}}^\dagger \hat{b}_{\mathbf{k}} e^{i\mathbf{k}\cdot\boldsymbol{\delta}_j} + h.c.)$$
$$+ \sum_{j=1}^{3} J'(\hat{a}_{\mathbf{k}}^\dagger \hat{a}_{\mathbf{k}} e^{i\mathbf{k}\cdot\mathbf{a}_j} + \hat{b}_{\mathbf{k}}^\dagger \hat{b}_{\mathbf{k}} e^{-i\mathbf{k}\cdot\mathbf{a}_j}) + h.c.$$
$$+ \frac{\Delta}{2} (\hat{a}_{\mathbf{k}}^\dagger \hat{a}_{\mathbf{k}} - \hat{b}_{\mathbf{k}}^\dagger \hat{b}_{\mathbf{k}}), \qquad (2.32)$$

which is equivalent to a two-level system at every quasimomemtum $\mathbf{k}$ and thus the Hamiltonian can be written in the convenient form

$$\hat{H}(\mathbf{k}) = \hat{\sigma}_0 h_0(\mathbf{k}) + \hat{\boldsymbol{\sigma}} \cdot \mathbf{h}(\mathbf{k}), \qquad (2.33)$$

where $\hat{\sigma}_0$ is the 2×2 identity matrix and $\hat{\boldsymbol{\sigma}}$ is a vector composed of the Pauli matrices:

$$\sigma_0 = \begin{pmatrix} 1 & 0 \\ 0 & 1 \end{pmatrix} \qquad \sigma_1 = \begin{pmatrix} 0 & 1 \\ 1 & 0 \end{pmatrix} \qquad \sigma_2 = \begin{pmatrix} 0 & -i \\ i & 0 \end{pmatrix} \qquad \sigma_3 = \begin{pmatrix} 1 & 0 \\ 0 & -1 \end{pmatrix}. \qquad (2.34)$$

With J' as defined in Equation 2.28, the $h_0(\mathbf{k})$ and the vector $\mathbf{h}(\mathbf{k})$ read

$$h_0(\mathbf{k}) = \sum_{j=1}^{3} 2t \cos(\phi) \cos(\mathbf{k} \cdot \mathbf{a}_j)$$

$$\mathbf{h}(\mathbf{k}) = \begin{pmatrix} \sum_{j=1}^{3} J \cos(\mathbf{k} \cdot \boldsymbol{\delta}_j) \\ -\sum_{j=1}^{3} J \sin(\mathbf{k} \cdot \boldsymbol{\delta}_j) \\ \frac{\Delta}{2} - \sum_{j=1}^{3} 2t \sin(\phi) \sin(\mathbf{k} \cdot \mathbf{a}_j) \end{pmatrix}. \qquad (2.35)$$

The eigenvalues as a function of quasimomentum, referred to as bands in the following, are determined by

$$E^{\pm}(\mathbf{k}) = h_0(\mathbf{k}) \pm |\mathbf{h}(\mathbf{k})|. \qquad (2.36)$$

The two bands touch at the Dirac cones if both inversion symmetry, and time-reversal symmetry are present [57, 137], otherwise a gap opens. The gap at quasimomenta $K := k_L(0, 1)^{\intercal}$ and $K' := k_L(0, -1)^{\intercal}$, with $k_L = 4\pi/(a3\sqrt{3})$, is

$$\Delta E(K) = \left| \Delta + 6\sqrt{3} \sin(\phi) \right| \qquad \Delta E(K') = \left| \Delta - 6\sqrt{3} \sin(\phi) \right|. \qquad (2.37)$$

Whenever $\Delta = \pm 6\sqrt{3} \sin(\phi)$ the gap closes and a topological phase transition occurs, where the Chern number of the bands change. If $\Delta = 0$, i.e., inversion symmetry is present, but $t \neq 0$ and $\phi \neq n \times \pi, n \in \mathbb{Z}$ the system is gapped and each band constitutes a Chern insulator with Chern number ± 1. If time-reversal symmetry is present, i.e., $J' \in \mathbb{R}$, the bands are topologically trivial and therefore their Chern number is 0. In the case of both, broken time-reversal symmetry and broken inversion symmetry the bands are trivial for $|\Delta| > \left| 6\sqrt{3} \sin(\phi) \right|$. Depending on the sign of Δ the gap closes either at K ($\Delta < 0$) or at K' ($\Delta > 0$). The resulting dispersion along the line $\Gamma \to K \to K' \to \Gamma$ is plotted in Figure 2.1 for various values of Δ showing the gap closing at K and K'. The points in the Brillouin zone Γ, K, K', M are illustrated in Figure 2.2a together with the Brillouin zone in the hexagonal lattice and a possible unit cell in reciprocal space.

As briefly mentioned before the quantity changing at the topological phase transition is the Chern number, or in a quasimomentum dependent fashion, the Berry curvature (cf. Section 2.1.2). To gain more insight into what happens at the phase transition, we will now approximate the Hamiltonian around the Dirac cones and calculate the Berry curvature. By expanding the Haldane Hamiltonian up to first order in $\mathbf{k}$ at the K (K') points we find

$$\hat{H}(K^{(\prime)} + \mathbf{k}) = -3t \cos(\phi) \hat{\sigma}_0 \mp \frac{3}{2} J a k_y \sigma_x + \frac{3}{2} J a k_x \sigma_y + \left(\frac{\Delta}{2} \pm 3\sqrt{3} \sin(\phi) \right) \hat{\sigma}_3, \qquad (2.38)$$
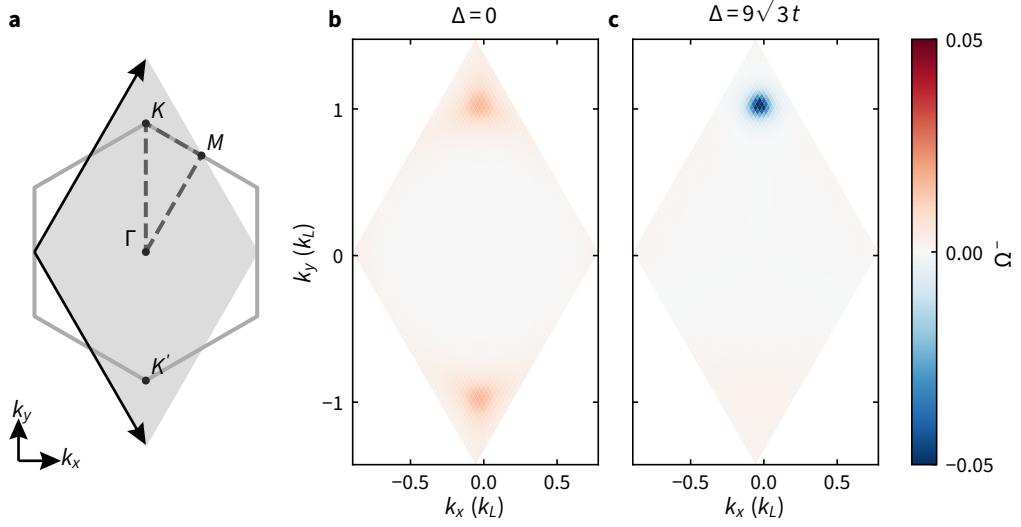
Figure 2.2 | **High symmetry path, Brillouin zone and Berry curvature in the Haldane model. a,** Brillouin zone of the hexagonal lattice (gray hexagon) with the high symmetry points Γ, M, K, K' (black points). One possible unit cell (gray shading) containing the same area as the Brillouin zone is spanned by the two reciprocal lattice vectors $\mathbf{K}_1$ and $\mathbf{K}_2$ (black arrows). Except for Figure 2.1c the dispersion is always plotted along the path indicated by the gray dashed line. **b,** Berry curvature in the Haldane model for $\Delta = 0$ in the topological regime. **c,** Berry curvature in the Haldane model for $\Delta = 9\sqrt{3}t$, i.e., in the trivial regime. In **b** and **c** $t/J = 0.1$ and $\varphi = \pi/2$.

where the $\mp$ corresponds to K and K' respectively. To see how the Berry Curvature is changing as Δ is modified, we can use Equation 2.16 to derive it from the expanded Hamiltonian for the lower band and find

$$\Omega_{K^{(\prime)}} = \mp \frac{9J^2 a^2 \left(\Delta/2 \pm 3\sqrt{3}t \sin(\phi)\right)}{8 \left|\mathbf{h}(K^{(\prime)} + \mathbf{k})\right|^3}. \tag{2.39}$$

We immediately see that for $|\Delta| > 6\sqrt{3}t \sin \phi$ the Berry curvature at K and K' have opposite sign, cf. Figure 2.2c. As the Berry Curvature is concentrated where the band gap between bands is small [138, 139], i.e., around the Dirac cones, the Chern number of the band is zero in this case and the bands are therefore topologically trivial. In the opposite case $|\Delta| < 6\sqrt{3}t \sin \phi$ the Berry curvature is of equal sign at both K and K' and the band is therefore topologically non-trivial as shown on the example in Figure 2.2b. The integrated Berry curvature over the Brillouin zone yields the Chern number of the band which is $\mathcal{C} = \pm 1$, depending on the sign of Δ. The findings for the shape and sign of the Berry curvature again highlight that a topological phase transition requires the bands to touch, and the sign changes of the Berry curvature occur exactly when the gap vanishes, here at K or K', cf. Equation 2.37.

An additional property of the Berry curvature of a two-band system is that the sum of Berry curvature of the two bands is zero at every quasimomentum, i.e., $\Omega^-(\mathbf{k}) = -\Omega^+(\mathbf{k})$, where the superscript $-(+)$ indicates the lower (upper) band.

2.2.3 Haldane model in a strip geometry

The previous approach is well suited for infinitely extended systems however there are also interesting states at the boundary of a finite system. The non-zero Chern number for the band indicates the presence of a chiral edge mode [55]. These edge modes are chiral conductive one-dimensional states located on the edge of a topologically non-trivial sample. The states are chiral in the sense that they only conduct charge in one direction. As the previously considered tight-binding model assumes an infinite lattice there are no edges and therefore no edge modes present. We can however slightly modify the system and consider a semi-infinite system, where one dimension is finite, while the other repeats infinitely. The quasimomentum along the finite direction is no longer a good quantum number, yet in the infinite direction quasimomentum still can give us intuition about the properties of the system and its eigenstates.

The honeycomb lattice features states located on the edge also in the topologically trivial case. These states are located on the edge of the sample but they are not chiral, i.e., they are not conductive and do not propagate. Figure 2.3 shows the dispersion of a semi-infinite strip terminated by a zigzag edge for different settings: a) in the trivial phase with only nearest neighbor tunneling, b) in the presence of a sublattice offset, c) at the phase transition where $\Delta = 6\sqrt{3}t$ and d) in the topological phase where $\Delta < 6\sqrt{3}t$. The bottom row of Figure 2.3 shows the real space wave function corresponding to the eigenstate highlighted by the gray circle in the upper row. The real space wave function for all settings are identical, highlighting that the topological nature is related to the entire band of the system and not only a single state. Depending on the topological regime the states located on the edge exhibit very different behavior. In the trivial phase, the edge states are flat, do not connect the two bands and therefore provide no chiral transport, note that these edge states do not occur on armchair terminated edges [140]. When reaching the phase transition the bands touch and subsequently the gap reopens with the edge mode connecting the two bands. When the edge modes connect the two bands there is robust chiral transport due to the edge modes.

To illustrate the chiral transport we can consider a toy model where we can separate the dynamics into a part parallel (y-direction) and a part perpendicular (x-direction) to the edge. This is in principle not justified in the honeycomb lattice, as the two directions do not separate, but we'll assume this for the sake of simplicity here. We model an idealized edge mode as a linear dispersion which bridges an energy gap ΔE across the entire Brillouin zone from $-\pi/L$ to π/L, where L is the length of the unit cell parallel to the edge i.e.,

$$E(k_y) = \frac{\Delta E L}{2\pi} k_y. \tag{2.40}$$

We assume a wave packet occupying all states of the edge mode in the Brillouin zone equally. The wave function parallel to the edge is therefore a superposition of plane waves with
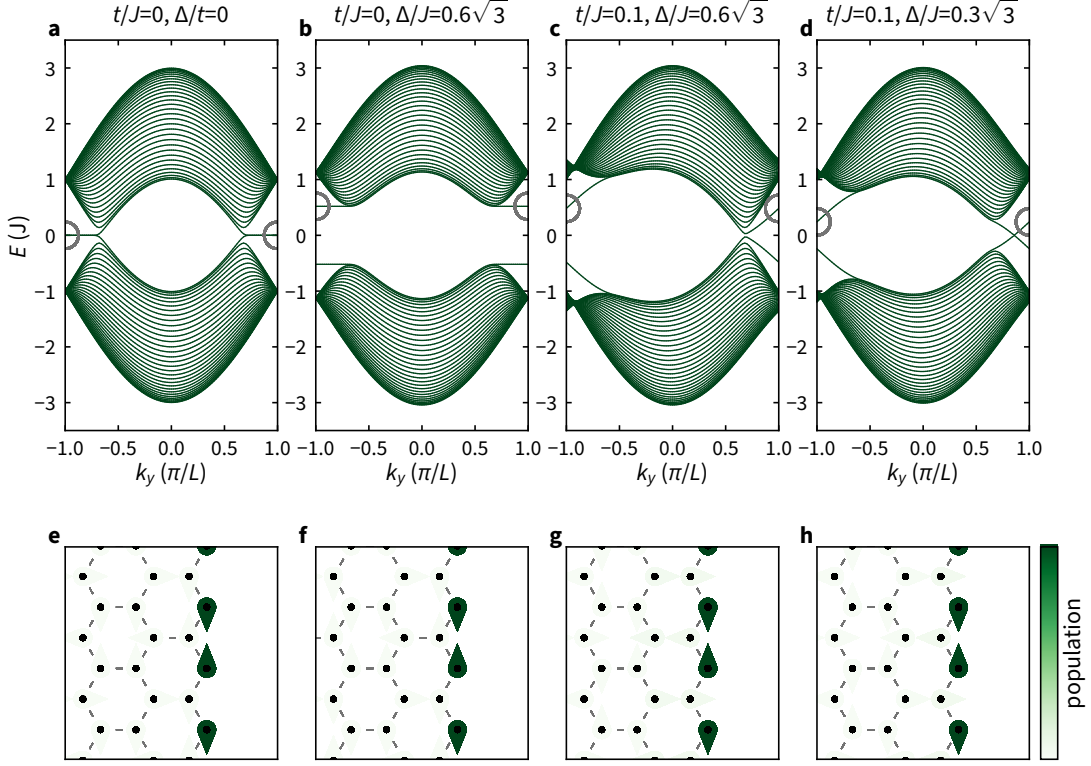
Figure 2.3 | **Dispersion of the Haldane model on a semi-infinite strip geometry for different combinations of sublattice offset Δ and complex tunneling J'.** The phase of the complex tunneling for all panels is $\varphi = \pi/2$. The gray circle in the top row indicates the energy and quasimomentum corresponding to the wave function shown in the bottom row. **a,** Dispersion of the trivial honeycomb lattice in the absence of next-nearest neighbor tunneling and sublattice offset. The trivial edge state is connecting the *K* to *K′* across the edge of the Brillouin zone while the group velocity of the edge mode is zero. **b,** Same as **a** but with $\Delta/J = 0.6\sqrt{3}$. The edge states on the two edges are now separated by Δ, but still have no group velocity. The bands are localized on each of the two edges, the upper state, highlighted by the gray circle (shown in **f**) lives on the *A* sites only and therefore on the right edge, while the lower edge state is located on the other edge of the system and on *B*-sites only. **c,** Same as **b** but with $t/J = 0.1$, i.e., the system is at the topological phase transition, as can be seen by the bands touching. The edge modes have now acquired a net slope, i.e., non-zero group velocity and are touching at the *K′* point. **d,** Same as **c** but with reduced $\Delta/J = 0.3\sqrt{3}$, i.e., further in the topological regime. The gap between the bands has increased and the edge modes now cross in between *K* and *K′* across the edge of the Brillouin zone. **e,** Real space wave function for the edge state at $k_y = \pm\pi/L$ located on the right edge. The edge mode is only located on *A*-sites and exhibits an phase gradient of π between adjacent sites with significant population. **f,** Wave function in the presence of an sublattice offset. **g,** Wave function at the topological phase transition. **h,** Wave function in the topological regime. The arrow indicates the phase of the wave function, while the shading represents the population, i.e., modulus squared of the wave function.

quasimomentum k_y and energy $E(k_y)$. As we occupy all states equally we can evaluate the resulting time-dependent wave function $\psi(t)$ by integrating all possible k_y states,

$$\psi(x,y,t) = \phi(x) \int_{-\pi/L}^{\pi/L} \mathrm{d}k_y \mathrm{e}^{-i\left(\frac{E(k_y)}{\hbar}t - k_y y\right)} \qquad (2.41)$$

$$= \phi(x) \frac{2 \sin\left(\frac{\pi}{L}\left(\frac{\Delta E L}{h} t - y\right)\right)}{\Delta E L t / h - y}, \tag{2.42}$$

where $\phi(x)$ includes the normalization and shape of the wave function perpendicular to the wall. The resulting wave function is propagating parallel to the wall with a group velocity $v_g = \hbar^{-1} \partial E(k_y) / \partial k_y = \Delta E L / h$. The wave packet does not disperse as a result of the linear slope of the edge mode. If the particles would be in bulk states, which would have a k_y-symmetric distribution and more importantly, the energies of the bands are also ky-symmetric, there would be no net motion, but the wave packet would disperse and not facilitate chiral transport. The edge modes are furthermore protected, i.e., immune to scattering, as the only state that is energetically close and additionally would allow backscattering is located on the opposite edge of the strip and therefore the overlap with this state is exponentially suppressed as the width of the strip increases.

In the following we will have a look at different terminations of the lattice, while still cutting the system such that the size of the strip's unit cell is minimized. Figure 2.4 shows the resulting dispersion for three semi-infinite systems with different edge termination. The most commonly studied terminations result in three different configurations of the lattice, the *zigzag*, *armchair* and *barbed* edge. These terminations can be obtained directly by cutting a two dimensional honeycomb lattice either parallel or perpendicular to a nearest-neighbor link. Together with the twig edge, an armchair edge where one sublattice is removed [141], these terminations can describe any edge possible in the honeycomb lattice. The resulting edge for an arbitrary cut will not be discussed and we focus on the most commonly studied edge types. As the twig edge cannot be realized with a straight cut and is therefore experimentally significantly harder to achieve with the presented platform, we continue with the zigzag, armchair and barbed edge. The three terminations are depicted in the bottom row of Figure 2.4. As a semi-infinite strip naturally has two edges, in order to only focus on one edge, we project the resulting eigenstates onto a region that only includes one edge and part of the bulk but excludes the opposite edge. Each eigenstate is depicted with the respective overlap with the introduced region (cf. Section 2.5.6). The projection directly reveals that we find one edge mode on the right edge.

The different terminations result in different unit cells for the semi-infinite strip. The unit cell of the zigzag and barbed edge is identical except for the termination with an A- or B site on the edge which exhibit different connectivity. The length of the unit cell in infinite direction is $L = \sqrt{3}a$. The armchair termination has a length of $L = 3a$. Due to the larger unit cell the maximum quasimomenta along the infinite direction k_y are smaller. For the zigzag and barbed edge the Dirac cones are resolved at their respective projection at $k_y = \pm \pi / (\sqrt{3}a)$. Depending on the orientation of the edge, the edge mode is centered at $k_y = 0$ for the armchair and barbed edge, or at the edge of the Brillouin zone for the zigzag terminated edge. The edge mode velocity also varies with the orientation of the edge, as can be seen by the slope of the edge modes in Figure 2.4.
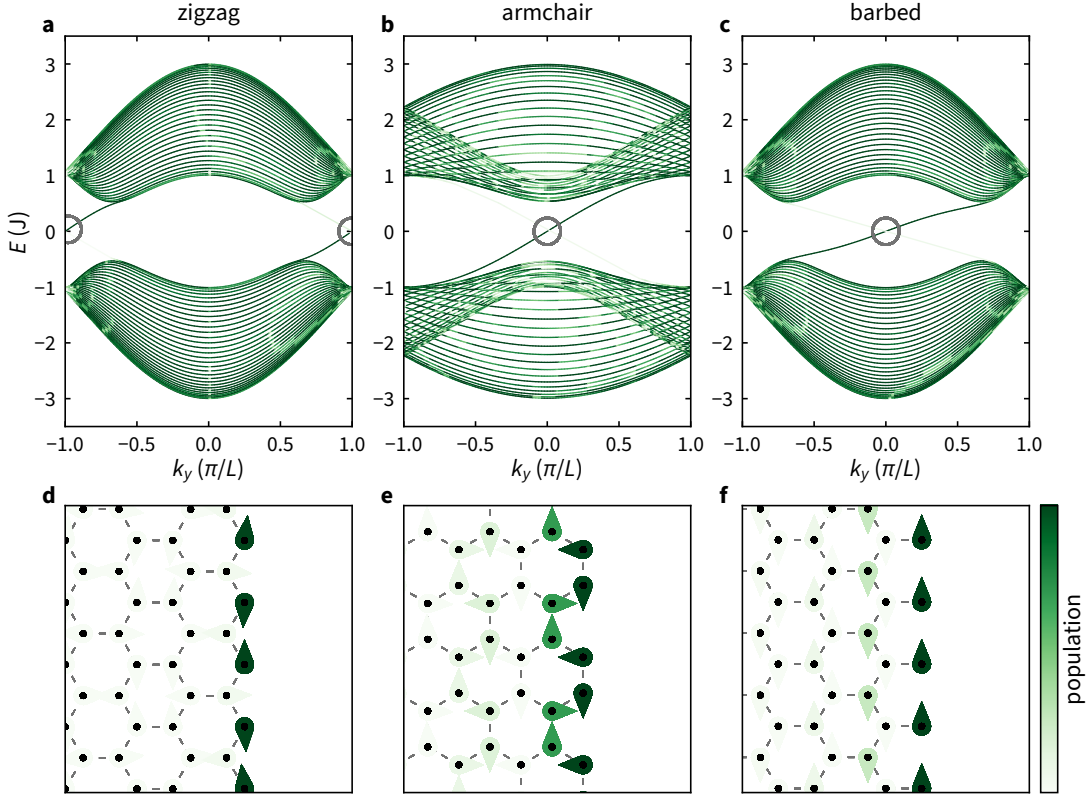
Figure 2.4 | Dispersion of the Haldane model on a semi-infinite strip geometry for different termina-tions and the respective wave functions of the edge mode in real space. The complex tunneling for all panels is $t/J = 0.1$ with phase $\varphi = \pi/2$. The shading of the dispersion is derived from the weight of each eigenstate on a region excluding the left edge, cf.Section 2.5.6. **a**, Dispersion of the zigzag terminated system. **b**, Dispersion of the armchair terminated system. **c**, Dispersion of the barbed terminated system. **d**, Real space wave function for the edge mode at $k_y = \pm\pi/L$ located on the zigzag edge. The edge mode is only located on A-sites and exhibits a phase gradient of π between adjacent sites with significant population. **e**, Wave function for the edge mode at $k_y = 0$ located on the armchair edge. In contrast to the zigzag edge the edge mode occupies both A- and B-sites. Even though the phase between adjacent unit cells is vanishing, there is a phase gradient within the unit cell. **f**, Wave function on the barbed edge at $k_y = 0$. The wave function is located exclusively on A-sites, the edge mode is not only located on the sites on the edge and additionally exhibits a phase gradient within the unit cell. The population, inidicated by the shading of the arrows, is normalized to the maximum population on a single site for the depicted state with the arrows' orientations indicating its complex phase.

2.3 Floquet engineering

As briefly mentioned in Section 2.2 electrically charged particles couple to a magnetic field via the vector potential related to it. Along with the coupling to the magnetic field comes broken time-reversal symmetry, enabling the quantum Hall effect. As atoms are charge neutral particles their momentum does not couple to a vector potential resulting from a magnetic field and therefore different methods to break time-reversal symmetry are required. The phase resulting from photon assisted tunneling can be used to engineer fluxes on a

lattice [142–144], alternatively the internal states of atoms can be utilized to mimic the effect of a magnetic field [145–147]. Utilizing the engineered flux enables the realization of magnetic field strengths going way beyond their solid state counterpart, and allow for the realization of the Harper-Hofstadter model in optical superlattices [89, 148]. A different path to break time-reversal symmetry is introducing a modulation in the time-domain. This can either be done by choosing an aperiodic modulation or modulating in a chiral way [88, 149]. By engineering the modulation protocol a variety of phenomena can be realized, in solid state samples a circularly polarized light field can induce a Hall response [83, 150–152] and alter other electronic or magnetic properties [153, 154]. In photonic waveguides topological band structures can be implemented by spatially modulating their shape [85, 155] and circular shaking in an optical honeycomb lattice enables the realization of the Haldane model [84, 109, 110]. Dynamical localization, i.e., the reduction of the tunneling amplitude, due to the periodic modulation of the lattice [156–158] and the Mott insulator to superfluid transition [159] induced by the modulated tunneling due to the Floquet drive can be realized. There is a plethora of other phenomena enabled by periodic modulation, which are not mentioned above. In the following we will introduce the essential principles of Floquet engineering to gain a basic understanding of the consequences of the time periodic modulation.

2.3.1 Time periodic Hamiltonian

For a periodic potential where continuous translation symmetry is broken but a discrete translation symmetry is preserved, and therefore momentum is no longer a conserved quantity we consider the periodic quasimomentum in the Brillouin zone and Bloch waves as the solution to the Hamiltonian. If we break time translation symmetry by introducing a periodic modulation of the system we therefore expect that energy is no longer a conserved quantity and we have in analogy to the spatial counter part a periodic quasienergy. Following the framework of Floquet theory we will show that quasienergy is periodic and how the evolution of the system is modified [160, 161].

We are looking for a solution to the time-dependent Schrödinger equation

$$i\frac{\partial}{\partial t}\left|\psi(t)\right\rangle = \hat{H}(t)\left|\psi(t)\right\rangle, \tag{2.43}$$

where the Hamiltonian is periodic in time $\hat{H}(t) = \hat{H}(t+T)$ and T is the period of the temporal modulation. Similar to Bloch waves, the solution again has to obey the periodicity of the Hamiltonian, i.e.,

$$\left|\psi_n(t)\right\rangle = \mathrm{e}^{-i\varepsilon_n t/\hbar}\left|\phi_n(t)\right\rangle, \tag{2.44}$$

where $\left|\phi_n(t)\right\rangle = \left|\phi_n(t+T)\right\rangle$ is a *Floquet mode* of the system. ε_n is the quasienergy of the Floquet mode which is only defined up to multiples of the modulation frequency $\hbar\omega$
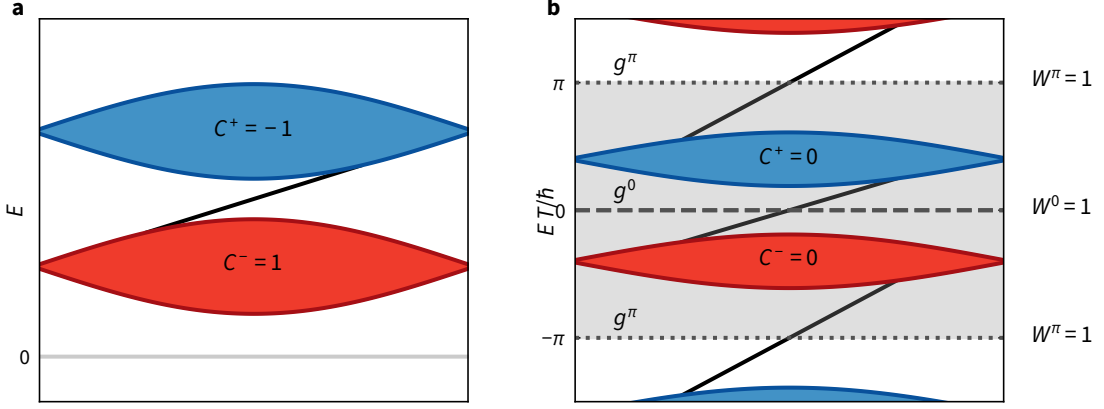
Figure 2.5 | **Energy spectrum of a static and time periodic system. a** Energy spectrum of a static system with non-zero Chern numbers. The edge mode is located in the gap between the bands. The energy is bounded below at $E = 0$ indicated by the gray line. **b** Floquet Brillouin zone of a periodically modulated system. The Floquet Brillouin zone (gray shading) hosts exemplary bands with Chern numbers $C^\pm = 0$. The Floquet copies of the bands are shown in the extended scheme. Due to the periodic energy structure we find two gaps in the system: g^0 (dashed line) in the center and g^π (dotted line) at the edge of the Floquet Brillouin zone. Each gap is characterized by a winding number W^0 or W^π counting the number of chiral edge modes.

with $\omega = 2\pi/T$. Inserting the solution into the time-dependent Schrödinger equation, we find for the Floquet modes

$$\left(\hat{H}(t) - i\hbar \frac{\partial}{\partial t} \right) |\phi_n(t)\rangle = \varepsilon_n |\phi_n(t)\rangle . \tag{2.45}$$

We immediately see that

$$|\phi_{n,m}(t)\rangle = \mathrm{e}^{-im\omega t} |\phi_n(t)\rangle , m \in \mathbb{Z} \tag{2.46}$$

is an equivalent solution which is only shifted by $m \times \hbar\omega$ compared to the previous quasienergy ε_n. All states with different m relate to the same physical state.

The indices n, m therefore correspond to a class of solutions, where the energy can be mapped to an equivalent *Floquet Brillouin zone*

$$\varepsilon \in \left] -\frac{\hbar\omega}{2}, \frac{\hbar\omega}{2} \right], \tag{2.47}$$

similar to the Brillouin zone for the quasimomentum. Figure 2.5 shows a comparison between a static and periodically modulated energy spectrum. In the periodically modulated case (Figure 2.5b) energy is periodic and bands can wrap around the Floquet Brillouin zone. Copies of the Floquet Brillouin zone are shown above and below to highlight the periodicity of the quasienergy. For the depicted two band model we find two energy gaps: g^0 in the center and g^π at the edge of the of the Floquet Brillouin zone. For the topological classification each gap can be described by a winding number W^0 and W^π counting the number of chiral edge modes as described in Section 2.5.2.

2.3.2 Effective Hamiltonian

The evolution of the system under a periodic Hamiltonian can be considered to be made up of consecutive pieces of duration T, where the system is always under the influence of the same repeating Hamiltonian. The coherent time evolution of a state $|\Psi(t)\rangle$ under the influence of an arbitrary Hamiltonian $\hat{H}(t)$ from an initial time t_i to a final time t_f is given by

$$|\psi(t_f)\rangle = \hat{U}(t_f, t_i) |\psi(t_i)\rangle = \mathcal{T} e^{-\frac{i}{\hbar} \int_{t_i}^{t_f} \mathrm{d}t \hat{H}(t)} |\psi(t_i)\rangle, \tag{2.48}$$

where $\mathcal{T}$ is the time-ordering operator. Therefore the time evolution during one period of the time-periodic Hamiltonian is governed by the operator

$$\hat{U}(t_0 + T, t_0) = \mathcal{T} e^{-\frac{i}{\hbar} \int_{t_0}^{t_0+T} \mathrm{d}t \hat{H}(t)}. \tag{2.49}$$

The time evolution operator over several periods results from the repetitive application, i.e.,

$$\hat{U}(t_0 + nT, t_0) = \prod_{k=1}^{n} \mathcal{T} e^{-\frac{i}{\hbar} \int_{t_0}^{t_0+T} \mathrm{d}t \hat{H}(t)} = \left(\hat{U}(t_0 + T, t_0) \right)^n, \tag{2.50}$$

furthermore it holds that

$$\hat{U}(t_0 + T, T) = \hat{U}(t_0, 0). \tag{2.51}$$

This means that we can also write

$$\hat{U}(t_0 + nT, T) = \hat{U}(t_0, 0) \left(\hat{U}(T, 0) \right)^n, \tag{2.52}$$

but we note that the commutation of $\hat{U}(t_0, 0)$ and $\hat{U}(t, 0)$ is only ensured at $t_0 = nT$. One important consequence of the illustrated properties is that knowledge of the evolution operator for one period is sufficient to fully predict the long term dynamics of the system except for an initial kick that is described by the evolution from time $t = 0$ to t_0. The evolution under the influence of the time-dependent Hamiltonian during one period described by $\hat{U}(t_0 + T, t_0)$ is ergo equivalent to the evolution of a *Floquet-Hamiltonian* $\hat{H}_\mathrm{F}$ which does not explicitly depend on time

$$\hat{U}(t_0 + T, t_0) = e^{-\frac{i}{\hbar} \hat{H}_\mathrm{F}(t_0) T}, \tag{2.53}$$

however the starting time t_0 is relevant for the time dynamics of the system. By appropriate choice of modulation protocol the evolution of the system can be designed to mimic a Floquet-Hamiltonian with properties that would not be attainable otherwise. The Floquet-Hamiltonian picture only holds for stroboscopic observation at integer multiples of the modulation period nT, $n \in \mathbb{Z}$.

To obtain the Floquet-Hamiltonian $\hat{H}_{\mathrm{F}}$ we evaluate the evolution operator Equation 2.49, which integrates the instantaneous Hamiltonian $\hat{H}(t)$ over one period [87]

$$\hat{H}_{\mathrm{F}}(t_0) = \frac{i\hbar}{T} \ln(\hat{U}(t_0 + T, t_0)). \tag{2.54}$$

This definition of the Floquet-Hamiltonian allows for straightforward numerical implementation to obtain the spectrum of the modulated system.

To describe the time evolution independent of t_0 we can introduce the unitary time-periodic micromotion operator $\hat{U}_{\mathrm{F}}(t) = \hat{U}_{\mathrm{F}}(t+T)$, which takes $\hat{H}(t)$ into a rotating reference frame, where we obtain the time independent *effective Hamiltonian* [88, 93]

$$\hat{H}_{\mathrm{eff}} = \hat{U}_{\mathrm{F}}^{\dagger}(t)\hat{H}(t)\hat{U}_{\mathrm{F}}(t) - i\hbar\hat{U}_{\mathrm{F}}^{\dagger}(t)\frac{\partial}{\partial t}\hat{U}_{\mathrm{F}}(t). \tag{2.55}$$

The Floquet-Hamiltonian and the effective Hamiltonian exhibit the same spectrum and are connected via [88, 93]

$$H_{\mathrm{F}}(t_0) = \hat{U}_{\mathrm{F}}(t_0)\hat{H}_{\mathrm{eff}}\hat{U}_{\mathrm{F}}^{\dagger}(t_0). \tag{2.56}$$

To obtain the time evolution between arbitrary times from t_i to t_f, assuming $t_f \geq t_i + nT, n \in \mathbb{N}_{\neq 0}$ and $0 < t_i < T$, we evaluate the time evolution in three parts: 1) from t_i to T, 2) from T to nT and 3) from nT to t_f. The time evolution is thus governed by [88, 92, 93, 162]

$$\hat{U}(t_f, t_i) = \hat{U}_F(t_f)e^{-\frac{i}{\hbar}\hat{H}_{\mathrm{eff}}(n-1)T}\hat{U}_{\mathrm{F}}^{\dagger}(t_i) \tag{2.57}$$

$$= e^{-\frac{i}{\hbar}\hat{K}(t_f)}e^{-\frac{i}{\hbar}\hat{H}_{\mathrm{eff}}(n-1)T}e^{\frac{i}{\hbar}\hat{K}(t_i)} \tag{2.58}$$

The Hermitian kick operators $\hat{K}(t)$ are also time periodic, i.e., $\hat{K}(t) = \hat{K}(t + T)$ and take care of all effects related to the initial starting time, such that a t_i-independent $\hat{H}_{\mathrm{eff}}$ can describe the evolution for all t_i [92]. The subperiod motion is usually termed *micromotion* as it captures the oscillations of the system due to the varying Hamiltonian. Depending on the specific driving protocol the micromotion can significantly influence the long time dynamics [92].

To avoid the dependence of the dynamics on the initial driving phase one possibility is to adiabatically connect the undriven and driven states of the system. This can be realized by slowly increasing the modulation amplitude to slowly deform the eigenstates of the initial static Hamiltonian into the eigenstates of the effective Hamiltonian. The time scale required for the initial ramp-up is strongly dependent on the exact modulation scheme. However slowly ramping up the modulation opens the possibility to also prepare the ground state of the effective Hamiltonian.

2.3.3 High frequency approximation

As discussed in the previous section the effective Hamiltonian is time-independent. For sufficiently large modulation frequencies compared to the characteristic energy scale of the system, e.g. the bandwidth of the first two energy bands, the effective Hamiltonian

can be evaluated in a perturbative expansion in units of $1/(\hbar\omega)$ [88, 92, 162]. To make this approximation we separate the Hamiltonian into a time-independent part $\hat{H}_0$ and a time-dependent part $\hat{V}(t)$

$$\hat{H}(t) = \hat{H}_0 + \hat{V}(t) \tag{2.59}$$

$$\hat{V}(t) = \sum_{j=1}^{\infty} \hat{V}^{(j)} e^{ij\omega t} + \hat{V}^{(-j)} e^{-ij\omega t}. \tag{2.60}$$

Note that the time average of $\hat{V}(t)$ is necessarily zero using this definition, all time-independent components have been expressed via $\hat{H}_0$. The expansion reads

$$\hat{H}_{\text{eff}} = \hat{H}_0 + \frac{1}{\hbar\omega} \sum_{j=1}^{\infty} \frac{1}{j} [\hat{V}^{(j)}, \hat{V}^{(-j)}] \tag{2.61}$$

$$+ \frac{1}{2(\hbar\omega)^2} \sum_{j=1}^{\infty} \frac{1}{j^2} \left([[\hat{V}^{(j)}, \hat{H}_0], \hat{V}^{(-j)}] + [[\hat{V}^{(-j)}, \hat{H}_0], \hat{V}^{(j)}] \right)$$

$$+ \mathcal{O}\left(\frac{1}{(\hbar\omega)^3} \right)$$

One can also find a perturbative expansion for the kick operator, but as we will always consider an adiabatic transition to the effective Hamiltonian it will not be reproduced here [92]. This approach will be used in the following to show the exact mapping of the tunnel modulated honeycomb lattice to the Haldane model as shown for the case of a cosine and stepwise modulation in Section 2.4.

2.4 The tunneling modulated honeycomb lattice

To implement topologically non-trivial bands for charge neutral particles such as ultra cold neutral atoms the system needs to be engineered in order to mimic e.g. the effect of a magnetic field on a charged particle resulting in a complex tunneling. In the honeycomb lattice one option is to shake the optical lattice in space, or alternatively to modulate the tunneling in a chiral way. A very simple model was proposed by Kitagawa et al. where the modulation consists of a three steps protocol which already offers a rich phase diagram [86]. As a stepwise modulation, with its infinitely fast transitions between the individual steps, is experimentally very challenging, the experimental implementation is closer to a continuous modulation where the tunneling is changing in a sinusoidal fashion. To show that the three-step and sinusoidal modulation yield similar phases we will in the following compare the resulting dispersions and topological phase diagrams.1.1

2.4.1 Modulation of the tunneling

In the following the setting will be as simple as possible in order to illustrate the essential effects of the modulation. The starting point shall be a tight binding Hamiltonian
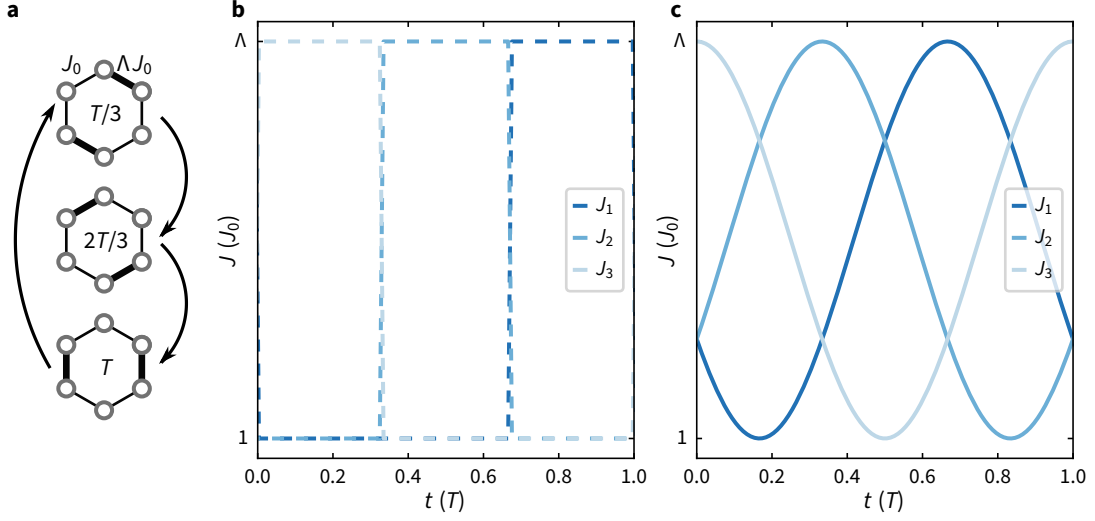
Figure 2.6 | Illustration of the stepwise and sinusoidal modulation. a, Illustration of the modulation protocol. The tunneling is periodically enhanced along the bonds of the lattice. The bare tunneling is J_0 and enhanced for each direction to a maximum ΛJ_0. **b**, Tunneling amplitudes during one period in the stepwise protocol. The tunneling J_j for each direction is sequentially enhanced, while the other two directions are unchanged. **c**, Tunneling amplitudes during one period in the cosine protocol. The tunnelings are enhanced with a phase difference corresponding to $2\pi/3$, it resembles the lowest Fourier component of the stepwise protocol.

with periodically modulated tunneling as illustrated in Figure 2.6a. We rewrite Equation 2.32 as a matrix where the first entry corresponds to an A-site and the second to the B-site of the unit cell.

$$\hat{H}(t) = \sum_{j=1}^{3} \begin{pmatrix} 0 & J_j(t)\mathrm{e}^{i\mathbf{k}\cdot\boldsymbol{\delta}_j} \\ J_j^*(t)\mathrm{e}^{-i\mathbf{k}\cdot\boldsymbol{\delta}_j} & 0 \end{pmatrix} \tag{2.62}$$

The tunneling is modulated in a periodic fashion, i.e., $J_j(t) = J_j(t + T)$, where T is the modulation period and $j \in \{1, 2, 3\}$ denotes the tunneling along direction $\boldsymbol{\delta}_j$, we can thus apply Equation 2.54 to obtain $\hat{H}_{\mathrm{eff}}$. In the following we want to show that the step-wise tunneling modulation

$$J_j^{\mathrm{step}}(t) = \begin{cases} J_3 = \Lambda J_0, J_1 = J_2 = J_0 & \text{for} \quad nT < t \leq nT + T/3 \\ J_2 = \Lambda J_0, J_1 = J_3 = J_0 & \text{for} \quad nT + T/3 < t \leq nT + 2T/3 \\ J_1 = \Lambda J_0, J_2 = J_3 = J_0 & \text{for} \quad nT + 2T/3 < t \leq (n+1)T \end{cases} \tag{2.63}$$

and a (co)sinusoidal modulation

$$J_j^{\mathrm{sin}}(t) = \frac{J_0}{2}\left(1 + \Lambda + (\Lambda - 1)\cos\left(\omega t + j\frac{2\pi}{3}\right)\right) \tag{2.64}$$

of the tunneling result in a similar phase diagram. The bare tunneling along the bonds is J_0, during the drive it is enhanced by a factor Λ, the modulation amplitude and we denote the modulation frequency as $\omega = 2\pi/T$. The tunneling as a function of time for the two modulation protocols is illustrated in Figure 2.6b and c. The drive protocol has a sense of *rotation*, we will refer to it as chirality κ. The chirality takes into account if the modulation occurs in a clockwise or anti-clockwise fashion, i.e., if the tunneling is enhanced along the bonds $(1, 2, 3)$ or $(1, 3, 2)$. The resulting band structure for the two modulation schemes is very similar. We will in the following compare the energy spectrum and topological phase diagram of the system.

2.4.2 Comparison in the high frequency limit

The high frequency limit will not give great insight into the entire phases this model can host, but will serve as a good starting point to explore the similarity and difference of the two modulation protocols. Expanding the Hamiltonian in units of $(\hbar\omega)^{-1}$ and following [92] the Floquet-Hamiltonian for a three steps protocol is given by

$$\hat{H}_{\mathrm{F}} = \hat{H}_0 + \frac{i\pi}{27\hbar\omega} \left(\left[\hat{V}_1, \hat{V}_2 \right] + \left[\hat{V}_2, \hat{V}_3 \right] + \left[\hat{V}_3, \hat{V}_1 \right] \right) + \mathcal{O}(\hbar\omega)^{-2}. \tag{2.65}$$

The resulting Floquet-Hamiltonian, also in the high frequency expansion, still depends on the initial driving phase of the modulation. The $\hat{V}_j$'s correspond to the operators describing the time-dependent part of the Hamiltonian during the j-th segment of the period. For the considered case here, we have

$$\hat{H}_0^{\mathrm{step}} = \sum_{j=1}^{3} \frac{J_0(\Lambda + 2)}{3} (\hat{\sigma}_1 \cos(\mathbf{k} \cdot \boldsymbol{\delta}_j) + \hat{\sigma}_2 \sin(\mathbf{k} \cdot \boldsymbol{\delta}_j)) \tag{2.66}$$

$$\hat{V}_j = \frac{2J_0(\Lambda - 1)}{3} (\hat{\sigma}_1 \cos(\mathbf{k} \cdot \boldsymbol{\delta}_j) + \hat{\sigma}_2 \sin(\mathbf{k} \cdot \boldsymbol{\delta}_j))$$

$$+ \sum_{i \neq j}^{3} \frac{J_0(1 - \Lambda)}{3} (\hat{\sigma}_1 \cos(\mathbf{k} \cdot \boldsymbol{\delta}_i) + \hat{\sigma}_2 \sin(\mathbf{k} \cdot \boldsymbol{\delta}_i)). \tag{2.67}$$

The specific amplitudes result from the requirement of the sequence of $\hat{V}_j$'s to have a zero time average over one period. The Floquet-Hamiltonian then resembles a Haldane model with complex next-nearest neighbor tunneling phase $\phi = -\pi/2$ and $\Delta = 0$ (cf. Equation 2.35) , i.e.,

$$\hat{H}_{\mathrm{F}}^{\mathrm{step}} = \hat{H}_0^{\mathrm{step}} + \frac{2\pi(\Lambda - 1)^2 J_0^2}{27\hbar\omega} \hat{\sigma}_3 \sum_{j=1}^{3} \sin(\mathbf{k} \cdot \mathbf{a}_j). \tag{2.68}$$

In a similar fashion we can evaluate the effective Hamiltonian in the sinusoidal modulation protocol, utilizing Equation 2.61, we only need to include the lowest order $(\hbar\omega)^{-1}$. With $\hat{V}(t)$, which is responsible for the modulation of the tunnel coupling here,

$$\hat{V}(t) = \sum_{j=1}^{3} \frac{J(\Lambda - 1)}{2} \left(\hat{\sigma}_1 \cos(\mathbf{k} \cdot \boldsymbol{\delta}_j) + \hat{\sigma}_2 \sin(\mathbf{k} \cdot \boldsymbol{\delta}_j)\right) \cos(\omega t + 2\pi j/3), \qquad (2.69)$$

we immediately find that only the fundamental frequencies $\pm\omega$ contribute, greatly simplifying the calculation. The effective Hamiltonian in this case results in

$$\hat{H}_{\text{eff}}^{\sin} = \hat{H}_0^{\sin} + \frac{J_0^2(\Lambda - 1)^2\sqrt{3}}{8\hbar\omega} \hat{\sigma}_3 \sum_{j=1}^{3} \sin(\mathbf{k} \cdot \mathbf{a}_j) \qquad (2.70)$$

with

$$\hat{H}_0^{\sin} = \sum_{j=1}^{3} \frac{J_0(\Lambda + 1)}{2} (\hat{\sigma}_1 \cos(\mathbf{k} \cdot \boldsymbol{\delta}_j) + \hat{\sigma}_2 \sin(\mathbf{k} \cdot \boldsymbol{\delta}_j)). \qquad (2.71)$$

The resulting effective Hamiltonian again corresponds to a Haldane model with phase $\phi = -\pi/2$ and $\Delta = 0$. We therefore find that, identical to the Haldane model, the Chern number of the lowest band will be $\mathcal{C}^- = \pm 1$ depending on the chirality of the drive for both modulation protocols. The second band will always exhibit the opposite Chern number of the lowest band.

Comparing $\hat{H}_{\text{eff}}^{\sin}$ and $\hat{H}_{\text{F}}^{\text{step}}$ one finds that the nearest neighbor tunneling in both cases is increasing with increasing Λ, thus increasing the bandwidth of the bulk bands. The next-nearest neighbor tunneling is, except for the prefactor being different by $\approx 7\%$, scaling identically with frequency and modulation amplitude

$$\tilde{J}^{\sin} = e^{\mp i\pi/2} \frac{J_0^2(\Lambda - 1)^2\sqrt{3}}{16\hbar\omega} \qquad (2.72)$$

$$\tilde{J}^{\text{step}} = e^{\mp i\pi/2} \frac{J_0^2(\Lambda - 1)^2\pi}{27\hbar\omega}. \qquad (2.73)$$

The gap ΔE at the Dirac points K and K' is directly connected to the next-nearest neighbor tunneling by

$$\Delta E(K) = 3\sqrt{3} \left| \tilde{J} \right|. \qquad (2.74)$$

For both modulation protocols, the complex next-nearest neighbor tunneling results in a topological gap opening at K and K'. Figure 2.8b compares the minimal gap at K derived in the high frequency expansion with the gap derived from the evolution operator obtained from the numerical evaluation of the Floquet-Hamiltonian. For large Λ the deviation from the high frequency approximation becomes visible. As introduced in Section 2.3.1, a time periodic Hamiltonian will have a periodic quasienergy spectrum with, in the case of a two-band model, two energy gaps: g^0 and g^π. The gap we discuss in the high frequency

approximation fundamentally is g_0, as there is no periodic quasienergy. The numerical evaluation however results in a periodic quasienergy spectrum, with an additional π-gap g^π, cf. Figure 2.5, the displayed minimal gap is always $\min\{g^0, g^\pi\}$.

The minimal gap at any quasimomentum in a Floquet modulated system is always upper bounded to $\hbar\omega/2$. When any of the gaps becomes of the same order as the modulation energy we can expect the system to significantly deviate from the high frequency expansion, as coupling in between Floquet copies, i.e., across the edge of the Floquet Brillouin zone, can be as strong as the coupling inside the Floquet Brillouin zone. Coupling between different Floquet copies is not included in the high frequency expansion [93].

To have an estimate of the modulation parameters leading to a coupling between Floquet Brillouin zones we can consider the largest gap ΔE, corresponding to the energy difference of between the two bands inside the Floquet Brillouin zone at Γ,

$$\Delta E(\Gamma) = 6J_{\text{eff}} \tag{2.75}$$

$$J_{\text{eff}}^{\sin} = \frac{J_0(\Lambda + 1)}{2} \tag{2.76}$$

$$J_{\text{eff}}^{\text{step}} = \frac{J_0(\Lambda + 2)}{3}, \tag{2.77}$$

The effective tunneling J_{eff} corresponds to the tunneling of the time-independent part of the Hamiltonian $\hat{H}_0$, and only depends on the modulation amplitude, therefore by scanning the modulation angular frequency ω, we can expect to find a point where the modulation energy $\hbar\omega$ equals the bandwidth ΔE. Whenever the bandwidth is an integer multiple of the drive the bands can touch and potentially hybridize. The band touching can only occur on high symmetry points of the Brillouin zone [163]. The critical modulation amplitude Λ_{crit} as a function of the modulation frequency of the two driving protocols then reads

$$\Lambda_{\text{crit}}^{\sin} = \frac{\hbar\omega}{3J_0} - 1 \tag{2.78}$$

$$\Lambda_{\text{crit}}^{\text{step}} = \frac{\hbar\omega}{2J_0} - 2. \tag{2.79}$$

Note that the high frequency approximation does not predict the closing of the gap and is only used to gain intuition for when gap closings can occur. Still the high frequency approximation nicely shows the effect of the modulated tunneling, resulting in complex next-nearest neighbor tunneling and the opening of a topological gap at the Dirac points for high frequencies.

2.5 Anomalous Floquet Phases

Periodic driving of system parameters can simulate the time evolution of an effective Hamiltonian. If the effective Hamiltonian can be obtained in a high frequency expansion as described in Section 2.3.3, it can be mapped to a static system [86]. The effective Hamiltonian can exhibit exotic properties that would otherwise be hard to obtain such as

topologically non-trivial band structures or sign inverted tunneling amplitudes compared to the static case. As the system is equivalent to a static Hamiltonian the topological bands are well described by their Chern number.

If the modulation frequency becomes comparable to the intrinsic energy scale of the Hamiltonian an *anomalous Floquet phase* can emerge where the topological characterization using Chern numbers is incomplete. The anomalous Floquet phase is a genuine out of equilibrium phase of matter and there exists no equivalent static counterpart. The periodicity of the quasienergy is crucial for the anomalous Floquet phase as its edge modes wrap around the Floquet Brillouin zone. The anomalous Floquet phase therefore requires a topological characterization using winding numbers, which extent the topological characterization to driven systems and will be discussed in Section 2.5.2.

To illustrate the properties of anomalous Floquet systems we will first consider a toy model to gain insight into the essential properties. We will then consider how the winding number is derived from the evolution operator of the system and related to the Chern number and how it changes at band touchings.

Anomalous Floquet phases have been implemented in several experimental platforms among photonic waveguides [112, 113, 164], structured microwave resonators [165, 166], nanophotonic lattices [167, 168], liquid crystal devices [169] and acoustic resonators [170].

2.5.1 Instructive example

To gain an intuitive understanding of the anomalous Floquet phase we can consider a toy model on a honeycomb lattice. Figure 2.7a shows the schematic protocol consisting of three time steps of equal duration $T/3$, where T is the period of the driving protocol. During each of the three time steps tunneling along the bold bond direction in the schematic is enabled, while the other two bond directions, depicted by the dashed lines, exhibit no tunneling. The tunneling along the allowed bonds is chosen such that a particle hops along this bond with unit probability. To realize the deterministic tunneling the duration during which tunneling is enabled is chosen such that every enabled tunneling realizes a π-pulse for the two level system consisting of the two connected sites, i.e.,

$$J = \frac{3\pi}{2T} \tag{2.80}$$

along the bonds with enabled tunneling and $J = 0$ on all other bonds. In this fine-tuned case the trajectory of the particles on the lattice can easily be reconstructed by following the path of a particle. The trajectory of a particle in the bulk and on the edge are shown in Figure 2.7b for the evolution during two periods of the drive. The steps of the drive are encoded in the color of the arrows indicating the tunneling, where lighter colors indicated earlier times. The particle in the bulk fulfills a cyclic motion around one plaquette, recurringly occupying the same site after every two periods. This time evolution, if we stroboscopically examine the system every $2T$, can be described by an effective Hamiltonian that is just the identity matrix $\hat{H}_{\text{eff}} = \mathbf{1}$. This is true for all bulk states.
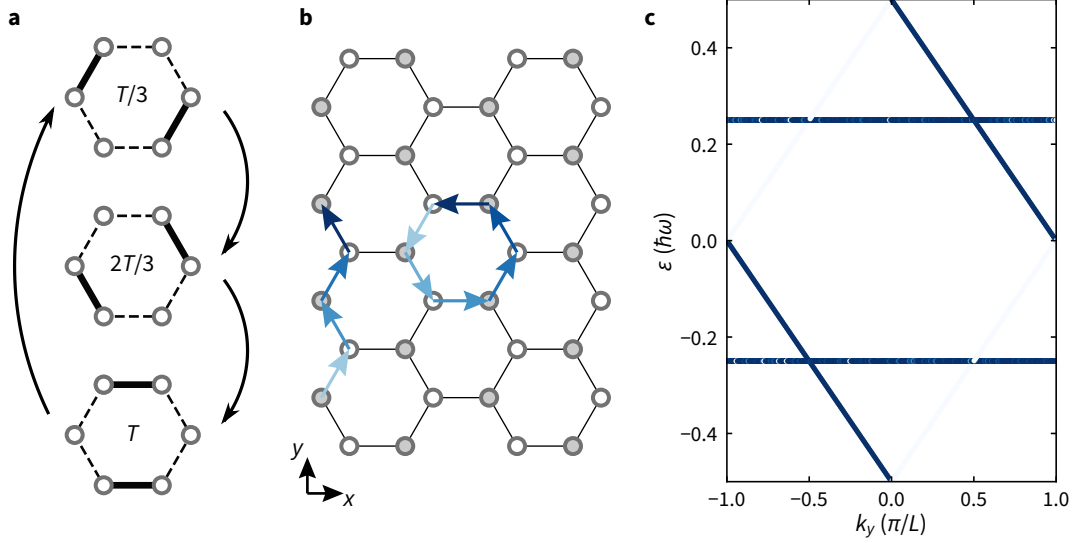
Figure 2.7 | **Toy model to illustrate the properties of the anomalous Floquet phase. a**, Modulation protocol for the toy model case. The tunneling along the dashed bonds is zero during every time step. The tunneling along the bold highlighted bonds is $J = 3\pi/(2T)$. The duration during which the tunneling is enabled therefore corresponds to the equivalent of a π-pulse between the two connected sites. **b**, Resulting trajectories in real space during two periods of the drive. A particle in the bulk is, irrespective of the initial site being an *A*- or *B*-site, performing loops around a plaquette. The motion during $2T$ in the bulk is illustrated by the arrows' color, where a darker arrow represents later times. All particles located in the bulk of the system will return to their initial position after $2T$. If the particle is initially located on the edge the resulting trajectory winds along the edge of the system, i.e., the motion corresponds to an edge mode of the system. The edge mode is enabled by the absence of the horizontal bonds on the edge, where the particle cannot move during one third of the period. The particles initially located on *A*-sites (white markers) on the edge still belong to the bulk. **c**, Resulting dispersion of the effective Hamiltonian on a semi-infinite strip in the fine-tuned case $J = 3\pi/(2T)$. The states are plotted with a weight resulting from a projection onto all states except a small region on the right edge. The bulk dispersion is entirely flat as expected from a trivial evolution where all states return to their initial position after one period. The dispersion of the edge is connecting the two flat bulk bands at zero energy and at energy $\pm\hbar\omega/2$. Each band has one edge mode entering and one edge mode leaving the band which corresponds to $\mathcal{C} = 0$.

A state on the edge however performs a very different trajectory, as illustrated on the left edge of Figure 2.7b. The particle starting on the edge first hops along the edge during the first step, then during the second step while the horizontal tunneling is enabled, it is not moving since there is no horizontal bond connecting this site to another. Afterwards the particle again follows the tunneling dictated by the drive and moves along the edge, until a horizontal tunneling would occur. But since there again is no horizontal bond on that site the particle cannot tunnel. This process repeats over and over and so the particle is transported along the edge. This behavior is clearly not covered by the effective Hamiltonian being simply the identity matrix. Depending on the initial phase of the drive, a particle localized on an edge site either performs a bulk or edge trajectory, but there is always an edge mode independent of the initial phase.

From this toy model we can immediately see that the Chern number of the bulk bands, which is described by the trivial evolution $\hat{H}_{\text{eff}} = \mathbf{1}$, is $\mathcal{C}^- = 0$. Considering Equation 2.16 we also immediately see that the Berry curvature in this case is vanishing in the entire Brillouin zone. Yet there still are propagating modes along the edge. This calls for a different description of the topology of this driven system and shows that the stroboscopic picture is incomplete for anomalous Floquet systems.

2.5.2 Topological characterization - winding numbers

When Kitagawa and coworkers conceived the driving protocol [86] introduced in Section 2.4 and the fine-tuned case described above, there was no complete picture of how to relate driven, out of equilibirum topological phases, to those of static systems. Rudner and coworkers then established a relationship between the *winding numbers* and the Chern number connecting the topology of the driven and static systems [87]. The winding number and its derivation from the evolution operator will be discussed in the following.

As illustrated in the instructive example before (Section 2.5.1), the anomalous Floquet phase realizes a system in which the bulk is topologically trivial, while there are topologically protected edge modes on the boundary of the system, or from an energy perspective there are edge modes located in both spectral gaps of the Hamiltonian [86, 87]. The Chern number is given by the difference in the number of chiral edge modes above and below a specific band, this still holds for the periodically driven case. But since energy is now periodic, even for the "lowest" band there is always an energy below as the spectrum is unbounded. Therefore any band of the system can have an edge mode entering from below and leaving above, i.e., every band in the system can have a vanishing Chern number.

We can therefore not predict the existence of edge modes from the Chern number alone, but require a different characterization. It still holds that the sum of the Chern numbers over N bands derived from N initially trivial bands sums to zero, $\sum_n^N \mathcal{C}^n = 0$ [171]. The Chern number stems from the effective Hamiltonian which is only accurate after averaging over one full period and does not consider the micromotion during the period. We can investigate the evolution operator more closely, as it also incorporates the micromotion. From the limit where the bulk evolution operator $\hat{U}(\mathbf{k}, t) = \mathbf{1}$ is described by the identity, we can then define the winding number as [87]

$$W(\hat{U}) = \frac{1}{8\pi^2} \int \mathrm{d}t \mathrm{d}k_x \mathrm{d}k_y \mathrm{Tr} \left(\hat{U}^{-1} \partial_t \hat{U} \left[\hat{U}^{-1} \partial_{k_x} \hat{U}, \hat{U}^{-1} \partial_{k_y} \hat{U} \right] \right). \tag{2.81}$$

The winding number directly gives the net number of chiral edge modes (counterclockwise minus clockwise) [87]

$$n_{\text{edge}} = W(\hat{U}). \tag{2.82}$$

However we must note that this definition only works in the case where all bands collapse onto each other and their evolution is described by the identity $\mathbf{1}$. In this case there is only one gap, where the winding number corresponds to the number of edge modes. If we want to

characterize a system away from this extreme limit, we need to find a map from the general Floquet operator $\hat{U}(\mathbf{k}, t)$ to the trivial Floquet operator $\hat{U}_\varepsilon(\mathbf{k}, t) = \mathbf{1} \, \forall \, \mathbf{k}$. Furthermore there needs to be a continuous interpolation between $\hat{U}_\varepsilon(\mathbf{k}, t)$ and $\hat{U}(\mathbf{k}, t)$, maintaining a gap around the quasienergy value ε_s which smoothly varies between the quasienergy of interest ε and $\hbar\omega/2$ [87]. Upon finding such an evolution operator, we can immediately compute the winding number, which counts the number of edge modes at quasienergy ε, via

$$n_{\text{edge}}(\varepsilon) = W(\hat{U}_\varepsilon). \tag{2.83}$$

In essence, we need to map the complicated general system to the trivial system without closing a gap, so that the winding number remains an invariant. The Chern number of the band located in between quasienergy ε and ε' is related to the winding numbers at these energies via

$$\mathcal{C}_{\varepsilon,\varepsilon'} = W(\hat{U}_{\varepsilon'}) - W(\hat{U}_\varepsilon). \tag{2.84}$$

This shows that the common bulk-boundary correspondence is invalid in periodically driven systems away from the high frequency limit, though it still holds in a slightly modified version. Now not the bulk band but rather the full evolution operator carries the information whether an edge mode exists, which can then be cast into the winding number. We can thus envision a modified bulk boundary correspondence, where the non-zero winding numbers, which still are topological invariants of the bulk, predict the presence of edge modes.

2.5.3 Obtaining the winding numbers - theory

Relating the winding number to quantities other than the evolution operator itself, can help us to gain an understanding of how we can experimentally determine them. As mentioned briefly before the sum of Chern numbers of the considered N bands sums to zero, but as we saw before, this does not give a full characterization of the topology of the system. In contrast to the static system where $N - 1$ topological invariants fully characterize the N bands, we require N invariants in the time periodic case. These N invariants can equivalently be the winding numbers in between the bands, or alternatively the $N - 1$ Chern numbers and the sum of the topological charges of the zone edge singularities, which describe how the Chern numbers of the bands change at a topological phase transition,

$$\mathcal{C}^1, ..., \mathcal{C}^n, \sum_i q_i^{\text{ZES}}. \tag{2.85}$$

The q_i^{ZES} are related to the degeneracies of the eigenvalues of the evolution operator, which can not be removed, across the edge of the Floquet Brillouin zone [172]. We will see in the following how the topological charge can be related to the band touching and change of Berry curvature at the singularity. Similar to the models described above and the experimental setup discussed later, we will consider a two dimensional Brillouin zone and an additional parameter λ describing the modulation parameter space across a topological phase transition at $\lambda_s = 0$ at $\mathbf{k}_s$. Under the assumption that only two of the N bands are

touching we can focus only on these two and assume the rest to be constant [111, 172–174], in that case we can describe the system by an effective two-level Hamiltonian as

$$\hat{H}_{\text{eff}}(\mathbf{k}, \lambda) = \hat{\boldsymbol{\sigma}} \cdot \mathbf{h}(\mathbf{k}, \lambda), \tag{2.86}$$

where $\mathbf{h}(\mathbf{k}, \lambda)$ takes values in $\mathbb{R}^3$ and vanishes at the band touching. We are only interested in the region located close to the degeneracy and can therefore expand Equation 2.86 around $\mathbf{P}_s = (\lambda_s, \mathbf{k}_s)$. If the band touching is non-degenerate and linear, the expansion to first order suffices [172]

$$\begin{aligned}
\mathbf{h}(\mathbf{P}) = (\lambda - \lambda_s) \frac{\partial \mathbf{h}(P)}{\partial \lambda} \bigg|_{\mathbf{P}_s} \\
+ (k_x - k_{x,s}) \frac{\partial \mathbf{h}(\mathbf{P})}{\partial k_x} \bigg|_{\mathbf{P}_s} + (k_y - k_{y,s}) \frac{\partial \mathbf{h}(\mathbf{P})}{\partial k_y} \bigg|_{\mathbf{P}_s}.
\end{aligned} \tag{2.87}$$

The partial derivatives constitute the Jacobian of $H_{\text{eff}}(\mathbf{k}, \lambda)$ at the singularity, as long as there are no gaps closing we can continuously deform the Hamiltonian homotopically until the Jacobian matrix coincides with the canonical basis. The orientation of the basis $\mathcal{O}$ which is equivalent to the sign of the determinant of the Jacobian matrix $J(\mathbf{P}_s)$, is given by

$$\mathcal{O} = \text{sgn}\left(\det(J(\mathbf{P}_s))\right) = \text{sgn}(\partial_\lambda \mathbf{h} \cdot \left(\partial_{k_x} \mathbf{h} \times \partial_{k_y} \mathbf{h}\right)). \tag{2.88}$$

With the canonical basis we can therefore write the Hamiltonian after the continuous deformation as

$$\hat{H}_{\text{eff}}(\mathbf{P}) = \mathcal{O}\hat{\boldsymbol{\sigma}}\mathbf{P}, \tag{2.89}$$

which exhibits a singularity at $\mathbf{P} = 0$, for which the Berry Curvature of the two bands is

$$\boldsymbol{\Omega}^{\mp}(\mathbf{P}) = \pm\mathcal{O}\frac{\mathbf{P}}{|\mathbf{P}|^3}, \tag{2.90}$$

where $\mp$ indicates the lower and upper band. The Berry flux Φ through a closed surface $\mathcal{S}$ containing the singularity can be easily calculated by transforming to spherical coordinates and picking the surface to be a sphere

$$\Phi^{\mp} = \int_{\mathcal{S}} \boldsymbol{\Omega}^{\mp}(\mathbf{P})\mathrm{d}\boldsymbol{\mathcal{S}} = \pm\mathcal{O}\int_0^\pi \mathrm{d}\theta \int_0^{2\pi} \mathrm{d}\varphi |\mathbf{P}|^2 \sin(\theta)\frac{\mathbf{P}}{2|\mathbf{P}|^3} \cdot \frac{\mathbf{P}}{|\mathbf{P}|} = \pm\mathcal{O}2\pi \tag{2.91}$$

We find that the Berry Flux is directly related to the orientation of the basis or the sign of the Jacobian matrix determinant, which is the topological charge at the singularity and determines how the winding numbers or Chern numbers of the two bands at the singularity change [171, 175]

$$Q_s = \text{sgn}\left(\det(J(\mathbf{P}_s))\right). \tag{2.92}$$

As measuring the Berry flux through a plane perpendicular to the λ-direction is significantly easier, as it breaks down to measuring the Berry Curvature in the k_x-k_y-plane, we deform the sphere through which we have so far measured the Berry flux. We deform the sphere into a cuboid of height ϵ in λ-direction and centered around $\mathbf{P}_s$ [111, 174]. As we can choose ϵ to be arbitrarily small, the entire Berry flux is penetrating the upper and lower faces of the cuboid, the flux through these surfaces for the lower band is

$$\Phi_{\pm\epsilon}^- = \int_{-k_x^0}^{k_x^0} \mathrm{d}k_x \int_{-k_y^0}^{k_y^0} \mathrm{d}k_y \boldsymbol{\Omega}^-(\lambda \pm \epsilon, \mathbf{k})\mathbf{e}_\lambda = \pm\pi Q_s. \tag{2.93}$$

Here we take both surfaces to be oriented along the unit vector in λ-direction $\mathbf{e}_\lambda$. In order to recover the previous result we need to take the difference of the two fluxes through the surfaces at $\lambda \pm \epsilon$

$$\Phi^- = \Phi_{+\epsilon}^- - \Phi_{-\epsilon}^- = 2\pi Q_s. \tag{2.94}$$

The Berry Curvature changes by $2\pi Q_s$ infinitesimally away from the phase transition. With the assumption of a linear band touching we already fixed $|Q_s| = 1$, therefore we are only interested in the sign change of the Berry flux. By probing the close vicinity of $\mathbf{P}_s$ we can directly relate the sign change of the Berry curvature to the topological charge at the singularity

$$Q_s = \mathrm{sgn}\left(\Omega^-(\mathbf{k}_s, \lambda + \epsilon) - \Omega^-(\mathbf{k}_s, \lambda - \epsilon)\right) = \Delta\Omega^-(\mathbf{k}_s) \tag{2.95}$$

For a periodically modulated lattice where there are gaps at quasienergy 0 and $\pm\hbar\omega/2$ we can quantify the topological charge in the gaps via the sign change of the Berry curvature of the band below the considered gap. As the Berry curvature of the two bands is equal in magnitude but of opposite sign, the charges can be determined by either of the two bands' Berry curvature:

$$Q_s^0 = \mathrm{sgn}(\Delta\Omega^-(\mathbf{k}_s)) = -\mathrm{sgn}(\Delta\Omega^+(\mathbf{k}_s)) \tag{2.96}$$

$$Q_s^\pi = \mathrm{sgn}(\Delta\Omega^+(\mathbf{k}_s)) = -\mathrm{sgn}(\Delta\Omega^-(\mathbf{k}_s)) \tag{2.97}$$

In this way we can determine the topological charge of the singularity. The winding number in gap j changes exactly by this topological charge when crossing the phase transition

$$\Delta W^j = W_{+\epsilon}^j - W_{-\epsilon}^j = Q_s^j \tag{2.98}$$

In this fashion, by tracking the winding numbers and determining the topological charge at the phase transitions it is possible to fully characterize the topology even in the driven case. We required the band touching to be linear and non-degenerate, but this derivation can be extended to also work for quadratic band touchings [172].

We experimentally reconstruct the winding numbers using the method presented above, and the results are presented in Section 4.4.

2.5.4 Phase transitions in the tunneling modulated honeycomb lattice

Coming back to the tunneling modulated honeycomb lattice with step and cosine protocol: we found that the high frequency approximation maps to the Haldane model and gives intuition regarding the effects that arise due to the modulated tunneling in the high frequency regime. However the high frequency approximation does not cover the full phase diagram of the model that can be explored with such Floquet drives. Especially the anomalous Floquet phase introduced in Section 2.5.1, where all Chern numbers are equal to zero cannot be represented in the high frequency approximation. One way to include band touchings across the edge of the Floquet Brillouin zone is to include more copies in the Floquet operator [93]. A different approach consists in evaluating the Floquet-Hamiltonian by numerically integrating the evolution over one period, cf. Equation 2.54. As the evolution operator is periodic, the Floquet-Hamiltonian exhibits an energy spectrum within the Floquet Brillouin zone. By construction the resulting states are periodic in energy and therefore include the band touching across the edge of the Floquet Brillouin zone.

Figure 2.8a shows the resulting energy spectrum obtained by numerically evaluating the evolution operator and obtaining the Floquet-Hamiltonian from it. The modulation frequency is $\hbar\omega/J_0 = 32/3$, the upper panel considers the stepwise modulation, the bottom panel is obtained from the sinusoidally modulated system. Overall the shape of the bands are very similar. For $\Lambda \neq 0$ we observe a gap opening at K, and for increasing Λ eventually a band touching and reopening in the π-gap at Γ. The touching in the π-gap occurs for $\Lambda \approx 3.3$ in the stepwise and $\Lambda \approx 2.5$ for the cosine modulation. The numerically obtained Λ match very well with the expression obtained from the high frequency limit by comparing the modulation frequency and the bandwidth of the system (cf. Equation 2.78 and Equation 2.79), $\Lambda_{\text{crit}}^{\sin} = 23/9$, $\Lambda_{\text{crit}}^{\text{step}} = 10/3$.

Figure 2.8b shows the resulting minimal gap $\Delta E_{\min}$ at Γ and K for varying Λ. We find that the gap at K behaves very similarly in the sinusoidal and step modulated case and even the prediction by the high frequency approximation matches well for $\Lambda < 5$. The minimal gap at Γ cannot be predicted by the high frequency expansion and we observe a closing at different Λ for the two modulation protocols. We find several touching points, where the gap at Γ vanishes. At each of these, the topological nature of the bands can change. To get a more intuitive picture why these phase transitions occur we can, instead of changing the modulation amplitude Λ as done in Figure 2.8, vary the modulation frequency ω. Upon varying the modulation frequency, we also change the size of the Floquet Brillouin zone compared to the bandwidth of the modulated system.

To illustrate the changing dispersion and the change of the other quantities at the phase transitions we will here focus on the step-wise modulated lattice. The different columns of Figure 2.9 show the same evaluation of a tunneling modulated system with $\Lambda^{\text{step}} = 4$ but varying modulation energy $\hbar\omega/J_0$, which is the same within each row. The two dimensional band structure is evaluated up to $k_L = \pm 4\pi/(3\sqrt{3}a)$, which corresponds to the distance from the center of the Brillouin zone Γ to K and K'. The Berry curvature is evaluated in a rhombic Brillouin zone centered around Γ, the dispersion along the high symmetry line $\Gamma \to M \to K \to \Gamma$ (cf. Figure 2.2a). The dispersion is shown in the extended Floquet zone
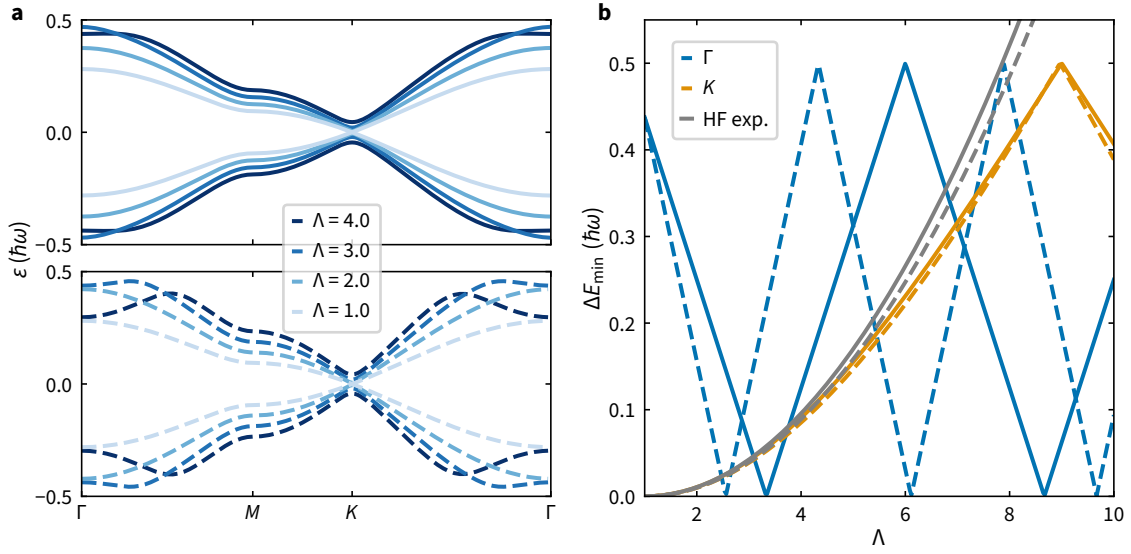
Figure 2.8 | Resulting dispersion and gap size for cosine and stepwise modulation. a, Dispersion in the tunneling-modulated lattice for the stepwise (top) and sinusoidal (bottom) modulation for a frequency $\hbar\omega/J_0 = 32/3$. In both cases the modulation first opens the gap at the Dirac points and increases the bandwidth of both bands, until the bands reach the edge of the FBZ and hybridize indicating the transition to the anomalous regime. **b,** Comparison of the minimal gap. The frequency is fixed to the value also used in **a** while the modulation amplitude is increased. The dashed (solid) lines correspond to the cosine (stepwise) modulation. The blue color shows the gap at Γ, the orange lines the gap at K. The gray lines show the high-frequency expansion, which agrees well for moderate amplitudes. As the bands become dispersive faster in the cosine modulation scheme, the gap closing at Γ occurs first in this case.

scheme with the copies of the bands above and below. The dashed horizontal line represents the edge of the Floquet Brillouin zone at $\pm\hbar\omega/2$. The strip dispersion is evaluated on a semi-infinite strip terminated by an zigzag edge. The color code in the right column indicates the topological phase, which is kept consistent throughout the thesis.

As we have seen before, in the high frequency limit the system maps to a Haldane model, where the modulation leads to a breaking of time-reversal symmetry and an opening of a gap at K and K'. The Floquet Brillouin zone is significantly larger than the bandwidth of the system in the high frequency limit and thus coupling between Floquet copies in the π-gap is absent. As this arguments holds for arbitrarily high frequencies, it is justified to deduce $W^\pi = 0$. Therefore the edge mode in the Haldane phase is located in the 0-gap, and we have a winding number $W^0 = 1$. Figure 2.9a shows the system for $\hbar\omega/J_0 = 28$. The Berry curvature is positive and concentrated at K and K', the sign of the Berry curvature at one of the Dirac cones has changed compared to the static lattice due to the chiral modulation of the tunneling amplitudes. The band structure compared to the static lattice is only slightly modified with the main difference being a gap opening at the Dirac points. In the strip geometry the 0-gap therefore hosts an edge mode connecting the K and K' points of the lower and upper band. The existence of this edge mode is expected from the Bulk boundary correspondence, as the Chern number of the lower band is $\mathcal{C}^- = 1$. The dispersion of the semi-infinite strip is derived from a system with an infinitely sharp wall
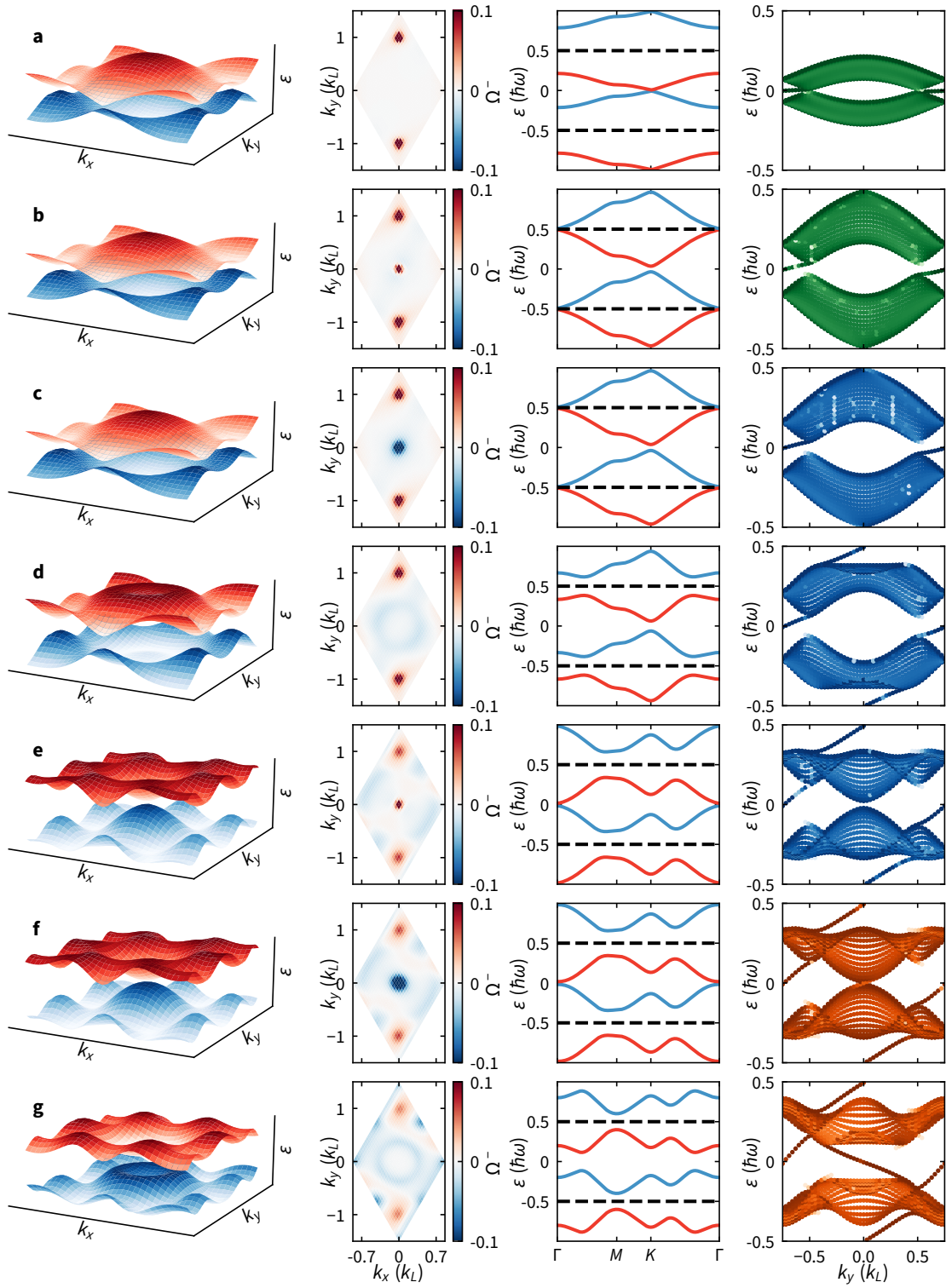
Figure 2.9 | Bandstructure, Berry Curvature, dispersion along the high symmetry line and dispersion of a strip terminated with zigzag edge. a, $\hbar\omega/J_0 = 28$. **b**, $\hbar\omega/J_0 = 12.2$. **c**, $\hbar\omega/J_0 = 11.8$. **d**, $\hbar\omega/J_0 = 9$. **e**, $\hbar\omega/J_0 = 6.1$. **f**, $\hbar\omega/J_0 = 5.95$. **g**, $\hbar\omega/J_0 = 5$. $\Lambda^{\text{step}} = 4$ in all panels.

separating the system at an zigzag edge into a low and high potential region. The potential $V_0 \gg J_0$, $\hbar\omega$ is significantly exceeding all other energy scales of the system. The spectrum is filtered to show only the states located in the low energy region of the wall while excluding the sites located at the numerical edge. The filtering is done by calculating the overlap of each state with the low energy region, this overlap is also reflected in the darkness of the data-points, with darker colors representing a stronger weight cf. Section 2.5.6.

As the modulation frequency is reduced, the size of the Floquet Brillouin zone is reducing proportionally and the band gap in the π-gap is decreasing. The bandgap at Γ is the largest in the 0-gap and conversely the smallest gap in the π-gap. We can therefore expect the bands to first touch at Γ when reducing the modulation frequency. Figure 2.9b shows the dispersion of the bands at $\hbar\omega/J_0 = 12.2$ shortly before the phase transition. The bands have not obviously changed their shape compared to Figure 2.9a. We observe a buildup of positive Berry curvature at Γ shortly before the band touching, additionally we observe a spreading and slight reduction of the Berry curvature at the K and K' points. After the band touching at $\hbar\omega/J_0 = 12$ the bands hybridize in the π-gap at Γ and a gap reopens, cf. Figure 2.9c, where $\hbar\omega/J_0 = 11.9$. The Berry curvature in the lowest band in the vicinity of Γ has changed from positive to negative by $\Delta\Omega^- = -2\pi$ indicating a topological charge $Q^\pi = -\operatorname{sgn}(\Delta\Omega^-) = 1$ and thus a winding number $W^\pi = 1$. Integrating the Berry curvature to obtain the Chern number we find $\mathcal{C}^- = 0$. Even though the band structure and dispersion of the system is not changing dramatically, the Berry curvature very clearly indicates the phase transition. After the band touching we find an edge mode in the π-gap as expected from $W^\pi = 1$. The depicted modulation frequencies were chosen such that the gap at Γ is approximately equal before and after the phase transition. The gap can be very well approximated by a linear function of slope 1 when measured in units of $\hbar\omega$. This topological phase will be referred to as the *anomalous phase*.

As we further lower the modulation frequency a moat in the dispersion around Γ emerges [176–178], cf. Figure 2.9d. The negative Berry curvature, which initially was localized at Γ, has spread along with the ring and is now concentrated in the degenerate minimum of the moat. The moat can intuitively be understood from the shape of the dispersion of the uncoupled bands. The center part of it originates from the e.g. initially upper band protruding through the lower band. At the point where the two bands cross in energy the modulation leads to a coupling and an opening of a gap forming an avoided crossing between the two bands resulting in the moat. The edge modes in both the 0-gap and the π-gap are now bridging the entire Brillouin zone, indicating that the edge modes are supported for any quasimomentum. As now both winding numbers are non-zero, we find that the Chern number which is related to the winding number of both bands via

$$\mathcal{C}^\mp = \pm(W^0 - W^\pi) = 0. \tag{2.99}$$

Even though $\mathcal{C}^\mp = 0$, the system exhibits edge modes clearly showing the anomalous character of this phase [86], highlighting that the Chern numbers are no longer sufficient to characterize the topology of this system [87].

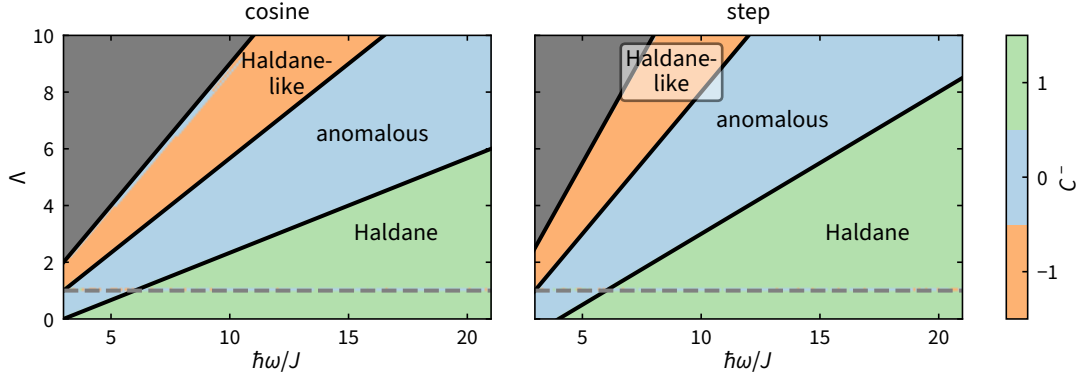**Figure 2.10 | Topological phase diagram in the tunnel modulated honeycomb lattice as a function of modulation frequency** ω **and amplitude** Λ**. a**, Stepwise modulation showing the Haldane phase for high frequency and small amplitude, the anomalous phase after crossing the first phase transition and the Haldane like phase after the second phase transition. The solid lines are the predictions from the effective bandwidth of the high frequency expansion. **b**, Cosine modulation showing the identical phases as **a**, with shifted phase transitions. The solid lines are again the predictions from the effective bandwidth of the high frequency expansion. There is a plethora of different phases located in the gray shaded area at small modulation frequencies, which are not futher characterized.

A second band touching occurs at Γ when further lowering the frequency of the drive, this time the 0-gap is closing at $\hbar\omega/J_0 = 6$. We again observe a peaking of the Berry curvature before the transition at $\hbar\omega/J_0 = 6.1$ and a subsequent inversion at $\hbar\omega/J_0 = 5.9$, cf. Figure 2.9e and f. With the gap closing the edge mode in the 0-gap is annihilated, ergo the winding number in the 0-gap is $W^0 = 0$, as there are no edge modes present in the 0-gap. The topological charge of this transition is $Q^0 = \text{sgn}(\Delta\Omega^-) = -1$, as the Berry curvature of the band below the gap is changing by $\Delta\Omega^- = -2\pi$. The size of the gap at the phase transition is now changing with a slope of 2, when measured in units of $\hbar\omega$. This is due to the fact that the bands are wrapping twice around the Floquet Brillouin zone, e.g. enabling the bands to hybridize with themselves wrapped around the Floquet Brillouin zone. The Chern number of the system after the phase transition is $\mathcal{C}^\mp = \mp 1$, exhibiting one edge mode in the W^π gap. The system exhibits topological properties closely related to the Haldane phase, we will therefore refer to this phase as the *Haldane-like phase*.

2.5.5 Phase diagram for step and sinusoidal modulation

To further characterize the resulting topological phases of the modulated tunneling scheme, in the following we will compare the topological phase diagram as a function of modulation amplitude and frequency. The quantity we will consider is the Chern number, note however that the Chern number is not sufficient to describe the out of equilibrium anomalous Floquet phase, it can still show where the topological phase transitions occur. We obtain the phase diagram by numerically time-integrating the evolution operator to get the Floquet-Hamiltonian, and subsequently calculate the Chern number from the resulting eigenstates. The resulting changes of the Chern numbers validate the accuracy of the predictions made for the occurrence of the gap closing in Section 2.4.2. Figure 2.10a shows the resulting phase

diagram for the stepwise modulation, the phase diagram for the sinusoidal modulation is shown in Figure 2.10b. As illustrated before both modulation schemes host a Haldane phase with $\mathcal{C}^- = 1$ in the high frequency limit. Once the bandwidth of the effective Hamiltonian matches the modulation frequency the transition to the anomalous phase with $\mathcal{C}^- = 0$ occurs in both modulation schemes, as predicted by Equation 2.78 and Equation 2.78. The black lines in Figure 2.10a and b show the respective prediction from the high frequency expansion also for the following transitions. Upon further reducing the modulation frequency ω or increasing the modulation amplitude Λ the Haldane-like phase emerges. The topological characterization of the anomalous phase is incomplete, when just considering the Chern number as further illustrated in Section 2.5.2. In the Haldane-like phase the Chern number is opposite in sign compared to the Haldane phase, i.e., $\mathcal{C}^- = -1$. The phase transitions occur at slightly different modulation parameters for the sinusoidal and stepwise modulation of the tunneling otherwise they result in an essentially equivalent phase diagram, when considering the first three phases connected to the high frequency limit.

As the two drives are closely linked it would be possible to connect the two phase diagrams without gap closings as the phases are topologically equivalent. We can introduce a parameter describing whether the drive is more linked to the step or sinusoidal drive, e.g. by removing frequency components $> \omega$ from the stepwise drive. By varying this parameter the stepwise modulation can be "smoothened" into the sinusoidal modulation, which would directly link the two phase diagrams. The respective phases will be connected without a gap closing, i.e., without phase transition in between.

The gray shaded area in Figure 2.10 covers a multitude of other phases occurring in the two modulation schemes with greatly varying Chern numbers. The phases differ between step and sinusoidal modulation and are not covered here. Experimentally realizing the corresponding phases might be very challenging as they occur at low modulation frequencies even compared to the energy scales related to the lattice. This renders the achievable minimal gap size also very small. The small gap between the bands proves experimentally very challenging as adiabatic probing becomes harder and a faithful determination of quantities concerning only a single band, such as the Chern number, become very difficult.

2.5.6 Tight binding in a finite system

The description of the dynamics in the lattice can be understood well in reciprocal space for an infinitely extended lattice, as a Fourier transform in that case results in quasimomenta well defined within one Brillouin zone. As these systems are infinitely extended they do not have an edge. If we want to study the behavior of the system on the edge, we need to crop the system to a finite size in at least one direction. A very convenient option is the semi-infinite strip displayed in Figure 2.11a. The system consists of a unit cell of size L_x in the finite and L along the infinite direction, which is repeated indefinitely in the y-direction. The unit cell, highlighted by a red rectangle, results in a zigzag edge. The tunneling within the unit cell is unaltered, while the tunneling to the adjacent copies, indicated by the fainter sites, gets multiplied by a factor $\mathrm{e}^{\pm i k_y L}$, where k_y is the quasimomentum along the infinite direction and $L = \sqrt{3}a$ for the displayed zigzag edge. The sign of the complex phase depends
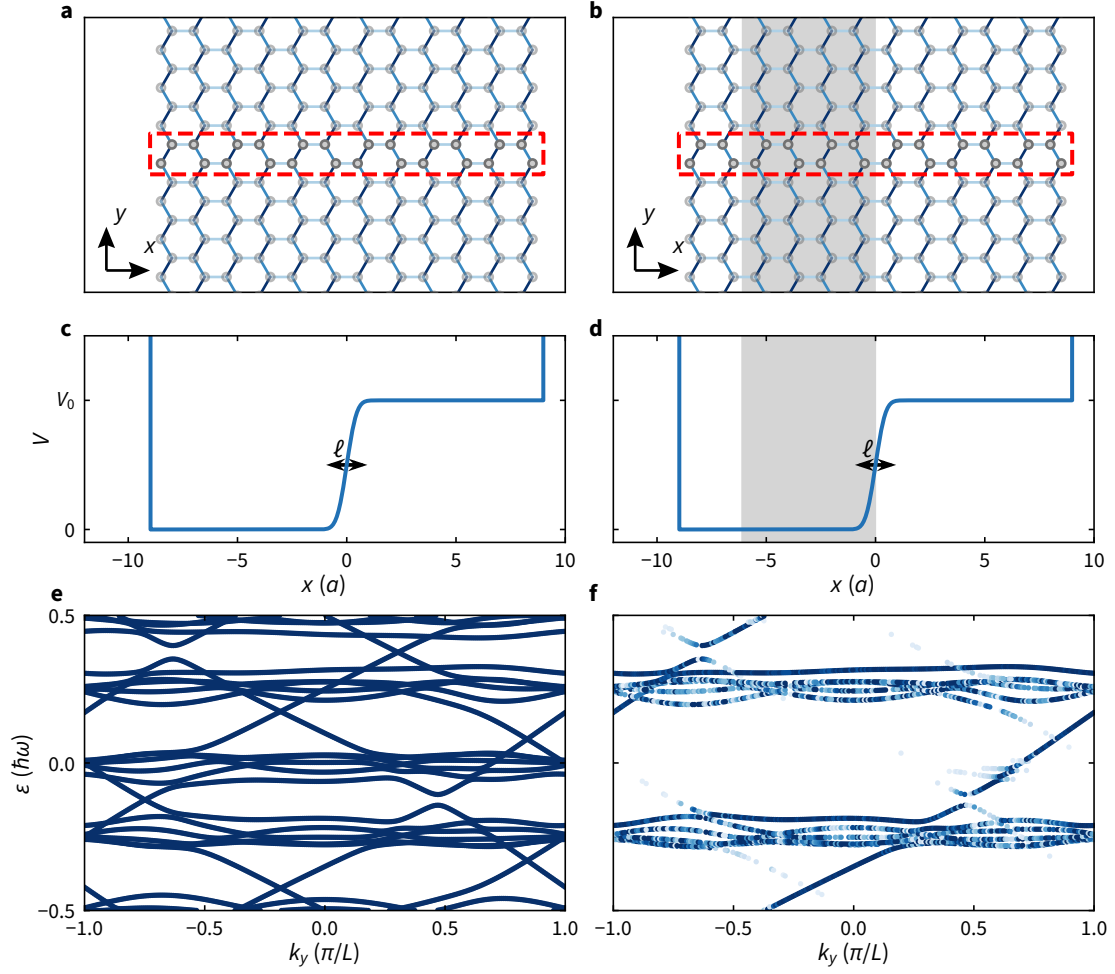
Figure 2.11 │ Geometry of a semi-infinite strip with a step potential in the center. a, Semi-infinite strip geometry with highlighted unit cell. The strip is finite along the *x*-direction and the solid drawn sites in the red rectangle represent the unit cell. The three types of bonds are drawn in different shades of blue and can be modulated in a time-dependent fashion. **b,** Same as **a** but with a region of interest highlighted. A specific region of the lattice can be selected to only investigate the eigenstates mainly located within the region. **c,** Potential energy *V* along the finite *x*-direction of the strip. The vertical lines on the left and right edge on the strip represent the numerical edges, which correspond to an infinitely high, infinitely sharp boundary. The edge of interest is located at the center of the strip in finite direction. The potential step is of height V_0 and width ℓ as indicated by the arrow. **d,** same as **b** but with the region of interest highlighted on the potential. The region includes a bulk region but only on one side of the edge and excludes the numerical edge. **e** Dispersion of the strip in the anomalous phase for quasimomenta in the infinite *y*-direction. All eigenstates are shown with equal weight. Two systems shifted by an energy $V_0 = 3.75\hbar\omega$ are visible but are hard to disentangle as the two spectra are folded and overlapping in the Floquet Brillouin zone. **f** Dispersion of the region highlighted in **b** and **d**, where darker data points have larger weight in the region. By projecting the eigenstates onto the selected region only the bulk at zero energy has significant weight and only the edge mode at the introduced edge is visible.

on the orientation of the tunneling along y. This results in quasimomentum in the infinite direction along y still being a good quantum number, while we find a finite number of modes

in the x-direction of the lattice. We can consider e.g. nearest-neighbor tunneling along three different bond directions $\boldsymbol{\delta}_j$ distinguished by their orientation illustrated by different shadings in Figure 2.11a. To modify the properties of the edge we can apply a potential offset between sites or regions of the semi infinite lattice as illustrated in Figure 2.11c and d. For clarity the potential outside of the strip has been set to ∞, as the numerical edge effectively constitutes an infinitely sharp and infinitely high potential barrier. Due to this numerical edge we can expect edge modes to be always located at the numerical edge in a topologically non-trivial system. However the properties of the numerical edge cannot be modified arbitrarily, we therefore introduce the previously mentioned potential offset in the center of the system, where we can control the height V_0 of the potential and its width ℓ. The potential energy within the system is modeled as

$$V(x) = \frac{V_0}{2} \left[\mathrm{erf} \left(\frac{2(x_0 - x)}{\ell} \right) + 1 \right], \tag{2.100}$$

where $\mathrm{erf}(x)$ is the error function, x_0 is the position of the edge in the finite direction, chosen here to be in the middle of the system, and ℓ encodes the width of the edge, defined as the length from 8% to 92% of the height of the edge. The resulting potential for $\ell = 1a$ is depicted in Figure 2.11c and d, where the edges of the numerical system are displayed as being of infinitely high potential energy. The resulting dispersion for the system in the anomalous phase ($\Lambda = 10$, $\hbar\omega/J_0 = 15$) is depicted in Figure 2.11e, where the potential height is $V_0 = 3.75\hbar\omega$, such that we can expect an edge mode to form on the edge introduced in the center as V_0 significantly exceeds all energy scales of the system. The dispersion includes the bulk of the system at $V = 0$ and the copy shifted by $V = V_0$ and folded in the Floquet Brillouin zone exhibiting edge modes on the numerical edges and the edge introduced in the center. To focus only on the part of the system at potential energy $V = 0$ we define a region of interest $\mathcal{S}$, illustrated by the gray shaded region in Figure 2.11b and d. The projection $\mathcal{P}(\mu, \mathcal{S})$ of each eigenstate $|\psi_\mu\rangle$ can be calculated according to

$$\mathcal{P}(\mu, \mathcal{S}) = \sum_{\text{site } j} \mathbf{1}_{\mathcal{S}}(j) \langle j|\psi_\mu\rangle, \tag{2.101}$$

where $\mathbf{1}_{\mathcal{S}}(j) = 1$ if site j belongs to the region $\mathcal{S}$ and 0 otherwise. We plot each point of the spectrum with its overlap encoded in the color where darker colors indicate a larger overlap. The dispersion depicted in Figure 2.11f shows that the bands corresponding to the high part of the potential energy are removed together with the edge mode on the left numerical edge. Only the anomalous edge mode in the 0 and π-gap of the spectrum located in the center of the system is still present. For clarity points with an overlap smaller than 10% are not displayed.

From the resulting solutions of the Floquet-Hamiltonian we can immediately plot the resulting eigenstates on the lattice. When plotting a wave function extending over several unit cells, the wave function in the adjacent unit cell is displayed with an additional a phase shift $k_y L$ corresponding to their quasimomentum.
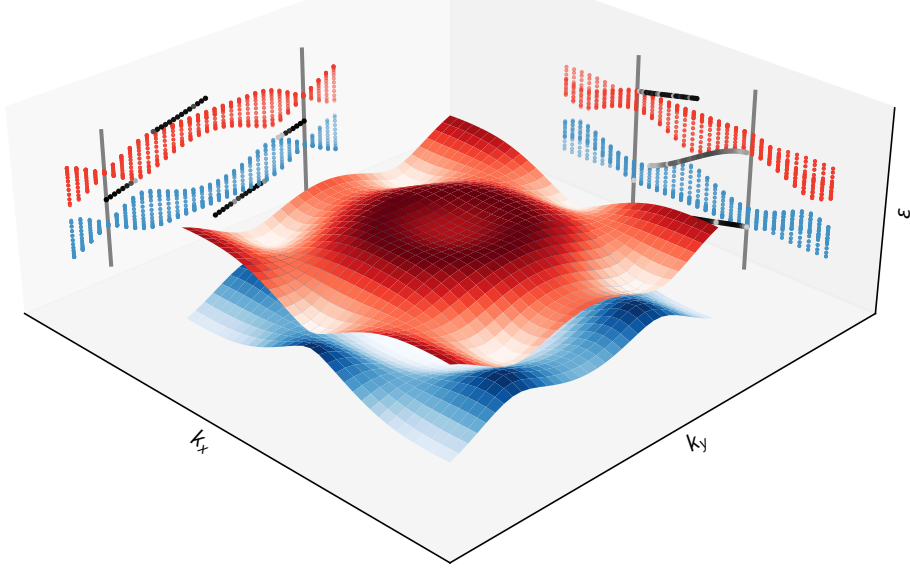
Figure 2.12 | Two-dimensional band structure as a function of k_x, k_y and projections along k_x and k_y. Dispersion of a two-dimensional modulated honeycomb lattice with $\Lambda = 4$ and $\hbar\omega/J_0 = 9$, i.e., in the anomalous regime. Integrating the dispersion along k_x or k_y results in the dispersion shown by the light blue and red points in the vertical projections. The dispersion of a strip (armchair termination right, zigzag termination left), plotted with weight obtained by projecting the state onto a region up to $4a$ from the edge to only show the edge mode dispersion, is also shown in the projections in varying shade of black. The vertical gray bars represent the maximum quasimomentum in the direction of the strip. The unit cell for a strip with armchair termination (right projection) is longer than the unit cell for an zigzag edge terminated strip(left projection), therefore the size of the Brillouin zone is smaller in the armchair case. The shape of the dispersion for the semi-infinite strip can therefore be understood as the resulting dispersion of a two dimensional system integrated along the finite direction. Note that this mapping is not fully justified and serves mainly as illustration, given that there are only a fixed number of modes in the finite direction of the strip and there is no continuum. However it suffices to explain e.g. the location of the K and K' points in the strip dispersion.

The dispersion of the resulting semi-infinite strip depends on the geometry of the system. The location of the Dirac cones in the Brillouin zone as well as the shape of the dispersion varies with the edge termination, as shown e.g. in Figure 2.4 for different terminations of the lattice in the Haldane model. One striking difference is the location of the K and K' points in the Brillouin zone of the strip for an armchair terminated compared to a zigzag terminated system. The size of the Brillouin zone in the infinite direction is limited to a maximum quasimomentum $k_{\max} = \pm\pi/L$, where L is the length of the unit cell in the periodic direction. The envelope of the dispersion can be intuitively understood by considering the projection of the quasimomenta along the finite direction as shown in Figure 2.12. The dispersion of a periodic system in the anomalous phase with $\Lambda = 4$ and $\hbar\omega/J_0 = 9$ is displayed along with the projected band structure of the upper and lower band along k_y (right) and k_x (left). On top of the integrated dispersion we show the dispersion obtained on a semi infinite strip in black. The dispersion of the semi infinite strip is displayed with $\mathcal{S}$ being located close to the edge ($\ell = 0.05$) to only highlight the edge mode and not show the bulk states. Taking a zigzag edge terminated strip, with the

infinite direction being the y-direction, we obtain a dispersion equivalent to the one of the infinite system projected along k_x, with the differing size of the Brillouin zone indicated by the vertical gray bars, and the presence of edge modes.

An armchair terminated system would result from the infinite lattice when applying a potential edge parallel to the y-direction with k_x remaining a good quantum number. In this case we obtain the dispersion with the envelope originating from the dispersion of the infinite system along k_y, as shown in the left panel of Figure 2.12. One main difference arising from the different orientation of the strips is the location of K and K', which are centered and overlapping with Γ in the Brillouin zone of the armchair geometry, compared to the zigzag geometry.

Experimental Setup

The experiments presented here rely on coherent ultracold matter waves in optical lattices. In order to obtain a coherent matter wave in an optical lattice we prepare a Bose–Einstein condensate (BEC) of ^{39}K and slowly ramp up the optical lattice in order to adiabatically transfer the cloud to the lowest band. The necessary experimental steps and tools used in the experiment will be outlined below. The overview will mainly focus on the newly introduced components of the setup such as the tweezer trap, and the programmable potentials enabled by the digital micromirror device (DMD), and only briefly summarize the essential steps to achieve a BEC. The experimental setup is described in greater detail in [179, 180] and more recent changes are covered in [174, 181, 182].

3.1 Laser Cooling and magnetic transport

3.1.1 Laser cooling

The experiment starts by loading a double-species 2D magneto-optical trap (MOT) of ^{87}Rb and ^{39}K from the background pressure in the 2D MOT. Atoms are cooled by two orthogonal pairs of counter-propagating, circularly polarized, red-detuned laser beams in two directions, while the combination with a transverse magnetic quadrupole field results in a transverse trapping [183, 184]. In the longitudinal direction a resonant beam pushes the rubidium atoms towards the 3D MOT chamber, the potassium atoms are cooled with an axial cooling beam that is reflected off a spatial filter in the differential pumping section between 2D and 3D MOT chambers [183, 185]. From these cold beams we load a 3D MOT [186, 187] in 2.5 s for rubidium and ≈ 0.2 s for potassium, the duration of the potassium MOT is adjusted on a weekly basis to optimize the final atom number and temperature of the BEC. The 3D MOT consists of three orthogonal pairs of counter-propagating, circularly polarized, red-detuned laser beams and a magnetic quadrupole field trapping the cloud in all spatial dimensions.

3.1.2 Magnetic transport and evaporation

Once the MOT-loading is finished, the cloud consisting of rubidium and potassium is simultaneously compressed by increasing the magnetic gradient [188], and we subsequently perform an optical molasses [186, 189] to cool the compressed cloud to sub-Doppler

temperatures. The cloud ends up in a mixture of spin states. To be able to transport all atoms in a magnetic trap we optically pump all atoms into the magnetically trappable $|F = 2, m_F = 2\rangle$ state. The first step of the magnetic transport is to load the cloud into a magnetic quadrupole trap, which is just strong enough to trap all potassium atoms but only rubidium atoms in $m_F = 2$, all other spin states are lost due to gravity or are magnetically anti-trapped. This trap is then compressed by increasing the current and the cloud is afterwards transported by a set of consecutive overlapping coils to the science chamber [190]. The transport between MOT and science chamber is guided through a differential pumping tube in order to achieve a lower background pressure in the science chamber. The last coil of the transport is also used to create a strong magnetic quadrupole field after the transport. We trap the cloud in this strong quadrupole field and apply a repulsive laser beam at 760 nm to the center of this magnetic quadrupole trap to prevent spin flip losses [191, 192].

While the atoms are held in the optically plugged quadrupole trap [193] for ≈ 10 s we apply a microwave field to evaporate the most energetic rubidium atoms by sweeping the microwave frequency [194, 195], while the remaining rubidium cloud sympathetically cools the potassium atoms which are unaffected by the microwave field [196–198]. The microwave field drives the transition from the trapped $|F = 2, m_F = 2\rangle$ to the anti trapped $|F = 1, m_F = 1\rangle$, which prevents heteronuclear spin changing collisions between Rb and K compared to a radio frequency evaporation via the $|F = 2, m_F = 1\rangle$ state [199, 200].

We ramp the optical trap up during the last 470 ms of the microwave evaporation while also reducing the confinement of the magnetic trap. We thereby transfer the cloud from the magnetic quadrupole into a far off resonant optical dipole trap [201]. To eliminate spin changing collisions [202] we transfer all atoms to their absolute ground states $|F = 1, m_F = 1\rangle$ via a microwave sweep for rubidium and a radio frequency sweep for potassium. To provide a quantization axis we apply a bias magnetic field during the last 70 ms of the magnetic quadrupole ramp down. Atoms that were not successfully transferred and remained in $|F = 2, m_F = 2\rangle$ are removed by a pulse of resonant light.

3.1.3 Feshbach Resonance

One important property of ^{39}K, which is routinely used in the experiment is the availability of several wide Feshbach resonances such as the resonance at $B_0 = 402.70(3)$ G [204–208]. There are several other narrower Feshbach resonances available to tune the scattering length for the $|F = 1, m_F = 1\rangle$ state, as well as resonances between different m_F states [204–208]. In the vicinity of a Feshbach resonance the s-wave scattering length a_s behaves as [7]

$$a_s = a_{BG} \left(1 - \frac{\Delta}{B - B_0}\right), \tag{3.1}$$

where a_{BG} is the background scattering length, Δ the width and B_0 the position of the resonance. The Feshbach resonance allows tuning the interaction strength of the ^{39}K atoms in the BEC, from strongly repulsive to non-interacting and eventually to attractive interactions without crossing the resonance. The resonance is very wide, which reduces the stability requirements on the absolute and relative magnetic field stability. The resonance
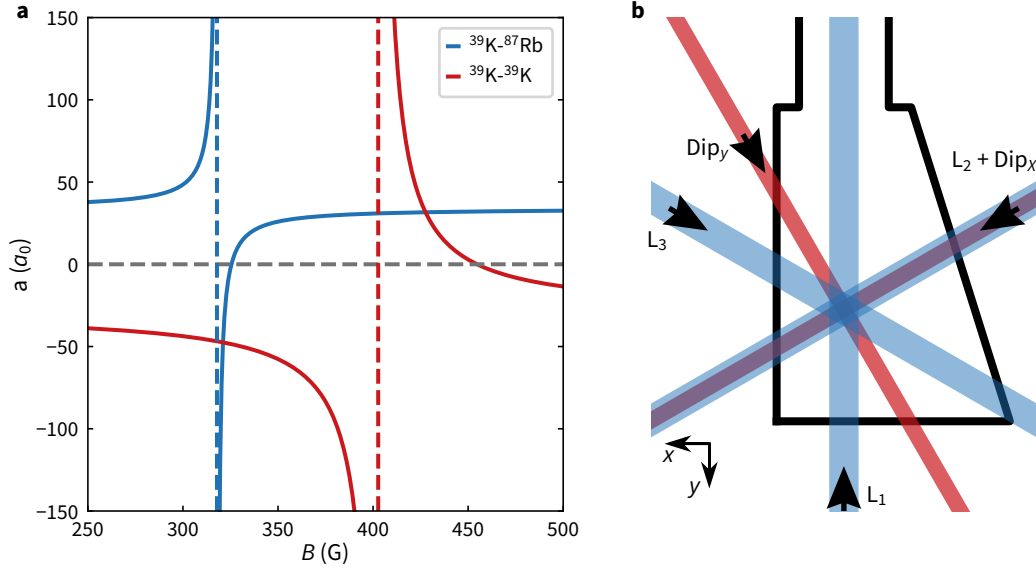
Figure 3.1 | Feshbach resonances and geometry of the crossed dipole trap and lattice. a, Scattering length in the vicinity of the Feshbach resonances. Interspecies Feshbach resonance for ^{39}K and ^{87}Rb (blue) with the position indicated by the vertical dashed line at $B_0 = 317.9(5)$ G with a width $\Delta = 7.6$ G and background scattering length $a_{BG} = 34a_0$ [196, 197, 203]. The intraspecies Feshbach resonance (blue) for ^{39}K with both atoms in $|F = 1, m_F = 1\rangle$ is located at $B_o = 402.70(3)$ G with a background scattering length of $a_{BG} = -29.0(3)a_0$ and a width of $\Delta = -52$ G [204–208]. **b** Geometry of the laser beams in the science chamber. The optical dipole trap is crossing under $\approx 90°$. One lattice beam (L$_2$) is overlapped with the x dipole beam, the other beams exhibit an angle of $120°$ with respect to the other two lattice beams. The glass cell was originally designed for a square lattice and the wedged design was chosen to avoid reflections of the lattice beams. The coordinate system of the absorption images with the directions x and y is also shown.

at $B_0 = 402.70(3)$ G exhibits $a_{BG} = -29.0(3)a_0$ and a width of $\Delta = -52$ G [204–208]. The Feshbach resonance between ^{87}Rb and ^{39}K at $B_0 = 317.9(5)$ G with a width $\Delta = 7.6$ G and background scattering length $a_{BG} = 34a_0$ is also utilized to enable faster thermalization by enhancing the scattering length during evaporation [186, 196, 197, 203]. The appearance of the Feshbach resonance relies on the presence of an molecular bound state that is energetically close to the scattering channel of two unbound atoms at large distance, the open channel. A Feshbach resonance occurs when the bound molecular state approaches the scattering state in the open channel. Even if the coupling is small, it can significantly mix the two states. The energy difference between the states can be e.g. magnetically tuned if the corresponding magnetic moments differ [7]. The Feshbach resonances utilized in the experiment are displayed in Figure 3.1a.

We currently use the Feshbach resonance to tune the scattering length of ^{39}K to $6a_0$ in the honeycomb lattice to probe the dynamics while reducing the heating. Tuning the scattering length also enables probing of different excitation processes during the modulation [209, 210]. Tuning the chemical potential in the BEC can also be beneficial when probing corrugations in the generated potential, as we can adjust the energy scale of

the particles compared to the potential independently. In the future we hope to be able to control the heating and e.g. probe the interacting Haldane model [211–213].

3.2 Optical Trap

3.2.1 Crossed optical dipole trap

The red-detuned crossed optical dipole trap at $\lambda = 1064\,\text{nm}$ crosses under an angle of $\approx 90\,°$ and captures the atoms in the maximum of intensity. The resulting potential is related to the local intensity via [201]

$$V_{\text{dip}}(\mathbf{r}, t) = \frac{\pi c^2}{2} \left(\frac{\Gamma_{D2}}{\omega_{D2}^3} \frac{2 + g_F m_F \mathcal{P}}{\Delta_{D2}} + \frac{\Gamma_{D1}}{\omega_{D1}^3} \frac{1 - g_F m_F \mathcal{P}}{\Delta_{D1}} \right) I(\mathbf{r}, t), \tag{3.2}$$

where c is the speed of light, $\Gamma_{D_1(D_2)}$ the natural linewidth and $\omega_{D_1(D_2)}$ the frequency of the $D_1(D_2)$ line, g_F the Landé factor, m_F the magnetic quantum number of the state, $\mathcal{P}$ characterizes the polarization of the light ($\mathcal{P} = 0, \pm 1$) for linearly and circularly $\sigma^\pm$ polarized light, and $\Delta_{D1(D2)}$ the detuning from resonance. The detuning is determined by

$$\frac{1}{\Delta_{D_1(D_2)}} = \frac{1}{\omega_L - \omega_{D_1(D_2)}} + \frac{1}{\omega_L + \omega_{D_1(D_2)}}, \tag{3.3}$$

where $\omega_L = 2\pi\lambda/c$ is the angular frequency of the trapping light, depending on the wavelength λ, the potential can be either repulsive or attractive. As the trap is red-detuned the optical trapping potential is attractive. The beams of the optical dipole trap in the setup are elliptical with an aspect ration of $\approx 1 : 10$, to create very oblate samples providing a suitable starting point to prepare truly two-dimensional samples in the future. The setup for one of the two crossed beams had to be rebuilt in a more compact way to free up space for the tweezer trap, speckle and DMD setup. The new setup shall be quickly summarized here. We derive the linearly polarized light from a polarization maintaining large mode area photonic crystal fiber[1] which is collimated by a 30 mm UVFS triplet collimator[2]. To filter the polarization we use a thin film polarizer[3]. Afterwards the beam is shaped by a cylindrical $3 : 1$ telescope in the horizontal direction and one $1 : 3$ telescope in the vertical direction[4]. A 400 mm lens then focuses the beam, we overlap it with one of the optical lattice beams on a dichroic mirror[5] and steer both beams into the science chamber. The focused beams of the crossed dipole trap exhibit waists of $\approx 30\,\mu\text{m} \times 300\,\mu\text{m}$ with the smaller waist in vertical direction. Size inequalities between the two beams are compensated by adjusting the power balance between them to initially achieve the deepest possible trap and eventually a trap providing isotropic trapping in the horizontal plane. The orientation of the cell geometry and laser beams is shown in Figure 3.1b.

---

[1] NKT Photonics LMA-PM-15
[2] Optosigma HFTLSQ-20-30PF1
[3] Optoman Brewster TFP (PAN1184)
[4] Edmund optics #37-607, Thorlabs LC4210-B, Edmund optics #37-607
[5] Optoman dichroic mirror (PAN1730)

The loading of the optical dipole trap from the magnetic trap is followed by a 1 s hold time at the maximum power, where the scattering length between ^{39}K and ^{87}Rb is tuned via the Feshbach resonance at $317.9(5)\,\mathrm{G}$ to $\approx 263a_0$ [196, 197, 203]. The magnetic field is derived from the same coils as the magnetic quadrupole field. By inverting the current in one of the coils the magnetic field is homogeneous and pointing in vertical direction out of the plane of the crossing optical dipole trap. We subsequently force the evaporation by exponentially ramping down the intensity of the optical dipole trap. Once the trap mainly supports only ^{39}K due to the smaller gravitational sag compared to ^{87}Rb, we change the magnetic field strength to the Feshbach resonance for ^{39}K. The Feshbach resonance at $402.70(3)\,\mathrm{G}$ [204–208] is used to tune the scattering length to of ^{39}K to $\approx 140a_0$. During a final slow evaporation ramp the scattering length is tuned to $\approx 44a_0$. We achieve an almost pure BEC of $\approx 2 \times 10^5$ atoms, where we can freely choose the scattering length with the Feshbach resonance. This presents the starting point for the actual experiment.

3.2.2 Optical Tweezer Trap

To control the spatial extent and the position of the cloud in the lattice in a very controlled manner, we implement an optical tweezer [42, 214–217]. The optical tweezer is a dipole trap at $1064\,\mathrm{nm}$, where the position is controlled by an acousto-optical deflector (AOD)[6]. The AOD diffracts an incoming collimated laser beam at an angle depending on the radio frequency driving it. This angular deviation is then mapped to a position by using a lens, whose focus coincides with the AOD position. A relay telescope shapes the beam to have the desired waist before the high resolution objective to achieve a tight focus in the atomic plane. The setup used is schematically depicted in Figure 3.2 along with other beams that are guided through the objective, which is further detailed in Section 3.4.

To be able to transfer atoms from the optical dipole trap into the tweezer and releasing a localized cloud from the tweezer to the lattice requires precise alignment of the respective foci to one another. For the experiments preparing edge modes, the atomic cloud is initially prepared in the tweezer trap but we eventually release it from this tweezer into the combined potential of the optical dipole trap and lattice. To prevent center of mass excitations in the vertical direction of the crossed dipole trap very fine alignment is necessary. To optimize the vertical overlap between the focus of the tweezer and the focus of the crossed dipole trap we scan the position of the objective in vertical direction with a stepper motor and track the evolution of the cloud after release from the tweezer for every position of the objective. If the alignment is correct and the two foci coincide, we observe no dynamics in the vertical direction. However even small displacements on the order of $1\,\mu$m lead to center of mass oscillations in the optical dipole trap. To characterize the relative displacement and optimize the overlap we load the atoms into the tweezer trap which is e.g. focused slightly below the crossed dipole trap as illustrated in Figure 3.3a. As the vertical trapping frequency of the small tweezer is not negligible compared to the crossed dipole trap, the combined minimum of the potential is slightly below the center of the crossed dipole trap and the cloud will start to move towards the focus of the dipole trap once the tweezer is switched off. The

---

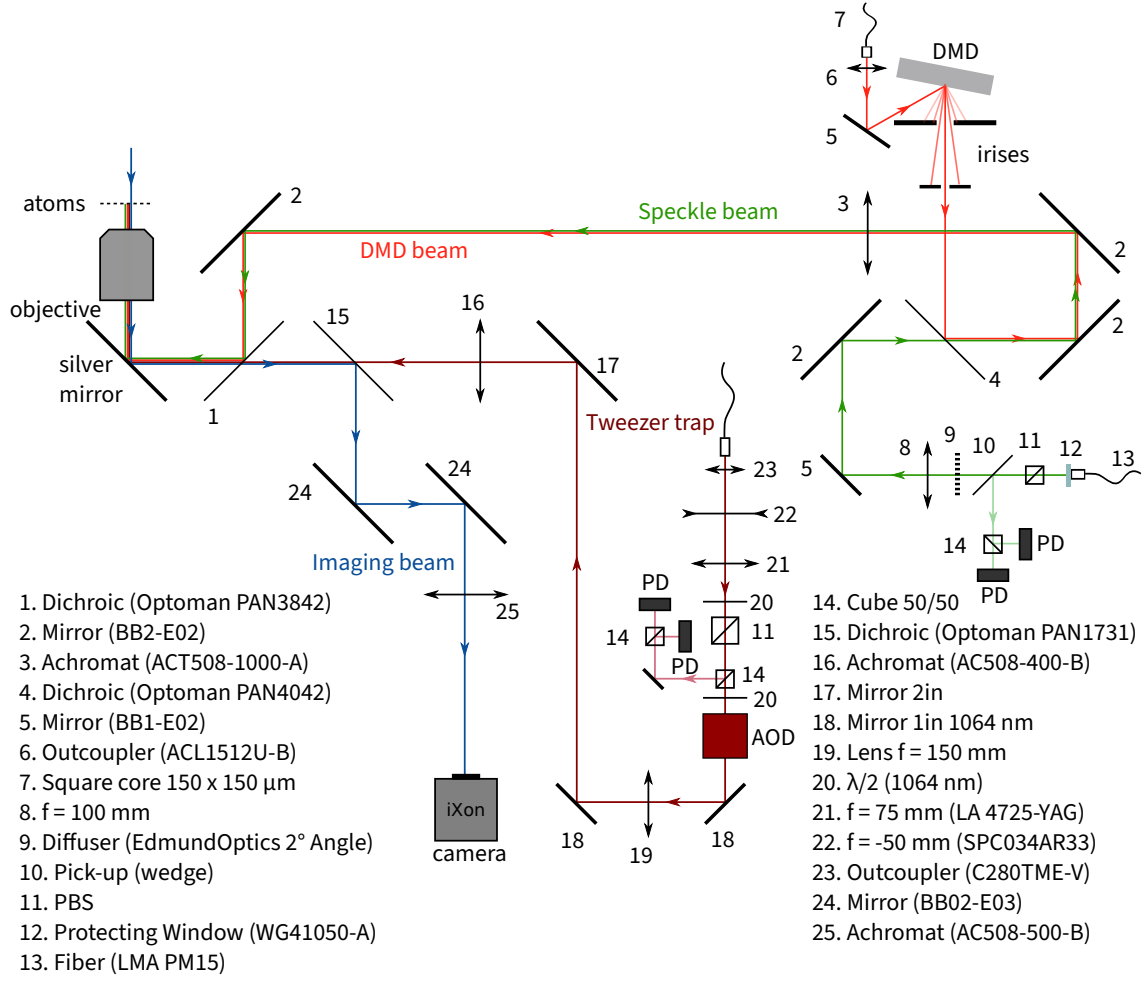[6]AA Optoelectronic DTSXY-400-1064

Figure 3.2 | Optical setup below the high resolution objective. Four different setups are guided through the objective. The imaging (blue), the DMD (red), the speckle setup (green) and the tweezer trap (dark red). The imaging beam is propagating through the cloud first, and then through the objective, propagating in opposite direction of the other beams. The different beams are separated or overlapped on several dichroic mirrors (components no. 1, 15, 4). The tweezer position in the plane of the atomic cloud can be tuned via an acousto-optical deflector. The DMD enables the projection of arbitrary potentials. The speckle beam enables the creation of random disorder potentials on the lattice.

excited cloud then continues to oscillate in the crossed dipole trap for a time t_{hold} until we release it completely and image it with a camera transversal to the optical axis of the objective after a $t_{\mathrm{tof}} = 7\,\mathrm{ms}$ time of flight. The spatial resolution along the transverse axis of the objective is not sufficient to observe the oscillation in situ. We therefore image the cloud after time of flight, where we map the velocity of the cloud to a position since

$$\omega_z \times t_{\mathrm{tof}} \gg 1, \tag{3.4}$$

where $\omega_z/(2\pi) = 330(30)\,\mathrm{Hz}$ is the vertical trap frequency of the crossed optical dipole trap. The longer time of flight magnifies the resulting oscillations significantly compared to the in situ oscillation. After performing this measurement for several t_{hold} we observe
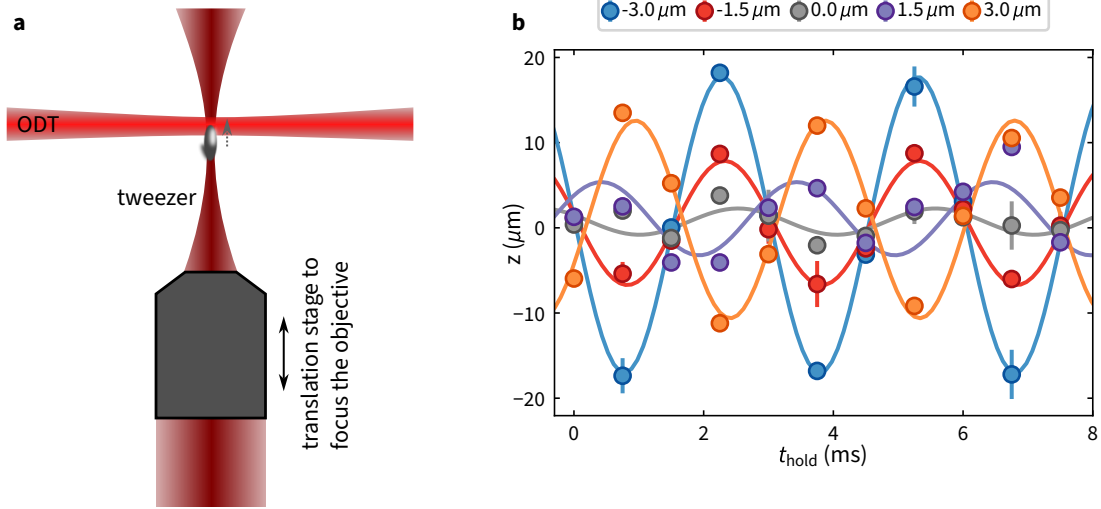
Figure 3.3 | Schematic of the focusing procedure to overlap the focus of the tweezer trap and the crossed dipole trap and experimental verification. a Schematic of the arrangement used to focus the tweezer. The focus of the tweezer is controlled by vertically moving the objective, which also shifts the location of the focus. In the case depicted here, the focus is below the crossed dipole trap (ODT) leading to a cloud that is initially trapped slightly below the center of the dipole trap. Upon release from the tweezer the cloud is dragged upwards as indicated by the dashed gray arrow and subsequently oscillates in the crossed dipole trap. The position of the objective is remote controlled via a closed loop stepper motor. **b** Representative measurement used to focus the tweezer. For several vertical positions of the objective indicated by the different colors of the data points, we observe the vertical position z after time of flight for several hold durations t_{hold}. The oscillations reverse their initial phase upon crossing the focus. The solid lines are a fit to the data with a damped sinusoidal function. The error bars correspond to the standard error of the mean.

an oscillation with an amplitude and initial phase depending on the relative alignment of the two foci. By adjusting the position of the infinity corrected objective we can move the focus of the tweezer to match the optical dipole trap. From the resulting amplitude and phase of the oscillation we can deduce the focus mismatch. Figure 3.3b shows an exemplary measurement where we vary the position of the objective in order to focus the tweezer trap on the crossed dipole trap. Depending on the relative distance we observe an oscillation with different initial phase clearly indicating an initial up- or downwards motion of the cloud.

The position of the focus needs to also match with the imaging of the cloud and the DMD potential (cf. Section 3.2.3). The initial position of the objective compared to the optical dipole trap was referenced by the imaging (cf. Section 3.4), we subsequently adjusted the tweezer trap with the aforementioned method but used the $f = 150\,\text{mm}$ lens (16 in Figure 3.2) to focus the tweezer trap. Knowing that the tweezer and imaging are both on focus, future alignment was done by collectively focussing all beams transmitted through the objective by translating the objective itself.

The estimated waist of the tweezer in the atomic plane is $\approx 1\,\mu\text{m}$. As we are not interested in the exact size of the beam but rather the trapping potential it creates, we characterize the trapping potential by exciting the cloud trapped in the tweezer and fit
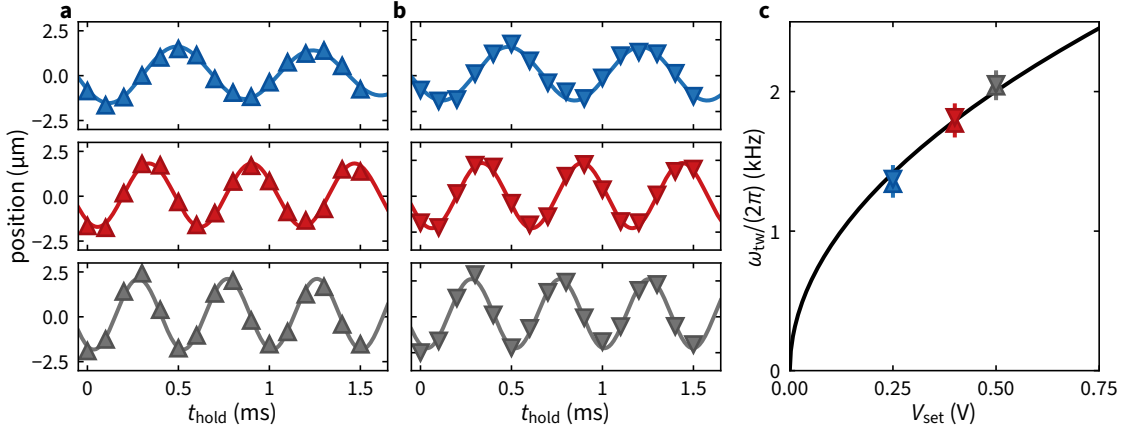
Figure 3.4 | Trap frequency calibration of the tweezer trap. We excite the tweezer in *x*- and *y*-direction and study the evolution of the velocity after an expansion in the dipole trap for various hold times after the excitation. **a,** Oscillation in *x*-direction for three settings of the control voltage which is proportional to the intensity, 0.25 V (blue), 0.4 V (red), 0.5 V (gray). The panels show the oscillation together with the resulting sinusoidal fit. **b** Oscillation in *y*-direction for the same settings as **a**. **c** Resulting oscillation frequency ω_tw as a function of the control voltage V_set together with a fit $\omega_\text{tw} = \alpha/(2\pi)\sqrt{V_\text{set}}$. We find $\alpha = 2.8(1)\,\text{kHz}/\sqrt{V}$ from fitting the *x* and *y* data simultaneously. The up facing triangles are the *x*, the down facing triangles the *y* data points. Error bars represent standard error of the mean and the respective fit errors. The data points are an average of up to 3 realizations.

its oscillation frequency. To excite the cloud we displace the optical tweezer in $215\,\mu\text{s}$ by $\approx 480\,\text{nm}$ in *x*- and *y*-direction, this creates a center of mass excitation in the cloud. After displacing the tweezer we hold the cloud in the trap for a variable amount of time t_hold then abruptly switch off the tweezer and let the cloud expand in the dipole trap for $0.5\,\text{ms}$ and subsequently take an absorption image. By the expansion in the dipole trap we map the momentum at the time of switching off the tweezer to a position in the dipole trap. We extract this position by fitting the resulting absorption images with a two-dimensional Gaussian and then fit a sinusoidal function to the *x*- and *y*-positions as a function of time t_hold from which we can extract the trapping frequency. This analysis assumes a harmonic approximation to the Gaussian trapping potential resulting from the tweezer. The resulting analysis is displayed in Figure 3.4, where we show the resulting oscillation in *x*- and *y*-direction together with the resulting trapping frequency. The two settings most commonly used in the experiment yield a trap frequency of $1.3(1)\,\text{kHz}$ and $2.0(1)\,\text{kHz}$. By tuning the trap frequency the spatial extent of the wave packet can be tuned to match a desired size.

The position of the trap can be dynamically controlled by changing the radio frequency input sent to the AOD. We use this functionality on the one hand to align the tweezer precisely to the center of the BEC, on the other hand we use linear sweeps of the frequency to accelerate the wave packet located in the tweezer. We prepare the wave packet at a desired (quasi-)momentum by displacing the tweezer shortly before releasing the cloud from the tweezer into the lattice or dipole trap. In most of the experiments we accelerate the wavepacket along the $y-$direction, which is antiparallel to L_1, cf. Figure 3.1, during a time δ_t, the coordinates of the tweezer are indicated by y^tw, the position of the center

of mass of the wave packet is $\langle y \rangle$. The motion of the tweezer during the linear frequency sweep is described by

$$y^{\text{tw}}(t) = y_{\text{i}}^{\text{tw}} + (y_{\text{f}}^{\text{tw}} - y_{\text{i}}^{\text{tw}})t/\delta_t. \tag{3.5}$$

To a good approximation the evolution of the wave packet follows the classical equation of motion

$$m_{\text{K}} \frac{\text{d}^2 \langle y \rangle}{\text{d}t^2} = -\nabla U(y,t), \tag{3.6}$$

where $U(y,t)$ is the optical potential of the tweezer, approximated by a parabola with trapping frequency ω_{tw}:

$$U(y,t) = \frac{m_{\text{K}} \omega_{\text{tw}}^2}{2} \left(y - y^{\text{tw}}(t)\right)^2. \tag{3.7}$$

Assuming the center of mass is initially at rest $\frac{\text{d}\langle y \rangle}{\text{d}t}(t = 0) = 0$ and the initial position of the cloud coincides with the initial tweezer position $\langle y \rangle(t = 0) = y_{\text{i}}$ we can integrate the equation of motion

$$\langle y \rangle(t) = y_{\text{i}}^{\text{tw}} + \frac{y_{\text{f}}^{\text{tw}} - y_{\text{i}}^{\text{tw}}}{\omega_{\text{tw}} \delta_t} \left[\omega_{\text{tw}} t - \sin(\omega_{\text{tw}} t)\right]. \tag{3.8}$$

At the end of the linear frequency ramp $t = \delta_t$ the final velocity of the center of mass v_y is

$$v_y(t = \delta_t) = \frac{y_{\text{f}}^{\text{tw}} - y_{\text{i}}^{\text{tw}}}{\delta_t} \left[1 - \cos(\omega_{\text{tw}} \delta_t)\right]. \tag{3.9}$$

The final velocity exhibits a ω_{tw} dependent maximum for ramp durations of $\delta_t = 2.33/\omega_{\text{tw}}$, the numerical factor arises from maximizing $x \mapsto [1 - \cos(x)]/x$, which is maximum for $x \approx 2.33$. The displacement $y_{\text{f}}^{\text{tw}} - y_{\text{i}}^{\text{tw}}$ can be chosen independently as long as the harmonic approximation is valid. We observe the breakdown of this approximation in the experiment for displacements of the tweezer that are large such that the Gaussian envelope of the tweezer trap is weaker than the harmonic approximation and we do thus not drag the cloud with the gradient we would expect. To experimentally measure the final velocity imposed by the moving tweezer we let the atoms evolve in the dipole trap after applying the linear displacement ramp and switch off all potentials except for the dipole trap. We measure the position of the center of mass of the cloud as a function of the evolution time that is varied between 0 and 1 ms. The position in the direction of the kick is linear with time, and we extract the corresponding velocity with a weighted linear fit (insets in Figure 3.5). The measured velocities range between $0\,\mu\text{m/ms}$ and $10\,\mu\text{m/ms}$, and are converted into a phase gradient via

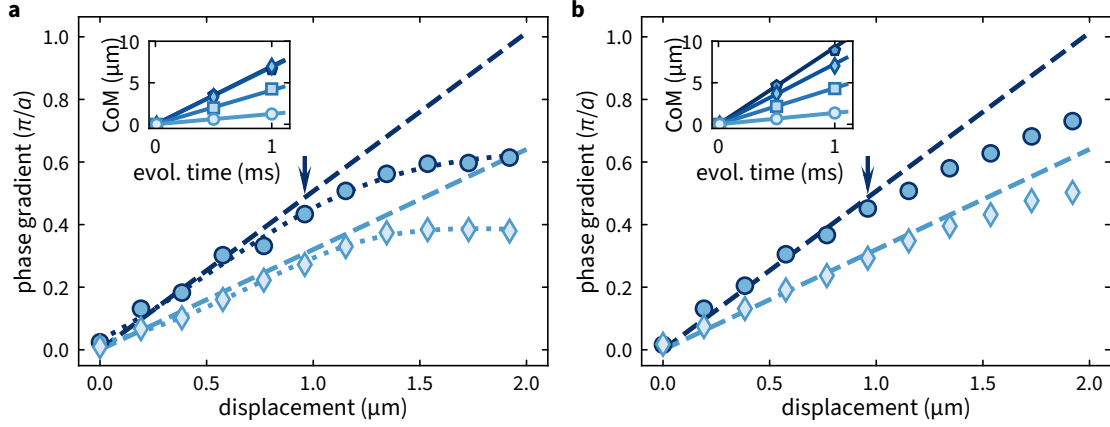$$\nabla \phi = \frac{m_{\text{K}}}{\hbar} v_y. \tag{3.10}$$

Figure 3.5 | Calibration of the applied phase gradient by displacing the tweezer. a, Phase gradient of the wave packet induced by displacing the tweezer in the lattice. The dotted lines are an interpolation of the measurements with an empirical function used in further evaluations. **b**, same as **a** but without the lattice potential while applying the kick. The velocity of the wave packet is measured as a function of the total displacement of the tweezer for two different in-plane trapping frequencies: $\omega_{\text{tw}}/(2\pi) = 1.3(1)$ kHz in light blue, and $2.0(1)$ kHz in dark blue. The dashed lines are the analytic predictions from the motion of a cloud in a harmonic potential. The inset shows the averaged measurement of center of mass (CoM) of the atoms after the kick and a variable evolution time (evol. time) in the optical dipole trap for the lowest value of ω_{tw} and displacements of $0.19\,\mu$m (circles), $0.78\,\mu$m (squares), $1.36\,\mu$m (diamonds), and $1.94\,\mu$m (pentagons). The linear weighted fits from which the velocity is extracted is shown in the inset, the associated uncertainty provides the error bar for the respective main graph which is smaller than the data points. The depicted datapoints in the insets are an average of 6 individual realizations for **a** and 16 realizations in **b**. The arrows at displacement $\approx 1\,\mu$m indicates the phase gradient that was used in measurements to populate the edge mode in the Haldane regime in Chapter 5.

Figure 3.5 shows the resulting phase gradient as a function of the displacement of the tweezer for two values of ω_{tw}. We show the resulting velocity after displacing the tweezer in the lattice in Figure 3.5a and in the dipole trap only in Figure 3.5b. In both cases we observe good agreement with the classical prediction for displacements up to $\approx 1\,\mu$m, after which the resulting velocity is reduced compared to the harmonic approximation. This displacement also matches the waist of the tweezer beam, where a deviation from the harmonic approximation can be expected. However we find that the harmonic approximation is valid in both cases, when giving the kick in the lattice or in the dipole trap, highlighting that initial state is dominated by the tweezer and the dispersion of the lattice is negligible. We find that the maximum phase gradient applied in the lattice is smaller compared to the phase gradient in the dipole trap for large displacements, yet it is still sufficient to reach the edge of the Brillouin zone.

3.2.3 Arbitrary binary potentials utilizing a DMD

Digital micromirror devices provide binary spatial control of the reflectivity by flipping microscopic mirrors into on and off positions. This offers unique control over the intensity pattern in a desired plane enabling arbitrary patterns to be realized [218] such as preparing different initial states of bulk BECs [219–221] as well as controlling the local potential on

individual lattice sites implementing boundaries, disorder or local energy shifts [222–224]. We use the DMD to create a controlled optical potential step in the lattice, inhibiting the tunneling across the boundary between the region with low and high potential. In order to create a clean potential with little corrugations and high spatial resolution, precise control of the imaging system and illuminating light source is necessary. Temporal coherent illumination with a narrowband laser source will inevitably lead to diffraction and thus unwanted corrugations of the desired potential [225, 226]. In order to reduce the resulting diffraction the optical coherence length, i.e., the distance over which a propagating light source will remain coherent and thus interfere, should be as short as possible. Assuming a Gaussian spectrum of the light source centered at λ the coherence length is inversely proportional to its emission bandwidth $\Delta\lambda$ [227]

$$l_c = \frac{2\ln(2)\lambda^2}{\pi\Delta\lambda}. \tag{3.11}$$

Fundamentally the illumination with a very wideband incoherent light source such as an LED would be ideal, but the extremely wide opening angle in combination with the large emission area renders high intensity illumination in combination with a demagnification of the DMD image impossible [228]. An alternative can be a superluminescent diode with a spectrum that can span tens of nanometers [229–231] which is subsequently amplified by one or two stages of tapered amplifiers [223, 232].

Due to the lack of superluminescent diodes around 700 nm, we have attempted to use a similar approach utilizing a laser diode with anti-reflection coated front facet[7] at $\approx 735\,\text{nm}$ to seed a two stage tapered amplifier[8] setup. We aimed at getting a potential height of $\approx h \times 10\,\text{kHz}$ in the experiment, and therefore required stable operation at $500\,\text{mW}$ after the second tapered amplifier. Unfortunately the operation of the laserdiode without feedback resulted in a very fast degradation of the output power, such that stable operation was not possible. The output spectrum of the system proved to be sufficiently wide with a $3\,\text{dB}$-bandwidth of $4\,\text{nm}$ centered at $730\,\text{nm}$ rendering this approach fundamentally viable.

In search for a more stable setup we tested the spectrum of broadband multimode laser diodes and eventually settled for a combination of four $\lambda = 638\,\text{nm}$ laser diodes[9] that are spatially multiplexed using a micro knife edging module[10]. The resulting spectrum exhibits a full width at half maximum bandwidth of $\Delta\lambda = 1\,\text{nm}$ which results in a coherence length of $l_c = 180\,\mu\text{m}$ providing temporal-incoherence and thus significantly reduced speckle contrast to $\approx 3\%$.

To deliver the beam from the light source to the experiment we use a square core multimode optical fiber[11], which additionally provides a spatially incoherent almost homogeneous square output mode. The square-core fiber maps the temporal incoherence into rapidly varying spatial incoherence thus reducing the speckle contrast due to the differential

---

[7]eagleyard Photonics EYP-RWE-0740-02000-1500-SOT02
[8]eagleyard Photonics EYP-TPA-0735-00500-3006-CMT03
[9]USHIO HL63623HD
[10]Lasertack Beam Combiner Module, fixed distance, 4 mm focal length
[11]Thorlabs FP150QMT

mode delays of the propagating modes in the fiber. The differential mode delay, i.e., the time delay between the fastest and slowest mode, can reach $\approx 100\,\text{ps/m}$ in a square core fiber [233], which corresponds to a delay per fiber length in free space of $\approx 3\,\text{cm/m}$ enabling significant reduction of the spatial coherence as the maximum delay significantly exceeds the coherence length of the light source. We additionally sweep the center frequency of the radio frequency drive to the acousto-optic modulator[12] used for stabilizing the intensity of the beam impinging on the DMD in order to change the input angle of the fiber coupling and thus additionally average different mode excitations in the fiber to further suppress speckle contrast to $\approx 3\%$, as depicted in Figure 3.7b. While the reduced temporal coherence reduces the speckle contrast it can enhance the optical resolution if the image formation happens incoherently [234], see also Section 3.4. The output beam of the square core fiber has very short range spatial coherence, i.e., in contrast to a single mode fiber the phase relation and therefore propagation direction at every point of the mode is uniform within the numerical aperture of the fiber. This effectively reduces the resolution limit, i.e., the minimal separation d between two points that the imaging system can project, to the Abbe limit or Rayleigh criterion [235, 236]

$$d = \frac{\lambda}{2\,\text{NA}}.$$

(3.12)

This however is only true if the size of the illuminated area and the NA of the fiber is matched to the objective's NA and the projected size of the potential, i.e., if the etendue is conserved. To achieve this we carefully matched the optics after the fiber to achieve a resolution as close as possible to the diffraction limit.

The optical setup behind the glass cell is depicted in Figure 3.2, this configuration was used for most of the presented measurements. The fiber tip is imaged with an aspheric condenser lens[13] onto the surface of the DMD[14] with a size of $\approx 5\,\text{mm} \times 5\,\text{mm}$. We then image the central diffraction order of the DMD image into the atomic plane using a telescope with an independently calibrated demagnification of 40.94 consisting of a $1\,\text{m}$ achromatic lens[15] and a custom objective[16] with effective focal length of $25\,\text{mm}$. This demagnification oversamples the DMD such that approximately 4 pixels on the DMD contribute to an area of one point spread function of the objective. Using this setup we image the fiber tip, which has an emission area of $\approx 150\,\mu\text{m} \times 150\,\mu\text{m}$, onto an area of $\approx 120\,\mu\text{m} \times 120\,\mu\text{m}$ matching the etendue of the fiber to the objective.

This setup is very simple and therefore comparatively easy to align. Two important requirements are the perpendicular alignment of the objective's optical axis with respect to the glass cell and minimizing the distance between optical axis and the atomic cloud. The strategy followed to achieve both is further elucidated in Section 3.4.

The objective is only achromatic for $767\,\text{nm}$ and $780\,\text{nm}$, therefore all other wavelengths require a refocusing, which in this case is achieved by laterally displacing the $1\,\text{m}$ achromatic

---

[12]Crystal Technologies AOMO 3200-125
[13]Thorlabs ACL1512U-B
[14]Vialux V-7000
[15]Thorlabs ACT508-1000-A
[16]Special Optics 54-25-25

lens to achieve a focused image in the atomic plane. To focus the DMD potential we display a checkerboard pattern on the DMD then adiabatically load the BEC into this potential and eventually take an in situ absorption image. We choose the checkerboard pattern such that there is still a significant modulation visible in the absorption images of the cloud. The resolution limit due to the incoherent illumination and wavelength is smaller than the resolution limit of the imaging [234]. For a defocused image the sharpest features are absent which becomes especially visible in the corners of adjacent cells which lead to a merging or separation of the individual cells of the checkerboard pattern if the potential is not on focus. We cannot directly quantify the achieved resolution but expect a performance that results in an edge width of $\approx 0.7\,\mu\mathrm{m}$[17].

To calibrate the height of the potential we abruptly apply an optical checker board potential for a short amount of time t_{hold} and observe the Kapitza-Dirac effect [237] after an expansion in the dipole trap for $10\,\mathrm{ms}$. We perform this measurement for several beam intensities of the beam illuminating the DMD displaying a checker board pattern with period $2d_{\mathrm{sq}}$. We image the cloud after the expansion in the dipole trap and record the population in the zeroth and first diffraction orders. The first diffraction orders appear at positions associated with the wave-vector of the potential $k_1 \propto 1/d_{\mathrm{sq}}$ which exhibit a kinetic energy of $E_{\mathrm{R}} = \hbar^2 k_1^2/(2m_{\mathrm{K}})$. In our experiments the kinetic energy does not exceed $h \times 1\,\mathrm{kHz}$. For potential heights exceeding the related recoil energy $V_0 > E_{\mathrm{R}}$ and hold durations $t_{\mathrm{hold}} \approx V_0/\hbar$ the diffraction experiments are in the Raman-Nath regime [238, 239]. The time evolution of the diffraction orders is directly related to the potential height as illustrated in the following.

The potential created by the DMD in the atomic plane is a checkerboard. We denote the potential as

$$V_{\mathrm{sq}}(x,y) = \frac{V_0}{2}\left[\mathrm{sq}\left(\frac{\sqrt{2}(x+y)}{L}\right)\mathrm{sq}\left(\frac{\sqrt{2}(x-y)}{L}\right) + 1\right], \tag{3.13}$$

where d_{sq} is the size of one square of the checkerboard, and V_0 is the height of the potential, and the function $\mathrm{sq}(x)$ is the 1-periodic function defined as

$$\mathrm{sq}(x) = \begin{cases} 1 & \text{if } 0 \le x < 1/2 \\ -1 & \text{if } 1/2 \le x < 1. \end{cases} \tag{3.14}$$

It will be useful to already note that $V(x,y)$ reaches only values 0 and V_0. We start with a BEC in the dipole trap, which we model as all the atoms being in the state of momentum $p = 0$, denoted as $|\mathbf{p} = 0\rangle$. After flashing the potential for duration t, the atoms end up in the state

$$|\psi(t)\rangle = \mathrm{e}^{\left(-i\frac{V(\hat{x},\hat{y})t}{\hbar}\right)}|\mathbf{p} = 0\rangle. \tag{3.15}$$

---

[17]Defined as the length from 8% to 92% of the height of an edge.

In the case where the potential V is a sinusoidal function in one direction, one gets the usual Kapitza-Dirac diffraction as in an optical lattice [238]. In general, we would have to decompose the evolution operator $\exp(-iVt/\hbar)$ in the momentum basis to know where the atoms at $|\boldsymbol{p} = 0\rangle$ end up, which can be tedious if the potential V is arbitrary. Here however, the potential is a checkerboard, which has the advantage of having only two values. The evolution operator can therefore be written as

$$\mathrm{e}^{-iV(\hat{x},\hat{y})t/\hbar} = \hat{1} + \left(\mathrm{e}^{iV_0t/\hbar} - 1\right) \frac{\mathrm{sq}\left(\frac{\sqrt{2}(\hat{x}+\hat{y})}{L}\right)\mathrm{sq}\left(\frac{\sqrt{2}(\hat{x}-\hat{y})}{L}\right) + \hat{1}}{2} \tag{3.16}$$

$$= \mathrm{e}^{iV_0t/(2\hbar)} \left(\cos\left(\frac{V_0t}{2\hbar}\right)\hat{1} + i\sin\left(\frac{V_0t}{2\hbar}\right) \frac{\mathrm{sq}\left(\frac{\sqrt{2}(\hat{x}+\hat{y})}{L}\right)\mathrm{sq}\left(\frac{\sqrt{2}(\hat{x}-\hat{y})}{L}\right)}{2}\right) \tag{3.17}$$

We can now write the spatial function that appears on the right of the expression as an inverse Fourier transform:

$$\frac{\mathrm{sq}\left(\frac{\sqrt{2}(\hat{x}+\hat{y})}{L}\right)\mathrm{sq}\left(\frac{\sqrt{2}(\hat{x}-\hat{y})}{L}\right)}{2} = \sum_{\{p_x,p_y\}} \tilde{S}(p_x, p_y)\exp\left(-ip_x\hat{x} - ip_y\hat{y}\right), \tag{3.18}$$

where $\tilde{S}$ is the Fourier transform of the function on the left. As a result, the state that we obtain is:

$$|\psi(t)\rangle = \mathrm{e}^{iV_0t/(2\hbar)}\cos\left(\frac{V_0t}{2\hbar}\right)|\boldsymbol{p} = 0\rangle + \sum_{\{p_x,p_y\}} i\mathrm{e}^{iV_0t/2\hbar}\sin\left(\frac{V_0t}{2\hbar}\right)\tilde{S}(p_x, p_y)|p_x, p_y\rangle. \tag{3.19}$$

The relative population $\mathcal{P}_0$ in the order 0 of the diffraction pattern is therefore

$$\mathcal{P}_0 = \cos^2\left(\frac{V_0t}{2\hbar}\right), \tag{3.20}$$

and the relative population $\mathcal{P}_{p_x,p_y}$ in any higher order of the pattern (i.e., any (p_x, p_y) that appears in the spectrum of the spatial pattern) is

$$\mathcal{P}_{p_x,p_y} = \sin^2\left(\frac{V_0t}{2\hbar}\right)|\tilde{S}(p_x, p_y)|^2. \tag{3.21}$$

We show an exemplary image of the diffraction orders after expansion in the dipole trap in Figure 3.6a. The resulting sinusoidal oscillation is shown in Figure 3.6b, we additionally allow the fit function to have an offset to account for imperfect background subtraction or diffraction into higher orders, which we do not count separately. The resulting slope of the potential is extracted by fitting the potential depths for three values of d_{sq} and we find $11.12(3)\,\mathrm{kHz/V}$.

The setup described above and depicted in Figure 3.2 has one major drawback - it is not easily possible to reduce the resolution, i.e., making the image more blurry, without affecting at the same time the resolution of the imaging and the size and depth of the small tweezer trap. This lies in the fact that the Fourier plane of the DMD is located
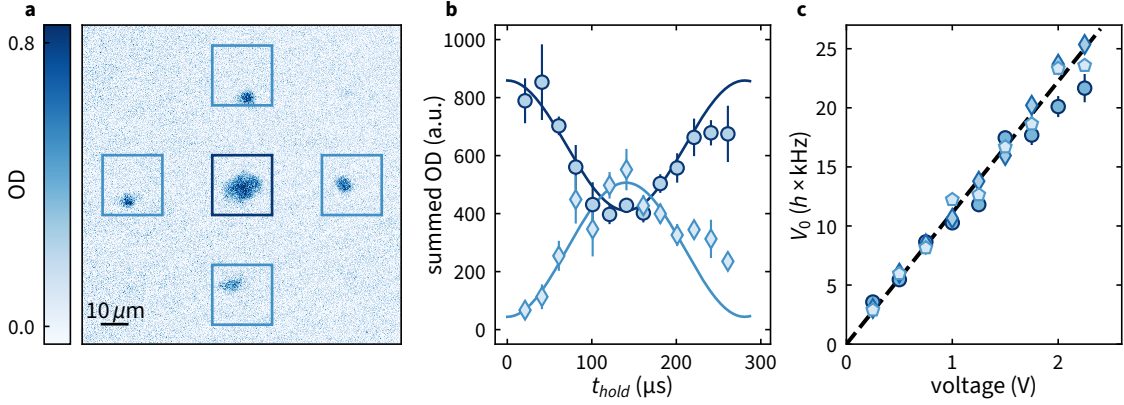
Figure 3.6 │ **Calibration of the DMD potential height. a**, Exemplary absorption image after diffraction from the checkerboard potential projected with the DMD with $d_{sq} = 1\,\text{mm}$ after an expansion of 10 ms. The light blue highlighted regions are summed up and constitute the first order diffraction orders, the dark blue highlighted region is the zeroth order. **b**, Measurement of the summed optical density in the regions corresponding to the zeroth (circles) and the first (diamonds) diffraction orders. The error bars correspond to the standard deviation of the population in the respective order for images taken with the same parameters. The solid lines show the sinusoidal fits from which the frequency is extracted. **c**, Height of the repulsive potential evaluated using sinusodial fits as shown in **b** as a function of the voltage used to control the laser intensity for three values of d_{sq}: 1.0 mm (circles), 1.3 mm (diamonds) and 1.7 mm (pentagons). The error bars correspond to the uncertainty of the fit, and the dashed black line is a weighted linear fit of all the measured points, which has a slope of 11.12(3) kHz/V.

very close to the objective, which is the plane where we would need to crop the Fourier components of the projected pattern. Cropping Fourier components there would also affect the imaging and the tweezer trap. If we crop the DMD beam in a different location, it mainly reduces the intensity without reducing the imaging resolution too much also leading to vignetting. To overcome this shortcoming we modify this setup and introduce an additional Fourier plane so we crop Fourier components of the DMD potential while leaving the other beam paths unaffected.

To implement a setup with an additional Fourier plane we image the DMD onto an intermediate plane p_1 with a $4f$-setup, cf. Figure 3.7a, consisting of an $f_1 = 150\,\text{mm}$ achromatic lens[18] and a $f_2 = 100\,\text{mm}$ singlet lens[19]. In between the two lenses we have placed an automated iris[20] to crop selectively the highest frequency components of the image down to a given radius. To verify the size of the iris opening we image the iris after each shot showing excellent repeatability of the iris opening d with a standard deviation of $15\,\mu\text{m}$ of the set diameter.

In the intermediate plane p_1 the resulting image can be observed with a removable camera[21]. We show two exemplary images for an iris with opening slightly smaller than the corresponding size of the objective's Fourier plane (Figure 3.7b) and maximally closed

---

[18]Thorlabs AC254-150-AB-ML
[19]Thorlabs LA1509-A
[20]Thorlabs ELL14 and SM1D12
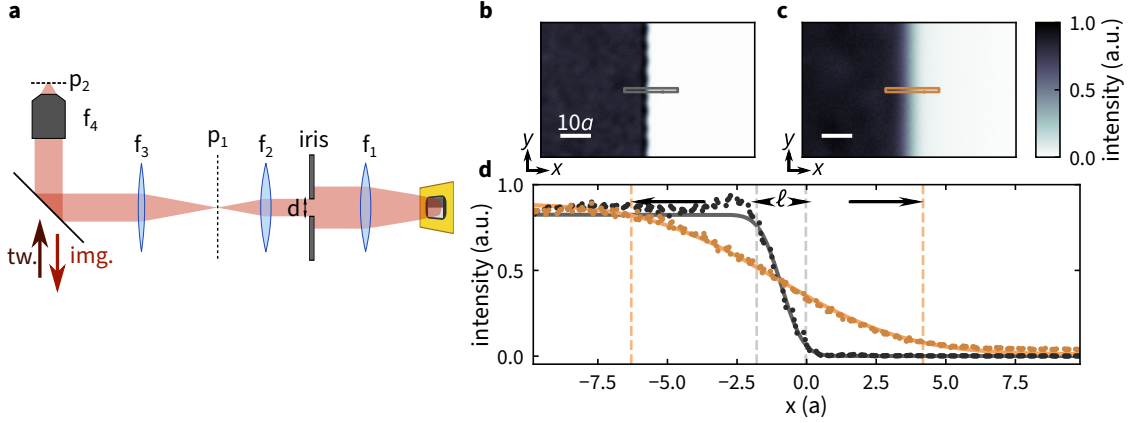[21]Allied Vision 1800 U-319m

Figure 3.7 | Setup and resulting width of an edge for the setup with tunable resolution. a, The DMD is imaged on the atomic plane (p_2). An iris of variable diameter d is added in the Fourier plane to vary the width of the potential step. The DMD light at 638 nm is overlapped with the tweezer beam (tw.) at 1064 nm with a dichroic plate and focused with a microscope objective. The imaging beam (img.) at 767 nm is propagating in the opposite direction and passing through the dichroic plate to reach the camera (not shown). **b,** Optical potential in the intermediate plane (p_1) generated with the DMD and recorded with a camera. The diameter of the iris, and thus the Fourier plane, is slightly larger than the corresponding size of the objective. The gray rectangle indicates the area integrated for the curve shown in **d**. **c,** Same as **b**, but the diameter of the iris is closed as much as possible to a minimum diameter of $d = 0.91(1)$ mm. The brown rectangle indicates the area integrated for the curve shown in **d**. The scale bar in **b** and **c** is $10a$ in the atomic plane p_2. **d,** Resulting edge width. The edge width is extracted for a position close to the atomic cloud. We show the data of the integrated signal highlighted by the rectangles in **b** and **c** together with the corresponding fit. The iris diameter corresponds to a diameter slightly larger than the diffraction limit (**b**) and the smallest iris diameter from Figure 5.22b (**c**).

($d = 0.91(1)$ mm, Figure 3.7c) iris together with a cut of the edge in Figure 3.7d. The images are scaled by the demagnification of the final telescope consisting of a $f_3 = 750$ mm achromatic lens[22] and the objective $f_4 = 25$ mm to represent the effective size in the plane of the experiment p_2. The fits in Figure 3.7d are fits to an edge defined in Equation 2.100 and result in widths of $\ell = 1.8a$ for the larger and $\ell = 10.5a$ for the smaller iris opening. We are therefore able to smoothly tune the width of the transition from high to low potential of the DMD over almost one order of magnitude, with the limit being the final iris opening restricted by the construction of the iris. Due to the spatially incoherent illumination of the DMD with the wideband laser source described above, it is necessary to adjust the set point of the potential height due to cropping of low frequency components located off axis. The incoherent illumination results in a random transversal distribution of Fourier components. To compensate for this we adjust the set point to always maintain the same transmitted optical power through the iris for all iris openings. In contrast a coherently illuminated image results in a bright central spot in the Fourier plane, where the cropping of Fourier components does not result in a reduced maximum intensity of the image and no adjustment of the set point would be necessary.

---

[22]Thorlabs AC508-750-A

3.2.4 Random optical disorder potentials - Speckle

In addition to the aforementioned controlled binary potential we have realized a setup to create random optical potentials. Anderson localization [240], i.e., the peculiar localization of non-interacting particles in random potentials can be investigated in a very controlled way in quantum gas experiments in one- [241, 242] and three-dimensional systems [243, 244]. In the presence of strong on-site interactions the interplay with disorder enables the study of many-body localization [245–247] and if or how these systems thermalize [246]. Investigations in two-dimensional systems are challenging as the percolation threshold, i.e., trapping in trivially enclosed regions of the disorder is significantly higher than in one and three dimensions [248–251].

Nevertheless the anomalous Floquet phase poses interesting phenomena in the presence of disorder [94, 95, 252]. In contrast to usual quantum Hall systems, where extended bulk states are required for the edge modes to exist [75], the anomalous Floquet Anderson Insulator hosts chiral edge modes in the absence of extended bulk states [94]. Furthermore disorder-induced topological phases should be in reach in this experiment [94, 253–262], where e.g. in a driven, disordered photonic honeycomb lattice with a sublattice offset the system can be brought to a topologically non-trivial regime by the disorder [113]. The presented experiment is able to test similar dynamics over potentially wider parameter range and verify how e.g. the shape of the edge influences the transition to the non-trivial regime.

The idea we initially pursued with the disorder setup was to inhibit the expansion dynamics [263–267] of bulk states, while the edge modes, which are more robust to disorder, still propagate in the system [74, 75, 268, 269].

Figure 3.8 shows a simulation of the proposed experiment comparing the expansion of a wave packet close to a potential barrier in the Haldane model with and without disorder. The disorder reduces the expansion of the bulk modes, while the edge mode is still propagating. The simulation is done for a static Haldane model without disorder in Figure 3.8a and c and with disorder in Figure 3.8b and d. We simulate a zero-centered normally distributed disorder with strength $\Delta/J = 0.5$ such that every lattice site is randomly shifted in energy by the disorder. The nearest neighbor tunneling is J, the next nearest neighbor tunneling $J'/J = 0.1 \times \mathrm{e}^{\pm i\pi/2}$. The sign of the phase affects the Chern number of the bands $\mathcal{C}$. If the sign of the phase is inverted the propagation direction of the edge mode is also reversed. The initial state in the simulation is a wave packet localized to a single site next to a sharp potential barrier with a height of $V_0/J = 50$. The depicted population of the resulting wavefunction $|\Psi|^2$ is evaluated after a free evolution in the lattice for $\approx 15\tau$, where $\tau = \hbar/J$ is the tunneling time. To more easily identify the edge mode we time evolve the system with a positive phase of the complex tunneling resulting in Ψ_+ and with opposite phase resulting in Ψ_-. The lower panels of Figure 3.8 show the differential signal after subtraction $\Delta|\Psi|^2 = |\Psi_+|^2 - |\Psi_-|^2$ after the same expansion time. The wave functions in the disordered lattice are an average over 200 independent disorder realizations to reduce fluctuations due to the individual realizations. Comparing the final wave function with and without disorder we immediately see that the occupation of the fastest states in the bulk is strongly reduced in Figure 3.8b. The disordered optical lattice offers the advantage to significantly reduce
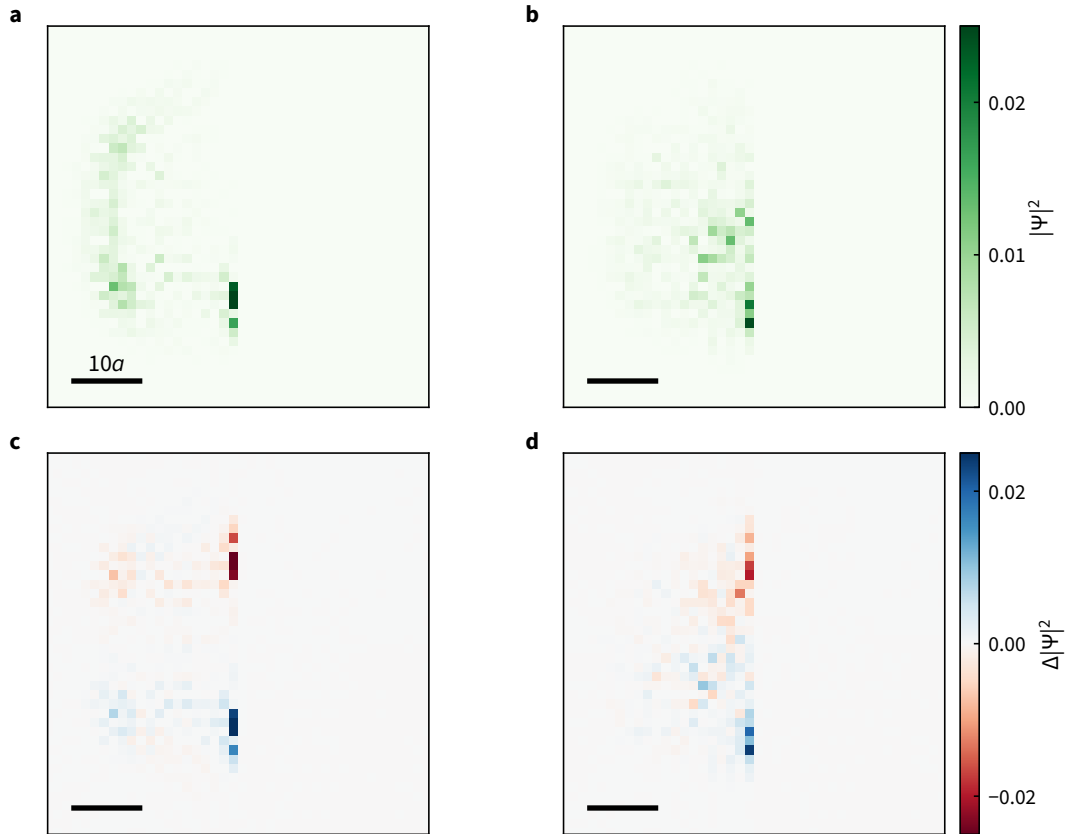
Figure 3.8 │ Simulation of the expansion dynamics in the Haldane model with and without Gaussian Disorder. We evaluate the time dynamics of a initially localized wave packet for $\approx 15\tau$ in the vicinity of a sharp edge. The simulation is done on a square of area $60a \times 60a$ with in total 2760 sites, the right half exhibits a potential $V_0/J = 50$ compared to the right half of the image. The images are rebinned in order to reflect the imaging resolution of the experiment. **a**, Evolution of the wave packet in the lattice without disorder, with the phase of the complex tunneling being positive. **b**, Evolution in the lattice with disorder of strength $\Delta/J = 0.5$. In contrast to the evolution without disorder the bulk states spread significantly less during the evolution. **c**, Difference signal after subtracting the signal with positive phase of the complex next nearest neighbor tunneling from the same evolution but with negative phase. The evolution happens in the clean lattice without disorder. **d**, Same as **c** but with disorder. The images show the average over 200 independent disorder realizations.

the occupation of states with high group velocity and therefore eases the detection of a chiral signal. This is especially relevant when the overlap with the edge mode is not as good, e.g. due to the fact that the exact location of the edge and the correct preparation protocol is unknown and disorder can help to detect a first signal.

The implementation in the experiment relies on a diode-pumped solid state laser[23] operating at $\lambda_{\mathrm{speckle}} = 532\,\mathrm{nm}$ and a holographic diffuser[24] introducing random phase shifts to the wavefront. The setup is depicted in Figure 3.2 and in more detail in Figure 3.9a. The

---

[23]Lighthouse Photonics Sprout G-15W
[24]Edmund Optics #35-693

output of the photonic crystal fiber[25] provides a mode field diameter of MFD $= 12.2\pm1.5$ nm, which translates to a divergence half angle of $\theta_0 = 1.6 \pm 2\,°$. To protect the fiber tip from potential dust we have placed an anti reflection coated window[26]in front of the fiber facet, low power residual reflections will not harm the optical performance as the wavefront is random after the diffuser. After a free propagation for adjustable distance the beam hits the fused silica holographic diffuser providing a full width at half maximum divergence angle for a collimated beam of $2\,°$. The diffuser is mounted off axis in a remote controlled rotation mount[27] to realize different random phases on the beam and therefore different disorder potentials. The divergence of the beam after the diffuser is then reduced with a $f_1 = 100$ mm focal length lens, in the focal plane p_1 of this lens we have a fully developed speckle pattern. This speckle pattern is then demagnified with a telescope consisting of an achromatic lens with $f_2 = 1000$ mm and the objective with $f_3 = 25$ mm. We positioned the diffuser such that we slightly overfill the rear focal plane of the objective, i.e., some of the power gets clipped on the objective in order to slightly enhance the power at high spatial frequencies to achieve a smaller speckle size.

The wavefront of speckle is random, therefore aberrations or lens errors do not matter, however it is still relevant to focus the speckle in order to achieve the smallest disorder correlation length and the largest intensity. The intensity-intensity auto-correlation of the speckle pattern, representing the correlation length of the disorder on the lattice in the setup, is defined as [226]

$$\langle I(\mathbf{r})I(\mathbf{r} + \Delta\mathbf{r})\rangle = \bar{I}^2(1 + |\mu(\Delta\mathbf{r})|^2), \tag{3.22}$$

where $\mathbf{r}$ and $\Delta\mathbf{r}$ are the position and the connecting vector in the focal plane, $\bar{I}$ is the mean intensity and $\mu(\Delta\mathbf{r})$ is the field-field correlator

$$\mu(\Delta\mathbf{r}) = \frac{\langle \mathbf{E}(\mathbf{r}) \cdot \mathbf{E}(\mathbf{r} + \Delta\mathbf{r})^*\rangle}{\sqrt{\langle |\mathbf{E}(\mathbf{r})|^2 \rangle \langle |\mathbf{E}(\mathbf{r} + \Delta\mathbf{r})|^2 \rangle}}. \tag{3.23}$$

Assuming illumination of a lens with a homogeneous temporally coherent beam we find that $\mu(\Delta\mathbf{r})$ in the focus of the lens solely depends on the numerical aperture NA of the lens. The assumption here is that the wavefront of the impinging field on the lens is δ-correlated as it would be the case for the light transmitted through a diffuser at sufficient distance. Assuming the lens exhibits a circular aperture we find

$$\mu(\Delta r) = 2\frac{J_1(\mathrm{NA}\,k\Delta r)}{\mathrm{NA}k\Delta r}, \tag{3.24}$$

where $k = 2\pi/\lambda_{\mathrm{speckle}}$ is the angular wave number of the light, Δr the radial distance between the two points of consideration and $J_1(x)$ the Bessel function of the first kind. We can identify a correlation length for the intensity correlations as the first zero-crossing

---

[25]NKT Photonis aeroGUIDE POWER
[26]Thorlbas WG41050-A
[27]Thorlabs ELL14K

of $\mu(\Delta r)$, i.e., the first root of $J_1(x)$ is $x_0 \approx 3.8$, after which the correlations are close to unity. Taking the values used in the experiment NA $= 0.5$ and $\lambda_{\text{speckle}} = 532\,\text{nm}$ we find a correlation length

$$r_c = \frac{x_0}{\text{NA}k} \approx 648\,\text{nm}. \tag{3.25}$$

The normalized covariance function, which in the signal processing context is usually referred to as *autocorrelation*, is related to Equation 3.22 via [226]

$$|\mu(\Delta \mathbf{r})|^2 = \frac{\langle I(\mathbf{r})I(\mathbf{r} + \Delta \mathbf{r})\rangle - \bar{I}^2}{\bar{I}^2}. \tag{3.26}$$

Unfortunately we are not able to homogeneously illuminate the rear focal plane of the objective and therefore need to take the Gaussian envelope of the beam into account. To gain some intuition on how the diffuser creates a speckle pattern, we can draw similarities between a Gaussian beam and the random phase front beam after a diffuser. A collimated Gaussian beam with waist w_0 a distance f away from the lens with focal length f will exhibit a waist $w_1 = \lambda f/(\pi w_0)$ after the lens, i.e., if the initial beam is large, the resulting beam will be small and vice versa. The two sizes are linked via the Fourier transforming property of the lens converting angles to positions and vice versa. In a similar fashion the size of the random wave front on the rear focal plane of the objective determines the size of the speckle grains, while the size of the individual phase patches directly affects the size of the envelope in the focal plane.

A linear phase gradient in the wavefront results in a displacement of the focus after the lens. The random wavefront of a beam after a diffuser, will result in random displacements after transmission through a lens. If we envision the wavefront after a diffuser to consist of many small patches with varying phase the average size of these patches will determine the size of the speckle pattern envelope, i.e., the area illuminated with the speckle.

To get an estimate of the size of the speckle grains after the diffuser we can approximate the wave front emitted from the diffuser by many small Gaussian beams with a half angle divergence of

$$\theta = \frac{\lambda}{\pi w_\phi}, \tag{3.27}$$

where the size of the phase patches for the aforementioned $\theta = 1°$ diffuser would be $w_\phi \approx 10\,\mu\text{m}$ large. After the $f_1 = 100\,\text{mm}$ lens the size of the phase patches determines the size of the envelope in the intermediate plane p_1, which should have increased by approximately $1.6\,\text{mm}$ due to the randomly introduced phase patches. The beam emerging from the fiber is diverging, therefore depending on where we position the diffuser compared to the fiber facet, we can adjust the size of the beam on the diffuser, and therefore also the envelope of the beam with random phase profile on the lens f_1, which eventually affects the size of the speckle grains in p_1. As the surface of the diffuser is imaged on the rear focal plane of the objective, which has a radius of $12.5\,\text{mm}$, we aim at a waist on the diffuser
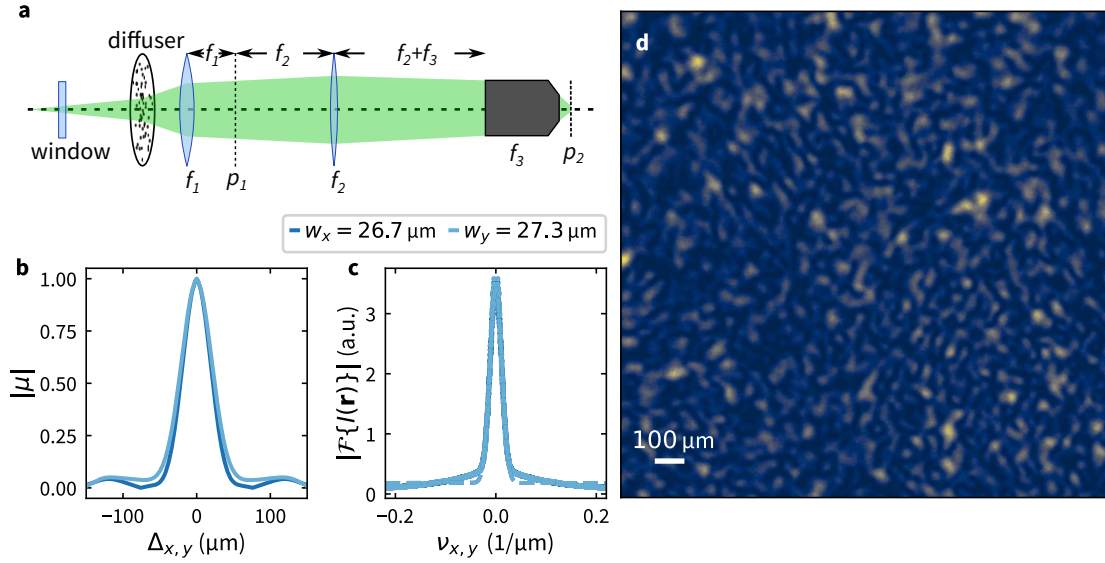
Figure 3.9 | Speckle setup and exemplary speckle pattern and its statistical properties. a, Setup to generate a speckle pattern in the focal plane of the objective. The beam is collimated after transmission through the diffuser by f_1, and the resulting speckle pattern in plane p_1 is imaged into the atomic plane p_2 by a telescope. **b,** Cut of the normalized covariance function of the speckle pattern displayed in **d** in x- (dark blue) and y-direction (light blue). **c,** Fourier transform of the speckle pattern displayed in **d**. The displayed spectra (dark blue x-, light blue y-direction) have been averaged along the orthogonal dimension in order to average the fluctuations. By fitting the Fourier transform of a Gaussian beam (dashed lines) to the spectra (points) we find a corresponding waist of $w_x = 26.7\,\mu$m and $w_y = 27.3\,\mu$m. **d,** Example of one experimental speckle realization in the rear focal plane of the objective.

of roughly 1/10 of that. As long as the beam in the rear focal plane is sufficiently large, the size of the speckle will be very close to the diffraction limit.

However we have experimentally observed that a 25 mm spherical singlet lens does not lead to speckle correlated on a length scale comparable to the diffraction limit because a significant fraction of the marginal rays exhibit too strong spherical aberrations and do not contribute to the interference pattern. We do not expect this to be the case for the actual objective as it should provide diffraction limited performance also at 532 nm. To estimate the size of the beam in the focal plane we image the speckle pattern located in the rear focal plane of the objective. An exemplary image for one realization of the speckle pattern is depicted in Figure 3.9d. We imaged the speckle pattern for various transversal positions of the diffuser but did, as expected, not find a significant variation of the speckle size, while the size of the envelope is changing. The normalized covariance function and the power spectrum for the displayed speckle pattern are presented in Figure 3.9b and d. After removing the zero frequency peak from the spectrum of the intensity $|\mathcal{F}\{I(\mathbf{r})\}|$, which corresponds to the average intensity of the speckle pattern, we can fit the power spectrum along the spatial frequencies ν_x and ν_y with the Fourier transform of a Gaussian beam and extract its effective waist. From the average waist of the speckle grains in x- and y-direction we can deduce the envelope of the speckle pattern in the focal plane of

the objective, which would be $\approx 160\,\mu$m, which is only slightly larger than the maximum size of the DMD created potential.

To numerically create a speckle pattern with the desired properties and to reproduce the experimental results we can emulate the properties of the diffuser by low-passing a random phase pattern with normally distributed probability, where the mean $\mu = 0$ and a standard deviation of $\sigma = 4\pi$. Assuming a Gaussian beam, and imprinting the random phases on this beam, one can use the Fresnel transfer function approach, an approximation of the Fresnel diffraction integral, to propagate this speckle pattern in space, such that the speckle pattern will emerge [226, 270, 271]. The Gaussian beam with random phases corresponds to the wavefront immediately after the diffuser $E(\mathbf{r}', z = 0)$, assuming N samples with a sample spacing δl, the samples in Fourier space will have coordinates k_x, k_y spaced by $1/(N\delta l)$. The beam $E(\mathbf{r}, z = 0)$ after a propagation of distance z is then given by

$$E(\mathbf{r}, z) = \mathcal{F}^{-1}\left\{\mathcal{F}\left\{E(\mathbf{r}', z = 0)\right\} e^{i\pi\lambda z(k_x^2 + k_y^2)}\right\}, \qquad (3.28)$$

where $\mathcal{F}^{(-1)}$ denotes the (inverse) Fourier transform. This approach can easily suffer from aliasing, i.e., the quadratic-phase transfer function is not sampled properly in Fourier space. To mitigate this one can zero pad the sample, or choose a sample length $N\delta l \ll w$, with w being the waist of the beam on the diffuser. The underlying approximations break down in the far field, i.e., the procedure works well for $w^2/(\lambda z) \gg 1$ [271]. The speckles resulting from the propagation will exhibit the size chosen in the low-pass filtering of the phase pattern and the envelope of the initial beam will remain unchanged, as the frequency components are not shifted but only acquire a complex phase, cf. Equation 3.28. To simulate the final speckle pattern we have implemented a second Fourier transform mimicking the role of the objective. The speckle pattern obtained with this approach reproduce the experimentally observed correlation lengths and envelopes of the beam.

3.3 Optical Lattice

The resulting trapping potential of an optical trap directly follows the spatial and temporal intensity distribution of the light field, cf. Equation 3.2. By interfering two or more laser beams defect-free periodic potentials can be created commonly referred to as optical lattices. The extraordinary degree of control and the moderate energy scales allow for observation of the system in real time, with momentum resolution and even directly observing the density distribution in the lattice [5, 6, 21].

3.3.1 Lattice Setup

In the experiment we use a titanium-sapphire laser[28] running at 745 nm to create an optical honeycomb lattice. The output of the lattice laser is split into three independent beams, where the intensity and frequency of each beam can be controlled with high bandwidth

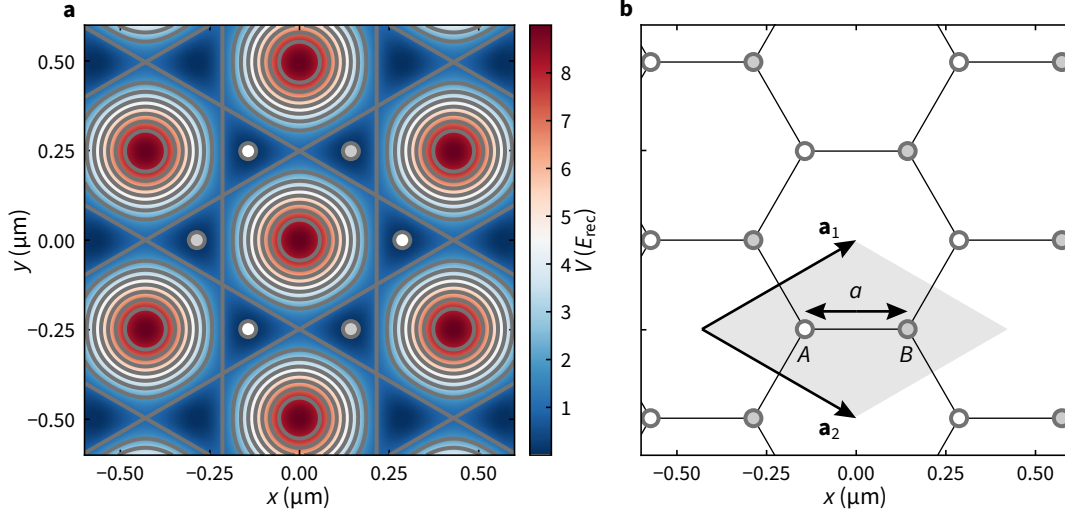---

[28]MSquared Solstis, later a Sirah Matisse CS

Figure 3.10 | **Optical lattice potential and geometry of the tight binding model. a**, Real space potential of the optical lattice. The lattice is derived from three blue detuned interfering beams under an angle of 120° with polarization out of plane. The potential is depicted for a $1E_{rec}$ deep honeycomb lattice, the centers of the plaquettes consitute a triangular lattice which is nine times stronger than the honeycomb potential. **b**, Resulting lattice sites and geometry of the lattice. The distance between an *A*- and a *B*-site is described by the lattice spacing *a* as indicated by the arrow. The unit cell indicated by the gray shaded area is spanned by the two lattice vectors $\mathbf{a}_1$ and $\mathbf{a}_2$ and contains one *A*- (white) and one *B*-site (gray).

by an acousto-optic modulator[29]. The laser beams cross at the position of the atomic cloud under angles of 120° and create an optical honeycomb lattice. Due to the wavelength at $\lambda_L = 745\,\text{nm}$, i.e., the beams are blue-detuned compared to the D1 and D2 lines in ^{39}K at $770\,\text{nm}$ and $767\,\text{nm}$, the generated optical potential is repulsive. The three beams propagate in plane along the directions

$$\mathbf{k}_1 = k_L \begin{pmatrix} 0 \\ 1 \\ 0 \end{pmatrix} \qquad \mathbf{k}_2 = k_L \begin{pmatrix} -\sqrt{3}/2 \\ -1/2 \\ 0 \end{pmatrix} \qquad \mathbf{k}_3 = k_L \begin{pmatrix} \sqrt{3}/2 \\ -1/2 \\ 0 \end{pmatrix}, \qquad (3.29)$$

with $k_L = 2\pi/\lambda_L$. The waist of the beams is $w_{0,h} \approx 400\,\mu\text{m}$ for the horizontal in plane waist and out of plane, in vertical direction $w_{0,v} \approx 100\,\mu\text{m}$. Astigmatic Gaussian beams, neglecting the time dependence, can be described by

$$\mathbf{E}(\mathbf{r}, \mathbf{k}) = \mathbf{E}_0 \frac{\sqrt{z_{R,1} z_{R,2}}}{\sqrt{q(\mathbf{k} \cdot \mathbf{r}, z_{R,1})} \sqrt{q(\mathbf{k} \cdot \mathbf{r}, z_{R,2})}}$$
$$\exp\left(-i \, |\mathbf{k}| \left(\frac{r_1^2}{2q(\mathbf{k} \cdot \mathbf{r}, z_{R,1})} + \frac{r_2^2}{2q(\mathbf{k} \cdot \mathbf{r}, z_{R,2})} \right) - i\mathbf{k} \cdot \mathbf{r} \right), \qquad (3.30)$$

with $q(z = \mathbf{k} \cdot \mathbf{r}) = z + iz_R$ being the complex beam parameter, $z_R = \pi w_0^2/\lambda$ the Rayleigh range and r_1, r_2 describe the directions along the two waists $w_{0,1}, w_{0,2}$ perpendicular to

---

[29]G&H AOMO 3200-124

the beam where θ is the angle between the axis of r_1 with respect to the electric field. The orientation of r_1 and r_2 perpendicular to the propagation are defined via

$$r_1 = -\sin(\theta)\frac{\mathbf{k} \times \mathbf{E}_0}{|\mathbf{k}|\,|\mathbf{E}_0|} \cdot \mathbf{r} + \cos(\theta)\frac{\mathbf{E}_0}{|\mathbf{E}_0|} \cdot \mathbf{r} \tag{3.31}$$

$$r_2 = \cos(\theta)\frac{\mathbf{k} \times \mathbf{E}_0}{|\mathbf{k}|\,|\mathbf{E}_0|} \cdot \mathbf{r} + \sin(\theta)\frac{\mathbf{E}_0}{|\mathbf{E}_0|} \cdot \mathbf{r}. \tag{3.32}$$

For simplicity we can consider only the plane wave part of the Gaussian beams, this does not capture the anti-confinement induced by the blue detuned lattice beams but allows for a simpler calculation. As the beams propagate in the x-y plane we can split the electric field into an out-of-plane and an in-plane part, which for each beam can have a phase difference α_j for elliptical polarizations, the field for beam j then reads

$$\mathbf{E}_j(\mathbf{r}, t) = \mathrm{e}^{-i(\mathbf{k}_j \cdot r - \omega_L t)}\left(\cos(\theta_j)\mathbf{E}_{s,j} + \sin(\theta_j)\mathrm{e}^{-i\alpha}\mathbf{E}_{p,j}\right), \tag{3.33}$$

where $\mathbf{E}_{s,j} = \mathbf{e}_z \cos(\theta)2\sqrt{I_j/(\epsilon_0 c)}$ is the out-of-plane component, $\mathbf{E}_{p,j} = \mathbf{e}_{\mathbf{k}\times\mathbf{e}_z}\sin(\theta)2\sqrt{I_0/(\epsilon_0 c)}$ the in-plane component, c is the speed of light, ε_0 the vacuum permittivity and I_j the peak intensity. The angle θ_j is defined compared to the z-axis and the propagation direction $\mathbf{k}_j$ here. The resulting intensity distribution $I(\mathbf{r}) = I_s(\mathbf{r}) + I_p(\mathbf{r})$ for the two polarizations is then given by

$$I_s(\mathbf{r}) = \frac{c\varepsilon_0}{2}\left|\sum_{j=1}^{3}\mathbf{E}_{s,j}(\mathbf{r}, t)\right|^2 = \frac{c\varepsilon_0}{2}\sum_{j,l=1}^{3}\sqrt{I_j I_l}\cos(\theta_j)\cos(\theta_l)\mathrm{e}^{-i(\mathbf{k}_j - \mathbf{k}_l)\cdot\mathbf{r}} \tag{3.34}$$

$$I_p(\mathbf{r}) = \frac{c\varepsilon_0}{2}\left|\sum_{j=1}^{3}\mathbf{E}_{p,j}(\mathbf{r}, t)\right|^2 = \frac{c\varepsilon_0}{2}\sum_{j,l=1}^{3}\sqrt{I_j I_l}\sin(\theta_j)\sin(\theta_l)\cos(\eta_j - \eta_l)\mathrm{e}^{-i(\mathbf{k}_j - \mathbf{k}_l)\cdot\mathbf{r}}\mathrm{e}^{i(\alpha_j - \alpha_l)} \tag{3.35}$$

If all beams are polarized out-of-plane and exhibit equal intensity the resulting intensity distribution reads

$$I(\mathbf{r}) = I_0\left(3 + 4\cos\left(\frac{\sqrt{3}}{2}k_L x\right)\cos\left(\frac{3}{2}k_L y\right) + 2\cos\left(\sqrt{3}k_L x\right)\right). \tag{3.36}$$

This intensity distribution constitutes the starting point for the experiments in the optical honeycomb lattice. The exemplary potential with the lattice sites of one plaquette is depicted in Figure 3.10a, the resulting lattice geometry is shown in Figure 3.10b. The intensity is up to a proportionality factor equivalent to the trapping potential, cf. Equation 3.2. The natural energy scale in an optical lattice is the recoil energy

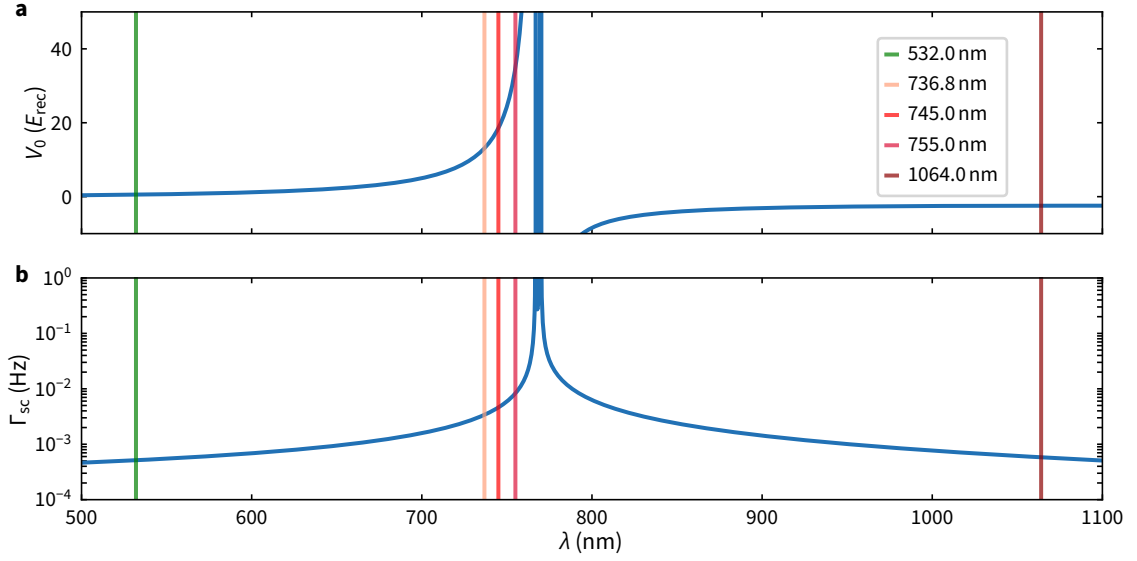$$E_{\mathrm{rec}} = \frac{\hbar^2 k_{\mathrm{L}}^2}{2m}, \tag{3.37}$$

Figure 3.11 | Lattice depth and scattering rate for various wavelengths. a, Maximum lattice depth at center of the lattice for beams with a power of 0.5 W, with waists of 400 μm $\times$ 100 μm. The lattice depth is evaluated in E_{rec} at the respective wavelength. The depth of the potential for red detuning ($\lambda_L > 767$ nm is evaluated for in plane polarization, and is opposite in sign. **b,** Scattering rate resulting from the trapping potential of a 1 E_{rec} honeycomb lattice at different detuning of the lattice. Close to the resonance of the D_1 and D_2 lines the scattering diverges as $1/\Delta$. The highlighted wavelengths show other easily available wavelengths which were also considered.

where in the case of ^{39}K the atomic mass $m_K = 6.47 \times 10^{-26}$ kg and therefore the recoil energy is $E_{rec} = h \times 9.23$ kHz. This energy corresponds to the kinetic energy an atom gains after emitting or absorbing one lattice photon.

During the course of this thesis the laser used to generate the lattice had to be replaced several times, during one replacement we also have changed the lattice wavelength from previously 736.8 nm to now 745 nm, as the smaller detuning provides a significantly deeper trapping potential as shown in Figure 3.11a. By reducing the detuning and operating the lattice closer to the resonance of the D1 and D2 we also find enhanced scattering, which is proportional to the intensity of the trapping light, equivalently to the depth of the resulting potential but scales unfavorably with $\Delta^{-2}_{D_1(D_2)}$. Operating the lattice further from resonance is therefore favorable as it reduces the resulting scattering of lattice photons, but requires higher laser power which limits the available range of detuning. Figure 3.11b shows the scattering rate resulting from the trapping potential with lattice depth 1 E_{rec} at the respective wavelength.

We have experimentally also tested the lattice at 755 nm, but have found the coherence time in the lattice to be insufficient for the experiments we want to conduct. We performed expansion experiments from a very localized wave packet released abruptly from the optical tweezer into the static optical lattice to perform a quantum random walk, (cf. Section 5.1.2) [263, 264, 266]. If the coherence of the state is maintained during the evolution, we expect a non-Gaussian distribution as well as interference fringes within the bulk of the area covered by the quantum walk [263]. Figure 3.12a and c show the
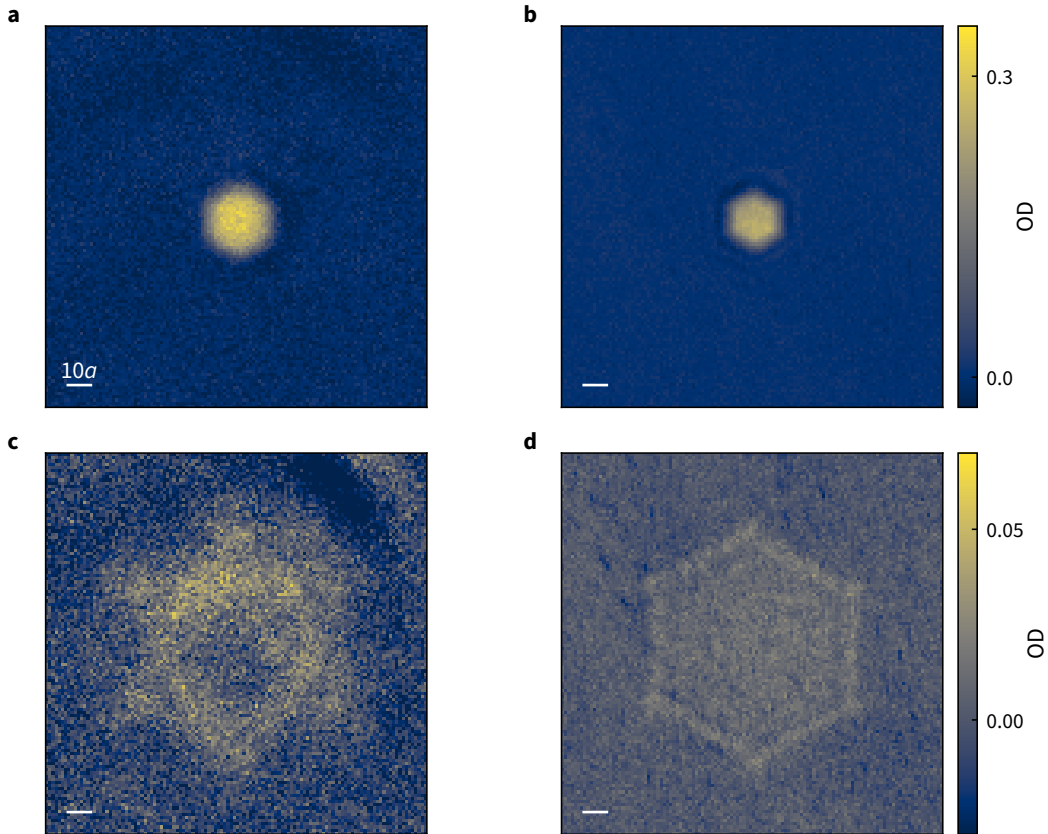
Figure 3.12 │ **Expansion dynamics in the optical lattice at** 755 nm **and** 745 nm. **a**, Expansion from a tightly confining optical tweezer in an $\approx 6\,E_{\mathrm{rec}}$ optical lattice derived from 755 nm light. The cloud expands for 1 ms after switching of the tweezer. **b**, Same as **a** but the lattice wavelength is 745 nm. **c**, Same as **a**, but after 5 ms of expansion in the lattice. **d**, Same as **c**, but the lattice wavelength is 745 nm. For clarity a background image has been subtracted in panels **a,c** to remove residual atoms that intially have not been trapped in the tweezer. The displayed images are averages over 302 independent realizations for **b,d** and 122 realizations for **a,c**.

evolution of the cloud after 1 ms and 5 ms in a honeycomb lattice generated by 755 nm laser light. The cloud does not show clean edges and significantly deviates from a hexagonal shape. The evolution of a cloud in a lattice derived from interfering 745 nm laser light is depicted in Figure 3.12b and d for 1 ms and 5 ms of expansion duration. The images clearly show a sharper edge and interference features in the bulk. We concluded that the approximately two times higher photon scattering rate is responsible for the reduced coherence and continued to use the lattice further off resonance at 745 nm which performed similar to 736.8 nm which had been used in previous experiments.

3.3.2 Calibration of the lattice depth

When generating the lattice potential for the experiment it is crucial to adjust the intensity of the interfering laser beams at the position of the cloud such that the three intensities are equal for each beam. The dynamics in the honeycomb lattice does not separate along
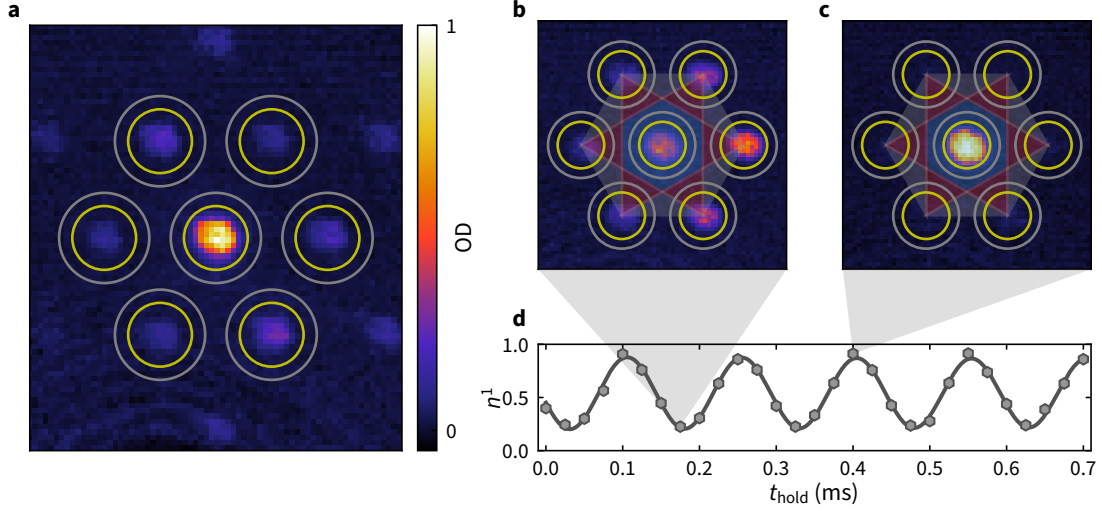
Figure 3.13 │ **Adjusting the intensties of the lattice beams and calibration of the lattice depth. a,** Momentum distribution observed after abruptly switching off the lattice. The lattice beams forming the potential exhibit an imbalance in intensity resulting in imbalanced population in the first order peaks. The yellow and gray circles indicated the area used to determine the weight in the respective orders. The area between yellow and gray is subtracted to remove background counts. **b,** Band occupation during the Stückelberg sequence with low population in the lowest band. The image is overlapped with the Brillouin zones of the first three zones. The displayed second (red) and third (gray) Brillouin zone map Γ to the same point after band mapping. **c,** same as b, but the band population is mostly in the lowest band. **d,** Resulting population oscillation as a function of hold time with the frequency reflecting the bandgap at Γ. The populations in **b** and **c** are indicated by the shaded triangle. The markers indicate the measured band population, the solid line is the result of the fit.

different directions of the lattice, therefore any slight imbalance directly influences the dynamics in both spatial directions. Slight inequality in the shape of the beam, or slight misalignment of the lattice beams with respect to the position of the cloud directly influences the resulting intensity at the position of the cloud, even if the power in each beam is identical. The power of each lattice beam is controlled in a closed loop with individual setpoint for each beam. To verify that the intensity in each beam at the location of the cloud is identical, we adiabatically load a BEC into the lowest band of the resulting lattice potential at a depth of $\approx 5.9\,E_{\mathrm{rec}}$, hold it in the lattice for $10\,\mathrm{ms}$ and subsequently abruptly switch off all confining laser beams and the lattice to perform a time of flight expansion for $3.5\,\mathrm{ms}$, after which we take an absorption image of the cloud. The resulting density distribution after time of flight reflects the momentum distribution in the lattice [272–274]. The envelope of the interference pattern is related to the Wannier function in the lattice, while the periodic features are related to the coherent interference of the Wannier functions after the expansion, analogus to the optical interference after transmission through a grating. The lattice sites are occupied with a BEC with flat phase, which results in coherent interference of the matter wave after time of flight whenever their momentum matches a combination of the reciprocal lattice vectors multiplied with $\hbar$. Due to a finite coherence length and a finite

time of flight the observed distribution is a convolution of the real space distribution of the cloud and its momentum distribution resulting in a finite width cloud at each of the peaks. As the envelope reflects the shape of the Wannier function the weight of the peaks is directly related to the intensity in each lattice beam. If one of the three beams exhibits less intensity compared to the other two it results in a Wannier function which is more extended in the direction of the weaker beam. Therefore the envelope of the cloud after time of flight is narrower in this direction compared to the other two and the resulting peaks perpendicular to the beam appear more pronounced. This scenario is depicted in Figure 3.13a, where we show an absorption image after time of flight, where the intensity of the lattice beams is imbalanced. The beam propagating from the lower left to the upper right of the image is weaker compared to the other two, resulting in weaker peaks along its propagation direction. To adjust the intensity of the lattice beams we count the number of atoms in each of the six first order peaks and adjust the intensity such that we find equal population in all peaks.

To calibrate the depth of the resulting lattice we perform a Stückelberg interferometry sequence [275–277]. The sequence starts with a BEC prepared in the ground state of the optical lattice with zero quasimomentum at Γ. The scattering length is set to $a_s = 6\,a_0$ to reduce any possible interaction effects. By detuning the frequency of two of the lattice beams we can apply a force in an arbitrary direction [174]. For simplicity we consider a linear change in frequency for one of the lattice beams. We find an acceleration of the interference pattern in the direction of this laser beam

$$a = \frac{2}{3}\lambda_L \frac{\Delta f}{\Delta t}. \tag{3.38}$$

The resulting force changes the quasimomentum linearly in time by

$$F\Delta t = \hbar\Delta k. \tag{3.39}$$

The resulting change in quasi momentum in the direction of the lattice beam is

$$\delta k = \frac{2\lambda_L m \Delta f}{3\hbar}. \tag{3.40}$$

One implicit assumption is the absence of any other restoring force such as the harmonic trap. Especially for small forces the harmonic trap can lead to a significant change of the resulting quasimomentum as the acceleration of the interference pattern inevitably translates the cloud trapped within it. Utilizing the frequency modulation of the lattice we accelerate the cloud through the Brillouin zone from Γ via M to Γ'. Γ' is located at the center of the neighboring Brillouin zone, is equivalent to Γ and only serves to distinguish whether the cloud is in the moving lattice or at rest. The force is chosen such that it coherently transfers a fraction of the cloud to the second band of the honeycomb lattice, i.e., the resulting state is a coherent superposition of the two bands at Γ' with energies E_Γ^1 and E_Γ^2:

$$|\Psi_{\Gamma'}\rangle = a_1 |\psi_{\Gamma'}^1\rangle + a_2 |\psi_{\Gamma'}^2\rangle \tag{3.41}$$

The frequency detuning is kept constant for a time t_{hold} and thus keeps the cloud at quasimomentum Γ' where the two states accumulate a dynamical phase according to

$$|\Psi_{\Gamma'}\rangle = a_1 |\psi_{\Gamma'}^1\rangle \, \mathrm{e}^{-iE_\Gamma^1 t_{\text{hold}}/\hbar} + a_2 |\psi_{\Gamma'}^2\rangle \, \mathrm{e}^{-iE_\Gamma^2 t_{\text{hold}}/\hbar}. \tag{3.42}$$

By inverting the force a fraction of the cloud is again transferred from the first to the second band and vice versa, the state can then be described by

$$|\Psi_\Gamma\rangle = a_1(\tilde{a}_1 |\psi_\Gamma^1\rangle + \tilde{a}_2 |\psi_\Gamma^2\rangle)\mathrm{e}^{-iE_\Gamma^1 t_{\text{hold}}/\hbar} + a_2(\tilde{a}_1 |\psi_\Gamma^2\rangle + \tilde{a}_2 |\psi_\Gamma^1\rangle \, \mathrm{e}^{-iE_\Gamma^2 t_{\text{hold}}/\hbar}. \tag{3.43}$$

Once the cloud is back at Γ we ramp the lattice potential to zero on a time scale slow compared to the energy gap in the lattice but fast compared to scattering and momentum redistribution processes, which maps the momentum distribution in the lattice to the free space dispersion of the particles [278]. This enables, neglecting the initial extent of the wave function in the trap, direct mapping of the resulting momentum to the band population and is referred to as *bandmapping*. After a time of flight, which directly relates the momentum to a position via $\mathbf{r} = \hbar \mathbf{k} t_{\text{tof}}/m$, we find the population of the second band located at the position related to Γ in the second band, while the population of the first band is still at located $\mathbf{k} = \mathbf{r} = \mathbf{0}$. The bandmapping procedure corresponds to a projection and subsequent measurement of the population in the respective band. The population in the first band after bandmapping is

$$\left|\langle\psi_\Gamma^1|\Psi_\Gamma\rangle\right|^2 = |a_1\tilde{a}_1|^2 + |a_2\tilde{a}_2|^2 + |a_1\tilde{a}_1 a_2\tilde{a}_2| \, 2\cos((E_\Gamma^1 - E_\Gamma^2)t_{\text{hold}}/\hbar + \varphi). \tag{3.44}$$

Upon repeating the experiment for various hold times t_{hold} we find the population in the lowest band oscillating with a frequency proportional to the energy gap at Γ enabling a direct determination of the band gap. This technique can be utilized to measure the band gap at any quasimomentum as long as a significant mixing is achieved when accelerating to the respective quasimomentum. An exemplary measurement of the energy gap at Γ is shown in Figure 3.13b together with two representative images after band mapping with most atoms in the lowest band, and an image where a large fraction of the population is in the second band. The measurement results in a frequency of $6.68(2)\,\text{kHz}$, corresponding to a $5.84\,E_{\text{rec}}$ deep lattice.

3.4 Imaging and Objective Alignment

High optical resolution in the atomic plane is crucial for any ultracold atom platform if any manipulation is to be performed in real space [6]. One very prominent example are quantum gas microscopes, where the occupation in an optical lattice can be frozen and subsequently imaged directly [36, 37], giving access to entirely new observables such as charge or spin correlators [279].

High spatial resolution also enables the preparation of peculiar initial states and its subsequent observation in bulk systems [219, 220], or deterministic preparation of vortices

[280] and by dynamically adapting and resorting the trapping geometry the assembly of defect free arrays with high fidelity [42, 43]. However, it requires precise control and calibration of the prepared potential [218, 221].

Prerequisite to achieve this is an imaging system with as little aberrations as possible. Especially optical systems with large numerical aperture are prone to suffer from aberrations. A first step to avoid as many aberrations as possible is careful optical design of the objective, as this requires a high level of expertise to design [281–283] and manufacture we outsource these steps.

Once the objective is mounted next to the glass cell, alignment perpendicular to the vacuum window and alignment of the optical axis to the optical trap is extremely crucial to achieve the desired performance of the objective. As the first experiments performed on this machine were done in reciprocal space [209, 210, 284, 285], where extremely fine spatial resolution was not necessary, the imaging path and objective were not aligned perfectly.

3.4.1 Density density correlations in a thermal gas

To extract information on the actual point spread function and aberrations present with the current configuration, we adapted the procedure developed in the group of Cheng Chin [286, 287]. In summary the idea is to image a thermal cloud which is correlated only on a very short length scale, extract the spatial frequency spectrum of these correlations and from the observed spectrum deduce the transmission function of the imaging system.

The equal time density density correlations $\kappa(\mathbf{r}_1, \mathbf{r}_2)$ in a thermal gas, where $\mathbf{r}_i$ are the positions under consideration is given by

$$\kappa(\mathbf{r}_1, \mathbf{r}_2) = \langle \hat{\Psi}^\dagger(\mathbf{r}_1)\hat{\Psi}(\mathbf{r}_1)\hat{\Psi}^\dagger(\mathbf{r}_2)\hat{\Psi}(\mathbf{r}_2)\rangle \tag{3.45}$$

$$= \langle \hat{\Psi}^\dagger(\mathbf{r}_1)\hat{\Psi}^\dagger(\mathbf{r}_2), \hat{\Psi}(\mathbf{r}_1)\hat{\Psi}(\mathbf{r}_2)\rangle + \langle \hat{\Psi}^\dagger(\mathbf{r}_1)\hat{\Psi}(\mathbf{r}_1)\rangle \, \delta(\mathbf{r}_1 - \mathbf{r}_2), \tag{3.46}$$

the $\Psi(\mathbf{r})$ are the bosonic field operators creating a particle at position $\mathbf{r}$. For a gas above quantum degeneracy the particles are uncorrelated down to a length scale comparable to the thermal de Broglie wavelength [288]

$$\lambda_{\text{th}} = \sqrt{2\pi\hbar^2/(mk_BT)}, \tag{3.47}$$

where k_B is the Boltzmann constant, m the mass of the particle and T its temperature. For a gas of ^{39}K at a temperature of $10\,\mu$K the thermal de Broglie wavelength $\lambda_{\text{th}} = 88\,$nm and is about an order of magnitude smaller than the imaging wavelength $\lambda_{\text{imag}} = 767\,$nm. Therefore the resolution limit which is on the order of λ_{imag} prevents the observation of these correlations and any visible correlations are not transmitted through the imaging system.

To obtain the *connected* density density correlations in the limit of $\lambda_{\text{imag}} \gg \lambda_{\text{th}}$ we subtract the trivial contribution of the random first order contribution and divide by the mean density to obtain

$$\kappa_C(\mathbf{r}_1, \mathbf{r}_2) = \delta(\mathbf{r}_1 - \mathbf{r}_2), \tag{3.48}$$

which resembles the correlations observed in an ideal gas [289]. This means that the frequency spectrum of these fluctuations is flat, i.e., it corresponds to white noise and all spatial frequencies are equally weighted.

3.4.2 Absorption Imaging

To observe the density fluctuations in the experiment we need to use a detector, in our case we use an EMCCD camera[30] to record absorption images [290]. To record the density distribution of the cloud we use a sequence of three images: we first send resonant light through the atomic sample and record it on the camera, then switch off all the trapping light in order to release all the atoms and take an image where we send the equivalent light pulse again and record it on the camera, finally in a third image we record a background image without sending any light pulse.

Depending on whether we image the cloud in situ or after time of flight, we use a slightly different imaging frequency. When imaging potassium in situ, we apply a magnetic field of around $403\,\mathrm{G}$ in order to tune the scattering properties to the desired strength as described in Section 3.1.3. This shifts the energies of the states and therefore the resonance where we image [187, 291]. In situ, as we are at moderate magnetic fields, the F, m_F are no longer the good quantum numbers and we image on the $|m_J = -1/2, m_I = 3/2\rangle$ to the $|m_J = -3/2, m_I = -1/2\rangle$ transition. As this transition is not fully closed due to the admixture of neighboring states, it limits the number of scattered photons and therefore the signal to noise of the final image. In a later stage of this experiment we have added an additional imaging laser to improve the number of scattered photons [292].

In time of flight imaging the magnetic field is switched off and we can image in the presence of only a small bias magnetic field to define a quantization axis. As the BEC is initially in the state that is adiabatically connected to the $|F = 1, m_F = 1\rangle$ state, in order to image on a closed transition with large transition dipole matrix element, we repump the atoms from their initial state to $|F = 2, m_F = 2\rangle$ and subsequently image on the transition to $|F = 3, m_F = 3\rangle$.

The *Beer-Lambert* law relates the observed reduction in intensity due to light being scattered by the atomic cloud to the column density $n_{\mathrm{col}}(x, y)$ by [187, 293]

$$I(\mathbf{r}) = I_0 e^{-\sigma_0 \int n(\mathbf{r}, z) dz} = I_0 e^{-\sigma_0 n_{\mathrm{col}}(\mathbf{r})}, \tag{3.49}$$

where σ_0 is the resonant scattering cross section, $\mathbf{r}$ the position in and z perpendicular to the atomic plane and I_0 the incident intensity. For a two-level system the resonant scattering cross section is simply given by $\sigma_0 = 3\lambda^2/(2\pi)$. This can be related to a saturation intensity, defined as the intensity where the radiative decay with rate Γ is equal to the Rabi frequency of the driving field, which reads

$$I_{\mathrm{sat}} = \frac{hc\pi\Gamma}{3\lambda^3}. \tag{3.50}$$

---

[30]Andor iXon 885

For imaging intensities significantly exceeding I_{sat} corrections, such as an intensity dependent scattering cross section need to be taken into account in order to extract the density with high fidelity [181, 293].

The resulting column density can then be extracted from the aforementioned three images taken with the camera via

$$n_{\text{col}}(\mathbf{r}) = -\frac{1}{\sigma_0} \ln \left(\frac{I_{\text{with}}(\mathbf{r}) - I_{\text{BG}}(\mathbf{r})}{I_{\text{without}}(\mathbf{r}) - I_{\text{BG}}(\mathbf{r})} \right), \tag{3.51}$$

where $I_{\text{with(out)}}$ corresponds to the picture with light and with(out) atoms, I_{BG} is the background picture taken without imaging light.

3.4.3 Extracting the modulation transfer function from absorption images

The quantity we initially extract is an atom number per pixel on the camera, which is related to the actual density by the magnification of the imaging system and the point spread function $\mathcal{P}(\mathbf{r})$. If the size of one point spread function is significantly larger than the size of one pixel A its influence on the calculation of the column density is simply given by the convolution of the actual density with the point spread function and the envelope of a pixel

$$n_{\text{exp}}(\mathbf{r}_j) = \frac{N_j}{A} = \int n(\mathbf{r}) \mathcal{P}(\mathbf{r}_j - \mathbf{r}) \, \Pi \left(\frac{\mathbf{r}_j - \mathbf{r}}{\sqrt{A}} \right) d\mathbf{r}, \tag{3.52}$$

$\mathbf{r}_j$ corresponds to the position of j-th pixel in the atomic plane and the area of the pixel is represented as

$$\Pi \left(\frac{r}{\sqrt{A}} \right) = \begin{cases} 0, & \text{if } |r| > \frac{\sqrt{A}}{2} \\ \frac{1}{2}, & \text{if } |r| = \frac{\sqrt{A}}{2} \\ 1, & \text{if } |r| < \frac{\sqrt{A}}{2}. \end{cases} \tag{3.53}$$

As we are not interested in the average envelope or mean value of each pixel, we will only consider fluctuations around the mean value $\bar{N}_j$ and mean value of the density $\bar{n}(\mathbf{r})$. We then find the fluctuations of the density $\delta n(\mathbf{r}) = n(\mathbf{r}) - \bar{n}(\mathbf{r})$, combining this with Equation 3.52 and taking the Fourier transform we end up with

$$\delta n_{\text{exp}}(\mathbf{k}) = \delta n(\mathbf{k}) \, \text{OTF}(\mathbf{k}) \, \text{W}(\mathbf{k}), \tag{3.54}$$

where $\delta n_{\text{exp}}(\mathbf{k}) = \sum_j \delta N_j e^{-ik \cdot r_j}$ is the discrete Fourier transform of the atom number fluctuations $\delta N_j = N_j - \bar{N}$ of the pixels, OTF represents the Fourier transform of $\mathcal{P}(\mathbf{r})$ and W the Fourier transform of the pixel window.

In the following we will argue that we can set $\text{W} = 1$ for all relevant $\mathbf{k}$. Assuming we have chosen a magnification such that the length of one pixel in the atomic plane $\sqrt{A} \ll \lambda$, the point spread function will essentially be constant across one pixel and therefore not alter the response of the imaging system. In our case we have a pixel size in

the atomic plane of $\sqrt{A} = 396\,\text{nm}$, while the wavelength is $\lambda = 766.7\,\text{nm}$. Alternatively we can consider one spatial dimension of

$$\text{W}(k) = \int_{-\infty}^{\infty} \Pi(x/\sqrt{A})\mathrm{e}^{ikx} = 2\sqrt{A}\,\text{sinc}(k2\sqrt{A}), \qquad (3.55)$$

and find that the Fourier transform of the window function falls off significantly slower than the point spread function and we can therefore approximate $\text{W}(k) \approx 1$ for the spatial frequencies of interest. We therefore have

$$\delta n_{\text{exp}}(\mathbf{k}) = \delta n(\mathbf{k})\,\text{OTF}(\mathbf{k}). \qquad (3.56)$$

As illustrated before the Fourier spectrum of a gas above quantum degeneracy is flat, i.e., $\delta n(\mathbf{k}) \approx 1$, and we can determine the optical transfer function from the noise spectrum of a thermal gas and therefore calibrate the performance of the imaging system. One assumption we have not explicitly discussed so far is the extent of the cloud along the imaging axis (z-direction), ideally the gas is confined to a single plane with extent much smaller than the Rayleigh range of the smallest optical features the objective can resolve. If the gas is significantly extended, the presence of the highest spatial frequencies can be detected, but we are averaging over the vertical extent of the cloud and therefore e.g. aberrations at these frequencies are averaged and not clearly visible.

As we are not able to a perfectly prepare a gas with flat density, such that we can directly subtract the mean value, we need to average several realizations. The individual fluctuations have a random phase on the image, therefore we have to average the absolute value of the optical transfer function $|\text{OTF}(\mathbf{k})| = \text{MTF}(\mathbf{k})$, which is equivalent to the *modulation transfer function*. For a perfect imaging system the optical and modulation transfer function are equivalent, since there are no phase shifts in the wavefront. Because each spatial frequency is independent, we can relate the two via a phase transfer function $\phi(\mathbf{k})$, i.e.,

$$\text{OTF}(\mathbf{k}) = \text{MTF}(\mathbf{k})\mathrm{e}^{i\phi(\mathbf{k})}. \qquad (3.57)$$

We now have to distinguish between coherent and incoherent imaging.

For a coherent imaging we effectively have an incoming plane wave E_0 which is scattered on the object and the scattered spherical dark wave ΔE is interfering with the incident wave and eventually this interference results in the image [286]. The point spread function therefore does not need to be strictly positive in this case, as the diffraction on the object and the resulting interference can lead to an in- or decrease in the resulting field strength and thus intensity in the image. As described before the atomic density is directly related to the transmission of the intensity t^2, where t is the transmission of the electric field. The camera detects two images, which are for simplicity background-noise free here, and are related to the transmission as

$$t^2 = \frac{I'}{I_0} \propto \frac{|E_0 + \Delta E|^2}{|E_0|^2} \approx 1 + 2\,\text{Re}\left[\frac{\Delta E}{E_0}\right], \qquad (3.58)$$

and we can relate the density to the negative logarithm of the transmission

$$n \propto -\ln(t^2) \approx -2\operatorname{Re}\left[\frac{\Delta E}{E_0}\right]. \tag{3.59}$$

The scattered field is directly related to the atomic density in the object plane, which we will for simplicity describe as a two dimensional arrangement of point sources emitting a field ϵ

$$\Delta E = \sum_i \epsilon p(\mathbf{k} - \mathbf{k}_i), \tag{3.60}$$

where $\mathbf{k} = 2\pi \mathbf{r}/(\lambda f)$ relates the position in the object plane to the wave vector after the lens with focal length f, the final imaging lens will again relate the wave vector to the position on the sensor. The dark field is proportional to the incident field but it picks up a phase δ_s depending on the exact detuning compared to resonance, i.e., $\epsilon \propto e^{i\delta_s} E_0$. We can therefore combine Equation 3.60 and Equation 3.59 to find, that the point spread function for coherent or absorption imaging will be given by

$$\mathcal{P}_c(\mathbf{r}) \propto \operatorname{Re}[e^{i\delta_s} p(\mathbf{k})]\big|_{\mathbf{k}=\frac{2\pi \mathbf{r}}{\lambda f}}. \tag{3.61}$$

We have so far not considered the transfer function for coherent imaging, fundamentally in a perfect system all frequencies of the field are transmitted with equal amplitude up to the maximum frequency. For an aberration free system the point spread function follows from the Fraunhofer diffraction. After a circular aperture we find

$$\mathcal{P}_c^{\text{ideal}} = \frac{J_1\left(\frac{2\pi\,\text{NA}\,r}{\lambda}\right)}{\frac{2\pi\,\text{NA}\,r}{\lambda}}. \tag{3.62}$$

The maximum spatial frequency is limited by the aperture stop of diameter D, which is usually given by the numerical aperture

$$\text{NA} = \sin\left(\arctan\left(\frac{D}{2f}\right)\right) \approx \frac{D}{2f} \tag{3.63}$$

of the lens closest to the atoms with focal length f. This leads to the maximum resolvable spatial angular frequency

$$k_{\max} = 2\pi\nu_{\max} = 2\pi\frac{\text{NA}}{\lambda}, \tag{3.64}$$

where $\nu_{\max}$ is the maximum spatial frequency.

Unfortunately no imaging system is perfect and there are always aberrations present. In order to quantify the aberrations we can use the Nijboer-Zernike theory of aberrations, which expands the wavefront of the image on the unit disk. This works very reliably and allows for an identification of the individual components of aberrations present in the system. After identifying the leading aberrations one can use the obtained knowledge to improve the system by trying to reduce the detected wavefront error. We can treat the accumulated aberrations as if they would all occur on the exit pupil and eventually

result in an aberrated point spread function on the detector. Following [286] we can
define a simplified pupil function

$$p(r_p, \theta_p) = \Pi\left(\frac{2r_p}{D}\right) e^{-\frac{4r_p^2}{D^2\tau^2}} e^{i\Theta(r_p,\theta_p)}, \tag{3.65}$$

with radius r_p and angle θ_p in the pupil plane. The radial envelope consists of a sharp cutoff
at the radius of the aperture $D/2$ and a Gaussian envelope reducing the amplitude with
increasing radius. The envelope can be physically motivated by the increasing angle of inci-
dence for marginal rays and therefore increased reflectivity of the surface as the anti reflection
coatings perform slightly worse for large angle of incidence. Additionally the phase term

$$\Theta(r_p, \theta_p) \approx S_0 \left(\frac{2r_p}{D}\right)^4 + \alpha\left(\frac{2r_p}{D}\right) r \cos(2\theta_p - 2\phi) + \beta\left(\frac{2r_p}{D}\right)^2 \tag{3.66}$$

accounts for spherical aberration S_0, astigmatism α with an axis oriented along $\theta_p = \phi$
and a defocus β. As discussed before, we can relate the point spread function to the
modulation transfer function via a Fourier transform

$$\mathcal{F}(\mathcal{P}_c(\mathbf{r})) = \text{OTF}_c(\mathbf{k}), \tag{3.67}$$

and therefore fit the obtained modulation transfer function with a pupil function

$$\mathcal{M}_c = \left| \mathcal{F}\left(\text{Re}\left[e^{i\delta_S}\mathcal{F}^{-1}(p)\right]\right)\right|. \tag{3.68}$$

We show two examples of an almost well aligned imaging system together with the
corresponding fit in Figure 3.14. We image ^{87}Rb atoms in situ in the crossed optical dipole
trap with a vertical waist of $\approx 30\,\mu$m and average the resulting images to obtain an average
image. We then calculate the Fourier transform of the difference between every image and
the mean of all images and subsequently average the absolute value of the obtained Fourier
transforms. The result displayed in Figure 3.14a is obtained when the objective is vertically
aligned with the center of the atomic cloud. No aberrations are directly visible in both the
experiment and the fit to the data shown in Figure 3.14b. In contrast when longitudinally
displacing the objective by $10\,\mu$m, we obtain the image shown in Figure 3.14c. Here we
can clearly observe a concentric ring due to the defocus, where the ellipticity of the ring
is a result of astigmatism present in the system. One very striking difference between
experiment and theory are the features at high spatial frequencies, which are not resolved
in the experimental images. We believe that the missing contrast at high spatial frequency
is a result of averaging in longitudinal direction due to atoms being out of focus. The wave
function of the atomic cloud is randomly projected in every measurement and therefore the
position compared to the focus is randomly distributed preventing the clear identification of
aberrations at large spatial frequency. To also obtain this information we would require to
trap the cloud in a trap with significantly tighter confinement along the imaging direction.
This could be implemented by trapping the cloud in a vertical lattice, or alternatively by
using a colder sample in order to reduce the thermal occupation of higher states in the
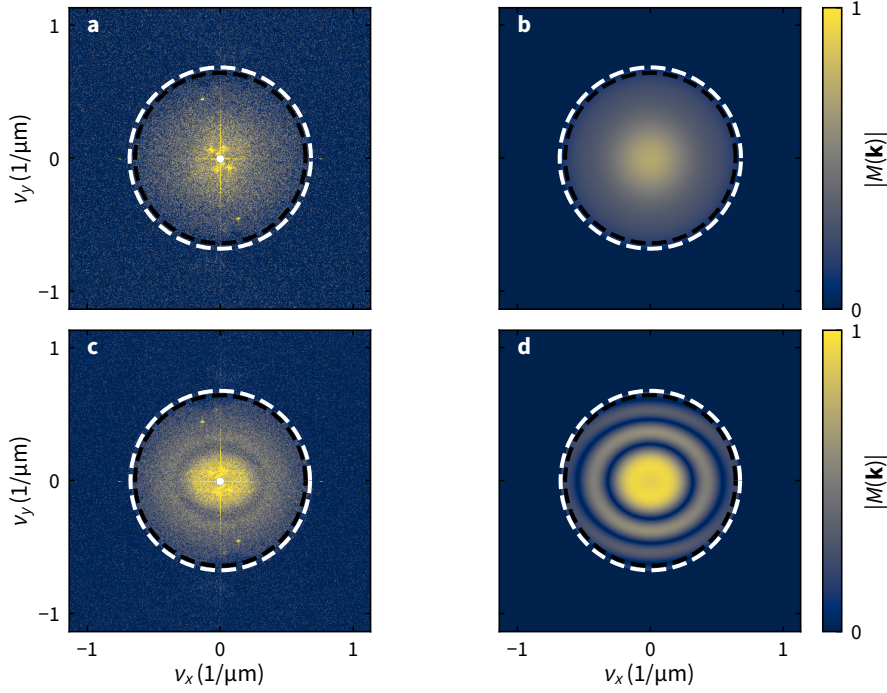
Figure 3.14 | **Resulting modulation transfer function and corresponding fits. a**, Experimentally obtained modulation transfer function $|\mathcal{M}(\mathbf{k})|$ from in situ absorption images of ^{87}Rb. The objective is aligned well, except for a slight displacement of the optical axis compared to the cloud of atoms. The black dashed lines correspond to the theoretical resolution limit of the objective $\nu_{max} = \mathrm{NA}\,/\lambda$. The white dashed line corresponds to the maximum frequency obtained by fitting the data with the model. The fitted cutoff frequency is slightly larger than the theoretical limit. **b**, Result of the fit obtained by fitting a model including spherical aberrations, astigmatism and defocus to the data presented in **a**. **c**, Experimentally obtained image with a defocus of $10\,\mu$m compared to **a**, the elliptical rings arising from the defocus and astigmatism are clearly visible. **d**, Result of the fit to the data in **c**. In contrast to the experiment there is still strong contrast at higher spatial frequencies, which we attribute to the averaging along the propagation direction in the experiment. The sample is not strictly two-dimensional and extents wider than the depth of focus at larger spatial frequencies. This significantly limits the lower bound of aberrations that can be extracted. The fitted cutoff frequency is slightly larger than the theoretical limit, which might be due to the slight displacement reducing the maximum angle in one direction, while increasing it in the other or a tilted imaging beam.

dipole trap. Assuming that the used commercial objective is performing well, we believe to not be limited by the vertical extent of the cloud as we try to perform all experiments in the ground state of the harmonic oscillator formed by the vertical direction of the optical dipole trap, where we have a an effective harmonic oscillator length of the BEC of $0.96\,\mu$m.

3.4.4 Alignment of the objective

The result presented in Figure 3.14 is the result of a very careful pre-alignment making sure that the objective is already very parallel to the window of the glass cell. To achieve good initial alignment we have covered the objective in order to align a reference beam perpendicular to the glass cell. As a starting point we overlapped a reference beam with the

imaging beam, where we were sure that it was hitting the atoms in order to not misalign the optical axis of the objective. Once the reference beam was perpendicular to the glass cell, we put a glass plate on top of the objective in order to have a flat surface perpendicular to the objective. The reflection emerging from the glass plate was then aligned to also be perpendicular to the glass cell, i.e., overlapping with the incoming beam. Once this was done the tip and tilt of the objective were correct and the only degree of freedom was the position of the optical axis compared to the cloud. In order to minimize this distance we translated the objective and measured the correlations of the thermal gas, if the two positions are not overlapping well, the Fourier plane is significantly cropped and only part of the correlations are visible. By translating the objective the size of the Fourier plane can be increased until it is eventually round. With this method we could obtain a radial distance of the center of the cloud and the optical axis of $\approx 150\,\mu$m.

To further improve the alignment we eventually used two reference beams with wavelength $532\,$nm, one from below the objective and one from above. The choice for $532\,$nm eased this procedure as also very faint reflections are easily visible by eye. The beam coming from above propagating through the glass cell, then through the objective was interferometrically aligned to the objective such that all the waves emerging from the several surfaces of the glass cell and objective form the most concentric patterns achievable. Subsequent tip, tilt and translations of the objective were then used to optimize this pattern as much as possible. The beam below, first transmitted through the objective, then the glass cell, was used in order to verify the objective alignment was as good as possible. The verification with the beam from below was slightly more sensitive as the available propagation distance was significantly longer ($\approx 2\,$m) compared to above ($\approx 0.7\,$m). With the reference beam from above we also had a measure to obtain the distance between the optical axis of the objective and the cloud. The beam was chosen such that it would have waist of $\approx 10\,\mu$m in the atomic plane, this results in a beam with a Rayleigh range long enough to pierce a hole visible in absorption imaging through the quadrupole trap. After taking an absorption image of the cloud we only need to translate the objective to the desired position. A few iterations of realigning the upper reference beam, piercing a hole through the cloud and translating the objective were necessary in order to align the optical axis to the center of the quadrupole trap and the center of the optical dipole trap to $< 10\,\mu$m. The final distance is significantly smaller than the diffraction limited field of view of the objective which spans approximately a disk with radius $75\,\mu$m.

3.4.5 Comparison of absorption and fluorescence imaging

Even though we currently do not perform fluorescence imaging, we still want to introduce the relation of the point spread function and the transfer functions for incoherent or fluorescence imaging. In contrast to absorption imaging we have no coherent background field, every atom is emitting a field with random phase compared to the other atoms, assuming the interparticle spacing is $> \lambda$ and superradiance does not occur [294, 295].
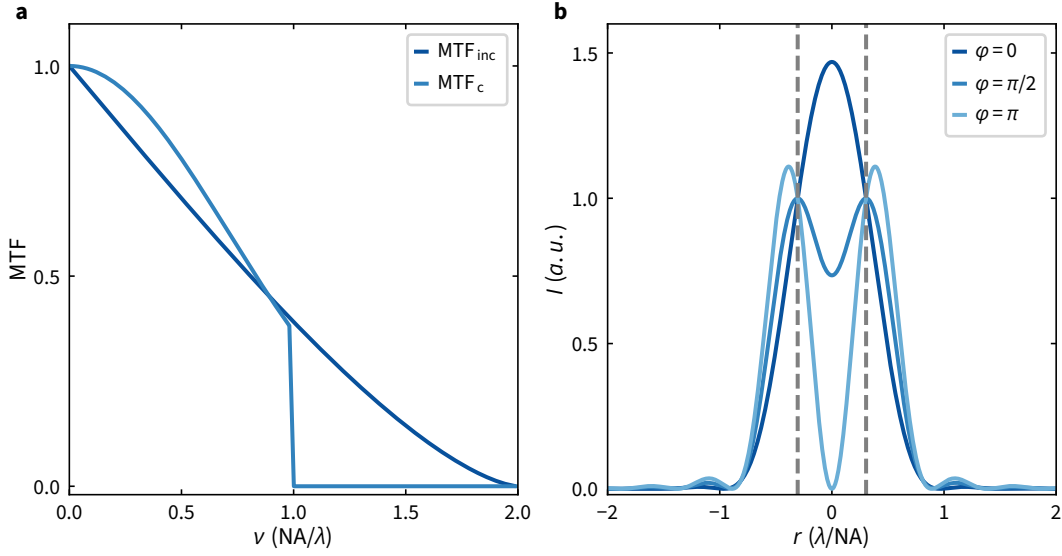
Figure 3.15 | Comparison of the modulation transfer function for coherent and incoherent imaging and coherent imaging of two point sources with varying relative phase of the emitted field. a, Modulation transfer function for coherent and incoherent imaging without aberrations. In the coherent case we have chosen an envelope falling off to e^{-1} at the cutoff frequency NA $/\lambda$. The incoherent modulation transfer function falls off smoothly and extents to higher frequency than the coherent one. The comparison here is potentially slightly misleading as we are comparing a field and intensity transfer function here. **b,** Resulting intensity distribution when imaging two point sources separated by $d = 0.61\lambda/NA$ with different relative phase. The case of $\varphi = \pi/2$ is equivalent to the case of two incoherent point sources. The dashed lines indicate the location of the two point sources.

For a perfect incoherent imaging system the optical transfer function can be calculated analytically. Starting from an ideal lens with circular aperture and numerical aperture NA we find, that the point spread function is given by a radially symmetric Airy disk

$$\mathcal{P}_{\text{inc}}(r) = \left(\frac{J_1\left(\frac{2\pi\,\text{NA}\,r}{\lambda}\right)}{\frac{2\pi\,\text{NA}\,r}{\lambda}} \right)^2, \tag{3.69}$$

where $J_1(r)$ is the first Bessel function of the first kind. In contrast to the absorption imaging case, we find that the point spread function here scales as the square of the Fourier transform of the pupil function, while the absorption imaging is linear. To obtain the optical transfer function we take the Fourier transform of the point spread function and find [296]

$$\text{OTF}_{\text{inc}}(\nu) = \mathcal{F}(\mathcal{P}_{\text{inc}}(r)) = \{p * p\}(r)$$

$$= \frac{2}{\pi} \left(\arccos\left(\frac{\nu\lambda}{2\,\text{NA}}\right) - \frac{\nu\lambda}{2\,\text{NA}}\sqrt{1 - \left(\frac{\nu\lambda}{2\,\text{NA}}\right)^2} \right) \text{ for } \nu < \lambda/(2\,\text{NA}). \tag{3.70}$$

This corresponds to the convolution of two circular pupil functions $p(r)$, which implies that the optical transfer function is always real and non-negative. A more intuitive picture for the convolution arises when considering how a certain spatial frequency arises in the image.

For a certain spatial frequency two rays emerging from the exit pupil separated by a specific distance need to interfere in the image plane. The convolution of the two pupil functions then evaluates how often this distance arises, the zero frequency components correspond to the maximum, while larger distance can be realized less often. We find that the smallest resolvable features in coherent or absorption imaging are two times larger compared to the resolution limit in incoherent imaging $\lambda/(2\,\mathrm{NA})$. Figure 3.15a shows the modulation transfer function for the coherent and incoherent case with the same numerical aperture. Even though this discussion suggests that the resolution limit of incoherent imaging is superior to coherent imaging, depending on the relative phase φ two coherently illuminated points can either be resolved or unresolved. The resulting intensity of two aberration free coherent point sources, as described in Equation 3.62, separated by a distance $d = 0.61\lambda/NA$, commonly referred to as the Rayleigh criterion of resolution is given by

$$I \propto \left| \frac{J_1\left(\frac{2\pi\,\mathrm{NA}}{\lambda}\left(r-d\right)\right)}{\left(\frac{2\pi\,\mathrm{NA}}{\lambda}\left(r-d\right)\right)} + \mathrm{e}^{i\varphi}\frac{J_1\left(\frac{2\pi\,\mathrm{NA}}{\lambda}\left(r+d\right)\right)}{\left(\frac{2\pi\,\mathrm{NA}}{\lambda}\left(r+d\right)\right)} \right|. \tag{3.71}$$

The resulting intensity distribution is shown in Figure 3.15b for three different relative phases φ. If the phase difference is zero or an integer multiple of 2π, the two point sources cannot be resolved. For a phase difference of $\pi/2$ we recover the same intensity distribution as obtained for two incoherent point sources, i.e., we would call it resolved. However when picking a relative phase of π, the intensity in between the two point sources drops to zero and the contrast is better than the incoherent case. As we are performing absorption imaging in the experiment, and we are not able to freely choose the phase of the wave for every atom, we therefore end up with the a fixed phase for all atoms corresponding to the case of $\varphi = 0$. In principle we could image the cloud with a quickly varying speckle pattern in order to recover the incoherent case as we are averaging over many different phase realizations.

Anomalous Floquet phases in the intensity modulated optical honeycomb lattice

In a system in the anomalous Floquet phase, the bulk-boundary correspondence is insufficient to predict the existence of edge states. The lower of the two bands exhibits $\mathcal{C}^- = 0$ but there are still chiral edge modes located at the edge of the system [86, 87]. Proper characterization of the topological invariants requires a characterization of at least one winding number and the knowledge of the Chern number of all other relevant bands or alternatively determination of all winding numbers. While the anomalous Floquet phase has successfully been implemented in many systems where the existence of edge modes could be probed [112, 113, 164–170], a full topological characterization of the anomalous Floquet phase was first realized in this experiment [111].

In this chapter we will characterize the topological invariants of the Haldane, anomalous and Haldane-like regimes. Following a path through the phase diagram we determine the parameters for which the closing of the gap occurs. By connecting the topological invariants of the system in the high-frequency limit to those at lower modulation frequency, we can track their evolution at the phase transitions to the anomalous and Haldane-like phase. We experimentally probe the Berry curvature using Hall deflections and deduce the change of the winding numbers when combining this information with the gap closing. The entire characterization relies on probing the bulk properties of the bands and does not require additional information e.g. about the edge of the sample.

This chapter summarizes the main findings; further details, such as the characterization of the second band or the mapping of the entire phase diagram can be found in [111] and are covered extensively in the PhD-thesis of Karen Wintersperger [174], where also details on the 6-band Floquet calculation are presented.

The following chapter is based on the joint work of Karen Wintersperger, Christoph Braun, F. Nur Ünal, André Eckardt, Marco Di Liberto, Nathan Goldman, Immanuel Bloch and Monika Aidelsburger [111].

4.1 The driving protocol

Realizing an analogue to a magnetic field acting on a charged particle, e.g. an electron, requires special efforts if the particle is neutral [80, 91, 297]. Several approaches have been successful in implementing the analogue of a magnetic fields in cold atoms, e.g. by rotating the gas [298, 299], driving Raman transitions in the bulk [300] or in a lattice [89, 144, 148, 301].

Techniques that are readily implemented on the experiment presented above involve phase shaking, i.e., the modulation of the phase of the optical lattice which can modify the tunneling in amplitude and phase [84, 156, 302–304], and chiral modulation of the tunneling amplitude, which was implemented on this experiment for the first time in a cold atom setting [86, 111].

The modulation of the tunneling amplitude is implemented by periodically varying the intensity in each of the laser beams. We break time reversal symmetry by choosing the modulation of each of the three lattice beams such that they exhibit a pairwise phase difference of $2\pi/3$. This leads to a variant of the modulation introduced in Section 2.4, where we modulate the intensity of the beams in a sinusoidal fashion, which leads to a slight modification of the modulation of the tunneling. The intensity of the three lattice beams is modulated according to

$$I_i(t) = I_0 \left(1 - m + m \cos\left(\omega t + \varphi_i\right)\right), \tag{4.1}$$

where m is the relative modulation amplitude, ω the modulation angular frequency, I_0 the base intensity leading to a balanced lattice, $\varphi_i = \kappa \frac{2\pi}{3}(i-1)$ the initial phase and $i \in [1, 2, 3]$ is the index of the laser beam. The parameter $\kappa = \pm 1$ indicates the chirality of the modulation i.e., if the modulation is performed with positive or negative sense of rotation. The resulting intensity modulation is depicted in Figure 4.1a. To illustrate the difference compared to the previously discussed case (cf. Section 2.4), where we assumed a sinusoidal modulation of the tunneling amplitudes, the resulting nearest neighbor tunneling amplitudes are shown in Figure 4.1b. The tunneling amplitudes are obtained by fitting an ab initio calculation [174, 180] with a two-band tight binding model. To fit the dispersion the three nearest neighbor tunneling amplitudes J_i and the next-nearest neighbor tunneling amplitudes $\tilde{J}_i$ are free parameters. The two-band model is keeping the distance and orientation of the nearest neighbor tunneling fixed, even though the sites are slightly translated throughout the modulation period, which would lead to a slight modification of the dispersion as discussed in Section A of the Appendix. The tunneling amplitudes still follow a similar pattern as the intensity, but the relation is non-linear. To good approximation the tunneling amplitudes can be described by

$$J_i(t) = J_m \mathrm{e}^{B \cos(\omega t + \varphi_i))} + J_0. \tag{4.2}$$

For a base depth of the lattice of $6\,E_{\mathrm{rec}}$ and an amplitude of $m = 0.25$ we fit the parameters $J_m = 0.21 E_{\mathrm{rec}}$, $J_0 = -0.06 E_{\mathrm{rec}}$ and $B = 0.79$. During the course of one period the maximal tunneling is ≈ 11 times the minimal tunneling. The next nearest neighbor tunneling is also
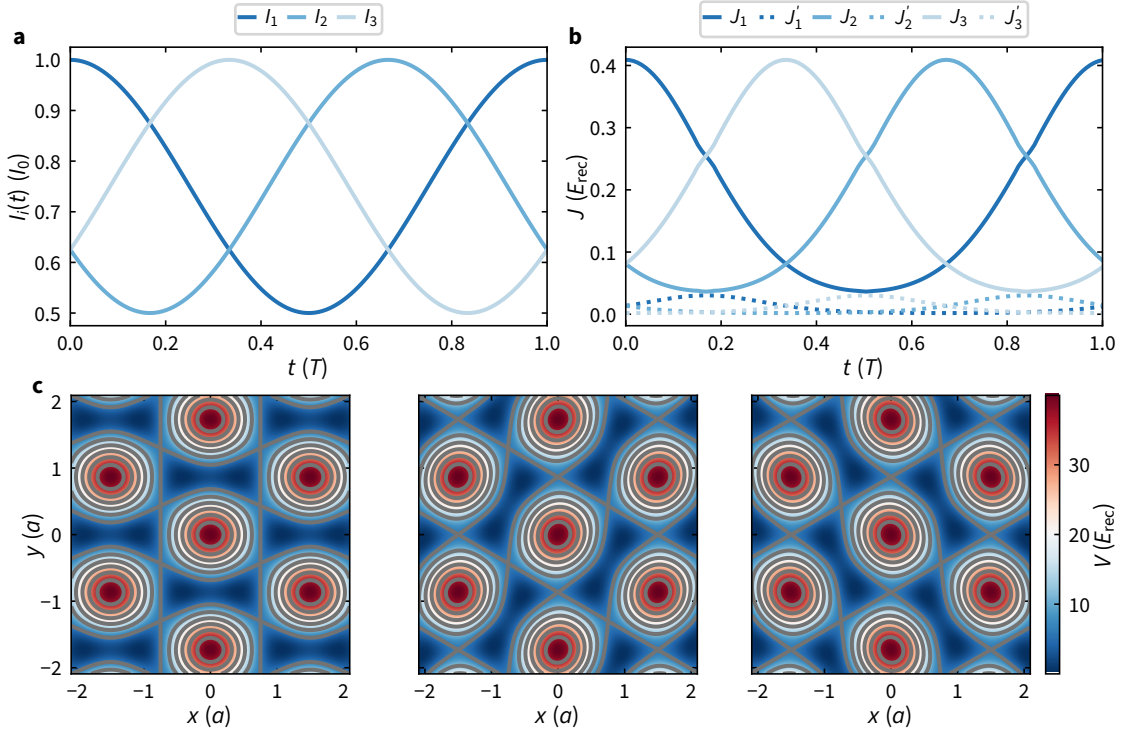
Figure 4.1 | Intensities during the modulation period resulting nearest neighbor tunneling and lattice potential a, Intensity of the lattice beams during one period. **b**, Nearest (solid) and next nearest (dotted) neighbor tunneling amplitude for a $6\,E_{\text{rec}}$ deep lattice with modulation amplitude $m = 0.25$. The two tunneling amplitudes are out of phase by $2\pi/3$, but otherwise follow a similar scaling. The maximum next-nearest neighbor tunneling is approximately 14 times smaller than the maximum nearest neighbor tunneling. **c**, Resulting lattice potential at times $t = 0T$ (left) $t = T/3$ (middle) and $t = 2T/3$ for a modulation amplitude $m = 0.25$. The base depth of the potential is $6\,E_{\text{rec}}$. The energy barrier along the three nearest neighbor tunnelings is reduced in a different direction at every time step leading to a chirality of the modulation and time reversal symmetry breaking.

modulated but is out of phase compared to the nearest neighbor tunneling

$$\tilde{J}'_i(t) = J'_m \mathrm{e}^{B' \cos(\omega t + \varphi_i + 2\pi/3))} + J'_0, \tag{4.3}$$

where we find the parameters to be $J'_m = 5.41 \times 10^{-3}\,E_{\text{rec}}$, $J'_0 = 0.93 \times 10^{-3}\,E_{\text{rec}}$ and $B' = -1.69$. The J_i are oriented along the $\boldsymbol{\delta}_i$ and the J'_i along the $\mathbf{a}_i$ as illustrated in Figure 2.1. The resulting fit parameters are stated without an error estimate, as the resulting uncertainty is dependent on the choice of grid size, which was chosen to be a 25×25 grid in the Brillouin zone. The stated values serve more as a reference for the energy scales involved and yield approximate results, as the influence of bands other than the two lowest band is still relevant [111, 174]. However the essential physics is entirely described by the two band model.
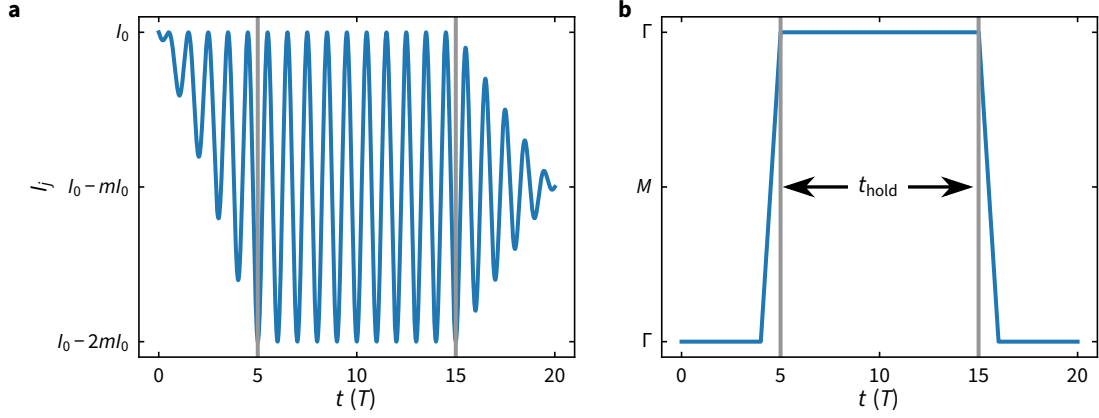
Figure 4.2 │ **Amplitude modulation and center of mass quasimomentum during the Stückelberg interferometry sequence a**, Intensity modulation of the lattice beams. The intensity of each lattice beam $I_j(t)$ is ramped up linearly during the first $5T$ of the modulation. The modulation amplitude is unchanged for a hold time $t_{hold} = NT$, with $N \in \mathbb{N}$ and then linearly ramped down again. The final value of the Intensity is $I_0(1-m)$, from which the lattice is then adiabatically ramped down, performing bandmapping. The population in the respective bands can be resolved after time of flight (not shown). **b**, Center of mass quasimomentum during the Stückelberg sequence. The quasi momentum of the cloud is changed non-adiabatically from Γ to Γ of the adjacent Brillouin zone here. The acceleration is chosen such that we arrive at Γ once the maximum modulation amplitude is reached. The return path is chosen equivalently, once the modulation amplitude is starting to be ramped down we start to also accelerate the cloud back to the center of the Brillouin zone. The acceleration to any other quasi momentum is performed equivalently only the end point is different.

4.2 The gap closings

As we have seen in Section 2.5.4 we require two ingredients for the phase transition to occur: 1) a closing of the quasi-energy gap in either the 0- or π-gap and 2) a sign change of the Berry curvature at the singularity, i.e., the band touching point.

In order to experimentally characterize the band gap we employ Stückelberg interferometry [275–277] as described in Section 3.3. The experiment starts with a BEC prepared at Γ in the lowest band of the lattice with a depth of $V = 6E_{rec}$. The lattice wavelength for the results presented in this Chapter 4 is $\lambda_L = 736.8\,\text{nm}$. To prepare the system adiabatically in the ground state of the modulated lattice and avoid kicking the system we ramp the modulation up slowly during the first $5T$ [92]. The modulation is increased linearly, then held constant during the hold time t_{hold}, and eventually ramped down again during $5T$ (cf. Figure 4.2a), subsequently the lattice is ramped down adiabatically to map the population in the two bands to momenta corresponding to the first and second band. The resulting population in the two bands can then be determined from an absorption image obtained after a time of flight $t_{tof} = 3.5\,\text{ms}$. As the system is periodically modulated, the sampling duration of the hold times is fixed to be a multiple of the modulation period NT with $N \in \mathbb{N}$.

We apply a strong force $Fa/h \approx 4\,\text{kHz}$ to accelerate the BEC to the quasi momentum **Q**, at which we want to probe the band gap. The trajectory in reciprocal space during the Stückelberg sequence is depicted in Figure 4.2b for $\mathbf{Q} = \Gamma$. The force is chosen such that

the population of the two bands are coupled, which coherently transfers population between the bands during the acceleration from Γ to the edge of the Brillouin zone eventually creating a superposition of the two bands at $\mathbf{Q}$. During the hold time at $\mathbf{Q}$ the cloud acquires a differential phase proportional to the energy difference of the bands, which leads to constructive or destructive interference when the cloud is accelerating back from $\mathbf{Q}$ to Γ, where again the population of the two bands is coupled coherently. For observation at NT the accumulated phase corresponds to the energy difference resulting from the effective Hamiltonian. The acceleration along the path $\Gamma \to M \to \Gamma$ in order to probe $\mathbf{Q} = \Gamma$ occurs in $t_\Gamma = 0.163\,\mathrm{ms}$, the acceleration $\Gamma \to M$ to probe $\mathbf{Q} = M$ in $t_M = 0.82\,\mathrm{ms}$ and the Force to reach $\mathbf{Q} = K$ from Γ is applied for $t_K = 0.094\,\mathrm{ms}$. The times are smaller or comparable to the ramp duration of the modulation ramp up, the start of the acceleration is adjusted in order to arrive at $\mathbf{Q}$ once the modulation is fully ramped up and the hold time begins.

The experimental realization is not a perfectly isolated two band system. Direct, i.e., single photon processes of the drive, or indirect multi-photon excitations can couple higher bands to the two bands of interest. This can lead to a slight deformation of the band if the process is off resonant or to an avoided crossing if the bands are coupled resonantly. The p-bands, the four next higher bands of the honeycomb lattice after the two s-bands, can couple to the two s-bands during the drive and create an additional population in a third band. This leads to an additional accumulation of phase during the hold time, resulting in a oscillation at a different frequency. To account for this additional phase accumulation and the resulting two frequency oscillation we fit a sum of two cosine functions to the resulting population in the first band as a function of the hold time

$$n^1(t) = \mathrm{e}^{-(t-t_1)\gamma} A_1 \cos(\omega_1(t - t_1)) + A_2 \cos(\omega_2(t - t_2)) + n_0^1. \qquad (4.4)$$

The parameters of the function $A_1, A_2, \gamma, \omega_1, \omega_2, t_1, t_2, n_0^1$ are free fit parameters. The frequency of the main oscillation, defined by the oscillation with the largest amplitude is the one we attribute to the energy gap between the two s-bands as we expect the coupling to the higher bands to be only a perturbation leading only to a small population in those bands. For most of the modulation parameters the amplitude of the second oscillation is indeed significantly smaller confirming the weak perturbation assumption. As the transfer between the bands during the acceleration does not work perfectly for all of the modulation parameters we allow for an offset of the population oscillation n_0^1. Additionally the cloud is extended in reciprocal space, ergo the dispersion within the wave packet's momentum space width leads to a dephasing. Furthermore loss of coherence due to heating or atoms that are scattering leads to a damping of the oscillations which is captured by the damping term γ. The extent in reciprocal space is small enough to describe the oscillation by a single frequency oscillation and damping term, where the frequency of the oscillation corresponds to the center of mass of the cloud.

The modulated system exhibits two gaps in the spectrum. The gap within the Floquet Brillouin zone, the 0-gap and the gap across the edge of the Floquet Brillouin zone, the π-gap. The minimum sampling rate we can take is $1/T$, otherwise the micromotion becomes

important and we cannot describe the system with the effective Hamiltonian. Therefore the maximum frequency we can faithfully sample is

$$\omega_{\mathrm{max}} = \frac{\omega}{2}. \tag{4.5}$$

This corresponds to a faithful determination of an oscillation with two samples per period at the maximum resolvable frequency. Unless the initial phase is very unfortunate and we always sample the zero crossing of the oscillation the frequency can be clearly distinguished from $\omega = 0$. The Nyquist–Shannon sampling theorem however strictly requires the sampling rate to be larger than twice the minimal frequency that can be measured. As we can not expect a gap to suddenly jump once it is close to $\hbar\omega_{\mathrm{max}}$ we can still distinguish the frequencies 0 and ω_{max} due to the gap we observe for parameters that are close to the one with maximum frequency. Higher frequencies $\omega' > \omega_{\mathrm{max}}$ that could potentially be present in the spectrum of $n^1(t)$ are creating an alias in the frequency range 0 to ω_{max} determined by $|\omega' - N\omega_{\mathrm{max}}|$, where $N \in \mathbb{N}$ is the integer closest to $\omega'/\omega_{\mathrm{max}}$. From this discussion we find that we cannot arbitrarily measure any gap in the system- not even when only considering two bands.

The energy width of Floquet Brillouin zone is $\hbar\omega$, for any $\mathbf{Q}$ we find that the 0-gap g^0 and π-gap g^π fulfill $g^0 + g^\pi = \hbar\omega$. Therefore by sampling with a rate $1/T$ we will always determine the gap

$$\Delta E_{\mathrm{exp}} = \min(g^0, g^\pi), \tag{4.6}$$

with $g^0, g^\pi \leq \hbar\omega/2$.

Measuring the gap at a single point in the phase diagram is not sufficient to directly identify whether the observed oscillation corresponds to the 0- or π-gap. In the high frequency limit however we can safely assume $g^\pi \gg \hbar\omega$ and therefore we can unambiguously identify the observed oscillation to correspond to a measurement of g^0. Upon lowering the modulation frequency, the two band gaps will become more and more similar in magnitude until $g^0 = g^\pi = \hbar\omega/2$. Afterwards $g^\pi < g^0$ and we therefore probe the π-gap, as now $g^\pi < \hbar\omega_{\mathrm{max}}$. Whenever the observed gap becomes equal to the maximum resolvable gap, the measured gap, after further reducing the modulation frequency, is the opposite gap compared to the one observed before the maximum. An equivalent description based on the alias of the larger of the two gaps gives an equivalent picture, meaning that due to the sampling frequency both, the frequency resulting from the π-gap, and the 0-gap result in the same detected frequency.

Figure 4.3a shows the raw data averaged over $3 - 4$ individual realizations of the population in the lowest band n^1 as a function of hold time t_{hold} and modulation frequency $\omega/(2\pi)$ probing the quasi-energy gap at Γ. We measure at a fixed modulation amplitude of $m = 0.25$ while changing the frequency. We immediately see how the modulation of the population in the lowest band becomes slower as the modulation frequency is reduced and eventually diverges at the gap closing around $\omega/(2\pi) \approx 11\,\mathrm{kHz}$, where there is no temporal modulation visible. Subsequently for further reduction of the frequency, the gap reopens,
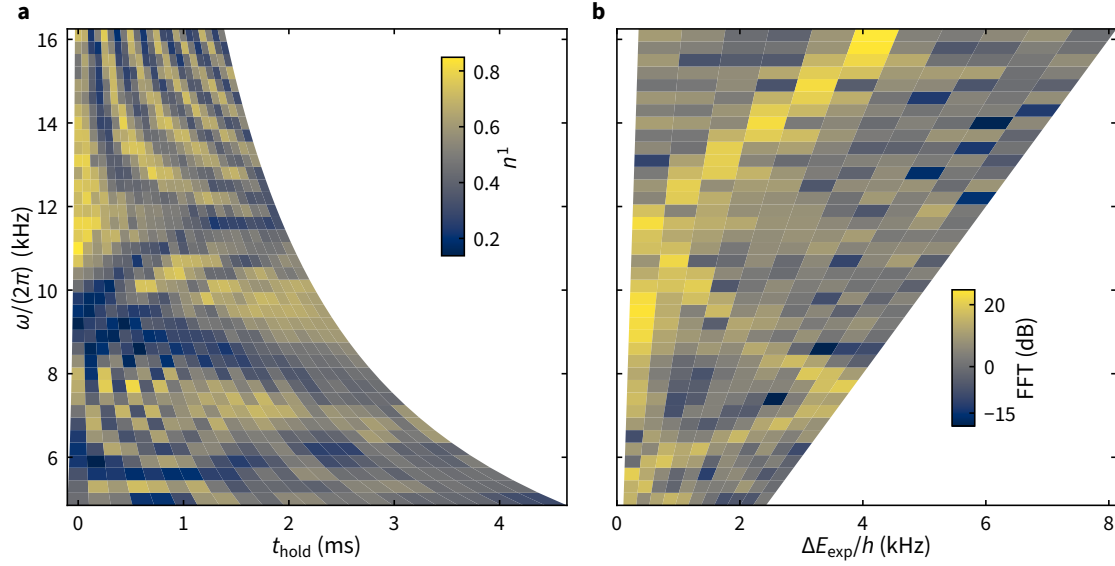
Figure 4.3 | Time trace of the population oscillation for various modulation frequencies and corresponding spectra. a, Resulting population oscillations. The population oscillation is measured using Stückelberg interferometry for various frequencies in the range $\omega/(2\pi) \in [5\,\text{kHz}, 16\,\text{kHz}]$ and fixed modulation amplitude $m = 0.25$ at Γ. The relative population of the lowest band $n^1(t)$ is measured varying the hold time for each modulation frequency. Each datapoint represents the mean of $3 - 4$ independent realizations. **b**, Spectrum of the population oscillation. We calculate the fast Fourier transform of the oscillations shown in **a** for every modulation frequency. The zero frequency component is not displayed. The gap opening and closing can be directly observed from the spectrum.

becomes maximal, where we observe alternating minima and maxima at every multiple of the sampling time at $\omega/(2\pi) \approx 8\,\text{kHz}$. Eventually we observe another gap closing around $\omega/(2\pi) \approx 5.5\,\text{kHz}$ before the frequency scan terminates. From the observed measurement we can clearly identify two gap closings and one peaking of the gap at $\hbar\omega/2$. An almost equivalent depiction is shown in Figure 4.3b, where we display the Fourier transform of each time trace. The spectrum nicely highlights the aforementioned reduction of the gap, as can be seen by the shift of the maximum frequency component of the spectrum towards lower frequency, which reaches zero at $\omega/(2\pi) \approx 11\,\text{kHz}$. The spectrum also captures the peaking of the gap at $\hbar\omega/2$ at $\omega/(2\pi) \approx 8\,\text{kHz}$. The presented measurement underlines the versatility of the Stückelberg interferometry approach to quantitatively determine the energy gap of the system in a momentum resolved way. Even though the measurement at a single modulation frequency is not sufficient to directly determine, whether the 0- or π-gap is currently the smaller of the two, a frequency scan starting from the high frequency limit allows to also identify the observed gap unambiguously. The measurement presented in Figure 4.3 does not directly connect to the high frequency limit.

To directly probe the system in the high frequency limit and extract the full information about which gap is measured we perform a slightly different sweep through the phase diagram as depicted in Figure 4.4. The phase diagram is calculated numerically and the phase boundaries are also confirmed experimentally over a wide parameter range [111, 174]. The measurement starts at $\omega/(2\pi) = 40\,\text{kHz}$ and $m = 0.1$, where any energy scale of the
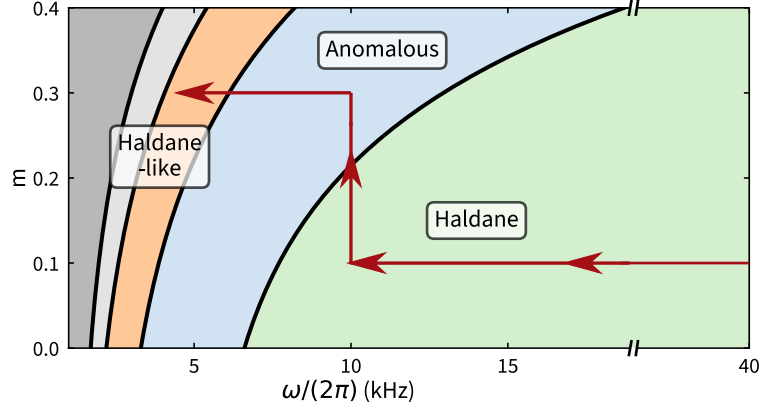
Figure 4.4 | **Path through the phase diagram.** The depicted path through the phase diagram smoothly connects the high frequency limit, where the system is in the Haldane regime, to the anomalous and Haldane-like phase. The trajectory combines a frequency sweep in the Haldane phase with an amplitude sweep crossing the transition from the Haldane to the anomalous phase and a final frequency sweep to probe the transition from the anomalous to the Haldane-like phase. The path is chosen such that the expected size of the gaps is experimentally easily accessible avoiding low frequency and low modulation amplitude resulting in very small gaps as well as high frequency and large modulation amplitude, where coupling to higher bands might become problematic.

system is significantly smaller than $\hbar\omega$, i.e., the system is in the high frequency limit and we can be sure that $g_0 \ll g_\pi$. We reduce the modulation frequency while keeping the modulation amplitude fixed down to $\omega/(2\pi) = 10\,\mathrm{kHz}$. This part of the sweep is entirely located within the Haldane regime, where due to the modulation the gap at K and K' has opened. The frequency sweep is followed by an increase of the modulation amplitude to $m = 0.3$ at fixed $\omega/(2\pi) = 10\,\mathrm{kHz}$, during which we expect the system to undergo a topological phase transition from the Haldane to the anomalous regime. The final part of the path through the phase diagram is another frequency sweep reducing the modulation frequency to $\omega/(2\pi) = 4.6\,\mathrm{kHz}$ at modulation amplitude $m = 0.3$. Here we find another phase transition from the anomalous regime to the Haldane-like regime.

This described path allows a smooth connection of the different phases to the high frequency limit where the topological characterization is known and we find bands with $\mathcal{C}^- = 1$ [84, 85].

To fully characterize the topological nature of the phase transitions we first identify where, and which gap is closing in the spectrum and consecutively measure how the Berry curvature is modified as we traverse the phase transitions. We perform Stückelberg interferometry at closely spaced points along the smooth path depicted in Figure 4.4 and extract the energy gap at the three high symmetry points of the Brillouin zone Γ, M and K. The measured energy gap at Γ is shown in Figure 4.5. In the high frequency limit we determine a band-gap that is close to the bandwidth of a static system as modulation is only introducing a weak perturbation. We measure the 0-gap. As we reduce the modulation frequency, we observe a peaking of the measured gap at a value of $\hbar\omega/2$ around $\omega/(2\pi) \approx 15\,\mathrm{kHz}$, and we find $g^0 = g^\pi$. Until we observe another maximum of the measured gap we now have identified
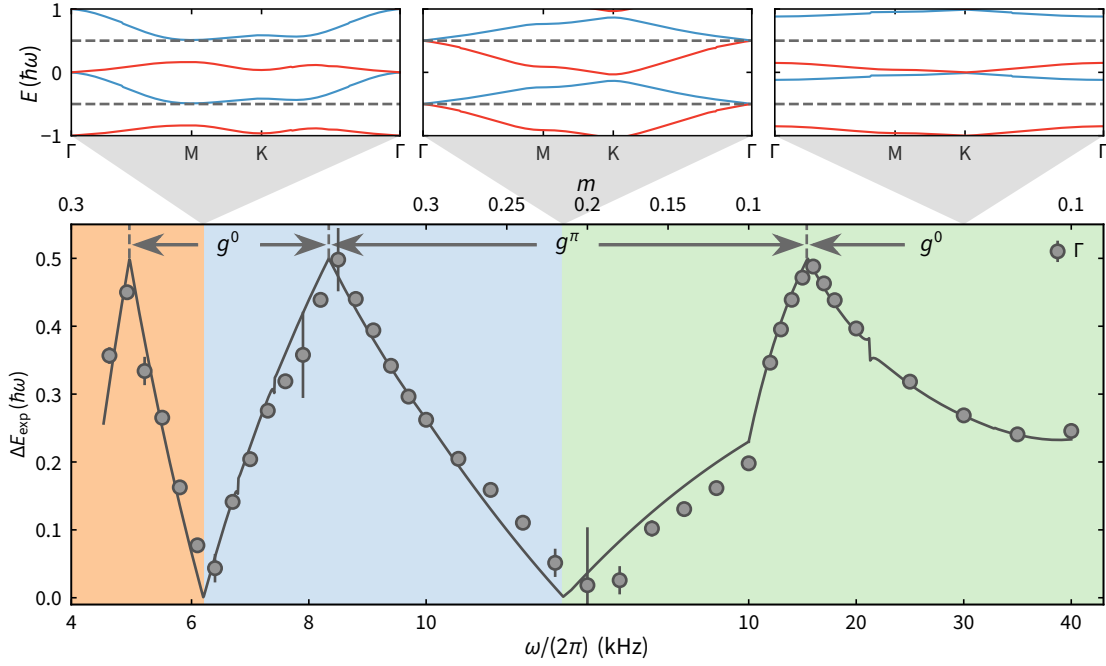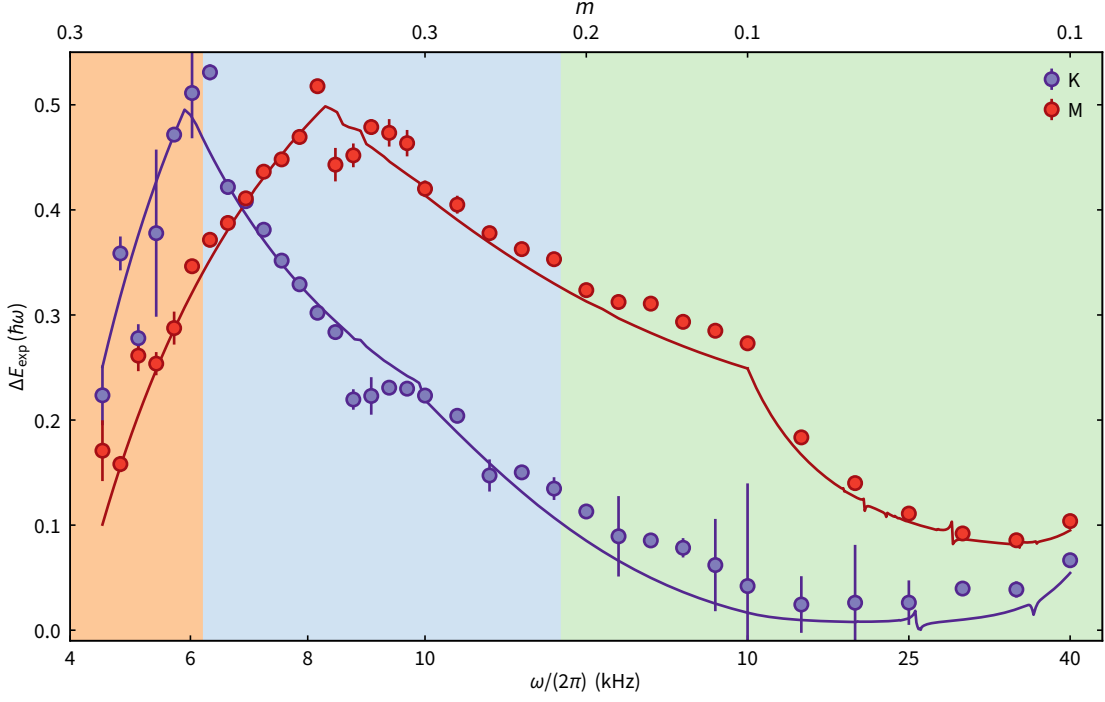
Figure 4.5 │ Observed minimal gap along the path through the phase diagram at Γ. The measured gap at Γ is the result of a fit to a Stückelberg interferometry sequence consiting of 23 time samples, where each is averaged over $3 - 4$ individual realizations. The solid line is the theoretical value obtained from a six band Floquet calculation of the modulated lattice. The different color shadings indicate the different topological phases, green Haldane, blue anomalous and orange Haldane-like. The phase transitions occur at the gap closing. At the cusps the measured gap changes as indicated by dashed lines and the indicator at the top. The resulting spectrum along the high symmetry line in the Haldane, at the phase transition to the anomalous phase and the transition to the Haldane-like phase is depicted in the top row for $m \in \{0.1, 0.215, 0.3\}$ and $\omega/(2\pi) \in \{30\,\text{kHz}, 10\,\text{kHz}, 6.2\,\text{kHz}\}$. The two band structures at the phase transition illustrate the band touching in the π- and 0-gap. Error bars denote fitting errors.

that we do measure the π-gap. Following the path through the phase diagram we find a gap closing at $m \approx 0.2$ and $\omega/(2\pi) = 10\,\text{kHz}$, where the π-gap is closing and the bands hybridize across the edge of the Floquet Brillouin zone. This gap closing indicates a possible change of the winding number characterizing the π-gap W^{π}. Another cusp of the experimentally determined gap is located at $m = 0.3$ at $\omega/(2\pi) \approx 8\,\text{kHz}$, where we now find $g^{\pi} = g^{0}$ and we therefore subsequently directly measure the 0-gap, which is closing at $\omega/(2\pi) \approx 6\,\text{kHz}$, where W^{0} might change. The solid line is the theoretical expectation for the gap between the two lowest bands extracted from a six band ab initio Floquet calculation [111, 174].

The upper panel of Figure 4.5 shows the band structure along the high symmetry line $\Gamma \to M \to K \to \Gamma$ calculated by projecting onto the lowest to bands of the six band ab initio Floquet calculation close to the phase transitions illustrating how the bands touch in the respective gaps as described above [111, 174].

To exclude any other gap closing and therefore additional possible phase transitions we also measure the energy gap at M and K. Measuring the gap at the three high symmetry points Γ, M and K is sufficient as gap closings can only occur at these points in our

Figure 4.6 │ **Observed minimal gap along the path through the phase diagram at *M* and *K*.** The measured gap is the result of a fit to a Stückelberg interferometry sequence consiting of 23 time samples, where each is averaged over $3 - 4$ individual realizations. The solid line is the theoretical value obtained from a six band Floquet calculation of the modulated lattice. The different color shadings indicate the different topological phases, green Haldane, blue anomalous and orange Haldane-like. The gap remains open across all phase transitions indicating no additional gap closing. Error bars denote fitting errors.

modulation scheme [163]. Figure 4.6 shows the observed gap at K and M along the path through the phase diagram (cf. Figure 4.4). We observe no gap closing at either of the two points in the Brillouin zone for the parameters investigated. However we also here observe a cusp in the observed gaps indicating that the π-gap in between the Floquet Brillouin zone is smaller compared to the 0-gap for $\omega/(2\pi) < 6\,\mathrm{kHz}$.

4.3 Deflection measurements

Several methods have been demonstrated in cold atom platforms to be able to experimentally detect Berry curvature [109, 284, 305]. The approach we will pursue here is based on locally resolving the Hall drift arising from Berry curvature traversed by the cloud [84, 108, 131]. The Berry curvature acts on the cloud in a similar fashion compared to a magnetic field leading to a transverse deflection [131, 306, 307] and is described by the semi-classical equation

$$\mathbf{v}_n(\mathbf{k}) = \frac{\partial \varepsilon_n}{\hbar \partial \mathbf{k}} - \frac{1}{\hbar}\mathbf{F} \times \mathbf{\Omega}(\mathbf{k}), \tag{4.7}$$

where $\mathbf{v}_n$ is the velocity a particle in the nth band with quasienergy dispersion $\varepsilon_n(\mathbf{k})$ experiences when a force $\mathbf{F}$ is applied. The Berry curvature $\mathbf{\Omega}(\mathbf{k})$ is assumed to extend the space to a third dimension perpendicular to the plane of quasimomentum and acts in analogy to a magnetic field leading to a transverse anomalous velocity. A filled band will only experience a net effect of the Berry curvature if the Chern number is non-zero otherwise the positive and negative contributions of the Berry curvature exactly cancel. The force accelerating the cloud has to be chosen such that the cloud adiabatically follows only a single band and no excitations to higher bands are created. We have experimentally probed the maximum force in order to not excite to higher bands, which would lead to a reduction of the observed perpendicular deflection. When applying a force to probe the Berry curvature, we observe on top of the velocity resulting from the dispersion $\partial\varepsilon_n(\mathbf{k})/\partial\mathbf{k}$ a transverse velocity proportional to the Berry curvature $\mathbf{\Omega}(\mathbf{k})$. Performing an acceleration along a path therefore leads to a transverse displacement if the Berry curvature is non-zero. Using a narrow cloud in momentum space allows for a quasimomentum resolved measurement of the Berry curvature.

When probing the entire Brillouin zone we expect to observe a net deflection in the Haldane regime, while observing no deflection in the anomalous phase, where the Chern number is vanishing. As it is not straight forward to fill the entire Brillouin zone with bosonic particles, we chose a slightly different approach to probe the entire Brillouin zone. Starting from a BEC located at the center of the Brillouin zone we measure the deflection resulting from an acceleration along different paths in reciprocal space chosen such that we effectively probe a large fraction of the Brillouin zone. The paths shown in Figure 4.7a were chosen to probe the deflection in the direction of $\Gamma \to K \to K'$ and $\Gamma \to M \to \Gamma$. We probe all six possible directions for each path to exclude any asymmetric imperfections and repeat the measurement in the Haldane and anomalous regime. The Berry curvature in the Haldane regime ($m = 0.25$, $\omega/(2\pi) = 16\,\text{kHz}$) is still concentrated at the Dirac points, while there is no Berry curvature elsewhere (cf. Figure 4.7). In the anomalous regime ($m = 0.24$, $\omega/(2\pi) = 10\,\text{kHz}$) we find, in addition to the still concentrated positive Berry curvature at K and K', negative Berry Curvature located at Γ.

The resulting deflection after performing the acceleration along the path is measured in a differential measurement. We modulate the lattice once with positive chirality, perform the experiment and record the resulting position of the cloud and subsequently repeat the experiment with opposite chirality, which leads to opposite sign, but otherwise identical, Berry curvature. Due to the inverted Berry curvature we measure a deflection in opposite direction. The difference in position between the two experiments constitutes twice the transversal deflection, while trivial motion due to the accelerated lattice is removed by this measurement technique. Figure 4.7 shows the resulting deflection along the paths in K and Γ direction for all 6 directions respectively in the Haldane and anomalous regime. We find positive deflections in the K direction for both regimes, while the deflection in the Γ direction is compatible with zero in the Haldane regime and negative in the anomalous regime.

As the Chern number results from the integration of the Berry Curvature in Brillouin zone, the observed deflections are compatible with $\mathcal{C}^- = 1$ in the Haldane regime. The deflections in the anomalous regime are well compatible with $\mathcal{C}^- = 0$ as the deflections
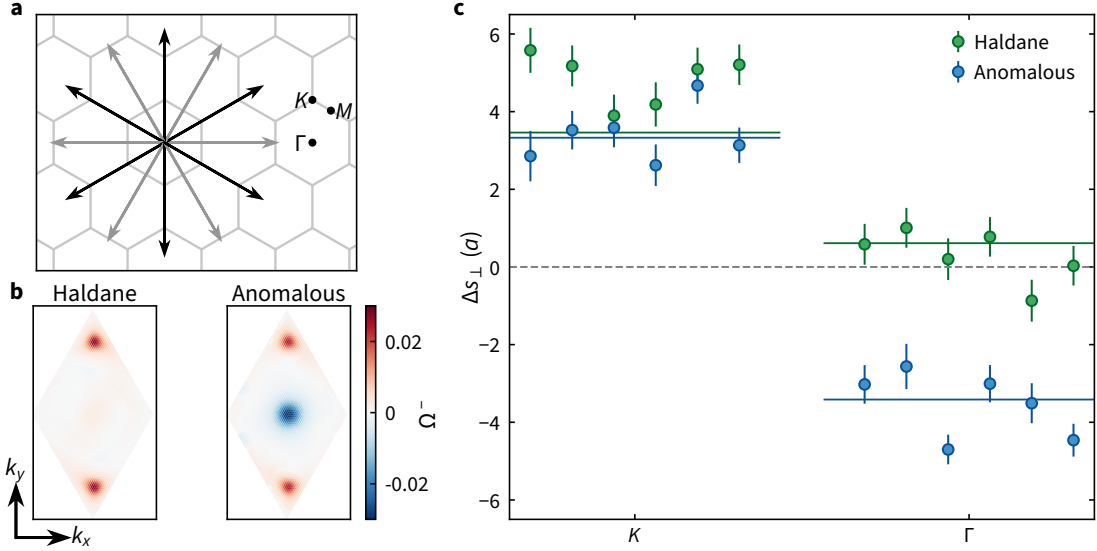
Figure 4.7 │ **Paths used to probe the Brillouin zone in the anomalous and Haldane regime and resulting measurement. a,** Paths used to probe the entire Brillouin zone. Starting from Γ the cloud is accelerated along 12 different paths to probe K and Γ along different directions. **b,** Berry curvature in the Haldane ($m = 0.25$, $\omega/(2\pi) = 16$ kHz) and anomalous regime ($m = 0.24$, $\omega/(2\pi) = 10$ kHz). **c,** Resulting transversal deflection probing the Berry curvature at K and Γ in the Haldane and anomalous regime along the different paths shown in **a.** The deflection in the Haldane regime is positive at K and small but positive at Γ. In the anomalous regime we observe a positive deflection at K and a negative deflection with equal magnitude at Γ.

are of equal magnitude but opposite sign when comparing Γ- and K-path. The solid lines represent the theoretical expectation without free parameters taking into account the Berry curvature distribution, harmonic trap and width of the cloud in reciprocal space [111, 174].

As illustrated in Section 4.2, the bands touch at Γ and simply holding a BEC at Γ while linearly ramping up the modulation amplitude in the anomalous regime will lead to an uncontrolled population in the two bands as a fraction of the population is transferred when the two bands touch. In order to avoid the band touching point we have developed ramp-up schemes for each of the three phases which keep the cloud at quasimomenta away from the band touching, while also maximizing the minimal gap. The modulation amplitude is always ramped in a linear fashion, while the frequency is swept such that the gap is maximal during the ramp-up. For the deflection measurements in the Haldane and anomalous regime this leads to an additional complication, where we have a quasi momentum $\mathbf{k}_0$ during which the system is ramped to the final modulation parameters and a final quasimomentum $\mathbf{k}_f$, at which we evaluate the deflection. The deflection during the ramp-up and acceleration to $\mathbf{k}_0$ is small, yet it is determined independently by recording the position at the end of the ramp-up and eventually subtracted from the full deflection observed after an acceleration to $\mathbf{k}_f$. The relative length of $\mathbf{k}_0$ and $\mathbf{k}_f$ is kept fixed for all directions (cf. Figure 4.8a).

Figure 4.8b shows the trajectory of m and ω during the ramp-up. For the preparation at high modulation frequency in the Haldane and anomalous regime the cloud is accelerated towards M in order to increase the gap at the position, where the cloud is located. For
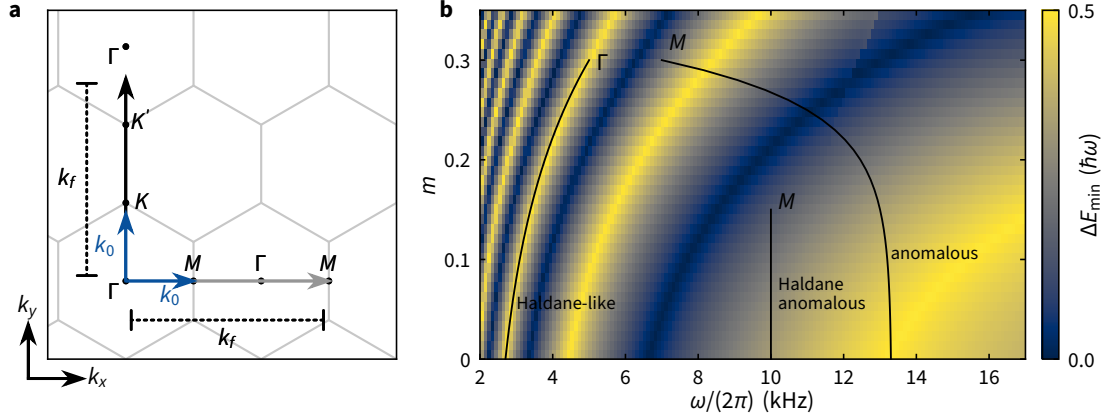
Figure 4.8 │ **Path through the Brillouin zone for deflection measurements and ramp-up trajectories for the three topological phases. a**, Path to probe the Berry curvature at Γ and *K*. The wave packet initialized in the lowest band of the static lattice is accelerated up to k_0 while the modulation is ramped up according to the path shown in **b** depending on the current phase. The deflection during the ramp-up is measured independently and subtracted from the full path. For the full path the wave packet is accelerated to k_f traversing most of the Berry curvature in the Brillouin zone. The magnitude of the final quasimomentum is equivalent along all measured directions. **b**, Paths in the phase diagram taken during the ramp-up. The wave packet is moved away from Γ to avoid transferring atoms to the second band during the band touching.

$\omega/(2\pi) > 8\,\text{kHz}$ in the Haldane and anomalous regime we use a linear ramp-up at fixed modulation frequency. In the anomalous regime for $\omega/(2\pi) < 8\,\text{kHz}$ we use the path crossing the gap closing between Haldane and anomalous phase. The cloud has already been moved away from Γ when crossing the phase transition from the Haldane to the anomalous regime, where the two bands touch, enabling high fidelity preparation of the cloud in the "lowest" band. In the Haldane-like regime however we do not need to have an acceleration during the ramp-up as Γ of the lowest band is always gapped, even for $m = 0$, enabling a direct ramp to prepare the cloud in the lowest band at Γ. We directly ramp the modulation amplitude up, while adjusting the modulation frequency to maximize the gap during the ramp.

If we had kept the cloud at rest at Γ and ramped the modulation up in the anomalous regime without crossing a phase transition, e.g. by keeping $\omega/(2\pi) = 6\,\text{kHz}$ fixed and linearly increasing the modulation amplitude, we would have ended up with the entire population in the second band of the Floquet band structure. As Γ and the minimum of the dispersion surrounding it which originally were part of the lowest band in the static lattice are now attached to the second band in the modulated case the cloud is "transferred" to the upper band. The attribution "lowest" band is not very well defined in the modulated band structure especially when the resulting bands emerge due to a coupling between the bands of the static lattice as is the case in the anomalous regime. However in principle a local attribution is still possible, where e.g. the minimum at Γ in the anomalous regime is characteristic of the lowest band in the static lattice, while the minima at the Dirac points are reminiscent of the second band.
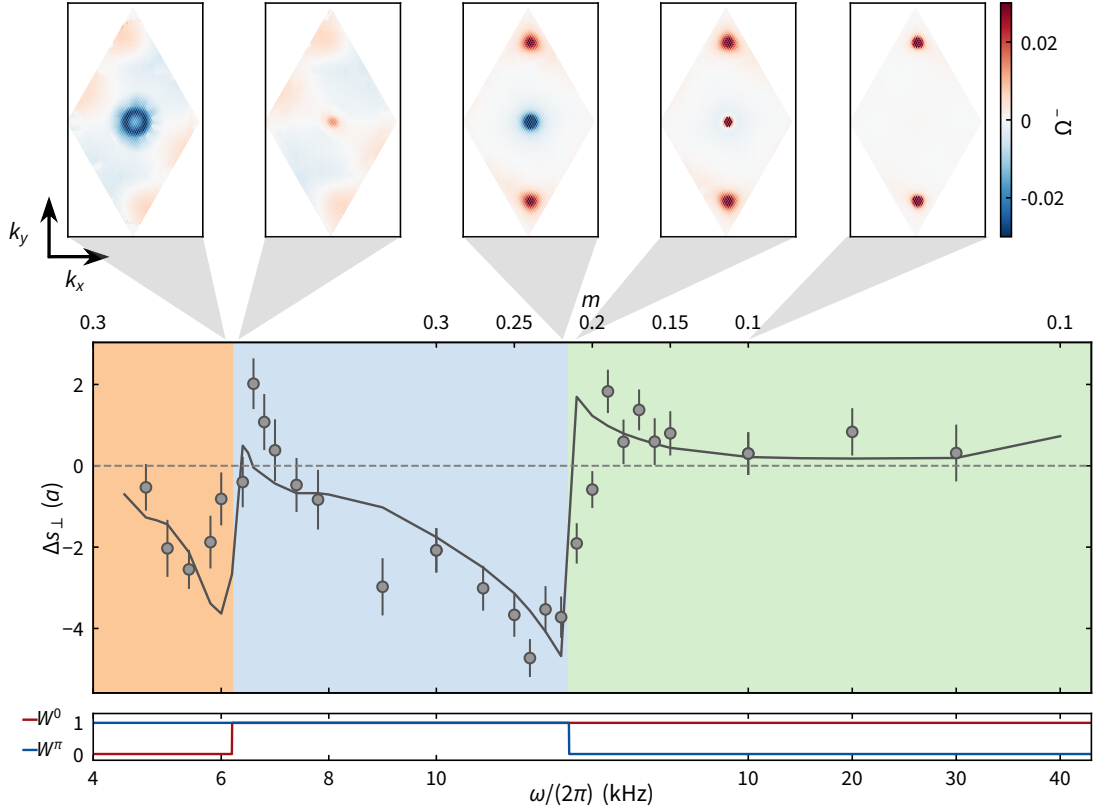
Figure 4.9 | Deflection at Γ probing the Berry Curvature across the phase diagram. The measured deflection (data points) probes the Berry curvature in a quasi-momentum resolved manner by accelerating the cloud across Γ. Each data point is an average over $30 - 40$ realizations with the error bars representing the standard error of the mean. The solid line is the theoretical expectation taking into account the momentum space width of the cloud and without free parameter. The background shading illustrates the three distinct phases being probed. In the bottom panel the winding numbers are shown. The top row highlights the Berry curvature in the Haldane regime (right) and at the phase transitions between the anomalous and Haldane-like regime (left) and the anomalous and Haldane regime (center). The residual asymmetry of the Berry curvature is related to the choice of initial phase. The depicted Berry curvatures are evaluated for parameters (left to right) $\omega/2\pi = \{6\,\text{khz}, 6.4\,\text{khz}, 10\,\text{khz}, 10\,\text{khz}, 10\,\text{khz}\}$ and $m = \{0.3, 0.3, 0.22, 0.21, 0.1\}$.

Having a consistent way to probe the same band throughout the phase diagram as illustrated in Figure 4.8b, we proceed to probe the Berry curvature at Γ along the path through the phase diagram presented in Figure 4.4. We accelerate the cloud from $\Gamma \rightarrow M \rightarrow \Gamma \rightarrow M$ to probe the deflection induced due to the Berry Curvature at Γ in the Haldane and anomalous regime. As described before the initial path $\Gamma \rightarrow M$ is traversed during the ramp-up in the Haldane and anomalous phase. The observed deflections in the Haldane regime are slightly positive even though there is no Berry curvature located at Γ (cf. Figure 4.9 top right). This stems from the fact that the cloud is extended in reciprocal space and a small fraction of the cloud still experiences the positive Berry curvature at K and K' leading to a positive deflection. When approaching the phase transition we

observe an increase of the detected deflection which results from the buildup of positive Berry curvature at Γ before the phase transition. The measured deflection flips sign at the phase transition and a distinct negative deflection is observed. The Berry curvature follows the same pattern: the positive peak before the phase transition flips sign and turns negative as illustrated by the Berry curvature at the phase transition. When getting further away from the transition, the Berry curvature spreads into a ring leading to constant negative deflection. Shortly before the phase transition to the Haldane-like regime we again observe a positive deflection and a jump to negative deflection at the phase transition to the Haldane-like regime at $\omega/(2\pi) \approx 6.2\,\text{kHz}$. The deflection in the Haldane-like regime is probed by ramping the modulation up while keeping the cloud located at Γ, and probing the path $\Gamma \to M \to \Gamma$. This results in an equivalent deflection compared to the path $M \to \Gamma \to M$, which is effectively probed in the Haldane and anomalous regime after the ramp-up. After the phase transition we again observe a reduction of the magnitude of the deflection when further going away from the phase transition. The deflections match quantitatively well with the theoretical model taking into account the momentum space width, path in reciprocal space, and the harmonic trap. The Berry curvature is derived from the six band Floquet calculation [111, 174]. The background shading illustrates the different topological phases as derived from the gap closing at Γ.

4.4 Obtaining the winding numbers - experiment

Combining the deflection and gap measurement we are now able to determine the winding numbers in the gaps throughout the phase diagram. The measurement of the quasienergy gap provides information regarding which gap is closing, while the deflection measurements show how the Berry Curvature is changing and whether its sign change is positive or negative at the phase transition, i.e., at the singularity. The band touchings are linear band touchings, and therefore the Chern and equivalently winding numbers can only change by ± 1.

We have already established that the Chern number of the lowest band in the Haldane phase is $\mathcal{C}^- = 1$, while the π-gap is trivial and therefore the winding number in the 0-gap is (cf. Equation 2.84)

$$W^0_{\text{Haldane}} = \mathcal{C}^-_{\text{Haldane}} + W^\pi_{\text{Haldane}} = 1. \tag{4.8}$$

The π-gap hosts no edge modes in the Haldane regime and we therefore only have a single edge-mode in the 0-gap.

As discussed in Section 2.5.3 for a linear band touching the observed sign change of the Berry curvature allows for the determination of the topological charge at the singularity which in turn can be directly related to the winding number. The winding number can only change if the respective gap is closing. At the phase transition from the Haldane

to the anomalous regime we observe a gap closing of the π-gap. The deflection changes from positive to negative, i.e.,

$$\mathrm{sgn}(\Delta s_\perp^-(\Gamma)) = \mathrm{sgn}(\Delta(\mathbf{\Omega}^-(\Gamma)) = -1 = -Q_s^\pi \tag{4.9}$$

and the change of the winding number in the π-gap is therefore (cf. Equation 2.97)

$$\Delta W^\pi = 1. \tag{4.10}$$

The winding numbers and Chern number of the bands in the anomalous phase are

$$
\begin{aligned}
W_{\mathrm{anomalous}}^0 &= 1 \\
W_{\mathrm{anomalous}}^\pi &= 1 \\
C_{\mathrm{anomalous}}^- &= W_{\mathrm{anomalous}}^0 - W_{\mathrm{anomalous}}^\pi = 0.
\end{aligned}
\tag{4.11}
$$

The winding number directly counts the number of edge modes in the gap, we therefore have two edge modes now, one in the 0-gap, one in the π-gap. Both winding numbers have the same sign i.e., the edge modes have the same slope and are therefore propagating in the same direction.

The 0-gap closes at the transition from the anomalous to the Haldane like regime. Arguing in an analogue fashion we find for the topological charge at the gap closing of the 0-gap

$$\mathrm{sgn}(\Delta s_\perp^-(\Gamma)) = \mathrm{sgn}(\Delta(\mathbf{\Omega}^-(\Gamma)) = -1 = Q_s^0 \tag{4.12}$$

Therefore the winding number in the zero gap changes by (cf. Equation 2.96)

$$\Delta W^0 = -1 \tag{4.13}$$

and we find for the Chern and winding numbers

$$
\begin{aligned}
W_{\mathrm{Haldane-like}}^0 &= 0 \\
W_{\mathrm{Haldane-like}}^\pi &= 1 \\
C_{\mathrm{Haldane-like}}^- &= W_{\mathrm{Haldane-like}}^0 - W_{\mathrm{Haldane-like}}^\pi = -1.
\end{aligned}
\tag{4.14}
$$

The slope of the edge mode is unchanged, but now is hosted in the π-gap in contrast to the Haldane phase. From a topological stand point the Haldane-like and the Haldane phase are equivalent and can be mapped onto each other by a unitary transformation changing the assignment of the lowest band. We are only able to distinguish the two phases with the additional knowledge gained by following the system through the phase diagram connecting it to the high frequency limit.

Fundamentally the system should be probed infinitesimally close to the singularity but this is experimentally not possible. Close to the band touching point the gaps become very small and remaining adiabatic with respect to these gap sizes is not feasible. Furthermore we would need to extract the Berry curvature locally at Γ only, experimentally we probe

a region given by the momentum space width of the cloud. However the sign change of the Berry curvature and the good agreement with the theoretical expectation justify the attribution of the winding numbers presented above.

The measurements presented above have allowed for a complete characterization of the topological quantities of the band structure in three different regimes. Furthermore the determination of the winding numbers enables counting the number of edge modes in every respective gap with a bulk system. In principle the system still exhibits an edge, however for the harmonically trapped system the edge is a very broad region [308].

Chiral edge modes in tunneling modulated optical lattices

The bulk-boundary correspondence directly connects the topological invariants of the bulk to the presence of edge states at the boundary of a sample [75–77, 309–311]. The Chern number counts the number of chiral edge modes in the gap above a given band minus the number of edge modes in the gap below it. These chiral edge modes are made up of states localized at the edge of the sample and form a conductive channel. Energetically the edge states are located in the gap between two bands, therefore they are immune to scattering on e.g. impurities as there are no states available to scatter into [57]. We refer to the edge of the sample as the interface to a system with different topological properties, such as the topologically trivial vacuum, compared to the system of interest, e.g. a quantum Hall system. A strong potential energy difference between two system can also result in a topological interface where the region where the potential energy is changing becomes topologically trivial. The robustness of the edge mode is directly linked to the topology of the bulk bands as they are absent once the system enters the topologically trivial regime. This way they also represent a sensitive probe to verify the topological nature of a system. For Floquet systems that can be mapped to static systems, such as the Haldane regime in the modulated vlattice, the Chern number correctly predicts the number of edge modes. However the anomalous Floquet phase presents a system, where the bulk-boundary correspondence is insufficient to predict the existence of edge states as we have a system with $\mathcal{C}^- = 0$ but still find edge states [86, 87]. As we have seen in the previous Chapter 4 the system should still host chiral edge states as predicted by the characterization with winding numbers [111, 174]. The winding numbers have been measured by observing bulk quantities of the system. The following chapter will illustrate the observation of edge modes located at a potential step in the system introduced by a programmable optical potential. We show how the edge modes are efficiently populated in different topological regimes and how they emerge as we increase the height of the potential step in the system. Furthermore we investigate how the width of the potential step affects the edge mode propagation in the Haldane regime.

> The following chapter is based on the joint work of Christoph Braun, Raphaël Saint-Jalm, Alexander Hesse, Johannes Arceri, Immanuel Bloch and Monika Aidelsburger [123].
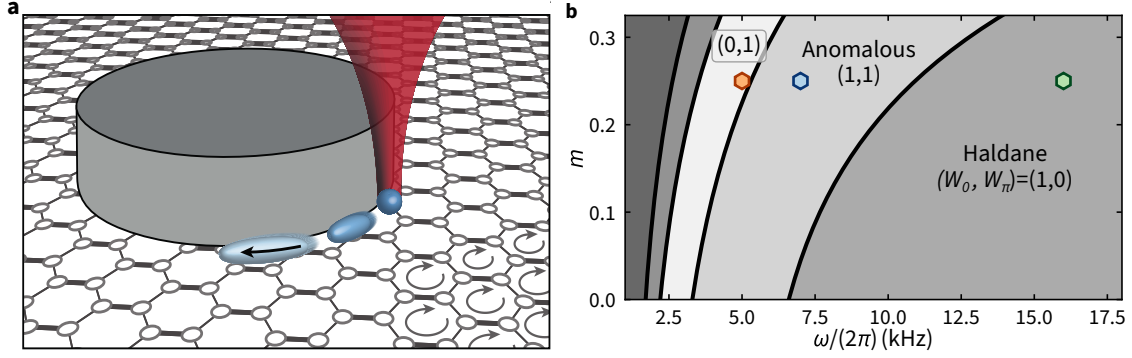
Figure 5.1 | Schematic of the setup and phase diagram. a, Illustration of the optical potential and the initial state. A potential step (gray cylinder) is applied on a selected region of the system to block the motion of particles in the modulated lattice (arrows), generating a sharp edge. The initial state is prepared by trapping a cloud of atoms (BEC, indicated in dark blue) in an optical tweezer (red) near the edge. After releasing the cloud, the atoms exhibit a chiral motion along the edge, illustrated by the different blue shadings. **b,** Phase diagram of the amplitude-modulated honeycomb lattice at depth $5.9\,E_{\text{rec}}$. The different topological regimes are characterized by the tuple of winding numbers (W_0, W_π) of the two quasienergy gaps. The hexagons mark the modulation parameters used in this work [$m = 0.25$, green: $\omega/(2\pi) = 16\,\text{kHz}$, blue: $\omega/(2\pi) = 7\,\text{kHz}$ and orange: $\omega/(2\pi) = 5\,\text{kHz}$].

5.1 Observation of edge modes

Topologically protected edge modes lie at the heart of the quantized conductivity in quantum Hall systems, both in the integer and fractional case. Should the topological invariants of a bulk system be inaccessible, the existence of robust chiral edge modes can still reveal if the system is in a non-trivial phase.

We present an experimental protocol to directly observe edge modes in optical lattices in real space. First we establish that the dynamics observed in the experiment correspond to a coherent evolution in the lattice, and that the prepared initial state occupies a large fraction of the Brillouin zone. Furthermore we show how to prepare and detect chiral edge modes in the modulated lattice and compare the their evolution to the topologically trivial case, where we observe no chiral transport. We show how to prepare edge modes in different geometries and different topological regimes.

5.1.1 Initial state preparation

The schematic experiment setup is depicted in Figure 5.1a, we prepare a small cloud of atoms in the tweezer trap (cf. Section 3.2.2) which is located close to a repulsive optical potential. To initiate the experiment we release the cloud from the tweezer into the modulated optical honeycomb lattice and observe its subsequent evolution. We have chosen three sets of parameters, where we investigate the existence and properties of the edge modes. We probe 1) the Haldane regime with $\mathcal{C}^- = 1$ and $W^0 = 1$, $W^\pi = 0$, 2) the anomalous regime where the Chern number vanishes $\mathcal{C}^- = 0$, but we still find edge modes $W^0 = 1$, $W^\pi = 1$ and 3) the Haldane-like regime where $\mathcal{C}^- = -1$ and the only edge state is located in the
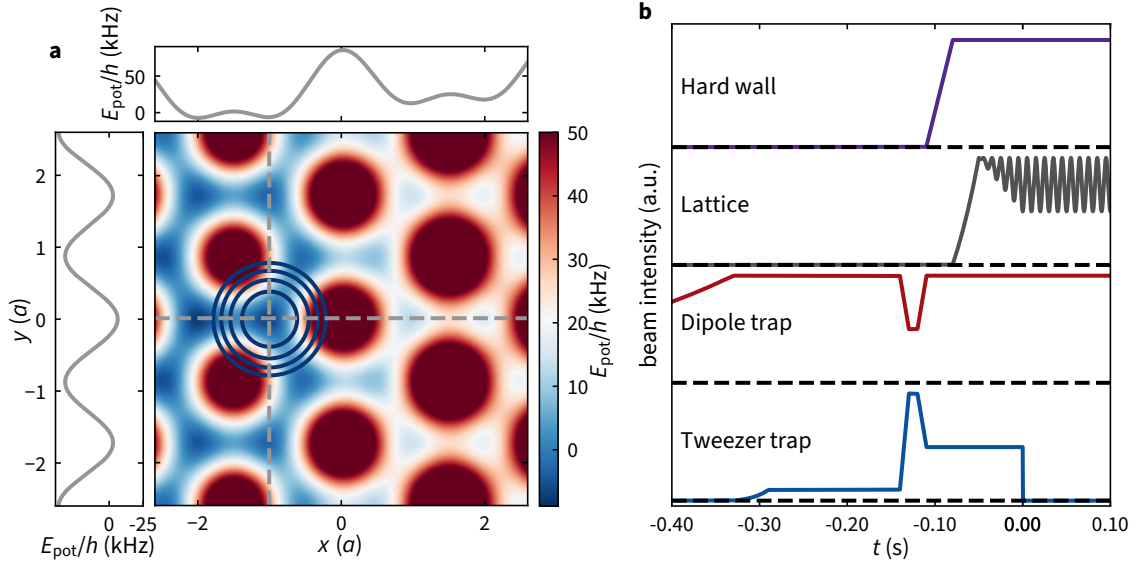
Figure 5.2 | Trapping potential of tweezer, lattice and edge potential and timing sequence. a Optical potentials before ramping up the tunneling modulation amplitude. The horizontal and vertical cut are indicated by the two gray dashed lines. The tweezer is assumed to have a waist of $1\,\mu m$ and $\omega_{tw} = 2.0$ kHz, the edge width is $\ell = 2.5a$, the height of the potential applied in the region $x > 0$ is $V_0 = 20$ kHz, the lattice depth is $5.9\,E_{rec}$. The color scale in the main image is saturating at the maxima in the center of the plaquette, to reflect the smaller energy changes of the tweezer and the wall as well. The contour lines are plotted in the same color scale and represent the potential of the tweezer alone, every contour line corresponds to an increase of $\approx h \times 0.2$ kHz. **b** Timing sequence to prepare edge modes in the intensity modulated optical honeycomb lattice. The intensity ramp of the individual beams is shown with respect to the switch off time of the tweezer trap marking $t = 0$, the starting point of the evolution in the lattice. The frequency of the modulation is reduced to show an oscillation on this coarse time scale.

π-gap $W^\pi = 1$, $W^0 = 0$. Compared to the bulk measurements presented before the phase diagram is qualitatively equivalent, but the phase transitions occur at slightly different parameters due to a change of lattice wavelength (cf. Figure 4.4 and Section 3.3) from 736.8 nm to $\lambda_L = 745$ nm. The parameters to probe the three topological regimes, Haldane (green), anomalous (blue) and Haldane-like regime (orange) are depicted in Figure 5.1b. The color attribution to the topological regimes will be kept consistent, whilst the static lattice which will be depicted in gray scale.

To probe the existence and dynamics of the edge modes we need to prepare and probe a highly excited state of the system. In contrast to a solid state sample, where the Fermi energy can be tuned to match the energy of the edge mode, we have no Fermi sea filling all states below the edge mode, but a BEC which macroscopically occupies a single state. We utilize the BEC where all atoms are in the same state to be able to achieve a good signal to noise ratio when populating the edge mode, yet careful preparation is still crucial. To prepare a wave packet in the target state we follow the sequence depicted in Figure 5.2b. After the evaporation in the crossed optical dipole trap we slightly compress it in order to generate a weakly confining potential when the blue detuned repulsive optical lattice is fully on to prevent atom loss. After the crossed dipole trap has ramped to it final value we

load a part of the cloud into the tweezer by adiabatically ramping up the tweezer beam intensity within 40 ms. The tweezer is overlapped with the center of the crossed dipole trap in order to guarantee optimal overlap between the two traps. The tweezer is not ramped to its final value yet to reduce losses occurring due to holding the cloud in the tweezer at high density for a long time. Only a small fraction of the cloud can be trapped in the tweezer.

After the loading time of 150 ms we remove all atoms which are not trapped in the tweezer as they would contribute an unwanted background signal when studying the dynamics of the cloud released from the tweezer. In order to release the unwanted atoms trapped only in the crossed dipole trap, we increase the intensity of the tweezer trap while simultaneously lowering the crossed dipole trap. The values are experimentally optimized in order to retain as many atoms in the tweezer as possible while achieving full removal of unwanted background atoms. The removal sequence consists of a 10 ms intensity ramp with a 10 ms hold time in the low power crossed dipole trap and compressed tweezer. The intensity of the tweezer is increased and is sufficient to hold the cloud against gravity, while the crossed dipole trap intensity is reduced and not sufficient to sustain atoms against gravity on its own.

After the unwanted atoms have been dropped from the crossed dipole trap we increase its intensity again back to its previous value, whilst the tweezer on the other hand is now ramped to its final value in 10 ms. After preparing atoms only in the tweezer trap we do now prepare the remaining potentials of the experiment. We switch the edge potential created by the DMD on and linearly ramp its intensity to its final value within 30 ms. Once the ramp of the edge potential is finished the optical honeycomb lattice is ramped up in an exponential fashion within 30 ms. The ramp-up of the lattice was verified to be adiabatic by ramping-up the lattice with a bulk BEC trapped in the crossed dipole trap and subsequently performing band mapping. We do not observe any excitations to the second band. Furthermore we require the system to be adiabatic compared to the harmonic oscillator levels of the tweezer with frequency $\omega_{\mathrm{tw}} \geq 1.3\,\mathrm{kHz}$. As we do not see excitations when ramping the lattice up in the crossed dipole trap, we expect to create no excitations in the tweezer. The potential energy landscape after switching on the lattice to $5.9\,E_{\mathrm{rec}}$, $E_{\mathrm{rec}} = \hbar^2 k_L^2/(2m_{\mathrm{K}}) = h \times 9.23\,\mathrm{kHz}$ is depicted in Figure 5.2a. The combination of crossed dipole trap and optical lattice leads to a residual harmonic trapping frequency in the $x - y$-plane of $\omega_r/(2\pi) = 17(1)\,\mathrm{Hz}$ and a vertical trapping frequency of $\omega_z/(2\pi) = 330(30)\,\mathrm{Hz}$. The modulation of the tunnel couplings is ramped to its maximum amplitude within the first $5T$, where $T = 2\pi/\omega$, of the drive. Once the modulation has reached its maximal amplitude, the tweezer trap is abruptly switched off projecting the state of the quantum harmonic oscillator onto the lattice. This switch-off time constitutes $t = 0$. For some experiments, an acceleration of the tweezer in order to kick the cloud as discussed in Section 3.2.2, and prepare it at a given quasimomentum is timed such that it ends at $t = 0$ as well. For a trap with the parameters of the tweezer trap $\{\omega_x, \omega_y, \omega_z\} = 2\pi \times \{2\,\mathrm{kHz}, 2\,\mathrm{kHz}, 0.33\,\mathrm{kHz}\}$, we trap $N_{\mathrm{atoms}} = 200$ (cf. Section 5.3) with a scattering length of $a_s = 6a_0$. We find a harmonic oscillator length

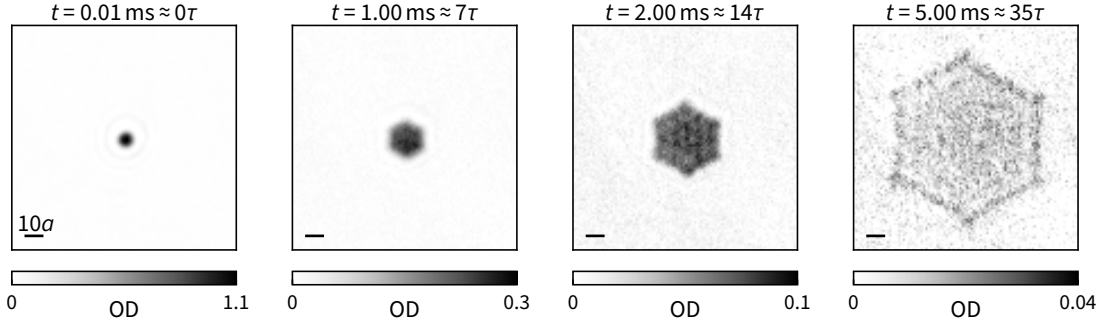$$a^{\mathrm{ho}} = \sqrt{\frac{\hbar}{m\omega}} \tag{5.1}$$

Figure 5.3 | Expansion dynamics in the static honeycomb lattice. The cloud is initially prepared in a tweezer with $\omega_{tw}/(2\pi) = 1.3(1)$ kHz and released into the static lattice with depth $5.9\,E_{rec}$. The first image is taken shortly after switching of tweezer and is representative of the initial state in the lattice. The subsequent evolution shows the coherent quantum walk of the cloud in the real space lattice. The momentum distribution of the cloud occupies a large fraction of the Brillouin zone. Every image is the average of 302 independent experiment repetitions. The tunneling time $\tau = \hbar/J_0 = 145$ ms is derived from the nearest neighbor tunnel coupling $J_0 = h \times 1.1(1)$ kHz.

of $\{a_x^{\mathrm{ho}}, a_y^{\mathrm{ho}}, a_z^{\mathrm{ho}}\} = \{0.36\,\mu\mathrm{m}, 0.36\,\mu\mathrm{m}, 0.89\,\mu\mathrm{m}\}$. The harmonic oscillator lengths in the x-y-plane are comparable to the lattice spacing $a = 287\,\mathrm{nm}$. Following the variational approach presented in [312, 313], we numerically find an effective harmonic oscillator length $\{a_x^{\mathrm{hoeff.}}, a_y^{\mathrm{hoeff.}}, a_z^{\mathrm{hoeff.}}\} = \{0.36\,\mu\mathrm{m}, 0.36\,\mu\mathrm{m}, 0.96\,\mu\mathrm{m}\}$, which shows that we are indeed in the weakly interacting regime, where the size of the condensate is only slightly modified due to interactions. The assumption for the variational approach is a harmonically trapped BEC, where the potential energy and interaction energy are not dominating the kinetic energy. The effect of the interactions is to reduce the peak density compared to the non-interacting case resulting in a spreading first along the axis of weakest confinement, here the vertical z-direction. The variational parameters are effective trap frequencies of the non-interacting ground state of a quantum harmonic oscillator. Subsequent minimization of the energy resulting from the Gross-Pitaevskii equation [314] results in the above stated values.

5.1.2 Expansion dynamics in the static lattice

To make sure that the dynamics after releasing the cloud from the tweezer trap into the lattice is coherent, we have studied the expansion of the cloud from the small dimple in the static lattice. Figure 5.3a shows the initial density distribution of the atoms $10\,\mu$s after releasing the cloud from the tweezer with a trap frequency $\omega_{tw}/(2\pi) = 1.3(1)$ kHz into the static honeycomb lattice. The measured signal is the convolution of the actual density distribution in the trap with the point-spread function of the imaging system. We expect the initial state to be significantly smaller then the point spread function of our imaging system. In the subsequent time evolution in the static lattice a hexagonal shape develops already after 1 ms. During the entire evolution we observe the characteristic hexagonal shape, which is expected to emerge during coherent expansion dynamics for a homogeneously populated band [265, 315]. Additionally, due to the interference of all the independent quasi-momenta,
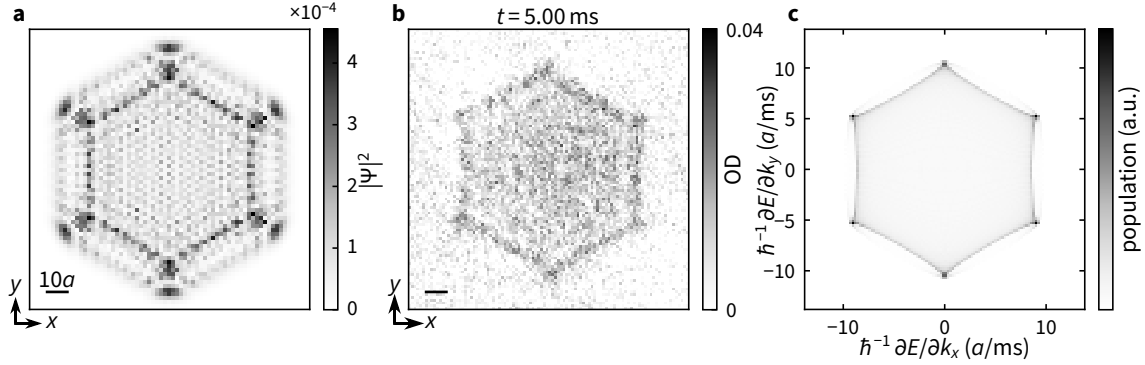
Figure 5.4 │ Comparison of experiment and numerical simulation for the expansion dynamics in the lattice. a, Two-band tight binding model. We evolve a two-band model in time on the optical lattice with parameters close to the experiment. The image is rebinned to implement a resolution similar to the experiment. **b** Experimental result of a quantum walk after 5 ms of expansion in the static lattice. **c,** Histogram of the occurring group velocities from an ab initio calculation. The scale bars represent 10a in the image, all images are scaled to show the same extent of the image. The plot limits in **c** are chosen such that they correspond to the equivalent positions after 5 ms expansion in **a** and **b**.

a coherent evolution displays an interference pattern within the hexagonal shape as can be observed in the expansion after $t = 2.0\,\text{ms}$ and $t = 5.0\,\text{ms}$ in Figure 5.3.

The hexagonal shape provides information about the spatial extent of the initial wave packet. A cloud with larger spatial extent would only occupy a small fraction of the Brillouin zone and therefore mostly occupy e.g. the minimum of the lowest band, where the dispersion would be radially symmetric. Therefore the expansion of a cloud with larger spatial extent would also be radially symmetric. If the wave packet is sufficiently localized a large fraction of the Brillouin zone is occupied and we observe the strongly varying velocity components within the Brillouin zone. This is explained by the quasi-momentum dependent group velocities $\partial_{\mathbf{k}} E(\mathbf{k})/\hbar$. From an ab initio band calculation we have evaluated the group velocity of the lowest band for all quasimomenta in the Brillouin zone and plot a histogram of the occurrence of every group velocity. In the lowest band of the honeycomb lattice we obtain the velocity distribution shown in Figure 5.4c. The image is scaled such that the plotted velocities correspond to the positions in the other figures after the 5 ms evolution time. We find the fastest velocities at the Dirac cones at K and K' and slightly lower group velocity towards M, therefore the expansion resembles the shape of the Brillouin zone. The semiclassical group velocity is sufficient to describe the shape of the expansion but does not capture the interference observed inside of the hexagon.

A two-band tight binding simulation with parameters close to the experimental realization is able to capture the interference fringes at the edge of the hexagon, and again confirms the hexagonal shape, cf. Figure 5.4a. We have fitted a two-band model to an ab initio band structure calculation and find a nearest neighbor tunneling $J = h \times 1.09\,\text{kHz}$ and a next-nearest neighbor tunneling of $J' = h \times 0.05\,\text{kHz}$. For the simulation we prepare a wavepacket localized to a single site and evolve the state in time for 5 ms. The state after 5 ms of expansion is shown in Figure 5.4a, to simulate the finite resolution we have rebinned
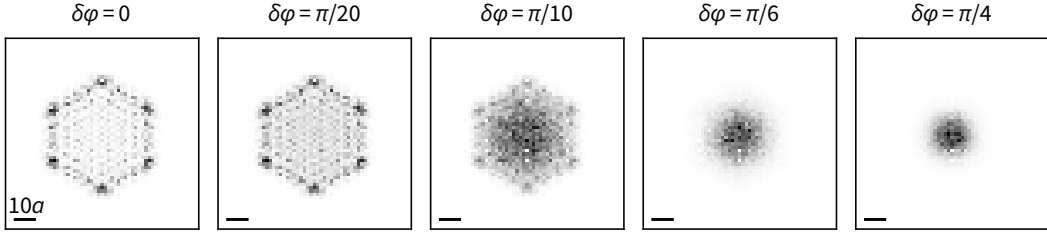
Figure 5.5 | Tight binding expansion with various strengths of decoherence. A two-band tight binding model with $J = h \times 1\,\text{kHz}$ is evolved in time for 3 ms while applying a normal distributed random phase $\delta\varphi$ on every state after every tunneling time τ. The decoherence leads to the absence of interference and eventually a Gaussian envelope of the population after expansion.

the resulting state to a similar spatial resolution as the experimental image shown in Figure 5.4b and Figure 5.3. These measurements confirm sufficient localization of the initial wave packet and support a coherent evolution in the lattice. We observe a similar quality of the expansion dynamics when letting the atoms evolve in the bulk of the modulated lattice in the three regimes as shown in Section 5.4.

In contrast, for an incoherent random walk a Gaussian distribution would be measured [263]. Figure 5.5 shows the resulting distribution of a quantum walk in the honeycomb lattice with varying degree of coherence. We numerically propagate a state in a two-band tight binding system with nearest neighbor coupling of $J = h \times 1\,\text{kHz}$ and no next nearest neighbor coupling for 3 ms in time. We perform a Trotter expansion where every time step is a duration of one tunneling time $\tau = \hbar/J$. To simulate the effect of decoherence we apply a random phase shift on every lattice site after each time step. The random phase on every site has a normal distribution with standard deviation of parameter $\delta\phi$. In the absence of dephasing ($\delta\phi = 0$) we recover the result presented above, where the quantum walk results in the hexagonal shape with interference fringes within the boundary. With increasing dephasing ($0 < \delta\phi \leq \pi/10$) the interference pattern inside the hexagon disappears due to an averaging of the constructive and destructive interference while the overall hexagonal shape is still maintained. For stronger dephasing ($\delta\phi \geq \pi/6$) we observe a radially symmetric shape with approximately Gaussian envelope. In a similar fashion the result can be interpreted as a temporally varying disorder potential resulting in a diffusive expansion of the wave packet. As the individual dephasing pattern strongly influences the evolution, the results presented in Figure 5.5 shows the average over 20 independent realizations.

5.1.3 Observation of edge modes in the anomalous regime

The observation of edge modes in photonic, mechanical or electrial devices fundamentally exhibits a natural infinitely sharp boundary [85, 115, 155, 316, 317]. With cold atoms, their observation was enabled by the concept of synthetic dimensions [147, 155]. There, one real-space dimension is replaced by internal degrees of freedom, and the finite number of coupled internal levels naturally creates a well-defined boundary [116–118]. In real-space, however, the edges of the cold atomic systems are typically smooth and defined by the
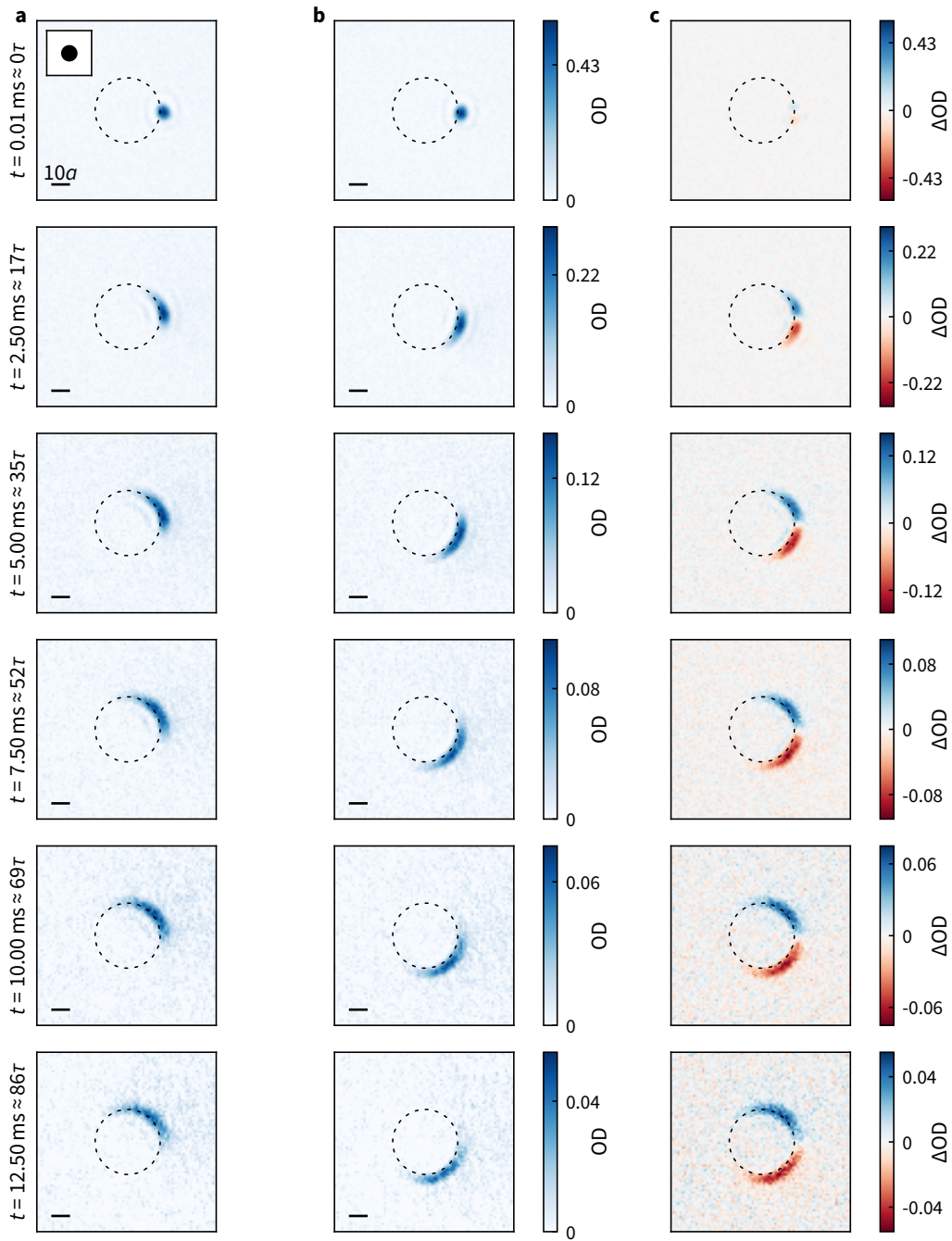
Figure 5.6 │ **Observation of anomalous Floquet topological edge modes on a repulsive disk potential.**
a, Time-evolution of the atoms $\kappa = +1$. **b**, same as **a** but $\kappa = -1$. **c** Difference image ΔOD. The evolution
times are indicated on the left most image of each row. The modulation parameters are $m = 0.25$
$\omega/(2\pi) = 7$ kHz. All absorption images are averages of $100 - 300$ individual experimental realizations. The
scale bar represents a length of $10a$. The position of the dashed lines is calculated from the programmed
pattern on the DMD.

harmonic trap significantly complicating the observation of edge modes as their velocity reduces and the signal spreads out [120, 308, 318]. In one dimension real-space edge states have been observed in engineered lattices [223, 319] and Rydberg atom arrays [320]. Despite several strategies that have been proposed for two spatial dimensions [119–122], their observation has so far remained elusive.

The characterization in reciprocal space (see Chapter 4) unambiguously proved the existence of edge modes in the anomalous Floquet phase [111]. However, showing the existence in a system where both, bulk and edge could be probed has not been implemented so far. To prove the existence of the edge mode we prepare a sample by the sequence illustrated in Figure 5.3b. The tweezer trapping frequency is chosen to be $\omega_{\text{tw}}/(2\pi) = 2.0(1)\,\text{kHz}$. The width of the edge potential is on the order of $0.7\,\mu\text{m}$, limited by the numerical aperture of the objective, cf. Section 3.2.3 and might potentially be further deteriorated due to aberrations in the imaging system. We generate an edge in the system by illuminating a selected area of the lattice with a repulsive potential which generates a potential step separating the system into an area of low and high potential energy. We position the tweezer close to the edge of the illuminated area, the position is varied transversal to the edge in order to optimize the preparation of the atoms in the edge mode. The precise alignment of the edge potential with respect to the symmetries of the honeycomb lattice is irrelevant as the edge modes are immune to scattering e.g. due to imperfections of the lattice potential. Equivalently defects in the lattice do not obstruct the propagation of the edge mode [79].

Figure 5.6 shows the time evolution of the system after abruptly switching off the tweezer in the anomalous regime, $m = 0.25$ and $\omega/(2\pi) = 7\,\text{kHz}$, corresponding to the blue marker in Figure 5.1a. The projected potential consists of an repulsive disk of height $V_0 = h \times 16.7(3)\,\text{kHz}$ and radius $5.8\,\mu\text{m}$ ($\approx 20a$) preventing the atoms from tunneling into this area. The shape of the potential is shown in the inset of Figure 5.6, where the repulsive potential is shown in black. The evolution times are stated in absolute units and additionally in nearest neighbor tunneling times of the static $5.9\,E_{\text{rec}}$ lattice, where $J_0 = h \times 1.1(1)\,\text{kHz}$ is the nearest neighbor tunnel coupling and $\tau = \hbar/J_0 = 145\,\mu\text{s}$ the tunneling time. After releasing the atoms from the tweezer we observe that the wave packet propagates along the potential boundary, following its shape, as is characteristic for chiral edge modes (Figure 5.6a). The chirality of the images shown in Figure 5.6a is $\kappa = 1$. Furthermore, while the potential is repulsive, the atoms remain close to the edge, propagate over more than $20a$ and do not scatter into the bulk of the system, indicating a good overlap of the initial wave packet with the edge mode. In addition, the wave packet disperses while propagating, due to the non-linear dispersion relation of the edge mode and as a result of the finite width of the edge [120, 308, 318]. The propagation is almost entirely unidirectional along the potential edge, even thought the edge is not following any symmetries of the lattice and can be viewed as consisting of an assembly of various missing sites in the unit cell. To highlight the chiral nature of the edge mode, the modulation direction is inverted to $\kappa = -1$ in Figure 5.6b. This changes the sign of the winding numbers and therefore the chirality of the edge mode, which propagates in
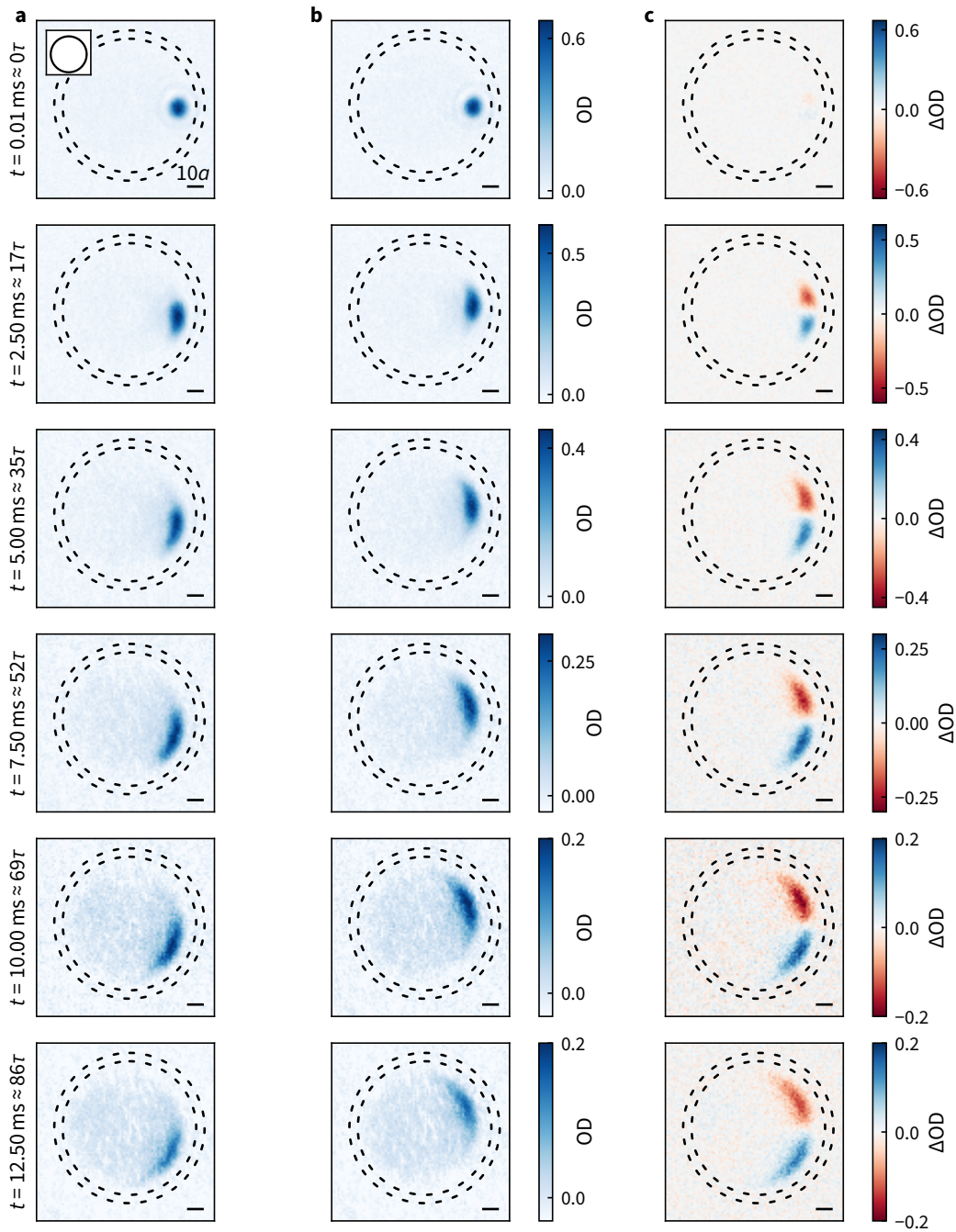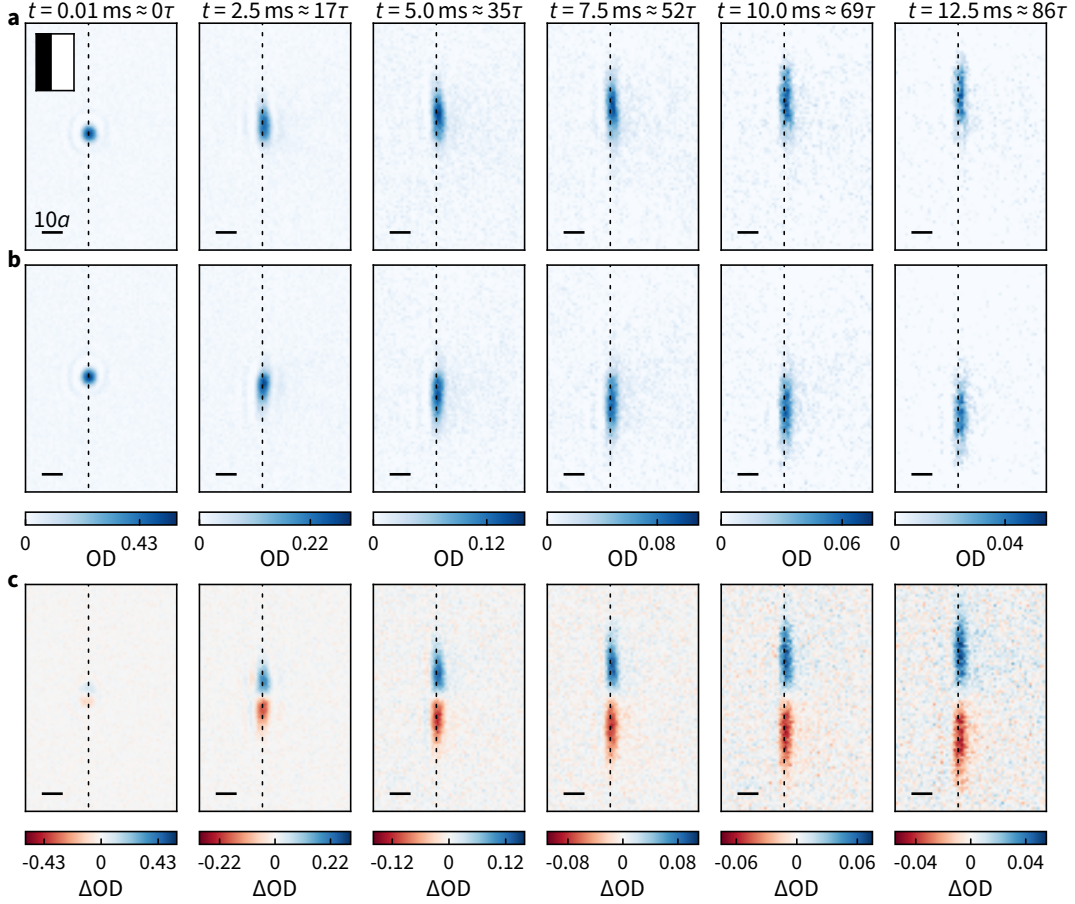
Figure 5.7 | Observation of anomalous Floquet topological edge modes inside a confining ring potential.
a, Time-evolution of the atoms $\kappa = +1$ **b**, same as **a** but $\kappa = -1$. **c** Difference image ΔOD. The evolution times are indicated on the leftmost image of each row. The modulation parameters are $m = 0.25$ $\omega/(2\pi) = 7$ kHz. All absorption images are averages of $40 - 160$ individual experimental realizations. The scale bar represents a length of $10a$. The position of the dashed lines is calculated from the programmed pattern on the DMD.

Figure 5.8 | Observation of anomalous Floquet topological edge modes next to a straight step potential. **a,** Time-evolution of the atoms after releasing the atoms from the tweezer into the modulated lattice ($\kappa = +1$), close to a straight potential edge represented by the dashed line. The inset illustrates the shape of the repulsive potential, which is shown in black. **b,** same as **a** but with opposite chirality of the modulation $\kappa = -1$. **c** Difference image ΔOD between the time evolution shown in **a** with $\kappa = +1$ and the evolution under the opposite chirality $\kappa = -1$ shown in **b**. The evolution times of **a** and **b** are indicated at on top of each column. The modulation parameters are $\omega/(2\pi) = 7$ kHz and $m = 0.25$ (blue marker in Figure 5.1a). All absorption images are averages of $100 - 300$ individual experimental realizations. The scale bar represents a length of $10a$. The position of the dashed lines is calculated from the programmed pattern on the DMD.

opposite direction compared to the case $\kappa = 1$ shown in Figure 5.6a. Figure 5.6c shows the difference between the images OD_κ taken for $\kappa = 1$ and $\kappa = -1$,

$$\Delta\mathrm{OD} = \mathrm{OD}_{\kappa=+1} - \mathrm{OD}_{\kappa=-1}, \tag{5.2}$$

where OD stands for optical density. Apart from the change in the propagation direction, we observe very similar behavior as the edge modes propagate. The programmable repulsive potential offers almost arbitrary control over the shape and orientation of the edge. In

Figure 5.7 we show experimental results for a repulsive potential that creates a ring shaped potential inside which the cloud is located in contrast to the measurements presented in Figure 5.6 where the edge mode propagates on the outside of an obstacle. The inset in Figure 5.7a illustrates the shape of the repulsive potential, which is shown in black. The height of the ring potential is $V_0 = 17.0(3)$ kHz with an inner radius of $13.3\,\mu$m ($\approx 47a$) represented by the dashed line. As the initial state is now located to the left of the wall compared to the measurement presented in Figure 5.6, where the initial state is aligned to the right of the wall, we do now observe that the state with $\kappa = 1$ (Figure 5.7a) is propagating in a clockwise fashion along the wall. This result further shows that we do not have an external force or an overall gradient in the system driving Bloch oscillations which would result in the same deflection for both orientations of the wall. Figure 5.7b shows the evolution for opposite chirality of the drive $\kappa = -1$ but otherwise identical experimental parameters. The difference signal (Figure 5.7c) also shows that upon inversion of the modulation chirality the edge mode also changes chirality, while e.g. the dispersion of the edge mode remains unchanged. We note that the images in Figure 5.7 show a different OD as we had improved the imaging system with an additional repumper similar to the technique presented in [292].

As the evaluation of the velocity in this curved geometry is not straightforward we have also investigated a straight edge, where the system is separated in to two regions: one region with low, and another region with high potential energy at energy $V_0 = h \times 16.7(3)$ kHz. At the interface between the two regions we again expect to detect an edge mode. The edge implemented in the experiment is oriented parallel to a zigzag edge of the system. Figure 5.8 shows the evolution of the system after release from the tweezer next to a straight edge. We observe the chiral propagation of the edge mode along the potential step depending on the chirality of the drive ($\kappa = 1$ in Figure 5.8a and $\kappa = -1$ in Figure 5.8b). For the longest evolution times ($t = 12.5$ ms), the center-of-mass position of the cloud travels approximately $20a$, and the fastest 20% of the atoms travel more than $30a$.

The straightforward identification of edge modes illustrates the potential of our experimental protocol for probing the topological properties of Floquet topological systems, where knowledge about the Chern numbers is insufficient, or where conventional methods for detecting bulk geometric properties are not applicable, e.g., in the presence of disorder or strong interactions.

5.1.4 Comparison to the static lattice

To rule out any trivial contribution to the chiral signal, we prepare the system in the topologically trivial band structure of the static lattice and for otherwise identical settings as in the anomalous Floquet regime. We first optimize the position of the tweezer to achieve the optimum overlap between the tweezer and the edge mode in the anomalous regime. Once the position leading to maximum overlap between tweezer and edge mode is found we alternatively take images in the static lattice and in the modulated lattice. The parameters in the anomalous regime are $m = 0.25$ and $\omega/(2\pi) = 7$ kHz (blue marker in Figure 5.1a) with varying chirality $\kappa = \{+1, -1\}$. For the realizations in the static lattice
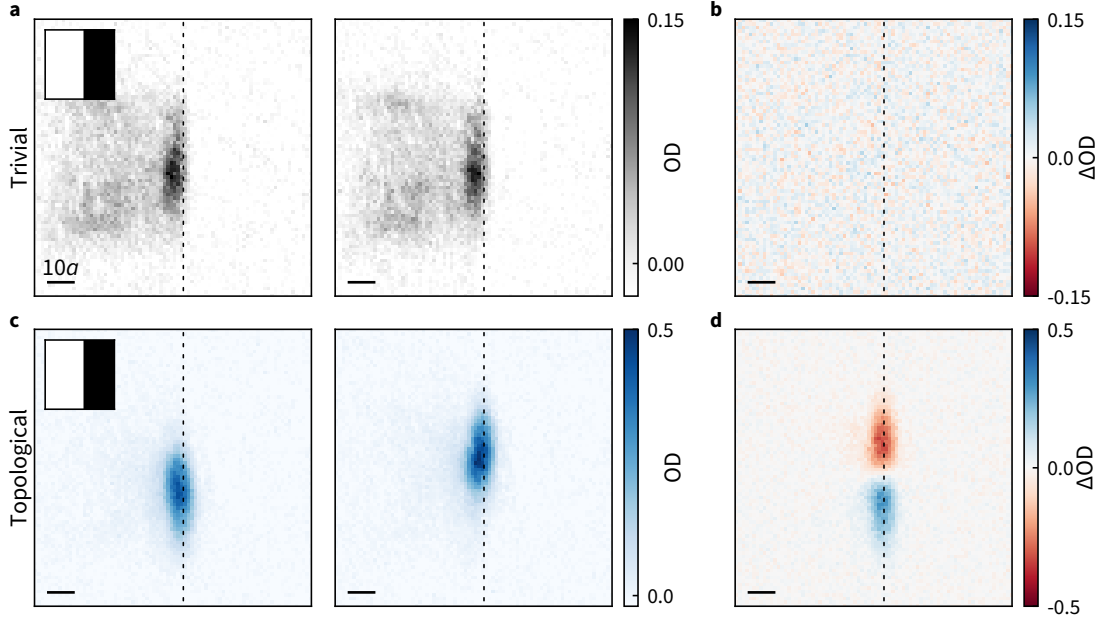
Figure 5.9 | **Comparison of the expansion in a trivial and topological band structure. a,** Evolution of a wave packet prepared in the unmodulated static lattice close to the edge imaged 5 ms after switching off the tweezer. The left images correspond to all parameters of the experiment equivalent to $\kappa = +1$, the right image to $\kappa = -1$. **b,** Difference image ΔOD for the dataset of **a** showing no chiral motion. **c** Evolution of the wave packet 5 ms after releasing the cloud from the tweezer in the modulated lattice in the anomalous regime. The initial position is identical to the dataset shown in **a**. The chirality of the left image is $\kappa = +1$, the right image $\kappa = -1$. **d** Difference image ΔOD for the dataset of **c** clearly highlighting the chiral motion in the topologically non-trivial phase. The images are the result of 67 individual realizations.

we keep all parameters of the programmed sequence identical except for the modulation amplitude which we set to $m = 0$. In this way we can perform the identical analysis and exclude e.g. systematic errors which might favor one over the other propagation direction also in the static lattice.

Figure 5.9 shows the result of the described experiment. In the static lattice (cf. Figure 5.9a) we observe a trivial localization due to the potential gradient similar to a Wannier-Stark ladder [321, 322] and expansion in the static lattice as described in Section 5.1.2. The expansion is slightly modified as atoms can be reflected from the wall or slowly tunnel from a localized state on the wall into the bulk. Nevertheless we expect to not observe any chiral or directional expansion on the edge. This expectation is confirmed, we observe a symmetric expansion about the initial position of the wave packet (cf. Figure 5.9a). The evolution of both "artificial" chiralities, as there is no sense of chirality for $m = 0$, is identical down to the noise floor of the images. Figure 5.9c shows the difference image ΔOD between the two "artificial" chiralities shown in Figure 5.9a. The potential height in these experiments is $V_0 = 17.0(3)\,\text{kHz}$, which is significantly exceeding the energy scales in the lattice which are on the order of $J_0 = h \times 1.1(1)\,\text{kHz}$. The individual sites located
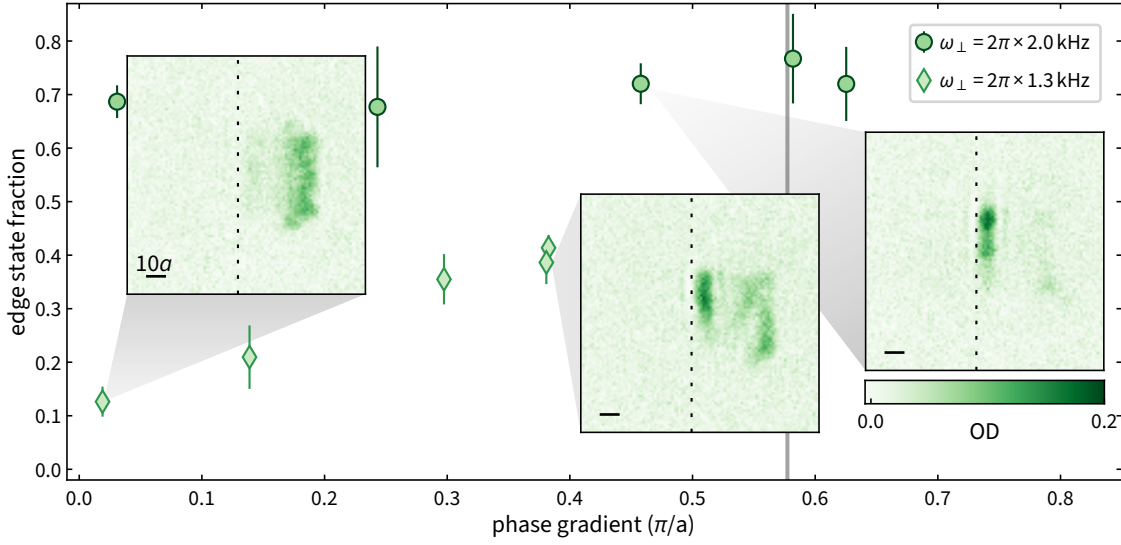
Figure 5.10 │ **Fraction of atoms in the edge mode after a time evolution of** 1.5 ms **as a function of the phase gradient applied to the initial wave packet.** The data points are averages over 4-5 independent realizations and the error bars represent the propagation of the background noise of the absorption image to the population fraction. The gray vertical line indicates the edge of the Brillouin zone for a system oriented parallel to a zigzag edge, where $k_y = \pi/L = \pi/(\sqrt{3}a)$. The insets show averaged absorption images (88-90 realizations) of the atomic cloud after a time evolution of 3 ms in the Haldane regime. The color bar below is common to all insets. The repulsive potential is applied in the region left of the dashed line in the insets.

on the slope of the potential are therefore decoupled in the direction perpendicular to the wall explaining the trivial localization on the edge.

In the anomalous regime we observe as described before the unidirectional propagation of the cloud, which is shown in Figure 5.9c, for which the difference image is shown in Figure 5.9d.

This experiment also rules out any potential systematic errors that might lead to the unidirectional propagation behavior of the edge modes. Yet it is interesting to see the close link between localization in the trivial case and the emergence of edge modes in the topological case resulting from the potential gradient.

5.1.5 Preparation in the Haldane regime

The phase diagram hosts a multitude of topological phases [86, 111, 174, 323] as shown in Figure 5.1. We have so far only explored the edge mode in the anomalous regime where the system is described by a Chern number $\mathcal{C}^- = 0$ and $W^0 = 1$ and $W^\pi = 1$, i.e., edge modes are located in both of the gaps. The Haldane regime exhibits only a single edge mode in the 0-gap and is fully described by the Chern number $\mathcal{C}^- = 1$, as long as we assume the high frequency expansion holds. Probing this edge mode proved experimentally more challenging compared to the anomalous regime as the overlap with the edge mode that can be achieved by releasing the cloud from a static tweezer, which imprints no phase

profile parallel to the edge, is not very large. However applying a kick to the cloud by displacing the tweezer linearly in time improves the fraction of atoms in the Haldane edge mode significantly. The kick accelerates the cloud to a finite velocity which is equivalent to aphase gradient across the cloud (cf. Section 3.2.2). To prepare the system in the Haldane regime we use a modulation amplitude $m = 0.25$ and modulation frequency $\omega/(2\pi) = 16$ (green marker in Figure 5.1a) and prepare the system next to a straight edge with height $V_0 = h \times 2.2(1)\,\mathrm{kHz}$ oriented parallel to a zigzag edge of the lattice. The energy scale related to the modulation frequency is not exceeding the band width of the two s-bands of the system dramatically, therefore we cannot claim the system to be in the high frequency limit. However these parameters favor a relatively large gap at K of $\Delta E_K = h \times 1.4\,\mathrm{kHz}$, which should result in a greater velocity of the edge mode compared to a smaller gap, cf. Section 2.2. Even though we do not probe the system in the high frequency limit the system exhibits identical properties as it is still well gapped in the π-gap and we cannot expect a strong influence of the Floquet copies.

Releasing the wave packet from a tweezer with trapping frequency $\omega/(2\pi) = 1.3(1)\,\mathrm{kHz}$ into the modulated lattice results in a very poor preparation of the edge mode as shown in the left inset in Figure 5.10. Increasing the kick to apply a phase gradient which corresponds to a point closer to the edge of the one-dimensional Brillouin zone oriented parallel to the edge at $k_\mathrm{max} = \pi/(\sqrt{3}a) \approx 0.58\pi/a$ (gray vertical line in Figure 5.10) results in improved preparation of the edge mode as shown in the center inset. While the population in the edge mode is increased there is still significant population in the bulk of the system, which indicates that either the phase profile is not matching the edge mode, or that the density profile resulting from the tweezer does not match with the density profile of the edge mode and therefore results in a poor overlap of the wave function prepared in the tweezer and the edge mode. By increasing the intensity in the tweezer trap we can increase the trapping frequency to $\omega_\mathrm{tw}/(2\pi) = 2\,\mathrm{kHz}$ which reduces the spatial extent of the wave function. Having the smaller cloud we can not only apply a larger phase gradient to the cloud but also observe an improved loading into the edge mode, cf. the right inset in Figure 5.10 where we show a representative image for a phase gradient $\approx 0.45\pi/a$. We observe very little scattering into bulk states and a strong signal in the chiral edge mode in the Haldane phase. This highlights the two conditions that need to be matched in order to achieve good overlap with the edge mode: 1) the spatial extent of the wave functions need to match, and 2) the phase profile of the prepared wave packet needs to match the edge mode [121].

To quantify the occupation in the edge mode we evaluate the fraction of atoms in the edge mode compared to the bulk population: the edge fraction. We let the wave packet evolve for $t = 1.5\,\mathrm{ms}$, a time long enough to separate atoms near the edge from those scattered into the bulk modes, then the fraction of atoms in the edge mode is evaluated as a function of the imprinted phase gradient as described below. For the smaller tweezer trapping frequency (light green data points), we observe an overall poor overlap with the edge mode which increases as we increase the phase gradient close to the theoretical maximum of $0.58\pi/a$. Decreasing the initial spatial extent of the cloud further with a tighter tweezer reduces scattering into the bulk (dark green data points) while also reducing the influence of the initial phase gradient applied to the cloud. We interpret this reduced
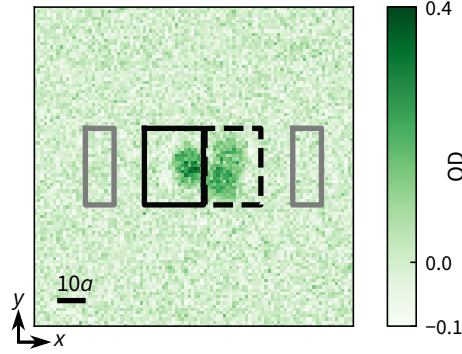
Figure 5.11 | **Evaluation of the fraction of atoms populating the edge mode.** Averaged absorption image after 1.5 ms of time evolution, together with the respective regions of interest used for the evaluation: close to the edge (solid black lines) and in the bulk (dashed black lines). The two background regions of half the size are indicated by the gray lines. This example corresponds to the $\omega_{tw}/(2\pi) = 1.3(1)$ kHz. data point of Figure 5.10 shown in the center inset.

dependence as the extent of the wave function approaching a single lattice site, where a phase difference between neighboring sites is not well defined as mainly one site is occupied.

In contrast to the Haldane regime we find an extremely robust behavior in the anomalous regime, where the fraction of atoms in the edge mode is largely independent of the properties of the initial wave packet. In this regime, the initial wave packet is projected onto both edge modes, one in the 0-gap and one in the π-gap, for each quasi-momentum. Varying the parameters of the initial state should only affect the relative weight between the two modes which we cannot independently resolve in the experiment. Section 5.1.6 discusses in detail how the edge states change in the different topological regimes and for different edge terminations.

The edge population fraction, displayed in Figure 5.10, is determined by integrating the OD in the respective regions of interest as illustrated in Figure 5.11. We prepare the initial state with varying trap frequency $\omega_{tw}/(2\pi) = 1.3(1)$ kHz and $2.0(1)$ kHz of the optical tweezer and different initial phase gradients. In order to ensure the optimum spatial overlap of the initial state with the edge mode, we additionally vary the position with respect to the edge potential. Several absorption images are taken with the same experimental parameters and averaged. To determine the size of the region of interest, we verify that the integrated optical density is unaltered for small changes in the size of the region of interest. Additionally, two regions of half the size of the previous ones are defined separated from the central region to evaluate the background value of the image as shown in Figure 5.11. We independently sum the optical density of the edge and bulk regions of interest and subtract the summed optical density in the background regions
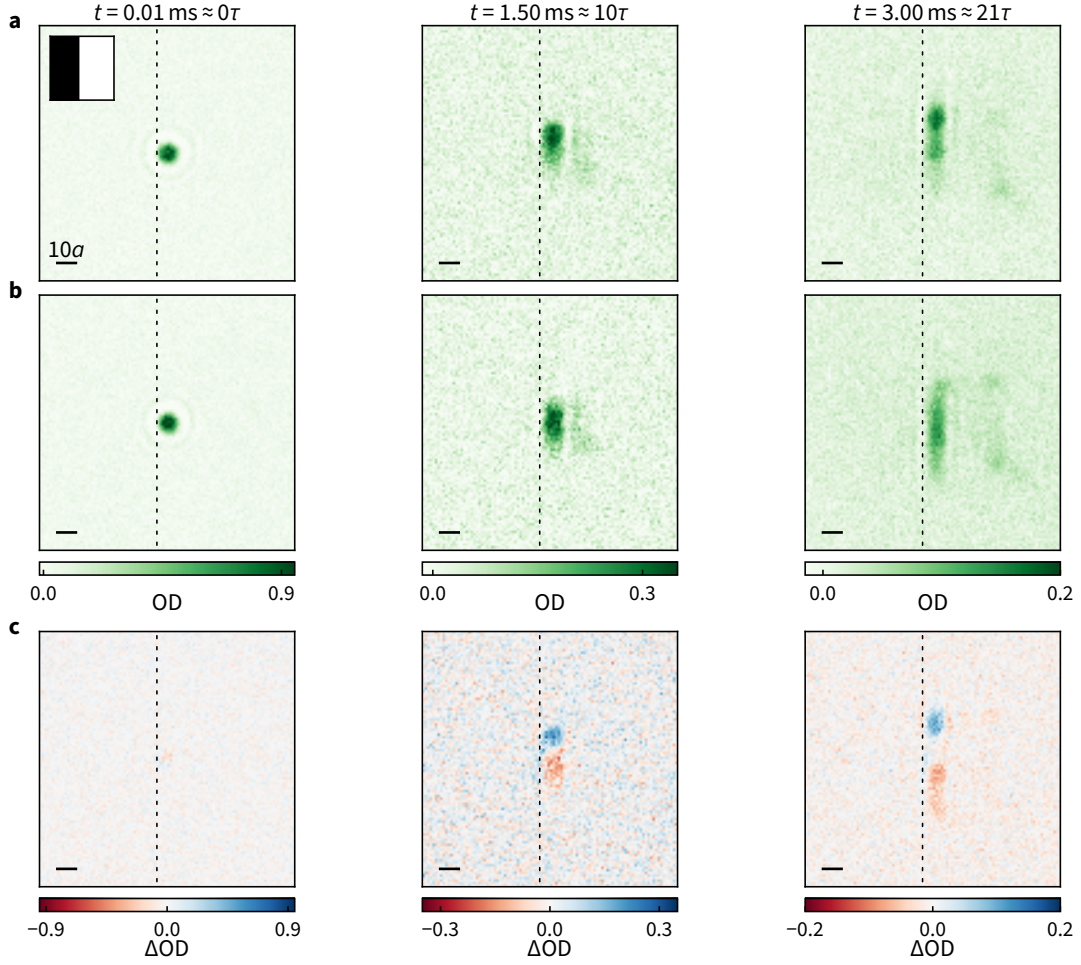
Figure 5.12 | Observation of the edge mode in the Haldane regime. a, Time-evolution of the atoms after releasing the atoms from the tweezer into the modulated lattice ($\kappa = +1$), close to a straight potential edge of height $V_0 = h \times 2.2(1)$ kHz represented by the dashed line. The inset illustrates the shape of the repulsive potential, which is shown in black. **b,** same as **a** but with opposite chirality of the modulation $\kappa = -1$. **c** Difference image ΔOD between the time evolution shown in **a** with $\kappa = +1$ and the evolution under the opposite chirality $\kappa = -1$ shown in **b**. The evolution times of **a** and **b** are indicated at on top of each column. The modulation parameters are $\omega/(2\pi) = 16$ kHz and $m = 0.25$ (green marker in Figure 5.1a). The data corresponds to the one highlighted by the inset for $\omega_{\mathrm{tw}}/(2\pi) = 2.0(1)$ kHz. All absorption images are averages of $4 - 90$ individual experimental realizations. The scale bar represents a length of $10a$. The position of the dashed lines is calculated from the programmed pattern on the DMD.

to obtain the signal from the bulk S_{bulk} and edge S_{edge}. These values are then used to compute the fraction p_{edge} of atoms in the edge region:

$$p_{\mathrm{edge}} = \frac{S_{\mathrm{edge}}}{S_{\mathrm{edge}} + S_{\mathrm{bulk}}}. \tag{5.3}$$

The error bar is evaluated using the standard deviation of the two values of the fraction obtained for the two opposite chiralities of the lattice modulation and the noise of the
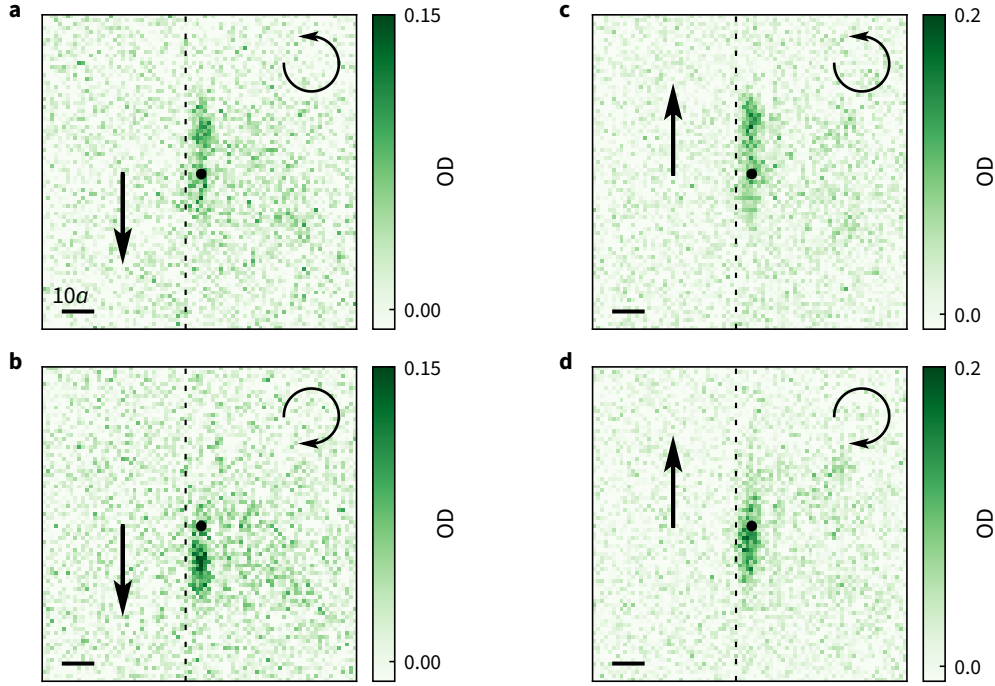
Figure 5.13 | Changing the direction of the kick in the Haldane regime. Each image **a-d** shows the evolution of the atoms with different parameters: the direction of the kick is indicated by the arrow on the left pointing up or down; the chirality of the modulation by the direction of the circular arrow on the top right, corresponding to $\kappa = -1$ in **a,c**, and $\kappa = 1$ in **b,d**. The cloud is prepared at $k_y \approx 0.43\pi/a$. The trap frequency of the tweezer is $\omega_{\mathrm{tw}}/(2\pi) = 2.0(1)$ kHz. The black point indicates the initial position of the cloud. The dashed line indicates, where the edge is located, and the scale bar on the bottom left represents a length of $10a$.

imaging system that is obtained from the standard deviation of the optical density in the background region.

As Figure 5.11 and Figure 5.10 only show one of the two chiralities of the drive we show the expansion dynamics in the Haldane phase in Figure 5.12. The shown data correspond to the one highlighted by the inset of Figure 5.10 for $\omega_{\mathrm{tw}}/(2\pi) = 2.0(1)$ kHz. Compared to the anomalous regime the dispersion of the edge mode and therefore the extent of the cloud parallel to the edge is larger, however the center of mass is still propagating in a chiral way.

To prepare the edge mode in the Haldane regime we need to apply a kick to the cloud, which results in a center of mass motion of the cloud compared to the lattice. We verify here that the direction of this velocity kick does not change the subsequent dynamics of the cloud, in particular that its direction of propagation along the edge is unaltered, and is solely determined by the chirality of the topological edge mode. Figure 5.13 shows averaged pictures of the evolution of a cloud of atoms in the Haldane regime under the two opposite chiralities of the lattice modulation (top and bottom row), and with an initial velocity kick that is applied in two opposite directions (left and right column). These pictures highlight the fact that the direction of propagation of the atoms along the edge is only determined by the chirality of the modulation, i.e., by the chirality of the topological edge mode. The

direction of the initial kick does not intervene, since the purpose of this kick is to bring the cloud of atoms from a flat phase profile closer to the phase profile corresponding to the edge of the Brillouin zone along the infinite direction of the lattice. A kick in the opposite direction results in the opposite phase gradient.

5.1.6 Edge states for different edge terminations

As we will see in the following the quasimomentum alone is not sufficient in order to determine whether a kick is needed in order achieve good overlap with the edge mode. The honeycomb lattice can be terminated with four high symmetry terminations: zigzag, armchair, barbed and the more recently discovered twig-shaped edge [141]. The twig-shaped edge consists of an armchair terminated system where either of the two sublattice sites is removed from the outermost row of the edge. This edge cannot be obtained by simply cutting an infinite honeycomb lattice with a straight cut. In the current setup this type of edge cannot be realized due to the lack of single site addressing with the DMD potential, and will therefore not be investigated further. Future experiments might be possible if the spatial resolution is sufficient to realize this type of edge e.g. in a quantum gas microscope. The zigzag edge and the barbed edge exist for the same orientation of the cut but are shifted with respect to one another. The sites on the edge have different connectivity, the zigzag edge has a connectivity of two, while the sites on the barbed edge have a connectivity of one. The armchair edge arises when cutting the system at a 90° angle compared to a zigzag or barbed edge. In contrast to the zigzag or barbed edge we do find both *A*- and *B*-sites located on the edge of the system. Terminating the system in different geometries results in different lengths of the unit cell parallel to the edge and therefore, according to the Nyquist–Shannon sampling theorem, the maximum resolvable spatial frequency, i.e., quasimomentum varies inversely proportional to the length of the unit cell. The unit cell for a zigzag or barbed edge has a length $L = \sqrt{3}a$, while the armchair edge unit cell is $L = 3a$ long. This results in different maximum quasimomentum along the edge, $k_{max} = \pm\pi/(\sqrt{3}a)$ for the zigazag and barbed edge, while for the armchair edge $k_{\max} = \pi/(3a)$. As illustrated in Section 2.5.6 and Figure 2.12 the shape of the band structure can be interpreted as the integration of the two dimensional Brillouin zone along the finite direction. Instead of quasimomentum in two dimensions the we now have *real* momentum in the finite direction and quasimomentum along the periodically repeating direction. Momenta that are larger than $k_{\max}$ are aliased, i.e., folded back to the Brillouin zone. This information however is not lost as there can still be a *real* momentum within the unit cell, which arises as a phase profile imprinted to the state within the unit cell.

Figure 5.14 shows the dispersion calculated for a stepwise modulation of the tunneling amplitudes with $\Lambda = 10$ in the Haldane regime, at $\hbar\omega/(\Lambda J_0) = 4.5$. The system is terminated with a zigzag edge (left column), armchair edge (center column) and a barbed edge (right column). In the Haldane regime we only find a single edge mode located in the 0-gap. The state highlighted by the downfacing triangle is plotted below the spectrum for each of the three terminations. The population on every site is encoded in the color bar which is normalized to the maximum population on a single site of the respective state.
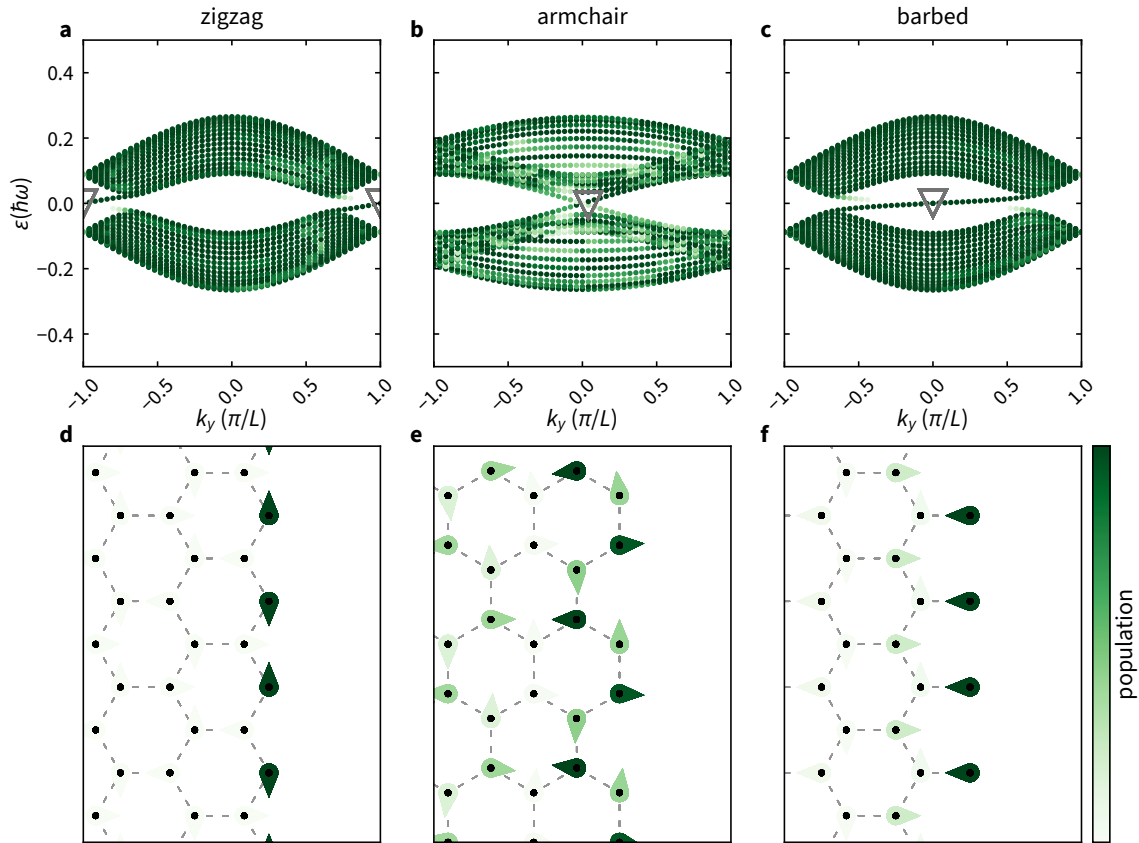
Figure 5.14 | Dispersion and exemplary edge states in the Haldane regime. a, Dispersion for a system terminated with a zigzag edge. **b**, Dispersion for a system terminated with an armchair edge. **c**, Dispersion for a system terminated with a barbed edge. **d**, Exemplary edge state on the zigzag edge in the 0-gap at the edge of the Brillouin zone (downfacing triangle in **a**). **e**, Exemplary edge state on the armchair edge in the 0-gap located at $k_y = 0$ (downfacing triangle in **b**). Even though the 0-gap edge state is located at $k_y \approx 0$ it still exhibits a phase profile within the unit cell and preparation of this edge mode would require a kick. **f**, Exemplary edge states on the barbed edge in the 0-gap (downfacing triangle in **c**). The population is mainly located on the edge, but the state still exhibits a phase gradient when comparing to the next most populated state. The states plotted in the bottom row are highlighted by the downfacing triangle in the upper row. The population, indicated by the shading of the arrows, is normalized to the maximum population on a single site for the depicted state with the arrows' orientations indicating its complex phase. The shading of the spectra corresponds to the overlap of the system with a region excluding the left numerical edge to only show one edge mode.

The orientation of the arrow tip on every site shows the phase of the state on this site, with adjacent unit cells shifted by the quasimomentum of the state. In contrast to the armchair and barbed edge, where the edge mode is located at zero quasimomentum $k_y = 0$, the edge mode in the zigzag terminated system is located at the edge of the Brillouin zone $k_y = \pm\pi/L$. The edge mode in the zigzag and barbed case are almost entirely located on a single site of the unit cell. As the edge mode on the zigzag edge has a phase difference of π between unit cells, a non zero phase profile is required in order to achieve good overlap with an edge mode. This observation confirms the experimental findings presented in

Section 5.1.5. Judging only by the location of the edge mode in quasimomentum we could expect to be able to prepare the armchair edge mode from an initial state with flat phase. This is not true. One key difference compared to the zigzag edge is the residual phase profile located within the unit cell of the armchair edge, where the most populated sites exhibit a phase shift of π. Therefore in order to populate the edge mode in the armchair edge geometry we also require a kick. Interestingly the extent of the state perpendicular to the wall is also significantly larger in the armchair geometry compared to the zigzag or barbed edge case and changes with the size of the gap. The smaller the gap, the more extended the state is; this is likely related to the existence of the trivial edge states present in the zigzag and barbed geometry but absent in the armchair geometry as introduced in Section 2.2.3.

In the experiment we do not prepare a infinitely sharp edge and therefore even though it is oriented parallel to a zigzag edge, we can expect the system to also have a slight barbed characteristic. The barbed edge would also require a kick, the phase profile along the edge is flat but the next most populated sites in the barbed edge case are also shifted with respect to the site on the edge, also resulting in a non-zero phase profile within the unit cell. The preparation of this state would therefore also require a phase gradient. This edge mode would also have a non-vanishing overlap with an extended wave packet with flat phase along the edge, experimentally we however do not observe a significant edge mode fraction for the weakly confining tweezer in Figure 5.10. Potentially we might not manage to observe the edge mode in the barbed case as its slope is approximately two times smaller compared to the zigzag edge.

As briefly mentioned in Section 5.1.5 the preparation of the edge mode in the anomalous regime does not require a kick and simply releasing the cloud from the tweezer is sufficient to achieve good overlap with the edge mode. Figure 5.15 shows the dispersion and resulting edge states in the 0- and π-gap in the anomalous system for different edge terminations at $\hbar\omega/(\Lambda J_0) = 1.5$.

The additional edge mode in the π-gap emerged from a singularity at Γ, while the edge mode in the 0-gap exists due to the rectified Berry curvature at K and K'. Considering the system shortly after the respective transition, the edge mode bridges the energy gap at this respective quasimomentum, because it could not have been generated elsewhere. Therefore the edge mode in the 0-gap exhibits a non-zero phase profile, while the edge mode emerging from the band touching at Γ in the π-gap has a flat phase profile as it is located around zero quasimomentum. This observation is confirmed along the zigzag and armchair edge: The edge state in the 0-gap still exhibits a phse profile varying along the edge, while the edge state in the π-gap exhibits a flat phase profile. The edge state on the barbed edge (cf. Figure 5.15c and f) does not follow this observation stritly, both edge states exhibit a flat phase profile. However, depending on the initial phase of the drive there is an instance, where the edge state in the 0-gap exhibits a phase profile within the unit cell, while the π-gap edge state always has a flat phase profile. This already shows the importance of the micromotion, i.e., the evolution within one modulation cycle, which is further discussed in Section 5.1.7.

Experimentally we also investigate the properties of the Haldane-like regime (orange marker in Figure 5.1a). In this regime the edge mode in the 0-gap is annihilated due to
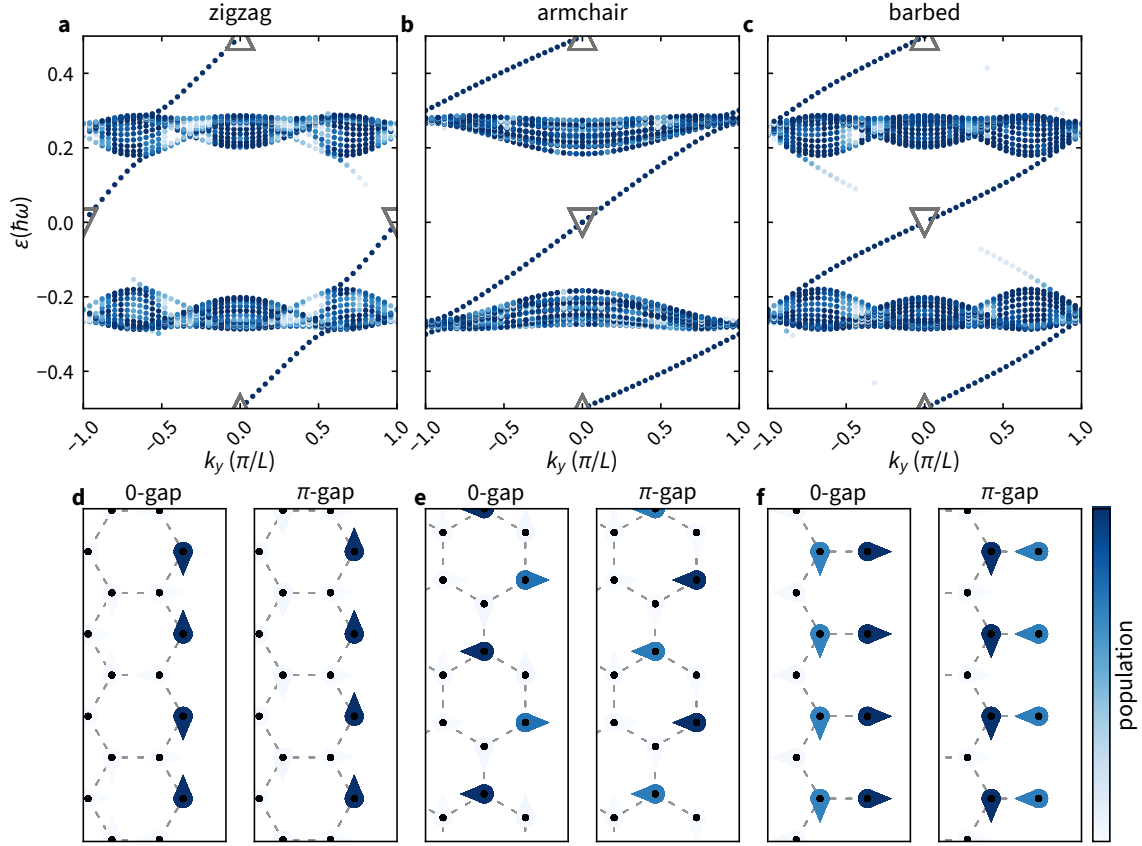
Figure 5.15 │ **Dispersion and exemplary edge states in the anomalous regime. a**, Dispersion for a system terminated with a zigzag edge. **b**, Dispersion for a system terminated with an armchair edge. **c**, Dispersion for a system terminated with a barbed edge. **d**, Exemplary edge states on the zigzag edge in the 0-gap located at the edge of the Brillouin zone (left, downfacing triangle in **a**) and π-gap located at $k_y = 0$ (right, upfacing triangle in **a**) **e**, Exemplary edge states on the armchair edge in the 0-gap located at $k_y = 0$ (left, downfacing triangle in **b**) and π-gap at $k_y = 0$ (right, upfacing triangle in **b**). Even though the 0-gap edge state is located at $k_y = 0$ it still exhibits a phase profile within the unit cell and preparation of this edge mode would require a kick. **f**, Exemplary edge states on the barbed edge in the 0-gap (left, downfacing triangle in **c**) and π-gap (right, upfacing triangle in **c**). This edge mode in the barbed case could be prepared without applying a kick in the anomalous regime, but its phase profile depends on the initial phase of the drive. The two states plotted in the bottom rows are highlighted by the up- (π-gap, right) and downfacing (0-gap, left) triangle in the upper row. The population, indicated by the shading of the arrows, is normalized to the maximum population on a single site for the depicted state with the arrows' orientations indicating its complex phase. The shading of the spectra corresponds to the overlap of the system with a region excluding the left numerical edge to only show on one edge mode.

a second band touching at Γ at the phase transition from the anomalous to the Haldane-like regime, cf. Section 4.2 and Section 4.3. In the dispersion of the semi infinite strip $(\hbar\omega/(\Lambda J_0) = 1.0)$ we still find a chiral edge mode in the π-gap and additionally states located in the 0-gap, which are however not topological, for the zigzag and armchair terminated system. The states in the 0-gap exhibit a vanishing group velocity when integrated over the entire Brillouin zone. Alternatively one can count the number of crossings of theses states at a given energy level in the gap, if the number is odd, the edge mode is topological, otherwise
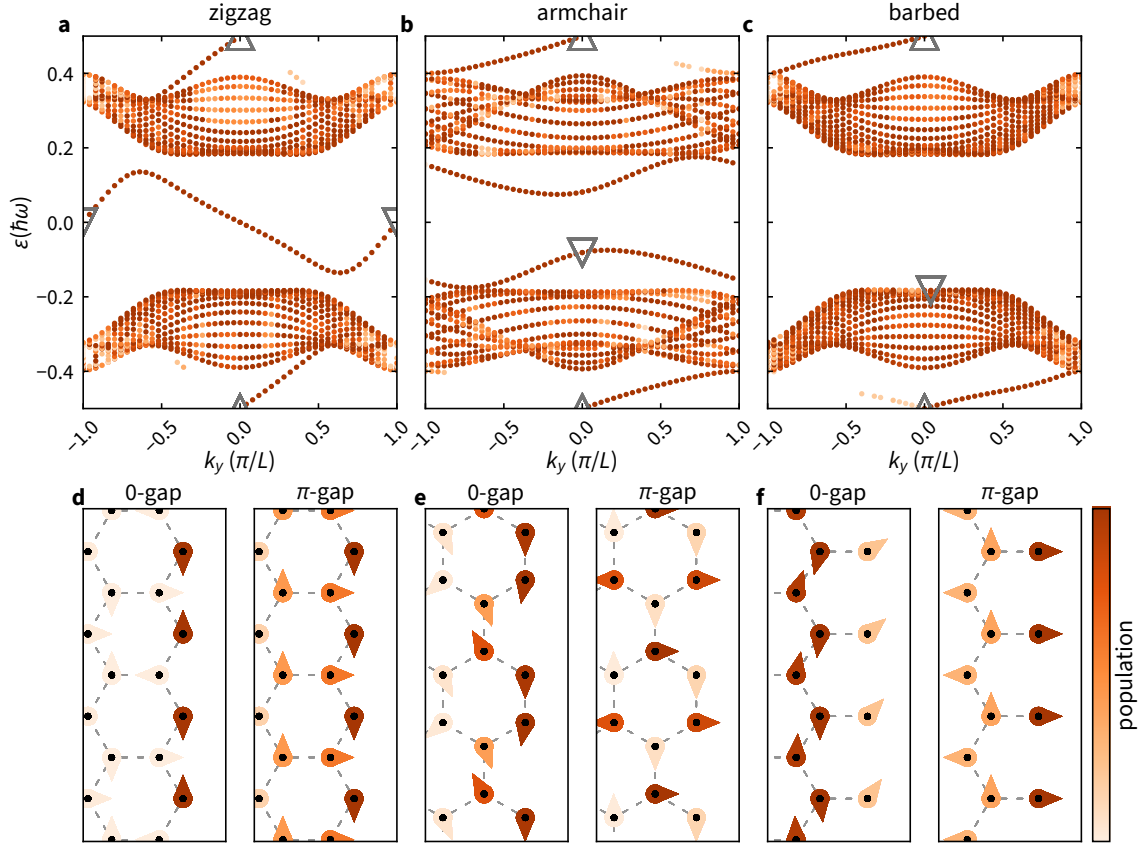
Figure 5.16 | Dispersion and exemplary edge states in the Haldane-like regime. a, Dispersion for a system terminated with a zigzag edge. **b**, Dispersion for a system terminated with an armchair edge. **c**, Dispersion for a system terminated with a barbed edge. **d**, Exemplary state located in the 0-gap on the zigzag edge at the edge of the Brillouin zone (left, downfacing triangle in **a**) and edge state in the π-gap located at $k_y = 0$ (right, upfacing triangle in **a**) **e**, Exemplary state on the armchair edge in the 0-gap located at $k_y = 0$ (left, downfacing triangle in **b**) and edge state in the π-gap at $k_y = 0$ (right, upfacing triangle in **b**). **f**, Lowest energy state on the barbed edge above the 0-gap (left, downfacing triangle in **c**) and edge state in the π-gap (right, upfacing triangle in **c**). For the left plot not the entire population is shown, there is also population in the bulk but none on the opposite edge. The two states plotted in the bottom rows are highlighted by the up- (π-gap, right) and downfacing (0-gap, left) triangle in the upper row. The population, indicated by the shading of the arrows, is normalized to the maximum population on a single site for the depicted state with the arrows' orientations indicating its complex phase. The shading of the spectra corresponds to the overlap of the system with a region excluding the left numerical edge to only show on one edge mode.

the states are trivial [57]. The edge modes in the 0-gap belong to the latter. As these states are still to a very large fraction located on the edge we also show these states in Figure 5.16.

For all three terminations we find the edge state located at $k_y = 0$ and exhibiting a gradient of phase within the unit cell but the mainly occupied states still exhibit the same phase (cf. right plots in Figure 5.16d,e,f). The trivial states located in the gap in the zigzag geometry are still fully located on the edge, similar to the edge mode in the Haldane regime (cf. Figure 5.14d). However, these states do not belong to a chiral edge mode as they do not bridge the 0-gap. All states connected to the shown state are localized on the right edge.

In the armchair geometry we find two trivial states located in the 0-gap, again both states are localized on the right edge and are not part of the bulk. On the barbed edge we find no trivial state in the gap (cf. Figure 5.16c), but the lowest energy state of the upper band (left plot in Figure 5.16f) is still localized to a large fraction on the right edge, yet it also has a significant weight in the bulk which is not shown, but no contribution on the opposite edge.

Currently the observation of these trivial states is not straight forward as we do not have means to distinguish propagating states from stationary states as the observation time so far is not long enough. We also want to note, that one could create a *false* edge mode experimentally by engineering a wave packet that only occupies the states in the gap at the edge of the Brillouin zone with positive slope, cf.e.g. Figure 5.16a. If there is negligible population in other states, one would still observe a state, at least initially, propagating on the edge. It would be interesting to see if there is a regime of modulation parameters, where a similar state emerges but the rest of the system is topologically trivial in contrast to the system here, where the bulk has a Chern number $\mathcal{C}^- = -1$.

5.1.7 Effect of the micromotion

The sub-cycle evolution during the Floquet drive is commonly referred to as micromotion [88, 92, 93]. In our experiment the effect of the micromotion should be negligible for observation at integer multiples of the drive cycle and a slow ramp-up of the modulation [92]. Numerically we calculate the evolution operator for one cycle of the drive to obtain the Floquet-Hamiltonian (see Section 2.3.2), therefore eigenstates of the Floquet-Hamiltonian carry information about the initial phase used to calculate the evolution operator. In the step wise tunneling modulation the evolution operator easily separates into the three parts of the period:

$$\hat{U}(T,0) = \hat{U}(T,2T/3) \cdot \hat{U}(2T/3,T/3) \cdot \hat{U}(T/3,0) \tag{5.4}$$
$$= \hat{U}_3 \cdot \hat{U}_2 \cdot \hat{U}_1, \tag{5.5}$$

where the U_i correspond to the part of the cycle, where the modulation along bond i is enhanced. From this decomposition we immediately see that the kick operator connecting one initial phase to another for a fixed chirality is simply given by the evolution operator during one third of the period. This analysis in principle holds for all modulation protocols as long as the evolution operators can be smoothly connected. If we restrict the initial phase to be one of the three presented above we have for the same chirality the three evolution operators with different initial phases:

$$\hat{U}_3 \cdot \hat{U}_2 \cdot \hat{U}_1, \tag{5.6}$$
$$\hat{U}_2 \cdot \hat{U}_1 \cdot \hat{U}_3, \tag{5.7}$$
$$\hat{U}_1 \cdot \hat{U}_3 \cdot \hat{U}_2. \tag{5.8}$$

For this stepwise drive investigating the initial phase of the drive is equivalent to considering different times within the modulation cycle. The application of one of the U_i on any of
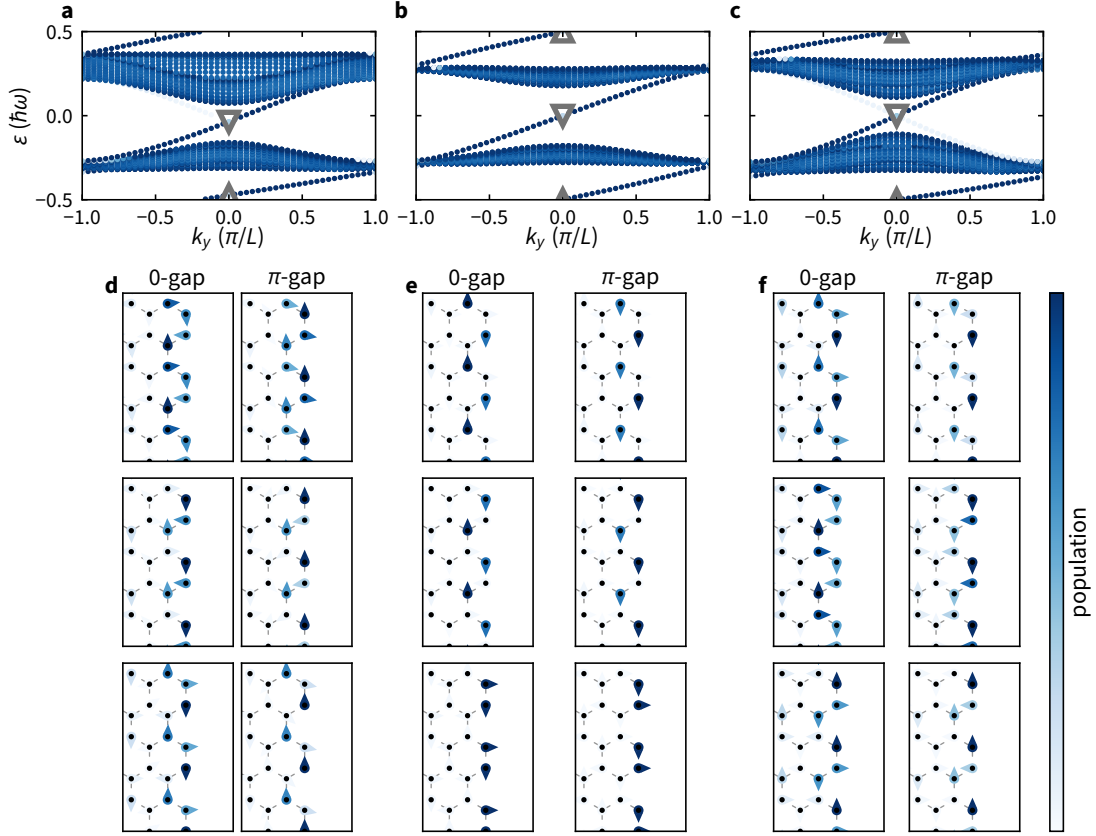
Figure 5.17 │ **Effect of the micro motion in the anomalous phase on the armchair edge. a**, Dispersion in the anomalous phase ($m = 0.25$, $\omega/(2\pi) = 7$ kHz), where the tunneling amplitudes are close to the implementation in the experiment. **b**, Dispersion for the step modulated lattice ($\Lambda = 10$, $\hbar\omega/(\Lambda J_0) = 1.5$). **c**, Dispersion for the sinusoidal modulation ($\Lambda = 10$, $\hbar\omega/(\Lambda J_0) = 2$) of the tunneling amplitude. **d**, Exemplary wave functions for the edge modes in the 0- (left, downfacing triangle in **a**) and π-gap (right, upfacing triangle in **a**) for different initial phase varying by $2\pi/3$ per row in the experiment modulation scheme. **e**, Exemplary wave functions for the edge modes in the 0- (left, downfacing triangle in **b**) and π-gap (right, upfacing triangle in **b**) for different initial phase varying by $2\pi/3$ per row in the stepwise modulated lattice. The weight on the sublattices changes between the different realizations, being mainly the A-, then the B-sublattice and eventually an equal mixture. **f**, Exemplary wave functions for the edge modes in the 0- (left, downfacing triangle in **c**) and π-gap (right, upfacing triangle in **c**) for different initial phase varying by $2\pi/3$ per row for the sinusoidal modulation. The weight on the sublattices changes similar to **e**, but since the bands are more dispersive, the attribution is not as clear. The states plotted in the bottom rows are highlighted by the up- (π-gap, right) and downfacing (0-gap, left) triangle in the upper panels. The population, indicated by the shading of the arrows, is normalized to the maximum population on a single site for the depicted state with the arrows' orientations indicating its complex phase. The shading of the spectra corresponds to the overlap of the system with a region excluding the left numerical edge to only show on one edge mode.

the eigenstate results in the eigenstate of the modulation with initial phase i, under the assumption that the chirality is maintained, i.e., the micromotion is equivalently described by considering different initial phases.

The model presented in Section 2.5.1 can be intuitively used to understand the role of the micromotion, i.e., the evolution within one modulation cycle. Whenever the tunneling is enabled along one of the three nearest neighbor tunneling bonds, the atom tunnels along this bond. In the bulk of the system this leads to particles encircling the plaquette. Applying only one of the three modulation operators would only move the particles along one of the bonds. By that the sub-cycle evolution moves the particles along the bonds of the plaquette and transfers atoms from one sublattice to the other. When going away from this fine-tuned case, the exact transfer between the sublattices is no longer true but we can expect to still observe a shift of the mean weight between the sublattices. Depending on the initial phase of the modulation we can for example expect the wave function to be mainly located on A-sites, while a shift of the initial phase by $2\pi/3$ would result on the wave function being mainly located on B-sites.

Figure 5.17a and d show the effect of a varying initial phase, i.e., micro motion of the drive for a modulation close to the experimental implementation (cf. Section 4.1). While the dispersion of the system is unchanged, the resulting eigenstates are varying and the shift from sublattice A to B is visible as the initial phase is changed. The bands in this implementation are dispersive and therefore the attribution to a single sublattice is incomplete. The step modulated lattice results in less dispersive bands as shown in Figure 5.17b, the resulting edge states (Figure 5.17e) for different initial phases of the drive are essentially fully located on either the A- or B-sublattice or exactly balanced between the two depending on the initial phase of the drive. For the cosine modulation (Figure 5.17c and f), which is closer to the experiment than the step modulated lattice as it also implements a continuous modulation of the tunneling, we observe a similar trend as in the implementation close to the experiment. The eigenstates are only partially localized to either of the two sublattices.

In the experiment we do currently not have the means to investigate the population on individual lattice sites, we can therefore not directly observe the exact instance of the edge mode in the experiment. Nevertheless we experimentally compared the evolution in the bulk for different initial phases and chiralities in order to verify the performance of the experiment and that the initial phase does not influence the evolution of bulk states.

As we have argued above, a smooth ramp connecting the static and the modulated system should result in a smooth transformation of the states between the two regimes and prevent strong effects of the initial phase. We therefore expect the system to evolve equivalently independent of the initial phase, furthermore in the bulk we expect to see no effect of the chirality of the drive. Figure 5.18 shows the expansion after $t = 2.5\,\mathrm{ms}$ in the Haldane regime ($m = 0.25$, $\omega/(2\pi) = 16\,\mathrm{kHz}$, green marker in Figure 5.1a) for the three possible initial phases (columns) of the drive and the two chiralities (rows) of the drive. We observe no difference in the bulk expansion for the different initial phases and chiralities as shown by the differential images in the bottom row of Figure 5.18. From the expansion images we can also deduce that system evolves coherently. We observe the characteristic hexagonal shape and interference fringes within the hexagon after the expansion.
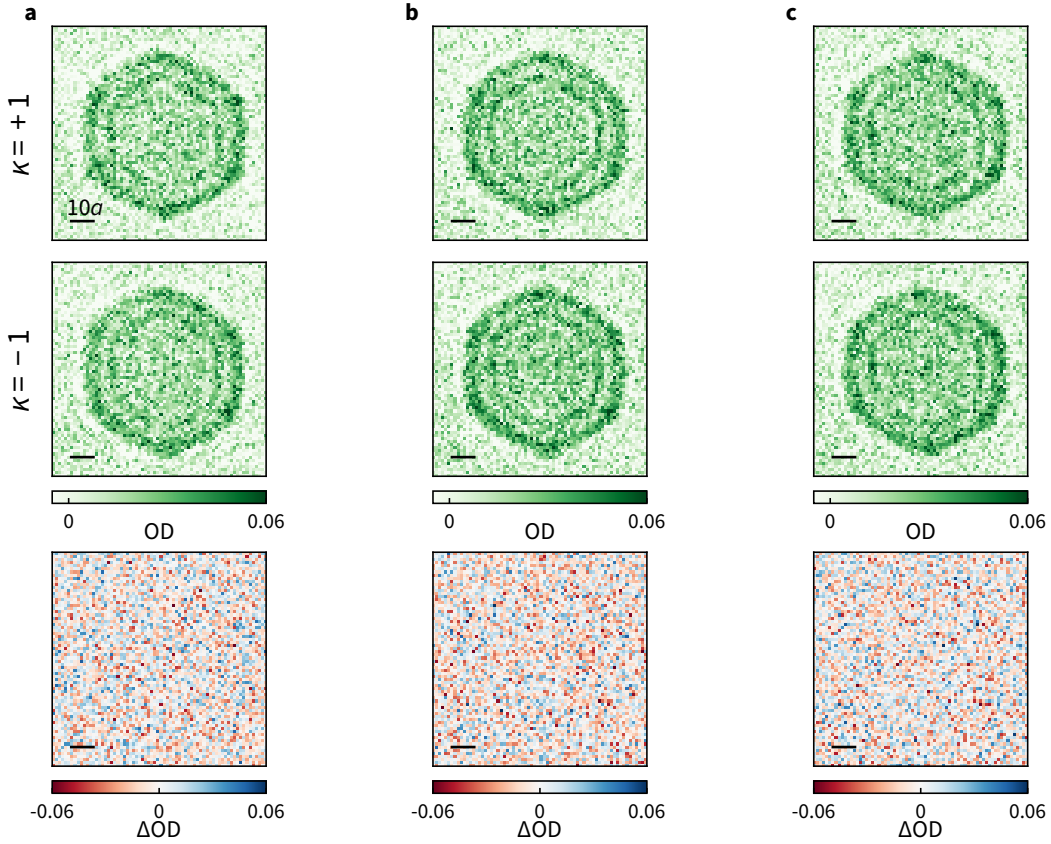
Figure 5.18 | Effect of the initial phase in the bulk expansion in the Haldane regime. Expansion after $t = 2.5$ ms in the Haldane regime ($m = 0.25$, $\omega/(2\pi) = 16$ kHz, green marker in Figure 5.1a) for different initial phases and opposing chirality. **a**, Expansion with initial phase 0 after ramping the modulation up for $5T$. The top row is for chiraltiy $\kappa = 1$, while the second row is $\kappa = -1$. The bottom row shows the difference between the two chiralities. **b**, same as **a** but with initial phase $2\pi/3$. **c**, same as **a** but with initial phase $4\pi/3$.

5.2 Changing the properties of the edge

The properties of the edge strongly influence the dynamics of the edge mode [100, 308, 318]. The unique control over the applied potential allows us to tune the width and height of the applied optical potential. We observe how edge modes emerge on the interface as we increase the height of the potential and how their velocity changes. Varying the width of the edge we show how the edge modes slow down for increasing width of the step potential.

5.2.1 Extracting the velocity of the edge mode

From the differential images we can qualitatively identify if an edge mode is present or not. However we cannot quantify how e.g. parameters of the potential step affect the resulting edge mode. One possible parameter to investigate the behavior of the edge mode is its velocity. We measure the velocity of the edge mode by first maximizing the spatial overlap of the initial cloud and the edge mode. To this end, the initial position of the tweezer
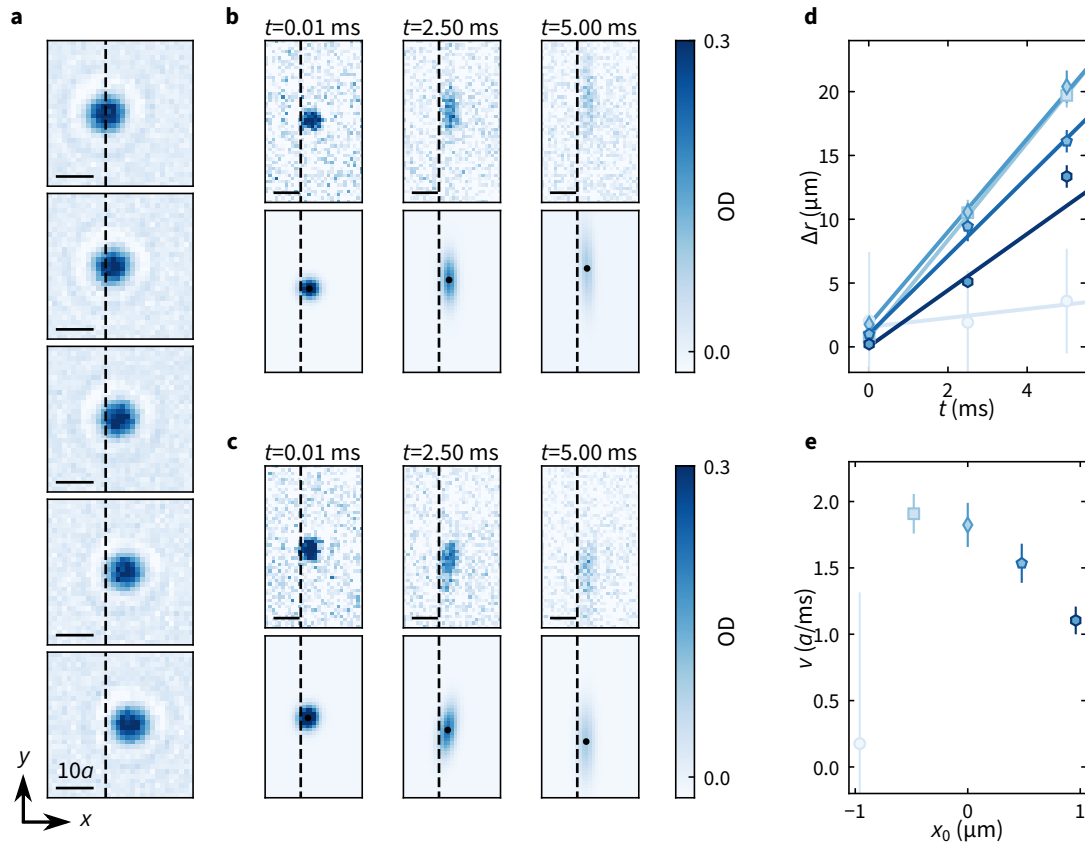
Figure 5.19 | Determination of the edge mode velocity. a, In situ images of atoms in the optical tweezer. The position of the tweezer is varied from top to bottom by steps of $0.48\,\mu$m in the x direction (perpendicular to the orientation of the edge), as emphasized by the vertical dashed line. The pictures are an average of five individual experimental realizations, performed without the edge potential in order to better see the displacement of the tweezer. The scale bar corresponds to $10a$. **b-c,** Evolution of the cloud for the two chiralities. The first line shows the average of the absorption images after an increasing evolution time, displayed with the same colorscale. The second line shows the result of the Gaussian fit that is performed on the averaged images. On these fits, the center of the Gaussian is indicated as a black dot. The error bar, which stems from a bootstrap analysis, is smaller than the marker. **d,** The absolute distance Δr between the center-of-mass positions of the time-evolved clouds with the two different chiralities is plotted as a function of the time. The five different markers correspond to the five initial positions, and the corresponding solid lines are linear fits. **e,** The slope of the fit is divided by a factor of two to obtain the average velocity of the edge mode. The measured velocity is plotted as a function of the initial position, and the final value that is selected is the maximum value of these points. The markers are the same as **d.** For the leftmost tweezer position the error bar is very large: the atoms are released on top of the potential step and no reliable velocity can be extracted.

is varied with respect to the edge by steps of approximately $0.5\,\mu$m. Figure 5.19a shows the five different initial position of the tweezer used to optimize the overlap between the initial state and the edge mode. In this measurement the wall potential is off such that the position of the wave packet directly reflects the position of the tweezer trap and is not additionally influenced by the repulsive edge. To extract the velocity we release the cloud from the tweezer and observe its subsequent evolution for various durations, and

for the two opposite chiralities of the modulation scheme. The top rows of Figure 5.19b and c show the evolution for the two chiralities in the anomalous regime and with an edge height of $V_0 = h \times 19.0(3)\,\mathrm{kHz}$, where each picture is the average of N_im experimental images. The position of the center of mass of these observed clouds are evaluated by fitting the averaged images with a Gaussian function with its center, its amplitude, its two sizes, its offset and the orientation of its eigenaxes as free parameters. The error bars of these fitted parameters are estimated with a bootstrap method: Among the N_im experimental images, a random draw with replacement of N_im of these images is performed. The chosen images (with possible repetition) are averaged and the resulting image is fitted with the same Gaussian function. This random drawing, averaging and fitting procedure is repeated 20 times, thus providing as many estimates for the parameters of the Gaussian. The error bar for the fitted parameters is given by the standard deviation of these obtained values.

Figure 5.19d shows the distance Δr between the center of mass of the wavepacket for the two chiralities plotted as a function of the time of evolution. The separation of the two clouds is linear with time: with one chirality of the modulation the cloud moves with average velocity $+v$ in the y-direction, and for the other chirality it moves with velocity $-v$. The slope of Δr as a function of evolution time is extracted by a linear fit, and is divided by a factor of two to obtain the average velocity of the edge mode. The error is estimated by taking the error of the linear fit. This velocity is extracted for all the initial positions of the tweezer with respect to the edge, as shown in Figure 5.19e, and displays a maximum when the overlap of the initial wave packet with the edge mode is maximized. The observable that is reported in the following is thus the maximal velocity that has been measured, along with its error bar.

5.2.2 Emergence of edge modes on a topological interface

In our experimental setup the topological interface is generated by a potential step. An edge mode arises whenever two topologically different systems are brought into contact and form an interface, e.g. a sample with $\mathcal{C}^- = 1$ having an interface to topologically trivial vacuum. A similar interface can be realized with a potential step, if the energetic difference between the two subsystems is large enough to completely decouple the two systems, then even though both systems might be topological an edge mode emerges. A more intuitive scenario would consist of a topologically non-trivial system without any gradient connected to a the same system with an adjustable gradient, i.e., a flat lattice connected to a tilted one. Upon increasing the tilt the individual sites located in the region with the tilt will be decoupled parallel to the tilt for a critical energy difference between the sites and the system will undergo a transition to a topologically trivial regime in the tilted area. We will now find an edge mode at the interface between the two systems. Experimentally we cannot engineer a region with and without tilt but create a potential comparable to a combination of the two scenarios described before. We create a low potential region, a few sites are located on the edge with a gradient and a region at high potential energy. In order to understand the characteristic energy scale of the potential needed for an edge
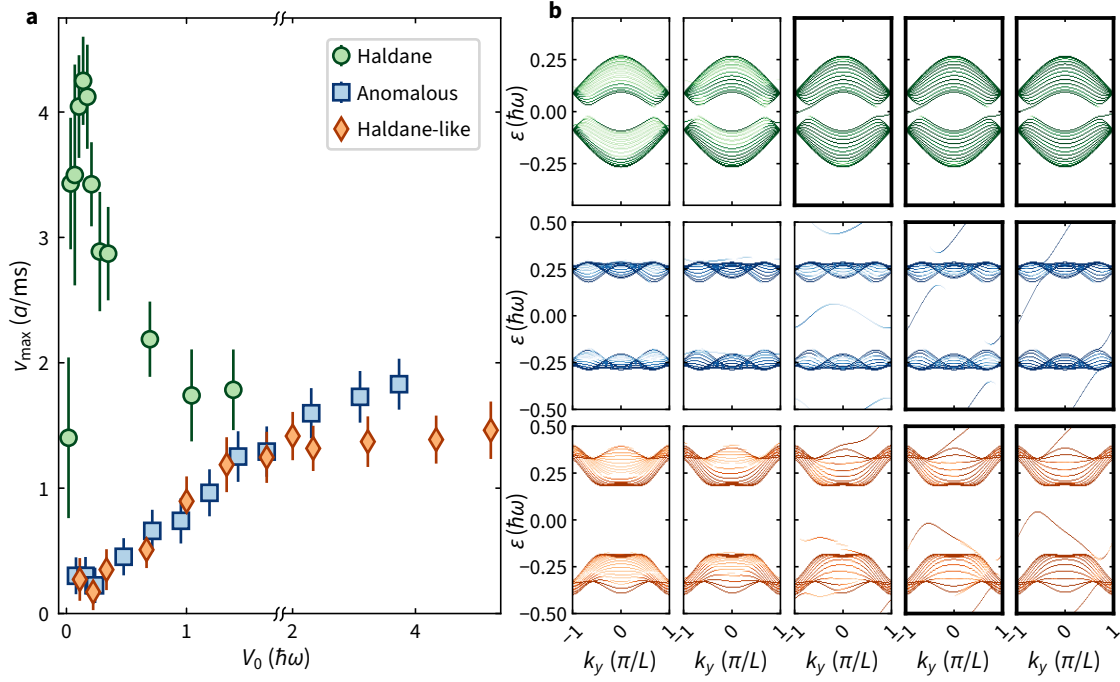
Figure 5.20 | **Emergence of edge modes with increasing potential height** V_0. **a**, Measured maximum edge mode velocity v_{max}. The modulation parameters for the three distinct topological regimes are indicated in Figure 5.1a. Each data point is the average of three data sets that have been taken on different days, and the error bars are calculated from their standard deviation and the uncertainty due to the evaluation of the edge mode velocity. **b**, Numerical simulations of the quasienergy spectrum using a step-wise modulated tight-binding model on a semi-infinite system for the three topological regimes: Haldane (top row), anomalous (middle row) and Haldane-like (bottom row). In the finite direction, an infinitely sharp potential step of height V_0 is applied in the middle of the system. The spectra show the eigenenergies whose eigenstates have a significant overlap with this low-potential region. The potential height is increased from the left to the right with $V_0/(\hbar\omega) = \{0.05, 0.1, 0.5, 1.5, 2.5\}$. The spectra where the edge modes are clearly visible are highlighted with a bold black frame.

mode to emerge at the interface, we investigate the maximum velocity v_{max} of the edge mode as a function of the height of the potential V_0.

We study the three topological regimes indicated by the colored hexagons in Figure 5.1: the Haldane regime with the edge mode in the 0-gap, the anomalous regime with edge modes in both the 0- and π-gap, and the Haldane-like regime where the topological edge mode is located in the π-gap.

In all three topological regimes we find that the group velocity of the atoms starts to increase as we increase the height of the potential (Figure 5.20a). In the Haldane regime the maximum velocity is reached for a potential on the order of $\approx 0.14\hbar\omega$, which matches the characteristic energy scale of the tunneling in the modulated lattice. For larger potential depths the velocity starts to gradually decrease. Intuitively, one may expect a saturation of the velocity as soon as the edge mode is established at the interface. We attribute the gradual slowing down observed in our experiment to potential corrugations and a smaller slope of the potential edge near the bottom of the potential, which becomes more significant as we

increase its height. The general trend observed in the anomalous and Haldane-like regime is similar, but distinctly different from the Haldane regime in terms of absolute values. Here, we find that the characteristic energy scale for the potential needed to reach the maximum group velocity is on the order of $\approx \hbar\omega$. For larger values we observe a saturation behavior.

To support the experimental results, we numerically investigate the semi-infinite strip geometry, where the potential energy of one half of the strip in the finite direction is increased by V_0, cf. Section 2.5.6. In order to visualize the appearance of the topological interface, we show the eigenenergies in the low-potential region in Figure 5.20b by projecting onto the low energy region of the system excluding the numerical edge. Similar to our experimental results we find that in the Haldane regime, the edge mode in the 0-gap emerges at a characteristic energy scale given by the largest tunneling during the period, which is about five times smaller than $\hbar\omega$. For the same potential height there are no clear signatures of edge modes in the anomalous and the Haldane-like regimes in any of the two gaps. Instead we find a characteristic energy scale on the order of $\hbar\omega$ for them to appear. In Figure 5.20b we highlight all spectra where we believe that edge modes can clearly be identified. This behavior is qualitatively consistent with our observations.

This measurement illustrates the stark contrast between the two regimes: The Haldane regime where the relevant parameters are related to the effective Hamiltonian, i.e., the edge mode emerges once the potential difference between the regions V_0 becomes comparable to the strongest effective tunneling. In the anomalous and Haldane-like regime, where the edge modes in the π-gap exist due to the modulation with a frequency smaller than the bandwidth of the system, the relevant energy scale for the edge modes to emerge is not related to the tunneling, which is the same as in the Haldane regime, but to the modulation frequency. This finding underlines the out of equilibrium nature of the latter two phases, as the relevant energy scale is related to the drive.

The two regions in the lattice exhibit an energy gap introduced by the potential step, in principle a resonant process such as the modulation might be able to couple the two. Fine tuning of the modulation frequency and properties of the potential step result in such a coupling and an annihilation of the edge mode. Numerically we find for an infinitely sharp edge, that the edge mode becomes trivial, i.e., it no longer cross the gap between the bands, whenever a frequency component of the modulation is strong enough and resonant with the potential energy difference V_0. We numerically find this phenomenon occurring for both the edge mode in the 0- and π-gap, i.e., independent of the topological regime we investigate. As this effect occurs only in the limit of an infinitely sharp edge and very select potential heights, we believe to not be able to observe it experimentally as also illustrated further below. Figure 5.21 shows the annihilation of the edge mode in the Haldane regime for three different modulation schemes: 1) the modulation close to the experimental implementation (cf. Section 4.1), 2) a step wise modulation of the nearest neighbor tunneling and 3) a sinusoidal modulation of the nearest neighbor tunneling as introduced in Section 2.4. The spectra in Figure 5.21 are again plotted with the overlap P of the respective eigenstate with the low energy region excluding the numerical edge. The edge is centered in the middle of the strip in the finite direction, a fully delocalized state will therefore have an overlap with the select region of $P \approx 0.5$. As expected in the absence of a wall we find no edge mode and
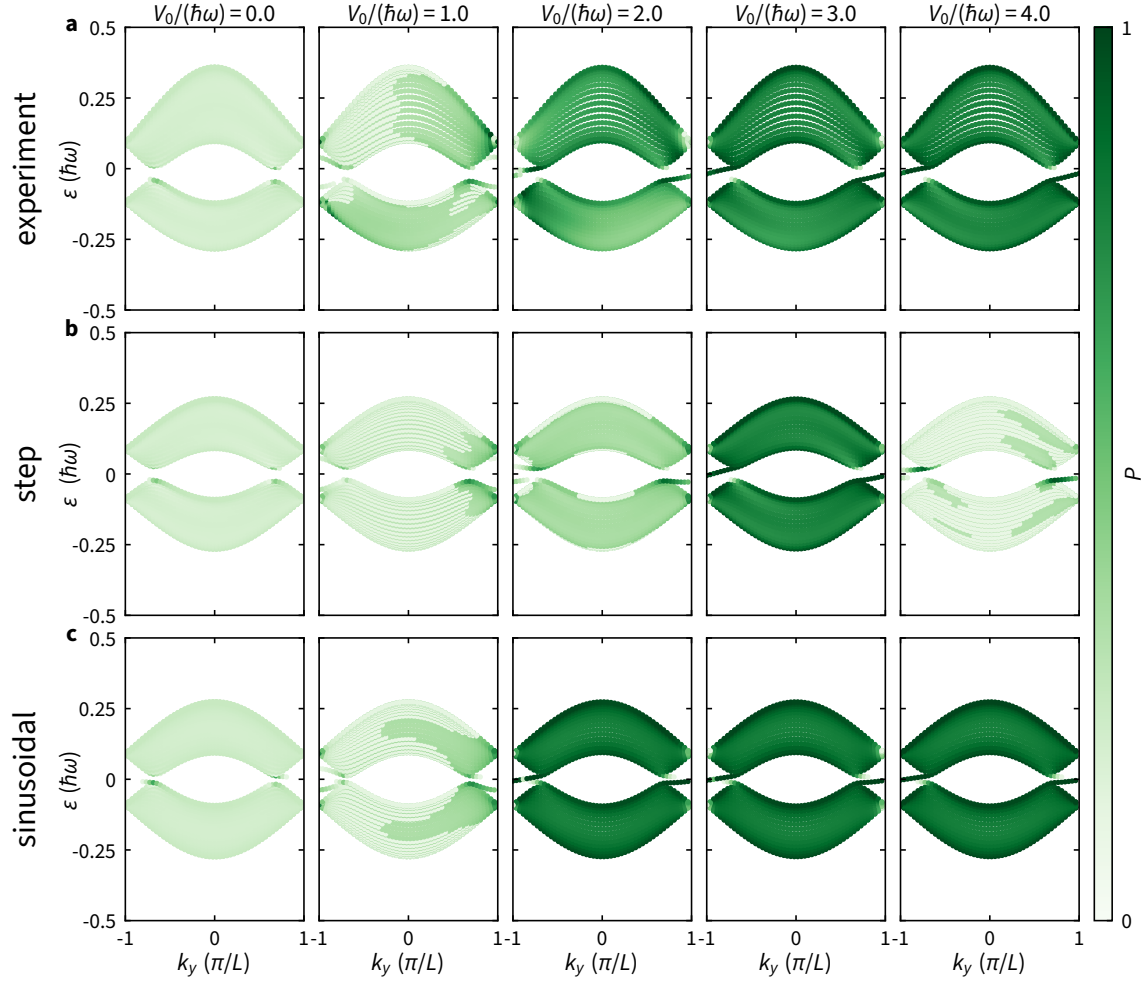
Figure 5.21 | Annihilation of the edge mode for $V_0 = \hbar\omega$. **a,** Resulting dispersion for different V_0 being an integer multiple of the modulation frequency for the modulation similar to the experiment ($m = 0.25$, $\omega/(2\pi) = 16\,\text{kHz}$). The shading of the spectrum corresponds to the overlap with the region in the low energy region of the potential. In the absence of a potential barrier in the center we observe no edge mode and the states are delocalized over the full sample. Even though we observe an edge mode for $V_0 < \hbar\omega$ it is absent at $V_0 = \hbar\omega$ and the states are also delocalized. For larger $V_0/\hbar\omega$ the effects become smaller and the system is full localized in the low energy region. **b,** same as **a** but for the step modulated drive ($\Lambda = 10$, $\hbar\omega/(\Lambda J_0) = 4.5$). We observe an annihilation of the edge mode for all but $V_0/(\hbar\omega) = 3$, as expected from the Fourier components of the drive. **c,** same as **a** but for the sinusoidal modulation of the tunneling amplitudes ($\Lambda = 10$, $\hbar\omega/(\Lambda J_0) = 6$). As the drive contains only a single frequency component ω, we only observe a coupling there and none for all others.

the states are delocalized over the entire strip as shown by the shading of the spectrum. We find an edge mode in the Haldane regime for $V_0 < \hbar\omega$ as long as the potential is higher than the largest tunneling in the lattice $V_0 > \Lambda J_0$ (cf. Figure 5.20b). For $V_0 = \hbar\omega$ in the infinitely sharp edge case $\ell = 0$, we find that the system again is to a large fraction delocalized over the entire strip and the edge mode is not longer crossing the 0-gap. The delocalization of the eigenstates across the entire system depicted as the shading of the dispersion and the edge mode not crossing the energy gap are closely linked. We observe this behavior

for all three modulation types. The Fourier decompositon of the sinusoidal modulation consists of a single tone at ω, we therefore observe no further resonance in the spectra (cf. Figure 5.20c). For the case of modulation similar to the experiment (cf. Section 4.1) we also find frequency components at multiples of the fundamental frequency with weights proportional to the modified Bessel functions of the first kind, leading to a significantly weaker coupling for $V_0/(\hbar\omega) = 2$. The case of the step modulated tunnel coupling provides a very clear picture for the coupling at different multiples of the drive frequency. Considering one of the three tunnel couplings we can write the modulation as a Fourier series. As we are only interested in the amplitude of the respective components we can shift the drive to enhance the coupling along the considered bond in the time $-T/6 \leq t < T/6$ and for the period of the drive we take the window $[-T/2, T/2)$. For the Fourier series

$$J(t) = \frac{a_0}{2} + \sum_{l=1}^{\infty} a_l \cos\left(\frac{l2\pi t}{T}\right) + \sum_{l=1}^{\infty} b_n \sin\left(\frac{l2\pi t}{T}\right) \tag{5.9}$$

we find the components

$$a_0 = \frac{J_0}{3}(2 + \Lambda), \tag{5.10}$$

$$a_l = \frac{\Lambda J_0}{l\pi} \sin\left(l2\pi\frac{T}{3}\right) \tag{5.11}$$

$$b_l = 0. \tag{5.12}$$

We immediately find that for $l = 3$ there is no Fourier component explaining the absence of the coupling for $V_0/(\hbar\omega) = 3$, this holds true for all resonances $n \times 3\hbar\omega$, $n \in \mathbb{N}$ of the drive frequency. This also shows that the coupling strength is decreasing $\propto n^{-1}$, which we also observe by the reducing gap at the edge of the Brillouin zone for higher harmonics of the drive.

5.2.3 Changing the width of the potential

The role of the microscopic shape of the edge potential is very intricate when combined with the electronic interactions of electrons and part of active research for both the integer and fractional quantum Hall effect [100–103, 324]. In the non-interacting limit the finite width of the potential edge has a large impact on the group velocity of the particles in the edge modes, as the dispersion of the edge mode hybridizes with the bulk modes, resulting in a significant reduction of the velocity [120, 308, 318].

We investigate this behavior by tuning the width of the potential edge in the Haldane regime (Figure 5.22a). The width of the edge is controlled by varying the diameter d of an iris placed in the Fourier plane of the imaging system that is used to project the DMD potential into the atomic plane (cf. Figure 3.7). Because of the incoherent illumination closing the iris leads to a reduction of the potential height. This is compensated by an increase of the total power of the beam to ensure the same potential height V_0 for all measurements. The width of the edge is measured by imaging the pattern in an intermediate plane, fitting the edge profile with an error function and extracting the characteristic length
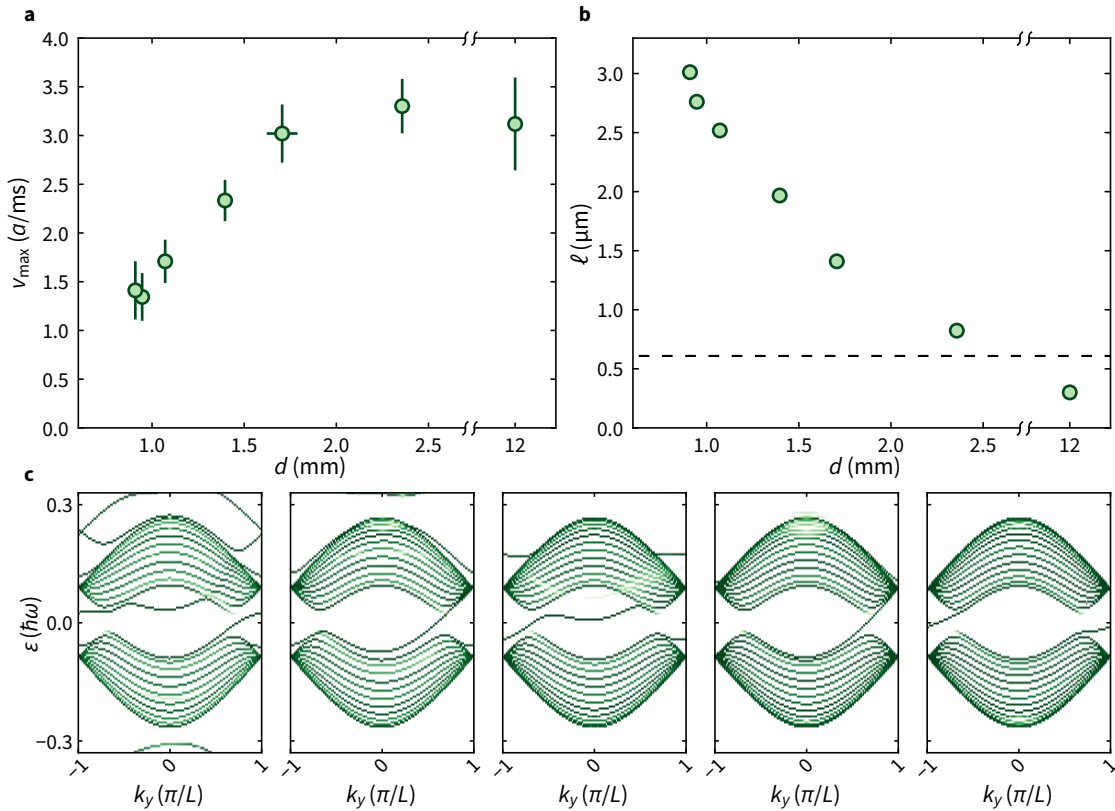
Figure 5.22 | Edge mode velocity for varying edge width. a, Measured edge mode velocity as the Fourier plane iris is closed for a repulsive potential with height $V_0/h = 1.10(2)$ kHz in the Haldane regime for $J_0 = 1.1(1)$ kHz, $\omega_{tw}/(2\pi) = 2.0(1)$ kHz and a phase gradient of $0.43(1)\pi/a$. The data points are averages of three individual datasets, and the error bars are evaluated from their standard deviation and the uncertainty of the evaluation of the velocity for each dataset. **b,** Estimated edge width of the pattern as a function of the diameter d of the iris in the Fourier plane. The dashed line corresponds to the theoretical resolution limit of the microscope objective. The edge width measured for an iris that is fully open (rightmost data point) is thus limited by the finite resolution of the objective. **c,** Floquet spectra simulated with the step-wise modulated tight-binding model in the Haldane regime (table in methods). The color indicates the overlap with a region covering the low-potential region. The height of the edge is fixed at $V_0/(\hbar\omega) = 1.5$, and its width is varied from left to right: $\ell/a = \{6, 4, 2, 1, 0.1\}$.

of this fit[1]. This length is then multiplied by the magnification between the intermediary plane and the atoms, which was calibrated independently to be 29.9 in this measurement. Figure 5.22b shows the resulting width as a function of the iris diameter. Note that the actual experimental value of the edge width at the atom position is most likely further increased by imperfect alignment and residual aberrations. The width of the wall is lower bounded by the resolution limit of the objective as indicated by the dashed horizontal line in Figure 5.22b, data points below this line are at least as wide as this value. We find that a smoothened edge leads to a significant reduction of the edge mode velocity, as expected [120, 308, 318]. This is further confirmed by numerical simulations using the

---

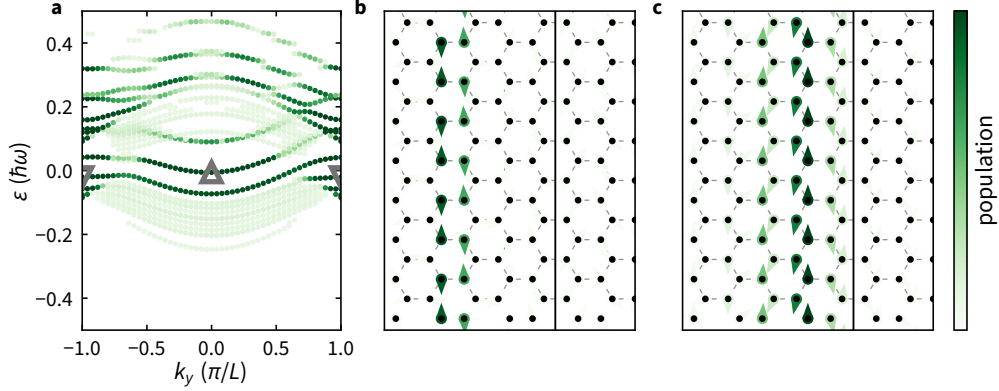[1]ℓ encodes the width of the edge, defined as the length from 8% to 92% of the height of the edge.

Figure 5.23 | Spectrum in the Haldane phase for $\ell = 10a$ and $V_0 = 2\hbar\omega/3$. a, Spectrum weighted by the state being localized up to $10a$ away from the edge. The state highlighted by the down facing gray triangle at $k_y = \pm\pi/L$ is depicted in **b**, the state at $k_y = 0$ indicated by the up facing grey triangle is plotted in **c**. **b,** Wave function of the state located at $k_y = 0$ in the gap between the bulk bands. The wave function is still very localized and not very spread out. Yet is still shows the same signatures as the states located at a infinitely sharp edge. **c,** Wave function of state located at $k_y = \pm\pi/L$ the state is located closer to the edge compared to **b** and more spread out. The population, indicated by the shading of the arrows, is normalized to the maximum population on a single site for the depicted state with the arrows' orientations indicating its complex phase.

step-wise modulated tight-binding model (Figure 5.22c). We introduce an edge of variable width ℓ into the center of the system. The edge is aligned such that it cuts the system along a zigzag edge for $\ell = 0$. Upon widening of the edge we observe the edge mode changing its properties. In the case of a very narrow wall we observe the edge mode connecting across the edge of the Brillouin zone between the Dirac points. For a wall of width $\ell = 2a$ the edge mode no longer crosses the edge of the Brillouin zone but traverses the Brillouin zone inside. The edge mode behaves similar to the barbed edge case (cf. Figure 5.14c). For the widest investigated wall we then observe several modes crossing the energy gap with significantly smaller average group velocity compared to the previous scenarios showing the same qualitative behavior we also observe in the experiment.

In Figure 5.23 we show the resulting dispersion for a system with an edge shaped as an error function with a width of $10a$. The energy difference between the low and high potential regions in the system is $V_0 = 2\hbar\omega/3$. The center of the edge at $V_0/2$ is highlighted by the vertical dark gray line in Figure 5.23b and c. We find several modes in the gap of the spectrum, where each state is weighted with its overlap with a region $10a$ from the center of the edge. This procedure reduces the visibility of the bulk in the low energy region and entirely masks the edge states resulting from the numerical edges and the bulk states located in the high energy region. Figure 5.23b and c show exemplary edge states located within the 0-gap at $k_y = 0$ and $k_y = \pm\pi/L$. The position of the edge modes compared to the infinitely sharp edge is significantly shifted and their position corresponds to the energetic order with higher lying states being located closer to the wall. We find a state with wider spread perpendicular to the wall in the region with larger slope of the potential, however this

might be an effect of the chosen edge shape and might vary strongly for a different shape. Nevertheless also these results are consistent with the experimentally observed results, where an increasing number of modes bridges the gap leading to a significantly reduced velocity of the resulting edge mode and the overall width of the edge mode i.e., the width of the region with sites that participate to this edge mode is also increased Experimentally we have not investigated the behavior of the anomalous and Haldane-like regime, as we are not able to generate a sufficiently high wall upon reducing the iris diameter.

5.3 Atom number and lifetime in the edge mode

We calibrate the observed number of atoms in the edge mode by estimating the Thomas-Fermi radius of a small BEC in the optical dipole trap in two ways. The first one is to fit the density profile of the cloud with an inverted parabola, and the second one is to calculate it via the Thomas-Fermi formula [313]:

$$R_{\mathrm{TF}} = \left(\frac{15 N_{\mathrm{at}} a_{\mathrm{s}} \hbar^2 \omega_z}{m_{\mathrm{K}}^2 \omega_r^3} \right)^{1/5},$$

$$(5.13)$$

where a_{s} is the s-wave scattering length of the atoms, m_{K} is the mass of a potassium atom, and ω_z (resp. ω_r) is the vertical (resp. radial) frequency of the optical dipole trap. In this formula, the number of atoms N_{at} is replaced by $\sigma_{\mathrm{sc}}\mathrm{OD}$, where σ_{sc} is the scattering cross-section of the imaging process, and OD is the summed optical density of the cloud. The exact value of σ_{sc} is unknown due to the proximity of the $^2P_{3/2}$ states during the imaging, and the comparison between the two values obtained for the Thomas-Fermi radius allows to calibrate this quantity, and therefore provide the proportionality factor between the optical density and the number of atoms.

We take a series of pictures of a small BEC in the optical dipole trap, and for each picture evaluate the Thomas-Fermi radius with the two methods above. Figure 5.24a shows the results, where the horizontal axis is rescaled by adjusting the value of σ_{sc} such that the Thomas-Fermi radii of the least dense clouds obtained with the two methods match: the solid line has a slope of one. We obtain a scattering cross-section of $\sigma_{\mathrm{sc}} = 0.085 \times 3\lambda_0^2/(2\pi)$, where $\lambda_0 = 767\,\mathrm{nm}$ is the wavelength of the imaging light. This value is then used to estimate the number of atoms that are loaded in the edge modes.

We measure the lifetime of the atoms in the edge state by summing the optical density of averaged pictures for various evolution times. We evaluate the error on this sum by averaging different subsets of images and computing the summed optical density on these averages, in a similar manner to the procedure described by a bootstrapping method (cf. Section 5.2.1). The summed optical densities and their respective error bars are then multiplied by the factor determined above to obtain the atom number. Figure 5.24b shows the atom number as a function of hold time for two experiments, one in the Haldane regime (green), and one in the anomalous regime (blue). We then fit each dataset with an exponential decay to evaluate the characteristic lifetime. In the Haldane regime this
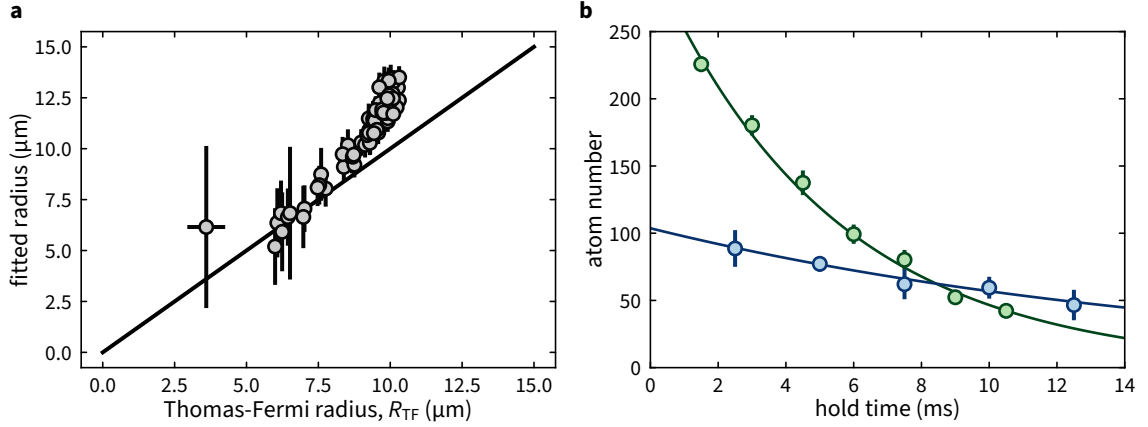
Figure 5.24 | Atom number calibration and lifetime of atoms in the edge state. a, Atom number cali-
bration. Each data point corresponds to an experimental realization of a BEC in the dipole trap. The two
estimated radial sizes of the cloud are plotted on the horizontal and vertical axes. The horizontal axis
is rescaled in order to match the estimated size of the cloud in the dilute regime. The solid line has a
slope of one, the vertical error bars represent the error of the fit of the radius, and the horizontal error is
estimated from the background noise of the absorption image. **b**, Lifetime in the edge mode. The number
of atoms in the edge mode is measured in two regimes: Haldane (green) and anomalous (blue). The error
bars correspond to the standard deviation of the atom numbers obtained by the bootstrapping method
(see text). The points are fitted with an exponential decay (solid lines), from which a lifetime is extracted
as the only free parameter. The presented data is an average over 10-38 averages for the blue and 27-72
averages for the green data points, the number of averages is increasing for longer hold times.

lifetime is 5 ms, and in the anomalous phase 17 ms. For reference, the lifetime of a bulk
BEC in the modulated lattice without any edge potential is measured to be around 100 ms.
The discrepancy of the bulk lifetime compared to the measurements of [111, 174] might be
explained by the different measurement techniques. We estimate the lifetime from a BEC
in the modulated lattice in situ, we are therefore not able to distinguish the population in
different bands. This method was chosen as we are not able to prepare the edge mode with
the small tweezer and image the cloud after time of flight. The measurements in [111, 174]
were taken after bandmapping and a long time of flight to exclude all populations in higher
bands. The reduced lifetime in the edge mode could be due to spurious dynamics in the
vertical direction: the Rayleigh length associated with the resolution of the potential edge
is around $3\,\mu$m, which is smaller than the vertical extension of the atoms prepared in the
tweezer. As a result, only part of the atomic cloud may be prepared in the edge mode and
the observed loss rate would then be a combination of heating in the modulated lattice
and losses along the vertical direction. In contrast, the lifetime of the atomic cloud in the
modulated lattice is measured by preparing a large BEC in the combined potential formed
by the dipole trap and the honeycomb lattice, which does not suffer from any mismatch of
potentials in the vertical direction. The modulation frequency in the anomalous regime is
$\omega/(2\pi) = 7\,$kHz, in the Haldane regime $\omega/(2\pi) = 16\,$kHz, for both regimes the modulation
amplitude $m = 0.25$ and the tweezer trap frequency $\omega_{\text{tw}}/(2\pi) = 2.0(1)\,$kHz. The height
of the optical step potential is $V_0 = h \times 16.7(3)\,$kHz for the anomalous edge mode and
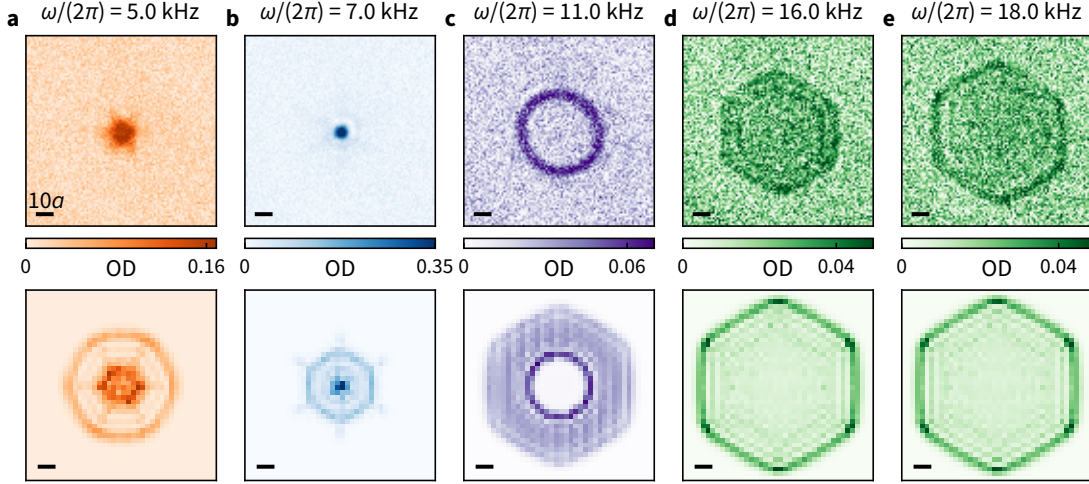$V_0 = h \times 5.6(1)\,$kHz in the Haldane regime.

Figure 5.25 │ **Expansion of a localized wave packet in the tunneling modulated lattice. a**, Expansion in the Haldane-like regime. **b**, Expansion in the anomalous regime. **c**, Expansion at the phase transition between anomalous and Haldane phase, the initial width of the Gaussian wave packet in the simulation is $\sigma = 1.4a$. **d**, Expansion in the Haldane regime. **e**, Expansion in the Haldane regime, but at $\omega/(2\pi) = 18$ kHz. The scale bar in the lower left of each image corresponds to $10\,a$, the modulation frequency in each column is indicated on the top image. The time of expansion in all images is $t = 3$ ms. The upper row is experimental data (modulation amplitude $m = 0.25$), the lower row represents a numerical simulation of the drive in a two-band tight binding approximation of an initial Gaussian wave packet with width $0.35a$ except for **c**.

5.4 Bulk expansion in the modulated lattice

As discussed in Section 2.5, the band structure of the modulated system significantly deviates from the static one. We can therefore assume to also find significantly different group velocities resulting from the modified dispersion. In the anomalous regime the dispersion exhibits a *moat* band, with a quasi degenerate ring surrounding Γ [178, 325]. Overall the bands in the Haldane-like and anomalous regime are significantly less dispersive and we expect significantly smaller group velocities of the bands. Similar to the experiments presented in Section 5.1.2 we perform a quantum walk in the modulated lattice. After ramping up the lattice and modulation the cloud is released from a tweezer with $\omega_{\mathrm{tw}} = 1.3(1)$ kHz and evolving in the lattice for 3 ms, when we take an absorption image of the cloud.

In the Haldane phase we observe a evolution similar to the static lattice: we observe a hexagonal outline with interference fringes inside of it due to the coherent evolution and the resulting interference of different paths.

The reduced group velocity in the anomalous and Haldane-like regime is directly reflected by the reduced spread after the expansion compared to the Haldane regime. A large fraction of the cloud barely spreads as shown in Figure 5.25a and b. Similar to the tight binding simulation we also observe a faint star-like pattern in the Haldane-like and a standing hexagon surrounding the central peak in the anomalous regime. The initial state in the simulations is assumed to be Gaussian wave packet with a standard deviation $\sigma = 0.35a$.

The evolution of the wave packet in the tight binding simulation in the vicinity of the phase transition does not show the ringlike structure for the same narrow initial state. By increasing the size of the wave packet to $\sigma = 1.4a$ we can reproduce a ring structure but additionally find a hexagonal shape surrounding the ring, which we do not observe in the experiment. For even larger initial states in the simulations we can recover the experimental observation, where we only find a ringlike pattern after the expansion. The absence of zero group velocity states is consistent between theory and experiment: the ringlike pattern emerges at the phase transition, where the bands touch and the dispersion in the π-gap forms a cone in the vicinity of Γ. Potentially the tight binding simulation produces a region with linear slope in momentum space that is significantly smaller than the one implemented in the experiment.

The larger initial state in the simulations does not match with the experiment in the other regimes. The discrepancy between the experimental observation and the tight binding simulation is currently not fully understood. In the Haldane regime we find a better match between theory and experiment. However, the size of the wave packet after $t = 3\,\mathrm{ms}$ of expansion is essentially unchanged in the simulation when comparing $\omega/(2\pi) = 16\,\mathrm{kHz}$ and $\omega/(2\pi) = 18\,\mathrm{kHz}$ (Figure 5.25d and e), while we observe a significant increase in the experimental realization. Potentially a weak admixture of the higher-lying p-bands of the band structure via a 2-photon resonance is responsible for the discrepancy. The two-band model does not account for this admixture. A more sophisticated survey of modulation parameters should reveal a regime where this coupling is absent, or at least significantly reduced. A straightforward approach would be to reduce the modulation amplitude which would reduce any possible admixture via higher photon processes of the drive significantly to identify the coupling to the p-bands as source of the varying size.

Conclusions and outlook

The work presented in this thesis highlights the versatility of the intensity modulated honeycomb lattice to probe the emerging topological features in momentum and real space. The presented Floquet drive results in a chiral, periodic modulation of the tunnel coupling in the lattice and opens up a rich phase diagram hosting conventional phases such as the Haldane phase and genuine out of equilibrium phases such as the anomalous Floquet phase.

Using a spatially extended ultracold bosonic cloud in the optical honeycomb lattice allowed for local measurements in momentum space. The narrow momentum space width enabled direct measurement of the energy gaps in the Floquet Brillouin zone. Following the behavior of the system from the high frequency limit as we decreased the modulation frequency we directly identified the gap closings. By probing the Berry curvature of a single band using deflection measurements we have fully reconstructed the topological invariants of the system. For modulation frequencies smaller than the band width of the lowest two bands we identified the anomalous Floquet phase, where the Chern number of the bulk band vanishes but chiral edge modes exist at the edge of the system.

Utilizing an optical tweezer we have prepared states in the lattice that exhibit an extent comparable to the lattice spacing. Such a localized cloud, in contrast to the bulk cloud used for the characterization in momentum space, occupied almost the entire Brillouin zone. Probing the expansion dynamics from the tweezer we additionally established the evolution of the system to be coherent. We have implemented a spectral and spatial incoherent light source to create programmable, low speckle binary potentials with high spatial resolution. By combining the spatially localized cloud, the high resolution programmable potential and the intensity modulated honeycomb lattice we have prepared the edge modes of the topological system.

We showed how to prepare the edge mode in three topological regimes and revealed the quasimomentum structure of the resulting edge modes. The observed results are qualitatively consistent with a simple stepwise modulation resulting in the same topological phases. We probed the emergence of edge modes on a topological interface as the height of the potential edge was varied. We identified the relevant energy scales in the Haldane regime to be related to the tunneling, while in the anomalous Floquet system edge modes emerge on edges with a potential energy difference larger than the drive frequency. Varying

the width of the optical step potential we showed that the edge mode slows down as the edge becomes wider, which is in agreement with theoretical expectations.

The presented experiment establishes a versatile platform to probe the topological nature of the systems in real and momentum space.

In the near future creating a quantum point contact where individual edge modes split or merge can be readily implemented in the presented system. In solid state systems the technique allows for the interference of edge modes [326, 327], direct determination of the coherence length of the edge mode [328] and investigation of edge reconstruction, i.e., induced quantum phase transitions at the edge due to electronic interactions [102]. Complications in the experiment might be preparing two wave packets with fixed phase difference for every experimental repetition or alternatively extending the lifetime of the state to enable coherent splitting and recombination.

With all necessary experimental tools implemented we want to also explore the interplay of the topological system with disorder. The transport on the edge is immune to scattering and disorder, however once all bulk states of conventional Chern insulators are localized the edge mode will also not be conductive anymore [75]. In contrast the anomalous Floquet insulator exhibits conductive edge modes even in the case where all bulk states have been localized [94]. The resulting anomalous Floquet Anderson insulator might be within reach for the experimental parameters [96].

Towards exploring a fully localized bulk, an experiment in a similar direction might investigate a disorder-induced phase transition from the Haldane to the anomalous Floquet phase [329]. The edge mode in the Haldane regime requires a kick to prepare a significant edge fraction. If we prepare a slightly extended state without applying a kick in the Haldane regime we observe no chiral signal as this initial state does not have a significant overlap with the edge mode. A transition from the Haldane to the anomalous regime would be accompanied by an edge mode in the π-gap, which requires no phase gradient. Thus detecting a chiral signal with the slightly extended initial state could serve as a sensitive probe to detect this phase transition. Similarly we can probe the robustness of the edge mode in the Haldane and anomalous regime.

In the absence of disorder but by adding an energy offset between A- and B-sites, the phase diagram of the intensity modulated lattice also hosts a phase with $\mathcal{C} = 2$ where the winding numbers are $W^0 = 1$ $W^\pi = -1$ [174, 323]. In contrast to a static system with $\mathcal{C}^- = 2$, where both edge modes would necessarily be located in a single gap and therefore have a slope with the same sign, the phase proposed here exhibits two counter propagating edge modes on the same edge where each is located on one of the two sublattices. Furthermore combining the preparation presented here with the detection scheme presented in [330], we will be able to resolve the localization of the two edge modes on their respective sublattice.

Additionally preparing the system with an A-B-offset in the modulated but topologically trivial regime would allow for investigation of the transition from the trivial to the topological Anderson insulator regime, or equivalently an Floquet-Anderson insulator regime by applying disorder to the system [113, 253–255, 261, 262]. In contrast to the disorder induced

transition from the Haldane to the anomalous phase the system here starts out in a topologically trivial regime.

In the current experiments we cannot prepare states of the system at a chosen energy, the proposed *cold-atom elevator* outlines a strategy to overcome this challenge [122]. By preparing a reservoir with tunable potential energy compared to the adjacent system of interest states with selected (quasi)energy can be launched into the system. Preparing an additional wall potential separating the two systems allows for a controlled coupling between the them by opening a few sites between the two. By tuning the energy difference between the reservoir and system, the excitation of bulk and edge modes can be probed in an energy selective manner and thus allows probing selectively e.g. the π- or 0-gap of the system.

One major challenge to overcome is the heating in driven systems, which in the long time limit will heat to infinite temperature [331, 332]. Identifying regimes where the heating is exponentially suppressed and therefore leads to a long-lived "prethermal" state [333–346] could allow for observation of the system on intermediate time scales. Alternatively careful engineering of the drive can also significantly reduce the amount of absorbed photons from the drive [347].

In the presence of interactions realizing a many-body localized bulk in combination with the Floquet drive [90, 348–351] while keeping the edge mobile [352] might prove as a viable probe for topology in the strongly interacting regime.

If the heating can be controlled without disorder, investigating the bosonic Haldane Hubbard model [353–357] might provide an interesting future direction. Local on-site interactions significantly enrich the phase diagram and experiments could provide experimental insights into the phase transition from a superfluid to a interaction dominated plaquette Mott insulator or a chiral superfluid [354, 355]. The plaquette Mott insulator is expected to host local chiral currents without long range order, which might be detectable via the method proposed in [358]. Recent progress towards the realization of a chiral superfluid [359] might indicate a possible preparation scheme which involves evaporatively cooling the system towards the ground state.

Even though the parameters are experimentally challenging, [360] provides a pathway to realize fractional quantum Hall states in a shaken optical honeycomb lattice. Probing the edge states in this regime could provide new insights by directly observing if additional co- and counter propagating or even neutral modes emerge [100–104]. The precise control over the edge potential's shape, width and height might provide new observables to tackle the question of the so-called edge reconstruction.
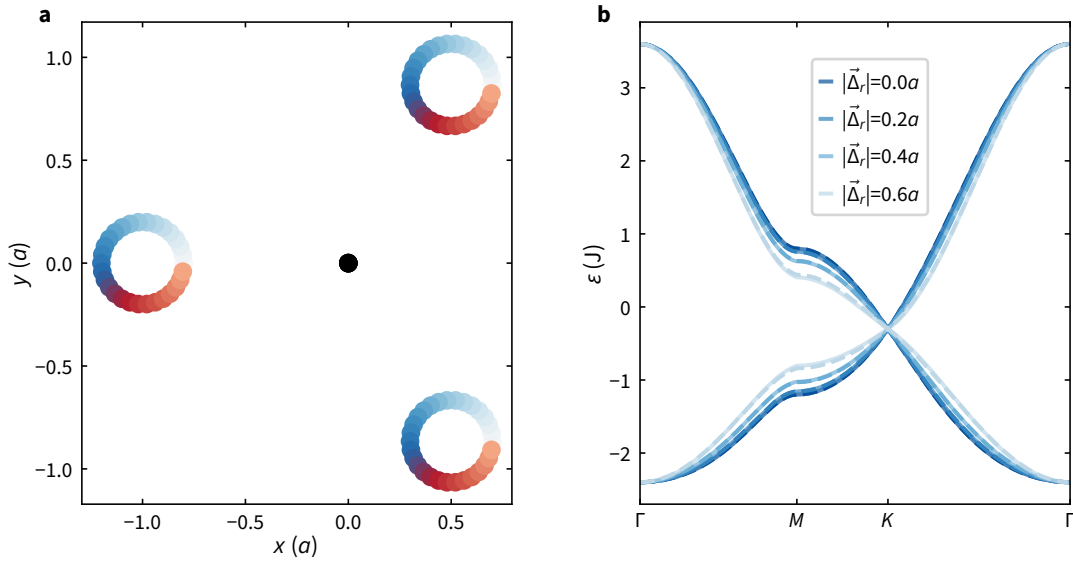
Appendices

Appendix A   Moving sublattice B

Figure A.1 │ Effect of moving sublattice B**. a**, Motion of the sublattice B in the reference frame of sublattice A. During one period, indicated by the color shading, the sites of sublattice B move on a circular path around the original position, while sublattice A (black) remains fixed. The depicted path represents $|\Delta_r| = 0.2a$. **b**, Effect of the moving sites on the band structure. The solid lines show the result obtained by Equation A.11, while the dashed lines are the result of a numerical integration of Equation A.2. The parameters are $t/J = 0.1, \varphi = 0, \Delta_{AB}/J = 0$.

When periodically modulating the lattice intensity, the optical potential is continuously varying. The varying potential landscape also leads to a motion of the A- and B-sites of the optical lattice. In the laboratory frame both sites move on an egg-shaped trajectory. Transforming to a frame, where the A-site is fixed in position and only the B-site is moving relative to the A-site is convenient. We can calculate the effect of the motion of the sites in a toy model where only the position is modulated while all other parameters are fixed. Starting from the Haldane model we introduce a simple motion of the B-site sub-lattice. For simplicity we approximate the motion as a circular motion of the B-site around its original place. For any motion of the sites $\mathbf{a}_j$ is not changing, but the δ_j are perturbed by a small shift $\mathbf{\Delta}_r$ as illustrated in Figure A.1a.

144

The shift in position is then given by:

$$\mathbf{\Delta}_r(t) = |\mathbf{\Delta}_r| \left(\sin(\omega t)\mathbf{e}_1 + \cos(\omega t)\mathbf{e}_2\right), \tag{A.1}$$

where $\mathbf{e}_1$ and $\mathbf{e}_2$ are two orthogonal unit vectors in the plane of the lattice. The Haldane Hamiltonian now reads:

$$\hat{H} = \frac{\Delta}{2}\sigma_z + \sum_{j=1}^{3} \begin{pmatrix} 2t\cos\left(\phi + \mathbf{k}\cdot\mathbf{a}_j\right) & Je^{i\mathbf{k}\cdot(\boldsymbol{\delta}_j + \mathbf{\Delta}_r(t))} \\ Je^{-i\mathbf{k}\cdot(\boldsymbol{\delta}_j + \mathbf{\Delta}_r(t))} & 2t\cos\left(\phi - \mathbf{k}\cdot\mathbf{a}_j\right) \end{pmatrix} \tag{A.2}$$

Applying a time-dependent gauge transformation

$$\hat{U}(t) = \begin{pmatrix} \exp\left(-\frac{i\mathbf{k}}{2}\cdot(\boldsymbol{\delta}_1 + \mathbf{\Delta}_r(t))\right) & 0 \\ 0 & \exp\left(\frac{i\mathbf{k}}{2}\cdot(\boldsymbol{\delta}_1 + \mathbf{\Delta}_r(t))\right) \end{pmatrix} \tag{A.3}$$

to the Hamiltonian according to $\hat{H}' = \hat{U}\hat{H}\hat{U}^\dagger + i\hbar\dot{\hat{U}}\hat{U}^\dagger$ We find after the transformation

$$\hat{H}' = \begin{pmatrix} \frac{\Delta}{2} + \sum_{j=1}^{3} 2t\cos\left(\phi + \mathbf{k}\cdot\mathbf{a}_j\right) & J(1 + e^{i\mathbf{k}\cdot(\boldsymbol{\delta}_2 - \boldsymbol{\delta}_1)} + e^{i\mathbf{k}\cdot(\boldsymbol{\delta}_3 - \boldsymbol{\delta}_1)}) \\ J(1 + e^{-i\mathbf{k}\cdot(\boldsymbol{\delta}_2 - \boldsymbol{\delta}_1)} + e^{-i\mathbf{k}\cdot(\boldsymbol{\delta}_3 - \boldsymbol{\delta}_1)}) & -\frac{\Delta}{2} + \sum_{j=1}^{3} 2t\cos\left(\phi - \mathbf{k}\cdot\mathbf{a}_j\right) \end{pmatrix} + \frac{\hbar\mathbf{k}}{2}\cdot\dot{\mathbf{\Delta}}_r(t)\,\sigma_z \tag{A.4}$$

We now find an additional term

$$\hat{V}(t) = \sigma_z\hbar\mathbf{k}\cdot\dot{\mathbf{\Delta}}_r(t)/2. \tag{A.5}$$

Assuming this is a small correction at high frequency we can expand the Hamiltonian in units of $(\hbar\omega)^{-1}$ [92, 162, 361–363]. The expansion for the effective Hamiltonian averaged over one period is given by Equation 2.61, where $\hat{H}_0$ is the static part of $\hat{H}'$, and $V^{(j)}$ are defined via Equation 2.60. Rewriting $\hat{H}'$ as a sum of Pauli matrices $\sigma_0 = I_2, \sigma_1, \sigma_2, \sigma_3$

$$\hat{H}' = \alpha\sigma_0 + \beta\sigma_1 + \gamma\sigma_2 + \delta\sigma_3 \tag{A.6}$$

with the coefficients

$$\alpha = \sum_{j=1}^{3} 2t\cos\phi\cos\left(\mathbf{k}\cdot\mathbf{a}_j\right) \tag{A.7}$$

$$\beta = J\left[1 + \cos(\mathbf{k}\cdot(\boldsymbol{\delta}_2 - \boldsymbol{\delta}_1)) + \cos\left(\mathbf{k}\cdot(\boldsymbol{\delta}_3 - \boldsymbol{\delta}_1)\right)\right] \tag{A.8}$$

$$\gamma = J\left[\sin\left(\mathbf{k}\cdot(\boldsymbol{\delta}_2 - \boldsymbol{\delta}_1)\right) + \sin\left(\mathbf{k}\cdot(\boldsymbol{\delta}_3 - \boldsymbol{\delta}_1)\right)\right] \tag{A.9}$$

$$\delta = \sum_{j=1}^{3} -2t\sin\left(\phi\right)\sin\left(\mathbf{k}\cdot\mathbf{a}_j\right) + \frac{\Delta}{2}, \tag{A.10}$$

we immediately find that only the terms $\propto \sigma_1, \sigma_2$ are affected by the motion of the B-sites, since $\hat{V}(t)$ commutes with the other terms. After evaluating Equation 2.61 up to second order one finds the effective Hamiltonian

$$H_{\text{eff}} = \alpha\sigma_0 + \left(\beta - \frac{|\mathbf{\Delta}_r|^2 |\mathbf{k}|^2}{4}\right)\sigma_1 + \left(\gamma - \frac{|\mathbf{\Delta}_r|^2 |\mathbf{k}|^2}{4}\right)\sigma_2 + \delta\sigma_3, \qquad (A.11)$$

we immediately find, that the effect of the moving sites becomes larger for increasing quasi-momenta $\mathbf{k}$ and increasing amplitude of the motion $\mathbf{\Delta}_r$. The correction does not lead to a gap opening but modifies the band curvature. To verify that the second order approximation properly captures the dynamics, Figure A.1 shows the resulting band structure resulting from Equation A.11 for varying amplitude of the position modulation together with the effective Hamiltonian obtained by integrating Equation A.2 over one period. Even though the B-sites are moving with respect to the A-sites the bands are not affected strongly by the motion as is visible by the deviations shown in Figure A.1b. Typical amplitudes for the modulation parameters used in the experiment are $\mathbf{\Delta}_r \approx 0.2a$, therefore the motion of the lattice sites is not a significant modification of the band structure.

Bibliography

[1] M. H. Anderson, J. R. Ensher, M. R. Matthews, C. E. Wieman, and E. A. Cornell, *Observation of Bose-Einstein Condensation in a Dilute Atomic Vapor*, Science **269**, 198 (1995).

[2] C. C. Bradley, C. A. Sackett, J. J. Tollett, and R. G. Hulet, *Evidence of Bose-Einstein Condensation in an Atomic Gas with Attractive Interactions*, Physical Review Letters **75**, 1687 (1995).

[3] K. B. Davis, M. .-. Mewes, M. R. Andrews, N. J. van Druten, D. S. Durfee, D. M. Kurn, and W. Ketterle, *Bose-Einstein Condensation in a Gas of Sodium Atoms*, Physical Review Letters **75**, 3969 (1995).

[4] B. DeMarco and D. S. Jin, *Onset of Fermi Degeneracy in a Trapped Atomic Gas*, Science **285**, 1703 (1999).

[5] I. Bloch, J. Dalibard, and W. Zwerger, *Many-Body Physics with Ultracold Gases*, Reviews of Modern Physics **80**, 885 (2008).

[6] C. Gross and I. Bloch, *Quantum Simulations with Ultracold Atoms in Optical Lattices*, Science **357**, 995 (2017).

[7] C. Chin, R. Grimm, P. Julienne, and E. Tiesinga, *Feshbach Resonances in Ultracold Gases*, Reviews of Modern Physics **82**, 1225 (2010).

[8] N. Navon, R. P. Smith, and Z. Hadzibabic, *Quantum Gases in Optical Boxes*, Nature Physics **17**, 1334 (2021).

[9] A. Görlitz, J. M. Vogels, A. E. Leanhardt, C. Raman, T. L. Gustavson, J. R. Abo-Shaeer, A. P. Chikkatur, S. Gupta, S. Inouye, T. Rosenband, and W. Ketterle, *Realization of Bose-Einstein Condensates in Lower Dimensions*, Physical Review Letters **87**, 130402 (2001).

[10] A. J. Leggett, *Bose-Einstein Condensation in the Alkali Gases: Some Fundamental Concepts*, Reviews of Modern Physics **73**, 307 (2001).

[11] C. A. Regal, C. Ticknor, J. L. Bohn, and D. S. Jin, *Creation of Ultracold Molecules from a Fermi Gas of Atoms*, Nature **424**, 47 (2003).

[12] S. Jochim, M. Bartenstein, A. Altmeyer, G. Hendl, S. Riedl, C. Chin, J. Hecker Denschlag, and R. Grimm, *Bose-Einstein Condensation of Molecules*, Science **302**, 2101 (2003).

[13] M. Greiner, C. A. Regal, and D. S. Jin, *Emergence of a Molecular Bose–Einstein Condensate from a Fermi Gas*, Nature **426**, 537 (2003).

[14] M. W. Zwierlein, C. A. Stan, C. H. Schunck, S. M. F. Raupach, S. Gupta, Z. Hadzibabic, and W. Ketterle, *Observation of Bose-Einstein Condensation of Molecules*, Physical Review Letters **91**, 250401 (2003).

[15] W. Zwerger, ed., *The BCS-BEC Crossover and the Unitary Fermi Gas*, Vol. 836, Lecture Notes in Physics (Springer, Berlin, Heidelberg, 2012).

[16] N. D. Mermin and H. Wagner, *Absence of Ferromagnetism or Antiferromagnetism in One- or Two-Dimensional Isotropic Heisenberg Models*, Physical Review Letters **17**, 1133 (1966).

[17] P. C. Hohenberg, *Existence of Long-Range Order in One and Two Dimensions*, Physical Review **158**, 383 (1967).

[18] V. L. Berezinsky, *Destruction of Long-range Order in One-dimensional and Two-dimensional Systems Possessing a Continuous Symmetry Group. II. Quantum Systems.* Sov. Phys. JETP **34**, 610 (1972).

[19] J. M. Kosterlitz and D. J. Thouless, *Ordering, Metastability and Phase Transitions in Two-Dimensional Systems*, Journal of Physics C: Solid State Physics **6**, 1181 (1973).

[20] Z. Hadzibabic, P. Krüger, M. Cheneau, B. Battelier, and J. Dalibard, *Berezinskii–Kosterlitz–Thouless Crossover in a Trapped Atomic Gas*, Nature **441**, 1118 (2006).

[21] I. Bloch, *Ultracold Quantum Gases in Optical Lattices*, Nature Physics **1**, 23 (2005).

[22] L. Tonks, *The Complete Equation of State of One, Two and Three-Dimensional Gases of Hard Elastic Spheres*, Physical Review **50**, 955 (1936).

[23] E. H. Lieb and W. Liniger, *Exact Analysis of an Interacting Bose Gas. I. The General Solution and the Ground State*, Physical Review **130**, 1605 (1963).

[24] B. Paredes, A. Widera, V. Murg, O. Mandel, S. Fölling, I. Cirac, G. V. Shlyapnikov, T. W. Hänsch, and I. Bloch, *Tonks–Girardeau Gas of Ultracold Atoms in an Optical Lattice*, Nature **429**, 277 (2004).

[25] T. Kinoshita, T. Wenger, and D. S. Weiss, *Observation of a One-Dimensional Tonks-Girardeau Gas*, Science **305**, 1125 (2004).

[26] M. Girardeau, *Relationship between Systems of Impenetrable Bosons and Fermions in One Dimension*, Journal of Mathematical Physics **1**, 516 (2004).

[27] H. Kadau, M. Schmitt, M. Wenzel, C. Wink, T. Maier, I. Ferrier-Barbut, and T. Pfau, *Observing the Rosensweig Instability of a Quantum Ferrofluid*, Nature **962**, 1 (2015).

[28] I. Ferrier-Barbut, H. Kadau, M. Schmitt, M. Wenzel, and T. Pfau, *Observation of Quantum Droplets in a Strongly Dipolar Bose Gas*, Physical Review Letters **116**, 215301 (2016).

[29] C. R. Cabrera, L. Tanzi, J. Sanz, B. Naylor, P. Thomas, P. Cheiney, and L. Tarruell, *Quantum Liquid Droplets in a Mixture of Bose-Einstein Condensates*, Science **359**, 301 (2018).

[30] P. Cheiney, C. R. Cabrera, J. Sanz, B. Naylor, L. Tanzi, and L. Tarruell, *Bright Soliton to Quantum Droplet Transition in a Mixture of Bose-Einstein Condensates*, Physical Review Letters **120**, 135301 (2018).

[31] F. Böttcher, J.-N. Schmidt, M. Wenzel, J. Hertkorn, M. Guo, T. Langen, and T. Pfau, *Transient Supersolid Properties in an Array of Dipolar Quantum Droplets*, Physical Review X **9**, 011051 (2019).

[32] L. Tanzi, E. Lucioni, F. Famà, J. Catani, A. Fioretti, C. Gabbanini, R. N. Bisset, L. Santos, and G. Modugno, *Observation of a Dipolar Quantum Gas with Metastable Supersolid Properties*, Physical Review Letters **122**, 130405 (2019).

[33] L. Chomaz, D. Petter, P. Ilzhöfer, G. Natale, A. Trautmann, C. Politi, G. Durastante, R. M. W. van Bijnen, A. Patscheider, M. Sohmen, M. J. Mark, and F. Ferlaino, *Long-Lived and Transient Supersolid Behaviors in Dipolar Quantum Gases*, Physical Review X **9**, 021012 (2019).

[34] L. Tanzi, S. M. Roccuzzo, E. Lucioni, F. Famà, A. Fioretti, C. Gabbanini, G. Modugno, A. Recati, and S. Stringari, *Supersolid Symmetry Breaking from Compressional Oscillations in a Dipolar Quantum Gas*, Nature **574**, 382 (2019).

[35] M. Guo, F. Böttcher, J. Hertkorn, J.-N. Schmidt, M. Wenzel, H. P. Büchler, T. Langen, and T. Pfau, *The Low-Energy Goldstone Mode in a Trapped Dipolar Supersolid*, Nature **574**, 386 (2019).

[36] W. S. Bakr, A. Peng, M. E. Tai, R. Ma, J. Simon, J. I. Gillen, S. Folling, L. Pollet, and M. Greiner, *Probing the Superfluid-to-Mott Insulator Transition at the Single-Atom Level*, Science **329**, 547 (2010).

[37] J. F. Sherson, C. Weitenberg, M. Endres, M. Cheneau, I. Bloch, and S. Kuhr, *Single-Atom-Resolved Fluorescence Imaging of an Atomic Mott Insulator*, Nature **467**, 68 (2010).

[38] C. Gross and W. S. Bakr, *Quantum Gas Microscopy for Single Atom and Spin Detection*, Nature Physics **17**, 1316 (2021).

[39] J. Koepsell, J. Vijayan, P. Sompet, F. Grusdt, T. A. Hilker, E. Demler, G. Salomon, I. Bloch, and C. Gross, *Imaging Magnetic Polarons in the Doped Fermi–Hubbard Model*, Nature **572**, 358 (2019).

[40] J. Vijayan, P. Sompet, G. Salomon, J. Koepsell, S. Hirthe, A. Bohrdt, F. Grusdt, I. Bloch, and C. Gross, *Time-Resolved Observation of Spin-Charge Deconfinement in Fermionic Hubbard Chains*, Science **367**, 186 (2020).

[41] G. Ji, M. Xu, L. H. Kendrick, C. S. Chiu, J. C. Brüggenjürgen, D. Greif, A. Bohrdt, F. Grusdt, E. Demler, M. Lebrat, and M. Greiner, *Coupling a Mobile Hole to an Antiferromagnetic Spin Background: Transient Dynamics of a Magnetic Polaron*, Physical Review X **11**, 021022 (2021).

[42] M. Endres, H. Bernien, A. Keesling, H. Levine, E. R. Anschuetz, A. Krajenbrink, C. Senko, V. Vuletic, M. Greiner, and M. D. Lukin, *Atom-by-Atom Assembly of Defect-Free One-Dimensional Cold Atom Arrays*, Science **354**, 1024 (2016).

[43] D. Barredo, S. de Léséleuc, V. Lienhard, T. Lahaye, and A. Browaeys, *An Atom-by-Atom Assembler of Defect-Free Arbitrary Two-Dimensional Atomic Arrays*, Science **354**, 1021 (2016).

[44] H. Bernien, S. Schwartz, A. Keesling, H. Levine, A. Omran, H. Pichler, S. Choi, A. S. Zibrov, M. Endres, M. Greiner, V. Vuletić, and M. D. Lukin, *Probing Many-Body Dynamics on a 51-Atom Quantum Simulator*, Nature **551**, 579 (2017).

[45] A. Keesling, A. Omran, H. Levine, H. Bernien, H. Pichler, S. Choi, R. Samajdar, S. Schwartz, P. Silvi, S. Sachdev, P. Zoller, M. Endres, M. Greiner, V. Vuletić, and M. D. Lukin, *Quantum Kibble–Zurek Mechanism and Critical Dynamics on a Programmable Rydberg Simulator*, Nature **568**, 207 (2019).

[46] W. Heisenberg, *Über den anschaulichen Inhalt der quantentheoretischen Kinematik und Mechanik*, Zeitschrift für Physik **43**, 172 (1927).

[47] S. Sachdev, *Quantum Phase Transitions*, 2nd ed. (Cambridge University Press, 2011).

[48] L. D. Landau, E. M. Lifshits, L. P. Pitaevskiĭ, L. D. Landau, and L. D. Landau, *Statistical physics*, Pergamon international library of science, technology, engineering, and social studies v. 5, 9 (Pergamon Press, Oxford ; New York, 1980).

[49] K. v. Klitzing, G. Dorda, and M. Pepper, *New Method for High-Accuracy Determination of the Fine-Structure Constant Based on Quantized Hall Resistance*, Physical Review Letters **45**, 494 (1980).

[50] K. von Klitzing, *The Quantized Hall Effect*, Reviews of Modern Physics **58**, 519 (1986).

[51] K. Von Klitzing, T. Chakraborty, P. Kim, V. Madhavan, X. Dai, J. McIver, Y. Tokura, L. Savary, D. Smirnova, A. M. Rey, C. Felser, J. Gooth, and X. Qi, *40 Years of the Quantum Hall Effect*, Nature Reviews Physics **2**, 397 (2020).

[52] R. Moessner and J. E. Moore, *Topological Phases of Matter*, 1st ed. (Cambridge University Press, 2021).

[53] B. Jeckelmann and B. Jeanneret, *The Quantum Hall Effect as an Electrical Resistance Standard*, Reports on Progress in Physics **64**, 1603 (2001).

[54] Bureau International des Poids et Mesures, *On the Revision of the International System of Units (SI)*, Resolution 1 of the 26th CGPM (2018).

[55] D. J. Thouless, M. Kohmoto, M. P. Nightingale, and M. Den Nijs, *Quantized Hall Conductance in a Two-Dimensional Periodic Potential*, Physical Review Letters **49**, 405 (1982).

[56] M. Nakahara, *Geometry, Topology and Physics, Second Edition* (Taylor & Francis, 2003).

[57] M. Z. Hasan and C. L. Kane, *Colloquium: Topological Insulators*, Reviews of Modern Physics **82**, 3045 (2010).

[58] X.-L. Qi and S.-C. Zhang, *Topological Insulators and Superconductors*, Reviews of Modern Physics **83**, 1057 (2011).

[59] A. Altland and M. R. Zirnbauer, *Nonstandard Symmetry Classes in Mesoscopic Normal-Superconducting Hybrid Structures*, Physical Review B **55**, 1142 (1997).

[60] C.-K. Chiu, J. C. Y. Teo, A. P. Schnyder, and S. Ryu, *Classification of Topological Quantum Matter with Symmetries*, Reviews of Modern Physics **88**, 035005 (2016).

[61] F. D. M. Haldane, *Model for a Quantum Hall Effect without Landau Levels: Condensed-Matter Realization of the "Parity Anomaly"*, Physical Review Letters **61**, 2015 (1988).

[62] C. L. Kane and E. J. Mele, *Quantum Spin Hall Effect in Graphene*, Physical Review Letters **95**, 1 (2005).

[63] B. A. Bernevig and S.-C. Zhang, *Quantum Spin Hall Effect*, Physical Review Letters **96**, 106802 (2006).

[64] B. A. Bernevig, T. L. Hughes, and S.-C. Zhang, *Quantum Spin Hall Effect and Topological Phase Transition in HgTe Quantum Wells*, Science **314**, 1757 (2006).

[65] M. Konig, S. Wiedmann, C. Brune, A. Roth, H. Buhmann, L. W. Molenkamp, X.-L. Qi, and S.-C. Zhang, *Quantum Spin Hall Insulator State in HgTe Quantum Wells*, Science **318**, 766 (2007).

[66] D. C. Tsui, H. L. Stormer, and A. C. Gossard, *Two-Dimensional Magnetotransport in the Extreme Quantum Limit*, Physical Review Letters **48**, 1559 (1982).

[67] R. B. Laughlin, *Anomalous Quantum Hall Effect: An Incompressible Quantum Fluid with Fractionally Charged Excitations*, Physical Review Letters **50**, 1395 (1983).

[68] H. L. Stormer, D. C. Tsui, and A. C. Gossard, *The Fractional Quantum Hall Effect*, Reviews of Modern Physics **71**, S298 (1999).

[69] B. I. Halperin, *Statistics of Quasiparticles and the Hierarchy of Fractional Quantized Hall States*, Physical Review Letters **52**, 1583 (1984).

[70] D. Arovas, J. R. Schrieffer, and F. Wilczek, *Fractional Statistics and the Quantum Hall Effect*, Physical Review Letters **53**, 722 (1984).

[71] C. Nayak, S. H. Simon, A. Stern, M. Freedman, and S. Das Sarma, *Non-Abelian Anyons and Topological Quantum Computation*, Reviews of Modern Physics **80**, 1083 (2008).

[72] X. Chen, Z.-C. Gu, and X.-G. Wen, *Local Unitary Transformation, Long-Range Quantum Entanglement, Wave Function Renormalization, and Topological Order*, Physical Review B **82**, 155138 (2010).

[73] A. Stern, *Non-Abelian States of Matter*, Nature **464**, 187 (2010).

[74] R. B. Laughlin, *Quantized Hall Conductivity in Two Dimensions*, Physical Review B **23**, 5632 (1981).

[75] B. I. Halperin, *Quantized Hall Conductance, Current-Carrying Edge States, and the Existence of Extended States in a Two-Dimensional Disordered Potential*, Physical Review B **25**, 2185 (1982).

[76] Y. Hatsugai, *Edge States in the Integer Quantum Hall Effect and the Riemann Surface of the Bloch Function*, Physical Review B **48**, 11851 (1993).

[77] Y. Hatsugai, *Chern Number and Edge States in the Integer Quantum Hall Effect*, Physical Review Letters **71**, 3697 (1993).

[78] H. Schulz-Baldes, J. Kellendonk, and T. Richter, *Simultaneous Quantization of Edge and Bulk Hall Conductivity*, Journal of Physics A: Mathematical and General **33**, L27 (2000).

[79] R. E. Prange, *Quantized Hall Resistance and the Measurement of the Fine-Structure Constant*, Physical Review B **23**, 4802 (1981).

[80] J. Dalibard, F. Gerbier, G. Juzeliūnas, and P. Öhberg, *Colloquium: Artificial Gauge Potentials for Neutral Atoms*, Reviews of Modern Physics **83**, 1523 (2011).

[81] F. Grossmann, T. Dittrich, P. Jung, and P. Hänggi, *Coherent Destruction of Tunneling*, Physical Review Letters **67**, 516 (1991).

[82] A. Eckardt, C. Weiss, and M. Holthaus, *Superfluid-Insulator Transition in a Periodically Driven Optical Lattice*, Physical Review Letters **95**, 260404 (2005).

[83] T. Oka and H. Aoki, *Photovoltaic Hall Effect in Graphene*, Physical Review B **79**, 081406 (2009).

[84] G. Jotzu, M. Messer, R. Desbuquois, M. Lebrat, T. Uehlinger, D. Greif, and T. Esslinger, *Experimental Realization of the Topological Haldane Model with Ultracold Fermions*, Nature **515**, 237 (2014).

[85] M. C. Rechtsman, J. M. Zeuner, Y. Plotnik, Y. Lumer, D. Podolsky, F. Dreisow, S. Nolte, M. Segev, and A. Szameit, *Photonic Floquet Topological Insulators*, Nature **496**, 196 (2013).

[86] T. Kitagawa, E. Berg, M. Rudner, and E. Demler, *Topological Characterization of Periodically Driven Quantum Systems*, Physical Review B **82**, 235114 (2010).

[87] M. S. Rudner, N. H. Lindner, E. Berg, and M. Levin, *Anomalous Edge States and the Bulk-Edge Correspondence for Periodically Driven Two-Dimensional Systems*, Physical Review X **3**, 031005 (2013).

[88] A. Eckardt, *Colloquium: Atomic Quantum Gases in Periodically Driven Optical Lattices*, Reviews of Modern Physics **89**, 011004 (2017).

[89] M. Aidelsburger, M. Atala, M. Lohse, J. T. Barreiro, B. Paredes, and I. Bloch, *Realization of the Hofstadter Hamiltonian with Ultracold Atoms in Optical Lattices*, Physical Review Letters **111**, 185301 (2013).

[90] F. Harper, R. Roy, M. S. Rudner, and S. Sondhi, *Topology and Broken Symmetry in Floquet Systems*, Annual Review of Condensed Matter Physics **11**, 345 (2020).

[91] C. Weitenberg and J. Simonet, *Tailoring Quantum Gases by Floquet Engineering*, Nature Physics **17**, 1342 (2021).

[92] N. Goldman and J. Dalibard, *Periodically Driven Quantum Systems: Effective Hamiltonians and Engineered Gauge Fields*, Physical Review X **4**, 031027 (2014).

[93] A. Eckardt and E. Anisimovas, *High-Frequency Approximation for Periodically Driven Quantum Systems from a Floquet-space Perspective*, New Journal of Physics **17**, 093039 (2015).

[94] P. Titum, E. Berg, M. S. Rudner, G. Refael, and N. H. Lindner, *Anomalous Floquet-Anderson Insulator as a Nonadiabatic Quantized Charge Pump*, Physical Review X **6**, 1 (2016).

[95] A. Kundu, M. Rudner, E. Berg, and N. H. Lindner, *Quantized Large-Bias Current in the Anomalous Floquet-Anderson Insulator*, Physical Review B **101**, 041403 (2020).

[96] A. Dutta, E. Sen, J.-H. Zheng, M. Aidelsburger, and W. Hofstetter, *The Anomalous Floquet Anderson Insulator in a Continuously Driven Optical Lattice*, 2023, arXiv:2312.13589, preprint.

[97] H. Bartolomei, M. Kumar, R. Bisognin, A. Marguerite, J.-M. Berroir, E. Bocquillon, B. Plaçais, A. Cavanna, Q. Dong, U. Gennser, Y. Jin, and G. Fève, *Fractional Statistics in Anyon Collisions*, Science **368**, 173 (2020).

[98] J. Nakamura, S. Liang, G. C. Gardner, and M. J. Manfra, *Direct Observation of Anyonic Braiding Statistics*, Nature Physics **16**, 931 (2020).

[99] H. K. Kundu, S. Biswas, N. Ofek, V. Umansky, and M. Heiblum, *Anyonic Interference and Braiding Phase in a Mach-Zehnder Interferometer*, Nature Physics **19**, 515 (2023).

[100] C. d. C. Chamon and X. G. Wen, *Sharp and Smooth Boundaries of Quantum Hall Liquids*, Physical Review B **49**, 8227 (1994).

[101] L. Liang, J. Wang, W. Lin, B. G. Sumpter, V. Meunier, and M. Pan, *Electronic Bandgap and Edge Reconstruction in Phosphorene Materials*, Nano Letters **14**, 6400 (2014).

[102] R. Sabo, I. Gurman, A. Rosenblatt, F. Lafont, D. Banitt, J. Park, M. Heiblum, Y. Gefen, V. Umansky, and D. Mahalu, *Edge Reconstruction in Fractional Quantum Hall States*, Nature Physics **13**, 491 (2017).

[103] U. Khanna, M. Goldstein, and Y. Gefen, *Edge Reconstruction and Emergent Neutral Modes in Integer and Fractional Quantum Hall Phases*, Low Temperature Physics **48**, 420 (2022).

[104] A. Coissard, A. G. Grushin, C. Repellin, L. Veyrat, K. Watanabe, T. Taniguchi, F. Gay, H. Courtois, H. Sellier, and B. Sacépé, *Absence of Edge Reconstruction for Quantum Hall Edge Channels in Graphene Devices*, Science Advances **9**, eadf7220 (2023).

[105] H.-N. Dai, B. Yang, A. Reingruber, H. Sun, X.-F. Xu, Y.-A. Chen, Z.-S. Yuan, and J.-W. Pan, *Four-Body Ring-Exchange Interactions and Anyonic Statistics within a Minimal Toric-Code Hamiltonian*, Nature Physics **13**, 1195 (2017).

[106] J. Léonard, S. Kim, J. Kwan, P. Segura, F. Grusdt, C. Repellin, N. Goldman, and M. Greiner, *Realization of a Fractional Quantum Hall State with Ultracold Atoms*, Nature **619**, 495 (2023).

[107] C. Repellin, J. Léonard, and N. Goldman, *Fractional Chern Insulators of Few Bosons in a Box: Hall Plateaus from Center-of-Mass Drifts and Density Profiles*, Physical Review A **102**, 063316 (2020).

[108] M. Aidelsburger, M. Lohse, C. Schweizer, M. Atala, J. T. Barreiro, S. Nascimbène, N. R. Cooper, I. Bloch, and N. Goldman, *Measuring the Chern Number of Hofstadter Bands with Ultracold Bosonic Atoms*, Nature Phys. **11**, 162 (2015).

[109] M. Tarnowski, F. N. Ünal, N. Fläschner, B. S. Rem, A. Eckardt, K. Sengstock, and C. Weitenberg, *Measuring Topology from Dynamics by Obtaining the Chern Number from a Linking Number*, Nature Communications **10**, 1728 (2019).

[110] L. Asteria, D. T. Tran, T. Ozawa, M. Tarnowski, B. S. Rem, N. Fläschner, K. Sengstock, N. Goldman, and C. Weitenberg, *Measuring Quantized Circular Dichroism in Ultracold Topological Matter*, Nature Physics **15**, 449 (2019).

[111] K. Wintersperger, **C. Braun**, F. N. Ünal, A. Eckardt, M. D. Liberto, N. Goldman, I. Bloch, and M. Aidelsburger, *Realization of an Anomalous Floquet Topological System with Ultracold Atoms*, Nature Physics **16**, 1058 (2020).

[112] S. Mukherjee, A. Spracklen, M. Valiente, E. Andersson, P. Öhberg, N. Goldman, and R. R. Thomson, *Experimental Observation of Anomalous Topological Edge Modes in a Slowly Driven Photonic Lattice*, Nature Communications **8**, 13918 (2017).

[113] S. Stützer, Y. Plotnik, Y. Lumer, P. Titum, N. H. Lindner, M. Segev, M. C. Rechtsman, and A. Szameit, *Photonic Topological Anderson Insulators*, Nature **560**, 461 (2018).

[114] T. Biesenthal, L. J. Maczewsky, Z. Yang, M. Kremer, M. Segev, A. Szameit, and M. Heinrich, *Fractal Photonic Topological Insulators*, Science **376**, 1114 (2022).

[115] J. Ningyuan, C. Owens, A. Sommer, D. Schuster, and J. Simon, *Time- and Site-Resolved Dynamics in a Topological Circuit*, Physical Review X **5**, 021031 (2015).

[116] M. Mancini, G. Pagano, G. Cappellini, L. Livi, M. Rider, J. Catani, C. Sias, P. Zoller, M. Inguscio, M. Dalmonte, and L. Fallani, *Observation of Chiral Edge States with Neutral Fermions in Synthetic Hall Ribbons*, Science **349**, 1510 (2015).

[117] B. K. Stuhl, H.-I. Lu, L. M. Aycock, D. Genkina, and I. B. Spielman, *Visualizing Edge States with an Atomic Bose Gas in the Quantum Hall Regime*, Science **349**, 1514 (2015).

[118] T. Chalopin, T. Satoor, A. Evrard, V. Makhalov, J. Dalibard, R. Lopes, and S. Nascimbene, *Probing Chiral Edge Dynamics and Bulk Topology of a Synthetic Hall System*, Nature Physics **16**, 1017 (2020).

[119] N. Goldman, J. Beugnon, and F. Gerbier, *Detecting Chiral Edge States in the Hofstadter Optical Lattice*, Physical Review Letters **108**, 255303 (2012).

[120] N. Goldman, J. Dalibard, A. Dauphin, F. Gerbier, M. Lewenstein, P. Zoller, and I. B. Spielman, *Direct Imaging of Topological Edge States in Cold-Atom Systems*, Proceedings of the National Academy of Sciences **110**, 6736 (2013).

[121] N. Goldman, G. Jotzu, M. Messer, F. Görg, R. Desbuquois, and T. Esslinger, *Creating Topological Interfaces and Detecting Chiral Edge Modes in a Two-Dimensional Optical Lattice*, Physical Review A **94**, 043611 (2016).

[122] B. Wang, M. Aidelsburger, J. Dalibard, A. Eckardt, and N. Goldman, *The Cold-Atom Elevator: From Edge-State Injection to the Preparation of Fractional Chern Insulators*, 2023, arXiv:2306.15610, preprint.

[123] **C. Braun**, R. Saint-Jalm, A. Hesse, J. Arceri, I. Bloch, and M. Aidelsburger, *Real-Space Detection and Manipulation of Topological Edge Modes with Ultracold Atoms*, 2023, arXiv:2304.01980, preprint.

[124] N. W. Ashcroft and N. D. Mermin, *Solid State Physics* (Holt, Rinehart and Winston, New York, 1976).

[125] C. Kittel, *Introduction to Solid State Physics*, 8th ed (Wiley, Hoboken, NJ, 2005).

[126] A. Shapere and F. Wilczek, eds., *Geometric Phases in Physics*, Advanced Series in Mathematical Physics v. 5 (World Scientific, Singapore ; Teaneck, N.J, 1989).

[127] M. V. Berry, *Quantal Phase Factors Accompanying Adiabatic Changes*, Proceedings of the Royal Society of London. A. Mathematical and Physical Sciences **392**, 45 (1984).

[128] A. Bohm, A. Mostafazadeh, H. Koizumi, Q. Niu, and J. Zwanziger, *The Geometric Phase in Quantum Systems* (Springer, Berlin, Heidelberg, 2003).

[129] Y. Aharonov and D. Bohm, *Significance of Electromagnetic Potentials in the Quantum Theory*, Physical Review **115**, 485 (1959).

[130] Y. Aharonov and D. Bohm, *Further Considerations on Electromagnetic Potentials in the Quantum Theory*, Physical Review **123**, 1511 (1961).

[131] D. Xiao, M.-C. Chang, and Q. Niu, *Berry Phase Effects on Electronic Properties*, Reviews of Modern Physics **82**, 1959 (2010).

[132] R. G. Chambers, *Shift of an Electron Interference Pattern by Enclosed Magnetic Flux*, Physical Review Letters **5**, 3 (1960).

[133] F. Bloch, *Über die Quantenmechanik der Elektronen in Kristallgittern*, Zeitschrift für Physik **52**, 555 (1929).

[134] D. Tong, *Lectures on the Quantum Hall Effect*, 2016, arXiv:1606.06687, preprint.

[135] R. E. Prange and S. M. Girvin, eds., *The Quantum Hall Effect*, red. by J. L. Birman, H. Faissner, and J. W. Lynn, Graduate Texts in Contemporary Physics (Springer, New York, NY, 1990).

[136] R. Peierls, *Zur Theorie des Diamagnetismus von Leitungselektronen*, Zeitschrift für Physik **80**, 763 (1933).

[137] B. A. Bernevig and T. L. Hughes, *Topological Insulators and Topological Superconductors* (Princeton University Press, 2013).

[138] Y. Yao, L. Kleinman, A. H. MacDonald, J. Sinova, T. Jungwirth, D.-s. Wang, E. Wang, and Q. Niu, *First Principles Calculation of Anomalous Hall Conductivity in Ferromagnetic Bcc Fe*, Physical Review Letters **92**, 037204 (2004).

[139] O. Stejskal, M. Veis, and J. Hamrle, *The Flow of the Berry Curvature Vector Field*, Scientific Reports **12**, 97 (2022).

[140] C. L. Fefferman, S. Fliss, and M. I. Weinstein, *Edge States in Rationally Terminated Honeycomb Structures*, Proceedings of the National Academy of Sciences **119**, e2212310119 (2022).

[141] S. Xia, Y. Liang, L. Tang, D. Song, J. Xu, and Z. Chen, *Photonic Realization of a Generic Type of Graphene Edge States Exhibiting Topological Flat Band*, Physical Review Letters **131**, 013804 (2023).

[142] D. Jaksch and P. Zoller, *Creation of Effective Magnetic Fields in Optical Lattices: The Hofstadter Butterfly for Cold Neutral Atoms*, New Journal of Physics **5**, 56 (2003).

[143] F. Gerbier and J. Dalibard, *Gauge Fields for Ultracold Atoms in Optical Superlattices*, New Journal of Physics **12**, 033007 (2010).

[144] M. Aidelsburger, M. Atala, S. Nascimbène, S. Trotzky, Y.-A. Chen, and I. Bloch, *Experimental Realization of Strong Effective Magnetic Fields in an Optical Lattice*, Physical Review Letters **107**, 255301 (2011).

[145] Y.-J. Lin, R. L. Compton, A. R. Perry, W. D. Phillips, J. V. Porto, and I. B. Spielman, *Bose-Einstein Condensate in a Uniform Light-Induced Vector Potential*, Physical Review Letters **102**, 130401 (2009).

[146] Y.-J. Lin, R. L. Compton, K. Jiménez-García, J. V. Porto, and I. B. Spielman, *Synthetic Magnetic Fields for Ultracold Neutral Atoms*, Nature **462**, 628 (2009).

[147] A. Celi, P. Massignan, J. Ruseckas, N. Goldman, I. B. Spielman, G. Juzeliūnas, and M. Lewenstein, *Synthetic Gauge Fields in Synthetic Dimensions*, Physical Review Letters **112**, 043001 (2014).

[148] H. Miyake, G. A. Siviloglou, C. J. Kennedy, W. C. Burton, and W. Ketterle, *Realizing the Harper Hamiltonian with Laser-Assisted Tunneling in Optical Lattices*, Physical Review Letters **111**, 185302 (2013).

[149] M. Bukov, L. D'Alessio, and A. Polkovnikov, *Universal High-Frequency Behavior of Periodically Driven Systems: From Dynamical Stabilization to Floquet Engineering*, Advances in Physics **64**, 139 (2015).

[150] Z. Gu, H. A. Fertig, D. P. Arovas, and A. Auerbach, *Floquet Spectrum and Transport through an Irradiated Graphene Ribbon*, Physical Review Letters **107**, 216601 (2011).

[151] G. Usaj, P. M. Perez-Piskunow, L. E. F. Foa Torres, and C. A. Balseiro, *Irradiated Graphene as a Tunable Floquet Topological Insulator*, Physical Review B **90**, 115423 (2014).

[152] J. W. McIver, B. Schulte, F.-U. Stein, T. Matsuyama, G. Jotzu, G. Meier, and A. Cavalleri, *Light-Induced Anomalous Hall Effect in Graphene*, Nature Physics **16**, 38 (2020).

[153] M. S. Rudner and N. H. Lindner, *Band Structure Engineering and Non-Equilibrium Dynamics in Floquet Topological Insulators*, Nature Reviews Physics **2**, 229 (2020).

[154] J.-Y. Shan, M. Ye, H. Chu, S. Lee, J.-G. Park, L. Balents, and D. Hsieh, *Giant Modulation of Optical Nonlinearity by Floquet Engineering*, Nature **600**, 235 (2021).

[155] T. Ozawa, H. M. Price, A. Amo, N. Goldman, M. Hafezi, L. Lu, M. C. Rechtsman, D. Schuster, J. Simon, O. Zilberberg, and I. Carusotto, *Topological Photonics*, Reviews of Modern Physics **91**, 15006 (2019).

[156] H. Lignier, C. Sias, D. Ciampini, Y. Singh, A. Zenesini, O. Morsch, and E. Arimondo, *Dynamical Control of Matter-Wave Tunneling in Periodic Potentials*, Physical Review Letters **99**, 220403 (2007).

[157] A. Eckardt, M. Holthaus, H. Lignier, A. Zenesini, D. Ciampini, O. Morsch, and E. Arimondo, *Exploring Dynamic Localization with a Bose-Einstein Condensate*, Physical Review A **79**, 013611 (2009).

[158] C. E. Creffield, F. Sols, D. Ciampini, O. Morsch, and E. Arimondo, *Expansion of Matter Waves in Static and Driven Periodic Potentials*, Physical Review A **82**, 035601 (2010).

[159] A. Zenesini, H. Lignier, D. Ciampini, O. Morsch, and E. Arimondo, *Coherent Control of Dressed Matter Waves*, Physical Review Letters **102**, 100403 (2009).

[160] J. H. Shirley, *Solution of the Schr\"odinger Equation with a Hamiltonian Periodic in Time*, Physical Review **138**, B979 (1965).

[161] M. Grifoni and P. Hänggi, *Driven Quantum Tunneling*, Physics Reports **304**, 229 (1998).

[162] S. Rahav, I. Gilary, and S. Fishman, *Effective Hamiltonians for Periodically Driven Systems*, Physical Review A **68**, 013820 (2003).

[163] A. Bouhon, A. M. Black-Schaffer, and R.-J. Slager, *Wilson Loop Approach to Fragile Topology of Split Elementary Band Representations and Topological Crystalline Insulators with Time-Reversal Symmetry*, Physical Review B **100**, 195135 (2019).

[164] L. J. Maczewsky, J. M. Zeuner, S. Nolte, and A. Szameit, *Observation of Photonic Anomalous Floquet Topological Insulators*, Nature Communications **8**, 13756 (2017).

[165] W. Hu, J. C. Pillay, K. Wu, M. Pasek, P. P. Shum, and Y. D. Chong, *Measurement of a Topological Edge Invariant in a Microwave Network*, Physical Review X **5**, 011012 (2015).

[166] Z. Zhang, P. Delplace, and R. Fleury, *Superior Robustness of Anomalous Non-Reciprocal Topological Edge States*, Nature **598**, 293 (2021).

[167] F. Gao, Z. Gao, X. Shi, Z. Yang, X. Lin, H. Xu, J. D. Joannopoulos, M. Soljačić, H. Chen, L. Lu, Y. Chong, and B. Zhang, *Probing Topological Protection Using a Designer Surface Plasmon Structure*, Nature Communications **7**, 11619 (2016).

[168] S. Afzal, T. J. Zimmerling, Y. Ren, D. Perron, and V. Van, *Realization of Anomalous Floquet Insulators in Strongly Coupled Nanophotonic Lattices*, Physical Review Letters **124**, 253601 (2020).

[169] A. D'Errico, F. Cardano, M. Maffei, A. Dauphin, R. Barboza, C. Esposito, B. Piccirillo, M. Lewenstein, P. Massignan, and L. Marrucci, *Two-Dimensional Topological Quantum Walks in the Momentum Space of Structured Light*, Optica **7**, 108 (2020).

[170] Y.-G. Peng, C.-Z. Qin, D.-G. Zhao, Y.-X. Shen, X.-Y. Xu, M. Bao, H. Jia, and X.-F. Zhu, *Experimental Demonstration of Anomalous Floquet Topological Insulator for Sound*, Nature Communications **7**, 13368 (2016).

[171] F. Nathan and M. S. Rudner, *Topological Singularities and the General Classification of Floquet–Bloch Systems*, New Journal of Physics **17**, 125014 (2015).

[172] J. Bellissard, *Change of the Chern Number at Band Crossings*, 1995, arXiv:cond-mat/9504030, preprint.

[173] S. M. Young, S. Zaheer, J. C. Y. Teo, C. L. Kane, E. J. Mele, and A. M. Rappe, *Dirac Semimetal in Three Dimensions*, Physical Review Letters **108**, 140405 (2012).

[174] K. Wintersperger, *Realization of Floquet Topological Systems with Ultracold Atoms in Optical Honeycomb Lattices*, PhD thesis, Ludwig-Maximilians-Universität München (2020).

[175] F. N. Ünal, B. Seradjeh, and A. Eckardt, *How to Directly Measure Floquet Topological Invariants in Optical Lattices*, Physical Review Letters **122**, 253601 (2019).

[176] T. A. Sedrakyan, L. I. Glazman, and A. Kamenev, *Spontaneous Formation of a Nonuniform Chiral Spin Liquid in a Moat-Band Lattice*, Physical Review Letters **114**, 037203 (2015).

[177] T. A. Sedrakyan, V. M. Galitski, and A. Kamenev, *Statistical Transmutation in Floquet Driven Optical Lattices*, Physical Review Letters **115**, 195301 (2015).

[178] C. A. Bracamontes, J. Maslek, and J. V. Porto, *Realization of a Floquet-Engineered Moat Band for Ultracold Atoms*, Physical Review Letters **128**, 213401 (2022).

[179] L. Duca, *Probing Topological Properties of Bloch Bands with Ultracold Atoms in a Honeycomb Optical Lattice*, PhD thesis, Ludwig-Maximilians-Universität München (2015).

[180] T. Li, *Probing Bloch Band Geometry with Ultracold Atoms in Optical Lattices*, PhD thesis, Ludwig-Maximilians-Universität München (2016).

[181] M. Reitter, *Scattering Processes in Interacting Floquet Systems*, PhD thesis, Ludwig-Maximilians-Universität München (2017).

[182] J. Näger, *Parametric Instabilities of Interacting Bosons in Driven Optical Lattices*, PhD thesis, Ludwig-Maximilians-Universität München (2019).

[183] K. Dieckmann, R. J. C. Spreeuw, M. Weidemüller, and J. T. M. Walraven, *Two-Dimensional Magneto-Optical Trap as a Source of Slow Atoms*, Physical Review A **58**, 3891 (1998).

[184] J. Schoser, A. Batär, R. Löw, V. Schweikhard, A. Grabowski, Yu. B. Ovchinnikov, and T. Pfau, *Intense Source of Cold Rb Atoms from a Pure Two-Dimensional Magneto-Optical Trap*, Physical Review A **66**, 023410 (2002).

[185] J. Catani, P. Maioli, L. De Sarlo, F. Minardi, and M. Inguscio, *Intense Slow Beams of Bosonic Potassium Isotopes*, Physical Review A **73**, 033415 (2006).

[186] H. J. Metcalf and P. Van der Straten, *Laser Cooling and Trapping*, Graduate Texts in Contemporary Physics (Springer, New York, 1999).

[187] C. J. Foot, *Atomic Physics*, Oxford Master Series in Physics 7. Atomic, Optical, and laser physics (Oxford University Press, Oxford ; New York, 2005).

[188] W. Petrich, M. H. Anderson, J. R. Ensher, and E. A. Cornell, *Behavior of Atoms in a Compressed Magneto-Optical Trap*, JOSA B **11**, 1332 (1994).

[189] M. Landini, S. Roy, L. Carcagní, D. Trypogeorgos, M. Fattori, M. Inguscio, and G. Modugno, *Sub-Doppler Laser Cooling of Potassium Atoms*, Physical Review A **84**, 043432 (2011).

[190] M. Greiner, I. Bloch, T. W. Hänsch, and T. Esslinger, *Magnetic Transport of Trapped Cold Atoms over a Large Distance*, Physical Review A **63**, 031401 (2001).

[191] C. V. Sukumar and D. M. Brink, *Spin-Flip Transitions in a Magnetic Trap*, Physical Review A **56**, 2451 (1997).

[192] D. M. Brink and C. V. Sukumar, *Majorana Spin-Flip Transitions in a Magnetic Trap*, Physical Review A **74**, 035401 (2006).

[193] D. S. Naik and C. Raman, *Optically Plugged Quadrupole Trap for Bose-Einstein Condensates*, Physical Review A **71**, 033617 (2005).

[194] H. F. Hess, *Evaporative Cooling of Magnetically Trapped and Compressed Spin-Polarized Hydrogen*, Physical Review B **34**, 3476 (1986).

[195] K. B. Davis, M.-O. Mewes, M. A. Joffe, M. R. Andrews, and W. Ketterle, *Evaporative Cooling of Sodium Atoms*, Physical Review Letters **74**, 5202 (1995).

[196] F. Ferlaino, C. D'Errico, G. Roati, M. Zaccanti, M. Inguscio, G. Modugno, and A. Simoni, *Feshbach Spectroscopy of a K - Rb Atomic Mixture*, Physical Review A **73**, 040702 (2006).

[197] F. Ferlaino, C. D'Errico, G. Roati, M. Zaccanti, M. Inguscio, G. Modugno, and A. Simoni, *Erratum: Feshbach Spectroscopy of a K - Rb Atomic Mixture [Phys. Rev. A **73** , 040702 (2006)]*, Physical Review A **74**, 039903 (2006).

[198] L. De Sarlo, P. Maioli, G. Barontini, J. Catani, F. Minardi, and M. Inguscio, *Collisional Properties of Sympathetically Cooled K 39*, Physical Review A **75**, 022715 (2007).

[199] L. G. Marcassa, G. D. Telles, S. R. Muniz, and V. S. Bagnato, *Collisional Losses in a K-Rb Cold Mixture*, Physical Review A **63**, 013413 (2000).

[200] T. Rom, *Bosonische und fermionische Quantengase in dreidimensionalen optischen Gittern*, PhD thesis, Ludwig-Maximilians-Universität München (2009).

[201] R. Grimm, M. Weidemüller, and Y. B. Ovchinnikov, *Optical Dipole Traps for Neutral Atoms*, in *Adv. At. Mol. Opt. Phys.* Vol. 42 (2000), 95, pmid: 15731538.

[202] F. Mies, C. Williams, P. Julienne, and M. Krauss, *Estimating Bounds on Collisional Relaxation Rates of Spin-Polarized 87Rb Atoms at Ultracold Temperatures*, Journal of Research of the National Institute of Standards and Technology **101**, 521 (1996).

[203] A. Simoni, M. Zaccanti, C. D'Errico, M. Fattori, G. Roati, M. Inguscio, and G. Modugno, *Near-Threshold Model for Ultracold KRb Dimers from Interisotope Feshbach Spectroscopy*, Physical Review A **77**, 052705 (2008).

[204] C. D'Errico, M. Zaccanti, M. Fattori, G. Roati, M. Inguscio, G. Modugno, and A. Simoni, *Feshbach Resonances in Ultracold ^{39} K*, New Journal of Physics **9**, 223 (2007).

[205] M. Zaccanti, B. Deissler, C. D'Errico, M. Fattori, M. Jona-Lasinio, S. Müller, G. Roati, M. Inguscio, and G. Modugno, *Observation of an Efimov Spectrum in an Atomic System*, Nature Physics **5**, 586 (2009).

[206] M. Lysebo and L. Veseth, *Feshbach Resonances and Transition Rates for Cold Homonuclear Collisions between K 39 and K 41 Atoms*, Physical Review A **81**, 032702 (2010).

[207] S. Roy, M. Landini, A. Trenkwalder, G. Semeghini, G. Spagnolli, A. Simoni, M. Fattori, M. Inguscio, and G. Modugno, *Test of the Universality of the Three-Body Efimov Parameter at Narrow Feshbach Resonances*, Physical Review Letters **111**, 053202 (2013).

[208] R. J. Fletcher, R. Lopes, J. Man, N. Navon, R. P. Smith, M. W. Zwierlein, and Z. Hadzibabic, *Two- and Three-Body Contacts in the Unitary Bose Gas*, Science **355**, 377 (2017).

[209] M. Reitter, J. Näger, K. Wintersperger, C. Sträter, I. Bloch, A. Eckardt, and U. Schneider, *Interaction Dependent Heating and Atom Loss in a Periodically Driven Optical Lattice*, Physical Review Letters **119**, 200402 (2017).

[210] K. Wintersperger, M. Bukov, J. Näger, S. Lellouch, E. Demler, U. Schneider, I. Bloch, N. Goldman, and M. Aidelsburger, *Parametric Instabilities of Interacting Bosons in Periodically Driven 1D Optical Lattices*, Physical Review X **10**, 011030 (2020).

[211] T. I. Vanhala, T. Siro, L. Liang, M. Troyer, A. Harju, and P. Törmä, *Topological Phase Transitions in the Repulsively Interacting Haldane-Hubbard Model*, Physical Review Letters **116**, 225305 (2016).

[212] G. Salerno, M. Di Liberto, C. Menotti, and I. Carusotto, *Topological Two-Body Bound States in the Interacting Haldane Model*, Physical Review A **97**, 013637 (2018).

[213] P. Mai, B. E. Feldman, and P. W. Phillips, *Topological Mott Insulator at Quarter Filling in the Interacting Haldane Model*, Physical Review Research **5**, 013162 (2023).

[214] A. Ashkin, *Trapping of Atoms by Resonance Radiation Pressure*, Physical Review Letters **40**, 729 (1978).

[215] S. Chu, J. E. Bjorkholm, A. Ashkin, and A. Cable, *Experimental Observation of Optically Trapped Atoms*, Physical Review Letters **57**, 314 (1986).

[216] Y. Shin, M. Saba, T. A. Pasquini, W. Ketterle, D. E. Pritchard, and A. E. Leanhardt, *Atom Interferometry with Bose-Einstein Condensates in a Double-Well Potential*, Physical Review Letters **92**, 050405 (2004).

[217] H. Labuhn, D. Barredo, S. Ravets, S. de Léséleuc, T. Macrì, T. Lahaye, and A. Browaeys, *Tunable Two-Dimensional Arrays of Single Rydberg Atoms for Realizing Quantum Ising Models*, Nature **534**, 667 (2016).

[218] P. Zupancic, P. M. Preiss, R. Ma, A. Lukin, M. Eric Tai, M. Rispoli, R. Islam, and M. Greiner, *Ultra-Precise Holographic Beam Shaping for Microscopic Quantum Control*, Optics Express **24**, 13881 (2016).

[219] M. Aidelsburger, J. L. Ville, R. Saint-Jalm, S. Nascimbène, J. Dalibard, and J. Beugnon, *Relaxation Dynamics in the Merging of N Independent Condensates*, Physical Review Letters **119**, 190403 (2017).

[220] R. Saint-Jalm, P. C. M. Castilho, É. Le Cerf, B. Bakkali-Hassani, J.-L. Ville, S. Nascimbene, J. Beugnon, and J. Dalibard, *Dynamical Symmetry and Breathers in a Two-Dimensional Bose Gas*, Physical Review X **9**, 021035 (2019).

[221] Y.-Q. Zou, É. Le Cerf, B. Bakkali-Hassani, C. Maury, G. Chauveau, P. C. M. Castilho, R. Saint-Jalm, S. Nascimbene, J. Dalibard, and J. Beugnon, *Optical Control of the Density and Spin Spatial Profiles of a Planar Bose Gas*, Journal of Physics B: Atomic, Molecular and Optical Physics **54**, 08LT01 (2021).

[222] J.-y. Choi, S. Hild, J. Zeiher, P. Schauß, A. Rubio-Abadal, T. Yefsah, V. Khemani, D. A. Huse, I. Bloch, and C. Gross, *Exploring the Many-Body Localization Transition in Two Dimensions*, Science **352**, 1547 (2016).

[223] P. Sompet, S. Hirthe, D. Bourgund, T. Chalopin, J. Bibo, J. Koepsell, P. Bojović, R. Verresen, F. Pollmann, G. Salomon, C. Gross, T. A. Hilker, and I. Bloch, *Realizing the Symmetry-Protected Haldane Phase in Fermi–Hubbard Ladders*, Nature **606**, 484 (2022).

[224] S. Hirthe, T. Chalopin, D. Bourgund, P. Bojović, A. Bohrdt, E. Demler, F. Grusdt, I. Bloch, and T. A. Hilker, *Magnetically Mediated Hole Pairing in Fermionic Ladders of Ultracold Atoms*, Nature **613**, 463 (2023).

[225] Y. Deng and D. Chu, *Coherence Properties of Different Light Sources and Their Effect on the Image Sharpness and Speckle of Holographic Displays*, Scientific Reports **7**, 5893 (2017).

[226] J. W. Goodman, *Speckle Phenomena in Optics: Theory and Applications*, Second edition (The International Society for Optical Engineering, Bellingham, 2020).

[227] J. A. Izatt and M. A. Choma, *Theory of Optical Coherence Tomography*, in *Optical Coherence Tomography*, edited by W. Drexler and J. G. Fujimoto, red. by E. Greenbaum (Springer, Berlin, Heidelberg, 2008), 47.

[228] J. Chaves, *Introduction to Nonimaging Optics*, edited by J. Chaves, 2nd ed. (CRC Press, 2017).

[229] G. Alphonse, D. Gilbert, M. Harvey, and M. Ettenberg, *High-Power Superluminescent Diodes*, IEEE Journal of Quantum Electronics **24**, 2454 (1988).

[230] C.-F. Lin and B.-L. Lee, *Extremely Broadband AlGaAs/GaAs Superluminescent Diodes*, Applied Physics Letters **71**, 1598 (1997).

[231] Z. Q. Li and Z. M. S. Li, *Comprehensive Modeling of Superluminescent Light-Emitting Diodes*, IEEE Journal of Quantum Electronics **46**, 454 (2010).

[232] A. Smith, T. Easton, V. Guarrera, and G. Barontini, *Generation of Optical Potentials for Ultracold Atoms Using a Superluminescent Diode*, Physical Review Research **3**, 033241 (2021).

[233] D. Wei, *Development of a Spatially Incoherent Laser Source*, Masterarbeit, Technische Universität München (2019).

[234] M. Born, E. Wolf, and A. B. Bhatia, *Principles of Optics: Electromagnetic Theory of Propagation, Interference, and Diffraction of Light*, Seventh (expanded) anniversary edition, 60th anniversary edition (Cambridge University Press, Cambridge, 2019).

[235] J. W. S. Rayleigh, *XXXI. Investigations in Optics, with Special Reference to the Spectroscope*, The London, Edinburgh, and Dublin Philosophical Magazine and Journal of Science **8**, 261 (1879).

[236] M. Burkhardt and A. Yen, *Ernst Abbe's Theory of Image Formation in the Microscope*, in *Ernst Abbe's Theory of Image Formation in the Microscope* (SPIE, 2023).

[237] P. L. Kapitza and P. a. M. Dirac, *The Reflection of Electrons from Standing Light Waves*, Mathematical Proceedings of the Cambridge Philosophical Society **29**, 297 (1933).

[238] P. L. Gould, G. A. Ruff, and D. E. Pritchard, *Diffraction of Atoms by Light: The near-Resonant Kapitza-Dirac Effect*, Physical Review Letters **56**, 827 (1986).

[239] O. Morsch and M. Oberthaler, *Dynamics of Bose-Einstein Condensates in Optical Lattices*, Reviews of Modern Physics **78**, 179 (2006).

[240] P. W. Anderson, *Absence of Diffusion in Certain Random Lattices*, Physical Review **109**, 1492 (1958).

[241] J. Billy, V. Josse, Z. Zuo, A. Bernard, B. Hambrecht, P. Lugan, D. Clément, L. Sanchez-Palencia, P. Bouyer, and A. Aspect, *Direct Observation of Anderson Localization of Matter Waves in a Controlled Disorder*, Nature **453**, 891 (2008).

[242] G. Roati, C. D'Errico, L. Fallani, M. Fattori, C. Fort, M. Zaccanti, G. Modugno, M. Modugno, and M. Inguscio, *Anderson Localization of a Non-Interacting Bose–Einstein Condensate*, Nature **453**, 895 (2008).

[243] S. S. Kondov, W. R. McGehee, J. J. Zirbel, and B. DeMarco, *Three-Dimensional Anderson Localization of Ultracold Matter*, Science **334**, 66 (2011).

[244] F. Jendrzejewski, A. Bernard, K. Müller, P. Cheinet, V. Josse, M. Piraud, L. Pezzé, L. Sanchez-Palencia, A. Aspect, and P. Bouyer, *Three-Dimensional Localization of Ultracold Atoms in an Optical Disordered Potential*, Nature Physics **8**, 398 (2012).

[245] M. Schreiber, S. S. Hodgman, P. Bordia, H. P. Lüschen, M. H. Fischer, R. Vosk, E. Altman, U. Schneider, and I. Bloch, *Observation of Many-Body Localization of Interacting Fermions in a Quasirandom Optical Lattice*, Science **349**, 842 (2015).

[246] R. Nandkishore and D. A. Huse, *Many-Body Localization and Thermalization in Quantum Statistical Mechanics*, Annual Review of Condensed Matter Physics **6**, 15 (2015).

[247] D. A. Abanin, E. Altman, I. Bloch, and M. Serbyn, *Colloquium: Many-body Localization, Thermalization, and Entanglement*, Reviews of Modern Physics **91**, 021001 (2019).

[248] L. N. Smith and C. J. Lobb, *Percolation in Two-Dimensional Conductor-Insulator Networks with Controllable Anisotropy*, Physical Review B **20**, 3653 (1979).

[249] A. Weinrib, *Percolation Threshold of a Two-Dimensional Continuum System*, Physical Review B **26**, 1352 (1982).

[250] S. Pilati, S. Giorgini, M. Modugno, and N. Prokof'ev, *Dilute Bose Gas with Correlated Disorder: A Path Integral Monte Carlo Study*, New Journal of Physics **12**, 073003 (2010).

[251] L. Pezzé, M. Robert-de-Saint-Vincent, T. Bourdel, J.-P. Brantut, B. Allard, T. Plisson, A. Aspect, P. Bouyer, and L. Sanchez-Palencia, *Regimes of Classical Transport of Cold Gases in a Two-Dimensional Anisotropic Disorder*, New Journal of Physics **13**, 095015 (2011).

[252] P.-P. Zheng, C. I. Timms, and M. H. Kolodrubetz, *Anomalous Floquet-Anderson Insulator with Quasiperiodic Temporal Noise*, Physical Review B **108**, 094207 (2023).

[253] J. Li, R.-L. Chu, J. K. Jain, and S.-Q. Shen, *Topological Anderson Insulator*, Physical Review Letters **102**, 136806 (2009).

[254] C. W. Groth, M. Wimmer, A. R. Akhmerov, J. Tworzydło, and C. W. Beenakker, *Theory of the Topological Anderson Insulator*, Physical Review Letters **103**, 1 (2009).

[255] H. Jiang, L. Wang, Q. F. Sun, and X. C. Xie, *Numerical Study of the Topological Anderson Insulator in HgTe/CdTe Quantum Wells*, Physical Review B - Condensed Matter and Materials Physics **80**, 1 (2009).

[256] H. M. Guo, G. Rosenberg, G. Refael, and M. Franz, *Topological Anderson Insulator in Three Dimensions*, Physical Review Letters **105**, 2 (2010).

[257] E. Prodan, *Three-Dimensional Phase Diagram of Disordered HgTe/CdTe Quantum Spin-Hall Wells*, Physical Review B - Condensed Matter and Materials Physics **83**, 1 (2011).

[258] Y. Xing, L. Zhang, and J. Wang, *Topological Anderson Insulator Phenomena*, Physical Review B - Condensed Matter and Materials Physics **84**, 1 (2011).

[259] Y. Y. Zhang, R. L. Chu, F. C. Zhang, and S. Q. Shen, *Localization and Mobility Gap in the Topological Anderson Insulator*, Physical Review B - Condensed Matter and Materials Physics **85**, 1 (2012).

[260] J. Song, H. Liu, H. Jiang, Q. F. Sun, and X. C. Xie, *Dependence of Topological Anderson Insulator on the Type of Disorder*, Physical Review B - Condensed Matter and Materials Physics **85**, 1 (2012).

[261] P. Titum, N. H. Lindner, M. C. Rechtsman, and G. Refael, *Disorder-Induced Floquet Topological Insulators*, Physical Review Letters **114**, 056801 (2015).

[262] E. J. Meier, F. A. An, A. Dauphin, M. Maffei, P. Massignan, T. L. Hughes, and B. Gadway, *Observation of the Topological Anderson Insulator in Disordered Atomic Wires*, Science **362**, 929 (2018).

[263] W. Dür, R. Raussendorf, V. M. Kendon, and H.-J. Briegel, *Quantum Walks in Optical Lattices*, Physical Review A **66**, 052319 (2002).

[264] M. Karski, L. Forster, J.-M. Choi, A. Steffen, W. Alt, D. Meschede, and A. Widera, *Quantum Walk in Position Space with Single Optically Trapped Atoms*, Science **325**, 174 (2009).

[265] J. P. Ronzheimer, M. Schreiber, S. Braun, S. S. Hodgman, S. Langer, I. P. McCulloch, F. Heidrich-Meisner, I. Bloch, and U. Schneider, *Expansion Dynamics of Interacting Bosons in Homogeneous Lattices in One and Two Dimensions*, Physical Review Letters **110**, 205301 (2013).

[266] P. M. Preiss, R. Ma, M. E. Tai, A. Lukin, M. Rispoli, P. Zupancic, Y. Lahini, R. Islam, and M. Greiner, *Strongly Correlated Quantum Walks in Optical Lattices*, Science **347**, 1229 (2015).

[267] D. Wei, D. Adler, K. Srakaew, S. Agrawal, P. Weckesser, I. Bloch, and J. Zeiher, *Observation of Brane Parity Order in Programmable Optical Lattices*, Physical Review X **13**, 021042 (2023).

[268] Q. Niu and D. J. Thouless, *Quantised Adiabatic Charge Transport in the Presence of Substrate Disorder and Many-Body Interaction*, Journal of Physics A: Mathematical and General **17**, 2453 (1984).

[269] A. A. Greshnov and G. G. Zegrya, *Integer Quantum Hall Effect and Correlated Disorder*, Semiconductors **41**, 1329 (2007).

[270] D. P. Kelly, *Numerical Calculation of the Fresnel Transform*, Journal of the Optical Society of America A **31**, 755 (2014).

[271] J. W. Goodman, *Simulating Speckle with Mathematica*, SPIE PM vol. no. 355 (SPIE, Bellingham, Washington, USA, 2022).

[272] P. Pedri, L. Pitaevskii, S. Stringari, C. Fort, S. Burger, F. S. Cataliotti, P. Maddaloni, F. Minardi, and M. Inguscio, *Expansion of a Coherent Array of Bose-Einstein Condensates*, Physical Review Letters **87**, 220401 (2001).

[273] F. Gerbier, A. Widera, S. Fölling, O. Mandel, T. Gericke, and I. Bloch, *Phase Coherence of an Atomic Mott Insulator*, Physical Review Letters **95**, 050404 (2005).

[274] F. Gerbier, A. Widera, S. Fölling, O. Mandel, T. Gericke, and I. Bloch, *Interference Pattern and Visibility of a Mott Insulator*, Physical Review A **72**, 053606 (2005).

[275] E. C. G. Stueckelberg, *Theorie Der Unelastischen Stösse Zwischen Atomen*, Helvetica physica acta **5**, 369 (1932).

[276] S. Kling, T. Salger, C. Grossert, and M. Weitz, *Atomic Bloch-Zener Oscillations and Stückelberg Interferometry in Optical Lattices*, Physical Review Letters **105**, 215301 (2010).

[277] A. Zenesini, D. Ciampini, O. Morsch, and E. Arimondo, *Observation of Stückelberg Oscillations in Accelerated Optical Lattices*, Physical Review A: Atomic, Molecular, and Optical Physics **82**, 065601 (2010).

[278] M. Greiner, I. Bloch, O. Mandel, T. W. Hänsch, and T. Esslinger, *Exploring Phase Coherence in a 2D Lattice of Bose-Einstein Condensates*, Physical Review Letters **87**, 160405 (2001).

[279] T. A. Hilker, G. Salomon, F. Grusdt, A. Omran, M. Boll, E. Demler, I. Bloch, and C. Gross, *Revealing Hidden Antiferromagnetic Correlations in Doped Hubbard Chains via String Correlators*, Science **357**, 484 (2017).

[280] W. J. Kwon, G. Del Pace, K. Xhani, L. Galantucci, A. Muzi Falconi, M. Inguscio, F. Scazza, and G. Roati, *Sound Emission and Annihilations in a Programmable Quantum Vortex Collider*, Nature **600**, 64 (2021).

[281] Y. Zhang and H. Gross, *Systematic Design of Microscope Objectives. Part I: System Review and Analysis*, Advanced Optical Technologies **8**, 313 (2019).

[282] Y. Zhang and H. Gross, *Systematic Design of Microscope Objectives. Part II: Lens Modules and Design Principles*, Advanced Optical Technologies **8**, 349 (2019).

[283] Y. Zhang and H. Gross, *Systematic Design of Microscope Objectives. Part III: Miscellaneous Design Principles and System Synthesis: Systematic Design of Microscope Objectives. Part I/II/III*, Advanced Optical Technologies **8**, 385 (2019).

[284] L. Duca, T. Li, M. Reitter, I. Bloch, M. Schleier-Smith, and U. Schneider, *An Aharonov-Bohm Interferometer for Determining Bloch Band Topology*, Science **347**, 288 (2015).

[285] T. Li, L. Duca, M. Reitter, F. Grusdt, E. Demler, M. Endres, M. Schleier-Smith, I. Bloch, and U. Schneider, *Bloch State Tomography Using Wilson Lines*, Science **352**, 1094 (2016).

[286] C. L. Hung, X. Zhang, L. C. Ha, S. K. Tung, N. Gemelke, and C. Chin, *Extracting Density-Density Correlations from in Situ Images of Atomic Quantum Gases*, New Journal of Physics **13**, 070519 (2011).

[287] P. Törmä and K. Sengstock, eds., *Quantum Gas Experiments: Exploring Many-Body States*, Cold Atoms vol. 3 (Imperial College Press, London, 2015).

[288] M. Naraschewski and R. J. Glauber, *Spatial Coherence and Density Correlations of Trapped Bose Gases*, Physical Review A **59**, 4595 (1999).

[289] J. P. Sethna, *Statistical Mechanics: Entropy, Order Parameters, and Complexity*, Repr. 2012 (twice), Oxford Master Series in Physics Statistical, Computational, and Theoretical Physics 14 (Oxford Univ. Press, Oxford, 2012).

[290] W. Ketterle, D. S. Durfee, and D. M. Stamper-Kurn, *Making, Probing and Understanding Bose-Einstein Condensates*, 1999, arXiv:cond-mat/9904034, preprint.

[291] H. Haken and H. C. Wolf, *Atom- und Quantenphysik*, Springer-Lehrbuch (Springer, Berlin, Heidelberg, 2004).

[292] M. Hans, F. Schmutte, C. Viermann, N. Liebster, M. Sparn, M. K. Oberthaler, and H. Strobel, *High Signal to Noise Absorption Imaging of Alkali Atoms at Moderate Magnetic Fields*, Review of Scientific Instruments **92**, 023203 (2021).

[293] G. Reinaudi, T. Lahaye, Z. Wang, and D. Guéry-Odelin, *Strong Saturation Absorption Imaging of Dense Clouds of Ultracold Atoms*, Optics Letters **32**, 3143 (2007).

[294] R. H. Dicke, *Coherence in Spontaneous Radiation Processes*, Physical Review **93**, 99 (1954).

[295] G. Ferioli, A. Glicenstein, F. Robicheaux, R. T. Sutherland, A. Browaeys, and I. Ferrier-Barbut, *Laser-Driven Superradiant Ensembles of Two-Level Atoms near Dicke Regime*, Physical Review Letters **127**, 243602 (2021).

[296] J. W. Goodman, *Introduction to Fourier Optics*, 3rd ed (Roberts & Co. Publishers, Englewood, Colo, 2005).

[297] N. Goldman, G. Juzeliūnas, P. Öhberg, and I. B. Spielman, *Light-Induced Gauge Fields for Ultracold Atoms*, Reports on Progress in Physics **77**, 126401 (2014).

[298] K. W. Madison, F. Chevy, W. Wohlleben, and J. Dalibard, *Vortex Formation in a Stirred Bose-Einstein Condensate*, Physical Review Letters **84**, 806 (2000).

[299] V. Schweikhard, I. Coddington, P. Engels, V. P. Mogendorff, and E. A. Cornell, *Rapidly Rotating Bose-Einstein Condensates in and near the Lowest Landau Level*, Physical Review Letters **92**, 040404 (2004).

[300] Y.-J. Lin, K. Jiménez-García, and I. B. Spielman, *Spin–Orbit-Coupled Bose–Einstein Condensates*, Nature **471**, 83 (2011).

[301] Z. Wu, L. Zhang, W. Sun, X.-T. Xu, B.-Z. Wang, S.-C. Ji, Y. Deng, S. Chen, X.-J. Liu, and J.-W. Pan, *Realization of Two-Dimensional Spin-Orbit Coupling for Bose-Einstein Condensates*, Science **354**, 83 (2016).

[302] J. Struck, C. Ölschläger, M. Weinberg, P. Hauke, J. Simonet, A. Eckardt, M. Lewenstein, K. Sengstock, and P. Windpassinger, *Tunable Gauge Potential for Neutral and Spinless Particles in Driven Optical Lattices*, Physical Review Letters **108**, 225304 (2012).

[303] K. Jiménez-García, L. J. LeBlanc, R. A. Williams, M. C. Beeler, A. R. Perry, and I. B. Spielman, *Peierls Substitution in an Engineered Lattice Potential*, Physical Review Letters **108**, 225303 (2012).

[304] C. V. Parker, L.-C. Ha, and C. Chin, *Direct Observation of Effective Ferromagnetic Domains of Cold Atoms in a Shaken Optical Lattice*, Nature Physics **9**, 769 (2013).

[305] N. Fläschner, B. S. Rem, M. Tarnowski, D. Vogel, D.-S. Lühmann, K. Sengstock, and C. Weitenberg, *Experimental Reconstruction of the Berry Curvature in a Floquet Bloch Band*, Science **352**, 1091 (2016).

[306] H. M. Price and N. R. Cooper, *Mapping the Berry Curvature from Semiclassical Dynamics in Optical Lattices*, Physical Review A: Atomic, Molecular, and Optical Physics **85**, 033620 (2012).

[307] A. Dauphin and N. Goldman, *Extracting the Chern Number from the Dynamics of a Fermi Gas: Implementing a Quantum Hall Bar for Cold Atoms*, Physical Review Letters **111**, 135302 (2013).

[308] M. Buchhold, D. Cocks, and W. Hofstetter, *Effects of Smooth Boundaries on Topological Edge Modes in Optical Lattices*, Physical Review A **85**, 063614 (2012).

[309] R. Rammal, G. Toulouse, M. T. Jaekel, and B. I. Halperin, *Quantized Hall Conductance and Edge States: Two-dimensional Strips with a Periodic Potential*, Physical Review B **27**, 5142 (1983).

[310] A. H. MacDonald, *Edge States and Quantized Hall Conductivity in a Periodic Potential*, Physical Review B **29**, 6563 (1984).

[311] X.-L. Qi, Y.-S. Wu, and S.-C. Zhang, *General Theorem Relating the Bulk Topological Number to Edge States in Two-Dimensional Insulators*, Physical Review B **74**, 045125 (2006).

[312] G. Baym and C. J. Pethick, *Ground-State Properties of Magnetically Trapped Bose-Condensed Rubidium Gas*, Physical Review Letters **76**, 6 (1996).

[313] C. Pethick and H. Smith, *Bose-Einstein Condensation in Dilute Gases*, 2nd ed (Cambridge University Press, Cambridge; New York, 2008).

[314] L. P. Pitaevskiĭ and S. Stringari, *Bose-Einstein Condensation and Superfluidity*, First edition, International Series of Monographs on Physics 164 (Oxford University Press, Oxford, United Kingdom, 2016).

[315] U. Schneider, L. Hackermüller, J. P. Ronzheimer, S. Will, S. Braun, T. Best, I. Bloch, E. Demler, S. Mandt, D. Rasch, and A. Rosch, *Fermionic Transport and Out-of-Equilibrium Dynamics in a Homogeneous Hubbard Model with Ultracold Atoms*, Nature Physics **8**, 213 (2012).

[316] M. Hafezi, S. Mittal, J. Fan, A. Migdall, and J. M. Taylor, *Imaging Topological Edge States in Silicon Photonics*, Nature Photonics **7**, 1001 (2013).

[317] R. Süsstrunk and S. D. Huber, *Observation of Phononic Helical Edge States in a Mechanical Topological Insulator*, Science **349**, 47 (2015).

[318] T. D. Stanescu, V. Galitski, and S. Das Sarma, *Topological States in Two-Dimensional Optical Lattices*, Physical Review A **82**, 013608 (2010).

[319] M. Leder, C. Grossert, L. Sitta, M. Genske, A. Rosch, and M. Weitz, *Real-Space Imaging of a Topologically Protected Edge State with Ultracold Atoms in an Amplitude-Chirped Optical Lattice*, Nature Communications **7**, 13112 (2016).

[320] S. de Léséleuc, V. Lienhard, P. Scholl, D. Barredo, S. Weber, N. Lang, H. P. Büchler, T. Lahaye, and A. Browaeys, *Observation of a Symmetry-Protected Topological Phase of Interacting Bosons with Rydberg Atoms*, Science **365**, 775 (2019).

[321] G. H. Wannier, *Wave Functions and Effective Hamiltonian for Bloch Electrons in an Electric Field*, Physical Review **117**, 432 (1960).

[322] S. Y. Kruchinin, F. Krausz, and V. S. Yakovlev, *Colloquium : Strong-field Phenomena in Periodic Systems*, Reviews of Modern Physics **90**, 021002 (2018).

[323] M. F. Martínez and F. N. Ünal, *Wave Packet Dynamics and Edge Transport in Anomalous Floquet Topological Phases*, 2023, arXiv:2302.08485, preprint.

[324] V. Venkatachalam, S. Hart, L. Pfeiffer, K. West, and A. Yacoby, *Local Thermometry of Neutral Modes on the Quantum Hall Edge*, Nature Physics **8**, 676 (2012).

[325] J.-Y. Zhang, C.-R. Yi, L. Zhang, R.-H. Jiao, K.-Y. Shi, H. Yuan, W. Zhang, X.-J. Liu, S. Chen, and J.-W. Pan, *Tuning Anomalous Floquet Topological Bands with Ultracold Atoms*, Physical Review Letters **130**, 043201 (2023).

[326] Y. Ji, Y. Chung, D. Sprinzak, M. Heiblum, D. Mahalu, and H. Shtrikman, *An Electronic Mach–Zehnder Interferometer*, Nature **422**, 415 (2003).

[327] M. Carrega, L. Chirolli, S. Heun, and L. Sorba, *Anyons in Quantum Hall Interferometry*, Nature Reviews Physics **3**, 698 (2021).

[328] P. Roulleau, F. Portier, P. Roche, A. Cavanna, G. Faini, U. Gennser, and D. Mailly, *Direct Measurement of the Coherence Length of Edge States in the Integer Quantum Hall Regime*, Physical Review Letters **100**, 126802 (2008).

[329] J.-H. Zheng, A. Dutta, M. Aidelsburger, and W. Hofstetter, *Floquet Topological Phase Transitions Induced by Uncorrelated or Correlated Disorder*, 2023, arXiv:2309.07035, preprint.

[330] L. Asteria, H. P. Zahn, M. N. Kosch, K. Sengstock, and C. Weitenberg, *Quantum Gas Magnifier for Sub-Lattice-Resolved Imaging of 3D Quantum Systems*, Nature **599**, 571 (2021).

[331] A. Lazarides, A. Das, and R. Moessner, *Equilibrium States of Generic Quantum Systems Subject to Periodic Driving*, Physical Review E **90**, 012110 (2014).

[332] L. D'Alessio and M. Rigol, *Long-Time Behavior of Isolated Periodically Driven Interacting Lattice Systems*, Physical Review X **4**, 041048 (2014).

[333] M. Bukov, S. Gopalakrishnan, M. Knap, and E. Demler, *Prethermal Floquet Steady States and Instabilities in the Periodically Driven, Weakly Interacting Bose-Hubbard Model*, Physical Review Letters **115**, 205301 (2015).

[334] E. Canovi, M. Kollar, and M. Eckstein, *Stroboscopic Prethermalization in Weakly Interacting Periodically Driven Systems*, Physical Review E **93**, 012130 (2016).

[335] T. Mori, T. Kuwahara, and K. Saito, *Rigorous Bound on Energy Absorption and Generic Relaxation in Periodically Driven Quantum Systems*, Physical Review Letters **116**, 120401 (2016).

[336] D. A. Abanin, W. De Roeck, W. W. Ho, and F. Huveneers, *Effective Hamiltonians, Prethermalization, and Slow Energy Absorption in Periodically Driven Many-Body Systems*, Physical Review B **95**, 014112 (2017).

[337] S. A. Weidinger and M. Knap, *Floquet Prethermalization and Regimes of Heating in a Periodically Driven, Interacting Quantum System*, Scientific Reports **7**, 45382 (2017).

[338] D. Abanin, W. De Roeck, W. W. Ho, and F. Huveneers, *A Rigorous Theory of Many-Body Prethermalization for Periodically Driven and Closed Quantum Systems*, Communications in Mathematical Physics **354**, 809 (2017).

[339] A. Haldar, R. Moessner, and A. Das, *Onset of Floquet Thermalization*, Physical Review B **97**, 245122 (2018).

[340] K. Mallayya, M. Rigol, and W. De Roeck, *Prethermalization and Thermalization in Isolated Quantum Systems*, Physical Review X **9**, 021027 (2019).

[341] K. Mallayya and M. Rigol, *Heating Rates in Periodically Driven Strongly Interacting Quantum Many-Body Systems*, Physical Review Letters **123**, 240603 (2019).

[342] A. Rubio-Abadal, M. Ippoliti, S. Hollerith, D. Wei, J. Rui, S. L. Sondhi, V. Khemani, C. Gross, and I. Bloch, *Floquet Prethermalization in a Bose-Hubbard System*, Physical Review X **10**, 021044 (2020).

[343] P. Peng, C. Yin, X. Huang, C. Ramanathan, and P. Cappellaro, *Floquet Prethermalization in Dipolar Spin Chains*, Nature Physics **17**, 444 (2021).

[344] B. Ye, F. Machado, and N. Y. Yao, *Floquet Phases of Matter via Classical Prethermalization*, Physical Review Letters **127**, 140603 (2021).

[345] S. Ghosh, D. Sen, and K. Sengupta, *Detecting Prethermal Floquet Phases of Rydberg Atom Arrays*, Physical Review B **108**, 094302 (2023).

[346] G. He, B. Ye, R. Gong, Z. Liu, K. W. Murch, N. Y. Yao, and C. Zu, *Quasi-Floquet Prethermalization in a Disordered Dipolar Spin Ensemble in Diamond*, Physical Review Letters **131**, 130401 (2023).

[347] K. Viebahn, J. Minguzzi, K. Sandholzer, A.-S. Walter, M. Sajnani, F. Görg, and T. Esslinger, *Suppressing Dissipation in a Floquet-Hubbard System*, Physical Review X **11**, 011057 (2021).

[348] P. Ponte, Z. Papić, F. Huveneers, and D. A. Abanin, *Many-Body Localization in Periodically Driven Systems*, Physical Review Letters **114**, 140401 (2015).

[349] A. Lazarides, A. Das, and R. Moessner, *Fate of Many-Body Localization Under Periodic Driving*, Physical Review Letters **115**, 030402 (2015).

[350] D. A. Abanin, W. De Roeck, and F. Huveneers, *Exponentially Slow Heating in Periodically Driven Many-Body Systems*, Physical Review Letters **115**, 256803 (2015).

[351] D. A. Abanin, W. De Roeck, and F. Huveneers, *Theory of Many-Body Localization in Periodically Driven Systems*, Annals of Physics **372**, 1 (2016).

[352] F. Nathan, D. Abanin, E. Berg, N. H. Lindner, and M. S. Rudner, *Anomalous Floquet Insulators*, Physical Review B **99**, 195133 (2019).

[353] T. Neupert, L. Santos, C. Chamon, and C. Mudry, *Fractional Quantum Hall States at Zero Magnetic Field*, Physical Review Letters **106**, 236804 (2011).

[354] I. Vasić, A. Petrescu, K. Le Hur, and W. Hofstetter, *Chiral Bosonic Phases on the Haldane Honeycomb Lattice*, Physical Review B **91**, 094502 (2015).

[355] Y. Kuno, T. Nakafuji, and I. Ichinose, *Phase Diagrams of the Bose-Hubbard Model and the Haldane-Bose-Hubbard Model with Complex Hopping Amplitudes*, Physical Review A **92**, 063630 (2015).

[356] K. Plekhanov, G. Roux, and K. Le Hur, *Floquet Engineering of Haldane Chern Insulators and Chiral Bosonic Phase Transitions*, Physical Review B **95**, 045102 (2017).

[357] W. Hofstetter and T. Qin, *Quantum Simulation of Strongly Correlated Condensed Matter Systems*, Journal of Physics B: Atomic, Molecular and Optical Physics **51**, 082001 (2018).

[358] A. Rubio-García, C. N. Self, J. J. García-Ripoll, and J. K. Pachos, *Seeing Topological Edge and Bulk Currents in Time-of-Flight Images*, Physical Review B **102**, 041123 (2020).

[359] X.-Q. Wang, G.-Q. Luo, J.-Y. Liu, W. V. Liu, A. Hemmerich, and Z.-F. Xu, *Evidence for an Atomic Chiral Superfluid with Topological Excitations*, Nature **596**, 227 (2021).

[360] S. Miao, Z. Zhang, Y. Zhao, Z. Zhao, H. Wang, and J. Hu, *Bosonic Fractional Quantum Hall Conductance in Shaken Honeycomb Optical Lattices without Flat Bands*, Physical Review B **106**, 054310 (2022).

[361] W. Magnus, *On the Exponential Solution of Differential Equations for a Linear Operator*, Communications on Pure and Applied Mathematics **7**, 649 (1954).

[362] M. M. Maricq, *Application of Average Hamiltonian Theory to the NMR of Solids*, Physical Review B **25**, 6622 (1982).

[363] T. P. Grozdanov and M. J. Raković, *Quantum System Driven by Rapidly Varying Periodic Perturbation*, Physical Review A **38**, 1739 (1988).

Acknowledgements

I want to first thank all the great people who made this work possible and potentially are not explicitly mentioned below.

First of all I want to thank Immanuel Bloch for giving me the opportunity and trust to do my PhD in his group. I have really enjoyed the atmosphere and research environment he created making the research we do possible and fun. I especially want to mention the anticipation and excellent management during the COVID pandemic enabling us to uninterruptedly continue working on the experiment. I have greatly benefited from the discussions, the search for intuitive insights on the interpretation of our results and the encouragement he provided.

I want to express the same gratitude to Monika Aidelsburger for the supervision and support during my PhD. It was a pleasure to work with her, I really enjoyed the freedom she gave us on exploring our own ideas in the lab, and the understanding for exchanging the MSquared all the time. Though leading four experiments she was always happy to answer any questions and dedicated to bringing the experiment forward.

A big thanks goes to the whole Fermi2 team, we spent a lot of time together in the lab measuring but also fixing things and most of the times having fun doing it. I want to thank Karen Wintersperger for teaching me how our experiment works, how to make it work if it doesn't and exploring the honeycomb lattice together. I was really inspired by her energy and dedication to the experiment and its theory. I really admire the skill set she brought to the experiment. I want to thank Raphaël Saint-Jalm who has never ceased to listen to my ideas and taking great time in explaining all the things I did not understand. I really learned a lot from him in many different perspectives - although not planned we really had a nice Christmas Eve together. I want to thank Alexander Hesse for all the support during the new contributions we made to the experiment and challenging me to reconsider if we can't do things more clever, Johannes Arceri for taking on the responsibility in the lab more recently. I am convinced the experiment is in good hands and will be able to produce exciting results in the near future. During my PhD I had the pleasure to supervise and learn from the excellent students Valentin Weyerer, Justus Urbanetz and Simon Karch.

Many thanks goes to the whole Bloch and Aidelsburger group for the good atmosphere and the friendly and helpful and extremely supportive environment. I want to especially thank Nelson Darkwah Oppong, Oscar Bettermann, Giulio Pasqualetti, Etienne Staub, Tim Höhn, Hendrik van Raven, Alexander Impertro, Julian Wienand, Simon Karch for fun lunch breaks, many discussions and fun evenings. I want to thank Cesar Cabrera for many inspiring discussions, the fun times you provided with your open mindset and I am sorry for not being able to implement any of the many ideas you had for our experiment. I want to thank Sebastian Scherg and Thomas Kohlert for being excellent neighbors and fun colleages. I want to thank Till Klostermann and Simon Weinzierl for many fun running sessions and Lederhosentrainings. Even though the communication with the Garching part of the group had its ups and downs I want to thank all the MPQ colleagues for being supportive and helpful at all times.